

# **Satellite Microwave Sensing of Oceanic Cloud Liquid Water: Application to the Earth Radiation Budget and Climate**

By

Thomas J. Greenwald and Graeme L. Stephens

Department of Atmospheric Science  
Colorado State University  
Fort Collins, Colorado

Research was supported by NASA graduate student fellowship in Global Change Research (Grant #NGT-30046), NASA Research Grant Award #NAG-8-981, and NOAA grant NA37RJ0202.  
PI: G. Stephens



**Department of  
Atmospheric Science**

Paper No. 572

**SATELLITE MICROWAVE SENSING OF OCEANIC CLOUD  
LIQUID WATER: APPLICATION TO THE EARTH RADIATION  
BUDGET AND CLIMATE**

Thomas J. Greenwald and Graeme L. Stephens

Research Supported by NASA Graduate Student Fellowship in Global  
Change Research (Grant # NGT-30046), NASA Research Grant Award  
# NAG-8-981, and NOAA Grant NA37RJ0202.

Principal Investigator: Graeme L. Stephens

Department of Atmospheric Science  
Colorado State University  
Fort Collins, CO 80523

March 1995

Atmospheric Science Paper No. 572

## ABSTRACT

Understanding the various complex interactions of cloud properties with the Earth's radiation budget, thermodynamical processes and atmospheric dynamics is crucial in determining the role of clouds in global climate. The following research addresses one aspect of this broad problem by attempting to describe the large-scale characteristics of cloud liquid water and the relationships of this bulk cloud property to the temperature field and the radiation budget using satellite microwave sensing techniques and the latest satellite data sets from the Earth Radiation Budget Experiment (ERBE) and the International Satellite Cloud Climatology Project (ISCCP).

A method of remotely sensing integrated cloud liquid water over the oceans using space-borne passive measurements from the Special Sensor Microwave/Imager (SSM/I) is described. The technique is comprised of a simple physical model that uses the 19.35 and 37 GHz channels of the SSM/I. The most comprehensive validation to date of cloud liquid water estimated from satellites is presented. This is accomplished through a comparison to independent ground-based microwave radiometer measurements of liquid water at four different sites, which show that the satellite retrievals are consistent with the ground-based measurements for nonprecipitating cloud systems in the subtropics and middle to high latitudes. The comparison in the tropics, however, was less conclusive. Nevertheless, the retrieval method appears to have general applicability over most areas of the global oceans. A simple sensitivity and error analysis suggests that the liquid water estimates have total errors of roughly 30% under average conditions. However, the error can vary considerably depending on the atmospheric/surface conditions and on the amount of liquid water present in the cloud.

The spatial distribution and temporal variability of cloud liquid water across the world's oceans are investigated using observations over a 53-month period beginning in

July, 1987 and ending in December, 1991. Many spatial characteristics of cloud liquid water are found to be closely linked to known large-scale circulation patterns. The highest values of over  $0.15 \text{ kg m}^{-2}$  occur along principal routes of northern midlatitude storms and in areas dominated by tropical convection. The zonally averaged structure of cloud liquid water is distinctly trimodal, with maxima appearing in the midlatitudes and a single primary maximum in the tropics. The average marine cloud liquid water over the globe is estimated to be about  $0.11 \text{ kg m}^{-2}$ . Its highest seasonal variability, ranging from 20% to 30% of the annual mean, occurs in the tropics and at middle to high northern latitudes. Further comparisons of cloud liquid water to temperature for low clouds during the summer and winter seasons of 1990 reveal significant positive correlations at colder temperatures and negative correlations at warmer temperatures. The correlations also show strong seasonal and regional variation.

The relationship of cloud liquid water to the Earth's radiation budget is also investigated. The seasonal variation of cloud liquid water is found to coincide well with variations in cloud albedo and total cloudiness in many regions. The sensitivity of the net radiative fluxes at the top of the atmosphere to changes in cloud liquid water are large and nearly constant for low-lying stratiform clouds but are greatly reduced for clouds of greater vertical extent and high liquid water due to enhanced longwave effects. Another important result is that observational comparisons of cloud albedo and cloud liquid water in the North Pacific and North Atlantic during the summer exhibit reasonably large discrepancies with what is expected from theory.

## ACKNOWLEDGEMENTS

We thank the following individuals for their many helpful and insightful discussions during the course of this work: Paul Stackhouse, Darren Jackson, Dave Duda, and Frank Evans. We also appreciate the assistance of Kelly Dean in accessing the local satellite data archives. There are also many individuals who deserve recognition for their generosity in supplying various ground-based data sets and other related data; they include Ute Hargens, Jack Snider, C. Prabhakara, John Alishouse, Yong Han, Grant Petty, and Chris Kummerow.

This research was funded by a NASA Graduate Student Fellowship in Global Change Research (grant #NGT-30046), NASA research grant award #NAG8-981 and NOAA grant #NA37RJ0202.

## CONTENTS

<b>1 INTRODUCTION</b>	<b>1</b>
<b>2 RETRIEVAL OF CLOUD LIQUID WATER FROM PASSIVE MICROWAVE MEASUREMENTS</b>	<b>5</b>
2.1 The Microwave Absorption Spectrum . . . . .	5
2.2 A Brief History of Cloud Liquid Water Retrieval . . . . .	10
2.3 The Special Sensor Microwave/Imager . . . . .	12
2.3.1 Instrument characteristics and performance . . . . .	12
2.3.2 Data . . . . .	16
2.4 Development of a Physical Method to Estimate Cloud Liquid Water . . . . .	17
2.4.1 Model description . . . . .	18
2.4.2 Model calibration . . . . .	29
2.4.3 Precipitation effects . . . . .	32
<b>3 RETRIEVAL ERROR ANALYSIS AND VALIDATION</b>	<b>35</b>
3.1 Error and Sensitivity Analysis . . . . .	35
3.1.1 Simulations . . . . .	35
3.1.2 Error estimates . . . . .	39
3.2 Validation . . . . .	48
3.2.1 Comparison to visible reflectance method . . . . .	50
3.2.2 Comparison to surface-based measurements . . . . .	52
3.3 Comparison to Other Microwave Methods . . . . .	63
<b>4 GLOBAL CHARACTERISTICS OF MARINE CLOUD LIQUID WATER</b>	<b>70</b>
4.1 Data Description . . . . .	70
4.2 Spatial Distribution and Temporal Statistics . . . . .	72
4.3 Cloud Liquid Water-Temperature Sensitivity Analysis . . . . .	84
4.3.1 Data and analysis method . . . . .	84
4.3.2 Results . . . . .	87
4.4 Comparisons to General Circulation Models . . . . .	94
4.4.1 Model descriptions . . . . .	94
4.4.2 Results . . . . .	95
<b>5 OBSERVED RELATIONSHIPS BETWEEN CLOUD LIQUID WATER AND THE EARTH'S RADIATION BUDGET</b>	<b>104</b>
5.1 Radiation Budget Data . . . . .	104
5.2 Seasonal Aspects of the Relationships . . . . .	111
5.3 Cloud Liquid Water and Cloud Albedo . . . . .	125

<b>6 CONCLUSIONS AND FUTURE WORK</b>	<b>137</b>
<b>A Inventory of missing SSM/I data</b>	<b>157</b>
<b>B Improved retrieval algorithms</b>	<b>158</b>

## LIST OF FIGURES

2.1	Total atmospheric transmission as a function of frequency for different atmospheric conditions. Solid curve is for a completely dry atmosphere using the U.S. standard atmosphere. Dotted curves are for the McClatchey mid-latitude winter profile (integrated water vapor of $8.7 \text{ kg m}^{-2}$ ) and dashed curves are for the tropical profile (integrated water vapor of $42.3 \text{ kg m}^{-2}$ ). Thin dotted and dashed curves include a nonprecipitating cloud with an integrated liquid water content of $0.2 \text{ kg m}^{-2}$ . . . . .	6
2.2	Imaginary part of the refractive index of pure ice and water versus frequency (GHz) for different temperatures (K) based on the results of Ray (1972) and Warren (1984). Higher temperatures (300, 280, and 260 K) correspond to water and lower temperatures (220, 240, and 260 K) are for ice. . . . .	8
2.3	Mass absorption coefficient of pure liquid water ( $\text{m}^2 \text{ kg}^{-1}$ ) for small drops from 3 to 100 GHz for different temperatures (K). . . . .	9
2.4	Scan geometry of the Special Sensor Microwave/Imager (from Hollinger et al., 1987). . . . .	13
2.5	Water vapor retrievals for cloudless conditions from the method of Tjemkes et al. (1991) versus actual $W$ ( $\text{kg m}^{-2}$ ) using simulated brightness temperatures over a smooth ocean from 81 radiosonde profiles over the ocean. Also included is the corrected algorithm (filled circles) and the rms errors. The line of perfect agreement is also shown. . . . .	21
2.6	Calculations of 37 GHz brightness temperatures from the simple model (2.7) versus more detailed calculations (actual) under clear sky conditions. . . . .	23
2.7	Theoretical calculations of oxygen transmission at 19.35 and 37 GHz versus surface air temperature (K) for 81 radiosonde temperature profiles over the ocean. Also indicated are cubic fits to the data points for each frequency, whose coefficients are shown in Table 2.3. . . . .	26
2.8	Comparison of SSM/I-derived precipitable water ( $W$ , $\text{kg m}^{-2}$ ) and radiosonde measurements during the 1989 International Cirrus Experiment (ICE) and the 1990 Tropical Cyclone Motion (TCM) Experiment. . . . .	28
2.9	Scatter diagram of total water vapor optical depth at 37 GHz ( $\tau_{w37}$ ) versus $W$ retrieved from 19 GHz measurements ( $W_{19}$ , $\text{kg m}^{-2}$ ) for the cloud-free data set. Also shown is a linear least squares fit of the data where the slope corresponds to the water vapor absorption coefficient at 37 GHz ( $\kappa_{w37}$ ). . . . .	30
2.10	Histogram of integrated cloud liquid water ( $\text{kg m}^{-2}$ ) retrieved from the cloud-free data set. The mean and standard deviation are also given. . . . .	31
2.11	Global distributions for (a) January 1990 and (b) July 1990 of the number of satellite pixels with cloud liquid water retrievals greater than $0.5 \text{ kg m}^{-2}$ on a $2.5^\circ$ grid. These data provide an estimate of the precipitation frequency. . . . .	33

3.1	Vertical profiles of (a) cloud liquid water and temperature and (b) specific humidity used in the radiative transfer calculations. Also shown is the integrated water vapor ( $W$ ) for each humidity profile. . . . .	36
3.2	Scatter diagram of simulated brightness temperatures at 37v GHz versus those at 19.35v GHz for clear conditions (circles), nonprecipitating clouds (filled circles), and for a tropical mesoscale convective system (crosses). The ellipse illustrates the approximate range of brightness temperatures where the present liquid water retrieval method is valid. . . . .	39
3.3	Total error estimates of the cloud liquid water retrievals for a wind speed of (a) $6 \text{ m s}^{-1}$ and (b) $20 \text{ m s}^{-1}$ as a function of $L$ ( $\text{kg m}^{-2}$ ) and $W$ ( $\text{kg m}^{-2}$ ). . . . .	42
3.4	Same as Fig. 3.3 except that the error estimates are expressed instead as a percentage of the amount of liquid water $L$ . . . . .	43
3.5	Individual error contributions of different variables to the cloud liquid water retrievals for integrated water vapor values ( $W$ ) of (a) $60 \text{ kg m}^{-2}$ and (b) $10 \text{ kg m}^{-2}$ as a function of $L$ ( $\text{kg m}^{-2}$ ), where $u$ is wind speed, $T_c$ is cloud temperature, $T_s$ is sea surface temperature, $T_{19v}$ and $T_{37v}$ are brightness temperatures, $\kappa_{w19}$ and $\kappa_{w37}$ are the water vapor coefficients, and $Tr_{ox19}$ and $Tr_{ox37}$ are the oxygen transmissions. Calculations were done assuming a surface wind speed of $6 \text{ m s}^{-1}$ . . . . .	44
3.6	Same as Fig. 3.5 except for a near-surface wind speed of $20 \text{ m s}^{-1}$ . . . . .	45
3.7	(a) Global distribution and (b) zonal average of total error estimates in SSM/I cloud liquid water retrievals for 1990. In (b) the solid curve is the annual mean cloud liquid water excluding clear pixels (i.e. for $L < 0.025 \text{ kg m}^{-2}$ ) and the gray shading shows the error as one standard deviation above and below the annual mean. . . . .	49
3.8	Scatter diagram of cloud liquid water path ( $\text{kg m}^{-2}$ ) derived from the present method (SSM/I) versus the visible reflectance retrievals (AVHRR) over San Nicolas Island. Error bars represent the spatial variability of the measurements and are one standard deviation above and below the points. . . . .	53
3.9	Comparison of histograms of LWP ( $\text{kg m}^{-2}$ ) from the SSM/I and ground observations for cases in July 1987 over San Nicolas Island. . . . .	55
3.10	Comparison of histograms of LWP ( $\text{kg m}^{-2}$ ) from the SSM/I and ground observations for cases in March and April 1988 over Kwajalein Island. . . . .	56
3.11	(a) NOAA-10 visible image over Kwajalein Island for March 26, 1988, at 2000 UT. (b) SSM/I-derived cloud liquid water field for the same day at 1907 UT. Gray areas denote where $LWP > 0.5 \text{ kg m}^{-2}$ . . . . .	58
3.12	Comparison of histograms of LWP ( $\text{kg m}^{-2}$ ) from the SSM/I and ground observations for cases in October 1989 in the North Sea. . . . .	59
3.13	Fig. 3.12 continued. . . . .	60
3.14	Comparison of histograms of LWP ( $\text{kg m}^{-2}$ ) from the SSM/I and ground observations for cases in August and September 1989 over Saipan Island. . . . .	61
3.15	Fig. 3.14 continued. . . . .	62
3.16	Scatter diagrams of LWP ( $\text{kg m}^{-2}$ ) derived from the method of (a) Petty (1990) and (b) Alishouse et al. (1990) versus the present method for stratocumulus clouds off the west coast of California from July 16 to 18, 1987. . . . .	65

3.17	Scatter diagrams of LWP ( $\text{kg m}^{-2}$ ) derived from the method of (a) Hargens (1992) and (b) Alishouse et al. (1990) versus the present method over the North Sea from October 1 to 18, 1989. . . . .	67
3.18	Zonal distributions of liquid water ( $\text{kg m}^{-2}$ ) derived from the present method for August 1987 (solid), Seasat Special Multichannel Microwave Radiometer (SMMR) results from the study of Njoku and Swanson (1983) for July 11 to August 10, 1978 (dashed), and Nimbus 7 SMMR results from the method of Prabhakara et al. (1983) for August 1979 (dotted). . . . .	68
4.1	Global distribution of the annual mean cloud liquid water ( $\text{kg m}^{-2}$ ) over the oceans derived from SSM/I measurements and averaged from July 1987 to December 1991. . . . .	73
4.2	(a) Zonal average cloud liquid water ( $\text{kg m}^{-2}$ ) averaged from July 1987 to December 1991. Solid curve includes only cloudy pixels in the average while dotted curve include cloudy and clear pixels in the average. Areally weighted global means (GM) for each data set are also shown. (b) Seasonal zonal averages of cloud liquid water over the same 53-month period. . . . .	74
4.3	Global distributions of cloud liquid water ( $\text{kg m}^{-2}$ ) over the oceans derived from SSM/I measurements for (a) JJA and (b) SON. . . . .	76
4.4	Same as Figure 4.3 except for (a) DJF and (b) MAM. . . . .	77
4.5	Scatter diagram of monthly mean SSM/I cloud liquid water ( $\text{kg m}^{-2}$ ) versus ISCCP total cloudiness (%) for the summer months from July 1987 to June 1991 over the North Pacific. . . . .	78
4.6	Global distributions of (a) interannual and (b) intra-annual standard deviations of SSM/I cloud liquid water ( $\text{kg m}^{-2}$ ) from July 1987 to December 1991. . . . .	81
4.7	Areally weighted averages of cloud liquid water ( $L$ ) for the globe (top), northern hemisphere (middle), and southern hemisphere (bottom) as a function of month. Gray shading represents interannual variation as one standard deviation above and below the data points. . . . .	83
4.8	Cloud types as defined by ISCCP (from Rossow and Schiffer, 1991). . . . .	85
4.9	Zonal average distributions of the liquid water ( $\text{kg m}^{-2}$ ) of low clouds (cloud top pressures from 680–1000 mb) for JJA 1990 (solid curve) and DJF 1990 (dashed curve). Areally weighted global means (GM) are also given. . . . .	88
4.10	Global relationship between $\text{dln}L/\text{dT}$ ( $\text{deg}^{-1}$ ) for low clouds versus the temperature ( $^{\circ}\text{C}$ ) of the atmospheric layer from 680 mb to the surface. Each circle represents a temperature interval of width 15 K. Filled circle has a correlation below the 99% significance level. Light shading indicates the range of the relationship derived from an adiabatic assumption for clouds of varying thickness and height from 680 to 1000 mb. Also illustrated as squares is the sensitivity relationship using sea surface temperatures (SSTs) for the cloud liquid water data (all clouds) shown in Figure 4.1 as a function of SST. For these calculations the temperature interval is 9 K. . . . .	89
4.11	Scatter diagrams of the (a) annual mean cloud liquid water data from Figure 4.1 and (b) the cloud liquid water of low clouds averaged for the JJA and DJF seasons in 1990 versus sea surface temperature ( $^{\circ}\text{C}$ ). . . . .	91

4.12	Scatter diagrams of $\text{dlnL}/\text{dT}$ ( $\text{deg}^{-1}$ ) for low clouds as a function of temperature ( $^{\circ}\text{C}$ ) separated into midlatitude ( $35^{\circ}$ – $55^{\circ}$ ), subtropical ( $15^{\circ}$ – $35^{\circ}$ ), and tropical ( $0^{\circ}$ – $15^{\circ}$ ) latitude regions and the seasons of JJA and DJF for the (a) northern hemisphere and (b) southern hemisphere. Filled symbols are data points with correlations below the 99% significance level. . . . .	92
4.13	Global distributions of the annual mean cloud liquid water ( $\text{kg m}^{-2}$ ) over the oceans from (a) SSM/I measurements (which includes clear pixels) and model simulations from the (b) CSU GCM and (c) ECHAM model. The ECHAM model is the average of July and January simulations only (Note change in color table increments for the ECHAM model for $\text{LWP} > 0.12 \text{ kg m}^{-2}$ ). . . . .	96
4.14	Zonal means of the global distributions of cloud liquid water shown in Figure 4.13. . . . .	98
4.15	Seasonal zonal means of the cloud liquid water observations and model simulations for (a) DJF and (b) JJA (Note: ECHAM results are only January and July averages, respectively). . . . .	99
4.16	Scatter diagram of annual mean cloud liquid water ( $\text{kg m}^{-2}$ ) versus SST (K) for the CSU GCM. The observations are represented as the average liquid water within a 3 K SST bin, where the SST is the midpoint of the bin (filled squares). The gray shading shows the standard deviation of the observed liquid water within a given bin. . . . .	100
4.17	Scatter diagram of $\text{dlnL}/\text{dT}$ ( $\text{deg}^{-1}$ ) versus the layer temperature for low clouds (700 mb–1000 mb) for the CSU GCM over the (a) ocean and (b) land. The analysis method is the same as that described in section 4.3.1. Also shown for comparison is the relationship deduced from observations. Filled symbols are correlations that are not significant beyond the 99% confidence limit. . . . .	102
4.18	Zonal averages of the intra-annual standard deviation for the CSU GCM (dotted curve) and observations from 1987–1991 (solid curve) and for the year 1990 (dashed). . . . .	103
5.1	ERBE albedo directional models for different cloudiness types over an ocean surface, which are expressed as the albedo versus the cosine of the solar zenith angle $\mu_o$ . . . . .	107
5.2	Zonal averages of the total (solid) and clear sky (dotted) albedo for August 1987 (unadjusted) from ERBS. Also shown is the albedo normalized to a solar zenith angle of $18^{\circ}$ or $\mu_o = 0.95$ (adjusted) using the directional models in Fig. 5.1. . . . .	110
5.3	Global distributions over the oceans of the (a) annual mean normalized cloud albedo and (b) its intra-annual standard deviation derived from ERBS measurements over the period from July 1987 to February 1990. . . . .	113
5.4	Global distributions over the oceans of the intra-annual correlations between (a) cloud liquid water and cloud albedo and (b) cloud liquid water and ISCCP total cloudiness over the same time period as in Fig. 5.3. Negative correlations are represented as areas of white. . . . .	115
5.5	Zonal mean characteristics of the intra-annual standard deviations of cloud liquid water path (LWP) (solid curve), cloud albedo (dashed curve) and $C_{LW}$ (dotted curve) over the period from July 1987 to February 1990. . . . .	116

5.6	Global map depicting the six $10^\circ \times 10^\circ$ regions (A–F) used in the seasonal analyses of cloud liquid water and the Earth radiation Budget. Also shown is an additional area (Region G) included in the comparison involving the net radiative fluxes. . . . .	118
5.7	Seasonal time series of cloud liquid water path (LWP) (circles), cloud albedo (squares), total cloud amount (filled squares), and $C_{LW}$ (filled circles) averaged from July 1987 to February 1990 for regions (a) A and (b) B depicted in Figure 5.6. Each point represents a spatial average of the $2.5^\circ$ gridboxes within the $10^\circ \times 10^\circ$ region, which are then averaged in time. . . . .	119
5.8	Same as Fig. 5.7 except for regions C and D. . . . .	121
5.9	Same as Fig. 5.7 except for regions E and F. . . . .	123
5.10	(a) Scatter plot of the monthly mean net radiative cloud effect ( $C_{net}$ ) versus cloud liquid water for Region G. Each point is a $2.5^\circ$ gridbox average. Also shown is a least squares linear fit and the resultant correlation coefficient. (b) Scatter plot of $C_{net}$ versus cloud liquid water for Region E. Linear fits and their respective correlations are shown separately for cloud liquid water less than and greater than $0.11 \text{ kg m}^{-2}$ . . . . .	124
5.11	Locations of the $2.5^\circ$ gridboxes used in the cloud albedo and cloud liquid water comparison, which are separated into three general regions. The thin solid line indicates the boundaries of region 1. . . . .	126
5.12	Scatter plot of cloud albedo versus cloud liquid water path for solar zenith angles from $55^\circ$ to $65^\circ$ for Region 2. Curves represent theoretical calculations at a solar zenith of $60^\circ$ for plane-parallel clouds with various effective radii ( $r_e$ ) using the parameterization of Slingo (1989). . . . .	129
5.13	Scatter plot of cloud albedo versus cloud liquid water path for solar zenith angles from $65^\circ$ to $75^\circ$ for regions (a) 1 and (b) 2. Curves represent theoretical calculations at a solar zenith angle of $70^\circ$ . . . . .	130
5.14	Same as Fig. 5.13 except for region 3. . . . .	131
5.15	Scatter plot of cloud albedo versus cloud liquid water path for solar zenith angles from $75^\circ$ to $80^\circ$ for regions (a) 1 and (b) 2. Curves represent theoretical calculations at a solar zenith of $80^\circ$ . . . . .	132
5.16	Same as Fig. 5.15 except for region 3. . . . .	133
5.17	Histograms of the % occurrence of the average (a) zenith angle and (b) azimuth angle of the ERB measurements for the cloud albedo-LWP comparison. . . . .	135
B.1	Scatter diagram of downwelling brightness temperatures ( $T^-$ ) at the surface under clear sky conditions for the simplified model (computed) versus the detailed calculations (actual) at (a) 19.35 GHz, (b) 22.235 GHz, and (c) 37 GHz. Also shown are the line of perfect agreement and the rms differences. . . . .	160
B.2	Same as Fig. B.1 except for cloudy cases. . . . .	161
B.3	Scatter diagram of upwelling brightness temperatures at vertical polarization ( $T_v^+$ ) under clear conditions for the simplified model (computed) versus the detailed calculations (actual) at (a) 19.35 GHz, (b) 22.235 GHz, and (c) 37 GHz. Also shown are the line of perfect agreement and the rms differences. . . . .	162
B.4	Same as Fig. B.3 except for cloudy cases. . . . .	163
B.5	Scatter diagram of oxygen optical depth versus surface air temperature (K) at 19.35 (open circles), 22.235 and 37 GHz. . . . .	165

B.6	Scatter diagrams of total water vapor optical depth at 37 GHz ( $\tau_{w37}$ ) versus water vapor retrieved at (a) 19.35 GHz ( $W_{19}$ , $\text{kg m}^{-2}$ ) and (b) 22.235 GHz ( $W_{22}$ , $\text{kg m}^{-2}$ ) derived from the cloud-free data set. Also shown are linear least squares fit of the data where the slope corresponds to the water vapor absorption coefficient at 37 GHz ( $\kappa_{w37}$ ) and the linear correlation coefficient of the fit (R). . . . .	166
B.7	Histogram of integrated cloud liquid water ( $\text{kg m}^{-2}$ ) retrieved from the cloud-free data set for the 19/37 GHz method (solid) and the 22/37 GHz method (dotted). The mean and standard deviation are also given. . . . .	168
B.8	Scatter diagram of retrievals of $W$ for the improved algorithm versus near-coincident measurements of $W$ from radiosondes for the International Cirrus Experiment (ICE) and the Tropical Cyclone Motion (TCM) Experiment. Also shown is the line of perfect agreement. . . . .	169

## LIST OF TABLES

2.1	Effective 3-dB spatial resolution at the Earth's surface of the SSM/I channels (from Hollinger et al., 1987). V and H represent vertical and horizontal, respectively. . . . .	15
2.2	Average pre-launch measurements of NE $\Delta$ T (K) for the SSM/I at a scene temperature of 300 K (from Hollinger et al., 1987). V and H represent vertical and horizontal, respectively. . . . .	15
2.3	Cubic fit Coefficients for oxygen transmission $\mathcal{T}_{ox}$ and liquid water absorption $\kappa_{\ell}$ (from Petty, 1990) at 19.35 and 37 GHz. . . . .	27
3.1	Retrieval errors (%) attributed to uncertainties in cloud temperature $T_c$ based on simulated brightness temperatures for the cloud liquid water profiles in Figure 3.1. Also shown is the change in $T_c$ ( $\Delta T_c$ , K) necessary to match the retrieved integrated liquid water to the actual cloud liquid water ( $L$ , $\text{kg m}^{-2}$ ). . . . .	37
3.2	Selected cases for the AVHRR and SSM/I cloud liquid water comparison over San Nicolas Island . . . . .	51
5.1	Linear correlations between cloud liquid water ( $L$ ) and cloud albedo ( $\alpha_{cld}$ ), total cloud amount (TCA), and longwave cloud effect ( $C_{LW}$ ) for the six regions defined in Fig. 5.6 from July 1987 to February 1990. Correlations beyond the 99% significance level are denoted by an asterisk. . . . .	120
A.1	Monthly summary of missing SSM/I data for the DMSP F-8 satellite . . . . .	157
B.1	Cubic fit coefficients for oxygen optical depths ( $\tau_{ox}$ ) at 19.35, 22.235, and 37 GHz. . . . .	164

## Chapter 1

### INTRODUCTION

The importance of cloud liquid water in global climate has been a topic of recent debate. In particular, the cloud-climate feedback mechanism involving cloud liquid water is thought to be potentially significant to the problem of global climate change (Paltridge, 1980). Several modeling studies have emphasized the temperature dependence of cloud liquid water as being the driving force behind this feedback (e.g., Charlock, 1982; Somerville and Remer, 1984; Betts and Harshvardan, 1987). Some of these studies used in situ measurements of cloud liquid water over limited continental regions to conclude that cloud liquid water might provide a relatively large negative feedback on climate. However, the latest modeling efforts using general circulation models (GCMs), e.g., Taylor and Ghan (1992), seem to indicate that the cloud liquid water feedback may be more neutral since cloud longwave radiative effects tend to compensate for the increased albedos. Also, Twomey (1991) has raised doubts about whether a strong dependence of liquid water content on temperature actually exists, following a reinterpretation of the in situ measurements. Furthermore, even if adiabatic liquid water content were to increase with temperature there is no assurance that the clouds would possess greater liquid water in a warmer atmosphere since other, nonadiabatic microphysical processes might offset the adiabatic increase in liquid water, such as increased precipitation efficiency (Twomey, 1991). Other evidence contrary to the idea that cloud liquid water generally increases with temperature comes from recent satellite measurements of cloud optical depth from Tselioudis et al. (1992), which demonstrate that over most areas of the globe optical depth and temperature are anticorrelated.

Cloud feedback processes in general have been identified as one of several components of the climate system that must be understood before we can reliably predict climate

change. Unfortunately, there are presently large gaps in our knowledge about such fundamental questions as, What is the global distribution of cloud liquid water and ice water? What are the main physical processes that determine their distribution? and even more importantly, What are their respective radiative effects? Of course, one of the major reasons for these deficiencies is that global observations of cloud properties have only recently become available. In an effort to address these and other related issues, the Global Energy and Water Cycle Experiment (GEWEX) has proposed strategies to monitor cloud water and other cloud properties on a global scale.

A full understanding of the cloud liquid water feedback and to what extent it will ultimately affect climate and climate change will perhaps only be possible through the use of GCMs. Nevertheless, observations can play a key role in improving our understanding of the factors that govern cloud liquid water and also provide descriptions of the interactions of cloud liquid water with other variables of the climate system. These descriptions can also serve as sources of parameterization for simple climate models or as tests for the new generation of GCMs that explicitly include the prediction of cloud liquid water.

Observations of cloud liquid water from satellite-based systems have been limited exclusively to total column estimates using optical (e.g., Lojou et al., 1991) and passive microwave methods (e.g., Grody et al., 1980; Petty 1990). Despite their limitations, these types of measurements can be extremely useful in understanding the horizontal distribution of cloud liquid water (information about the vertical structure of cloud liquid water from satellite measurements may be possible in the future using cloud profilers, such as the 94 GHz radar proposed for TRMM-2 (Tropical Rainfall Measuring Mission)). The chief weaknesses of the optical methods include the effects of ice clouds and multi-level clouds and the nonlinearities arising from cloud brokenness/inhomogeneities within the field-of-view of the instrument. The microwave techniques by comparison represent a more direct approach but are less accurate in areas of precipitating cloud systems, involve relatively coarse resolution measurements, and are usually restricted to water surfaces, though retrievals may be possible over land when combined with IR methods (e.g., Jones and Vonder Haar, 1990). With the emergence of new spaceborne microwave instruments

of improved calibration and high stability, such as the Special Sensor Microwave/Imager (SSM/I), it will be possible, for the first time, to monitor successfully cloud liquid water on a global scale and over the long-term.

This research is an observational study that uses satellite data and microwave remote sensing techniques to investigate the global climatic characteristics and bulk radiative effects of cloud liquid water over the oceans. It relies on satellite measurements from a variety of different instruments and experimental programs, including the Defense Meteorological Satellite Project (DMSP), the Earth Radiation Budget Experiment (ERBE), and the International Satellite Cloud Climatology Project (ISCCP). The results of this work will hopefully provide important clues as to the role of cloud liquid water in global climate.

The central objectives of this research are to:

(1) Develop a simple physical method for retrieving integrated cloud liquid water over the global oceans from SSM/I measurements.

(2) Validate the retrieval method and supply an estimate of the total errors in the retrievals.

(3) Describe the global distribution and the yearly and seasonal variability of oceanic cloud liquid water and, further, investigate the sensitivity relationships between cloud liquid water and the temperature field.

(4) Examine the gross seasonal relationships between cloud liquid water and the Earth's radiation budget and explore the fundamental large-scale relationships between cloud albedo and cloud liquid water.

The motivation for developing a new cloud liquid water retrieval algorithm is that there is a conspicuous lack of rigorously tested global algorithms available for the SSM/I. This is unlike the retrieval of precipitable water (integrated water vapor) for which much research has been done and several different methods are available (e.g., Schuessel and Emery, 1990; Petty, 1990; Tjemkes et al., 1991). The current cloud liquid water algorithms for the SSM/I that have appeared in the literature are either statistically or semi-physically based (Alishouse et al., 1990; Petty, 1990; Hargens, 1992). The retrieval

method described in this research differs from the other methods in that it is entirely a physical approach. While statistical regression-type algorithms can, in some cases, achieve an accuracy comparable to physical methods, a physical model has the distinct advantage of allowing one to gain an understanding of the basic physical processes at work and to identify the important factors that influence the retrievals, which may eventually lead to more accurate retrievals.

A temperature sensitivity analysis similar to the one proposed for this research was conducted by Tselioudis et al. (1992) using observations of cloud optical depth. Assuming that the variations of optical depth are primarily due to changes in cloud liquid water, the results of Tselioudis et al. can be used to infer something about the relationship of cloud liquid water to temperature. The advantages of this study are the use of measurements of cloud liquid water and the elimination of possible effects from ice clouds at higher latitudes during the winter. In addition, this study differs from earlier comparisons of liquid water and the radiation budget, such as by Stephens and Greenwald (1991), in that we also explore the seasonal aspects of this relationship and provide a more indepth analysis.

The first part of this research presents an overview of the microwave spectrum and past microwave retrieval methods. Then a bispectral physical method is described that consists of a simultaneous estimation of integrated water vapor and cloud liquid water over the oceans. Chapter 3 is concerned with the error analysis and validation of the cloud liquid water retrievals; quantitative estimates of the retrieval errors are given. In Chapter 4 the retrieval method is applied to SSM/I measurements over a 53-month period to create a monthly mean climatology of cloud liquid water. Some of the shortcomings of these types of data are also discussed. The focus of this chapter is to examine the spatial and temporal characteristics of cloud liquid water and the global, regional and seasonal aspects of the coupling between cloud liquid water and the temperature field. In Chapter 5 a preliminary analysis is presented of the climatic relationships of cloud liquid water to the different components of the Earth radiation budget in terms of their seasonal variation. Also, the observed relationships between cloud albedo and cloud liquid water are described and compared with existing theory. In the final chapter we summarize our results, present the main conclusions of this work, and give suggestions for future research.

## Chapter 2

# RETRIEVAL OF CLOUD LIQUID WATER FROM PASSIVE MICROWAVE MEASUREMENTS

### 2.1 The Microwave Absorption Spectrum

Before proceeding to a discussion of cloud liquid water retrieval, it is essential to describe first some of the absorption characteristics of the atmosphere across the microwave spectrum. The microwave spectrum is usually defined as those frequencies ranging from about 3 GHz to 1000 GHz (or 10 cm to 0.3 mm). The objective here is to focus on frequencies less than about 300 GHz, which are relevant to many current microwave remote sensing applications.

There are several gaseous constituents of the atmosphere that give rise to absorption lines in the microwave portion of the electromagnetic spectrum. These lines are a consequence of energy transitions among allowable energy states of the molecules due to rotational and/or vibrational motion of their nuclei. The gases responsible for the strongest absorption lines are oxygen and water vapor. The oxygen molecule has no electric dipole moment by virtue of its symmetric charge distribution, but instead has a magnetic dipole moment that produces a broad complex of rotational transitions around 60 GHz and another somewhat weaker line near 118 GHz. Figure 2.1 shows the total atmospheric transmission versus frequency using the microwave transmission model of Liebe (1981) for different water vapor abundances based on the U.S. standard temperature profile and the standard profiles of McClatchey et al. (1972). The O<sub>2</sub> lines are very strong, even though magnetic dipole transitions are relatively weak, as a result of the vast number of oxygen molecules in the atmosphere. The absorption lines located near 60 GHz are often used in the remote sensing of vertical profiles of atmospheric temperature.

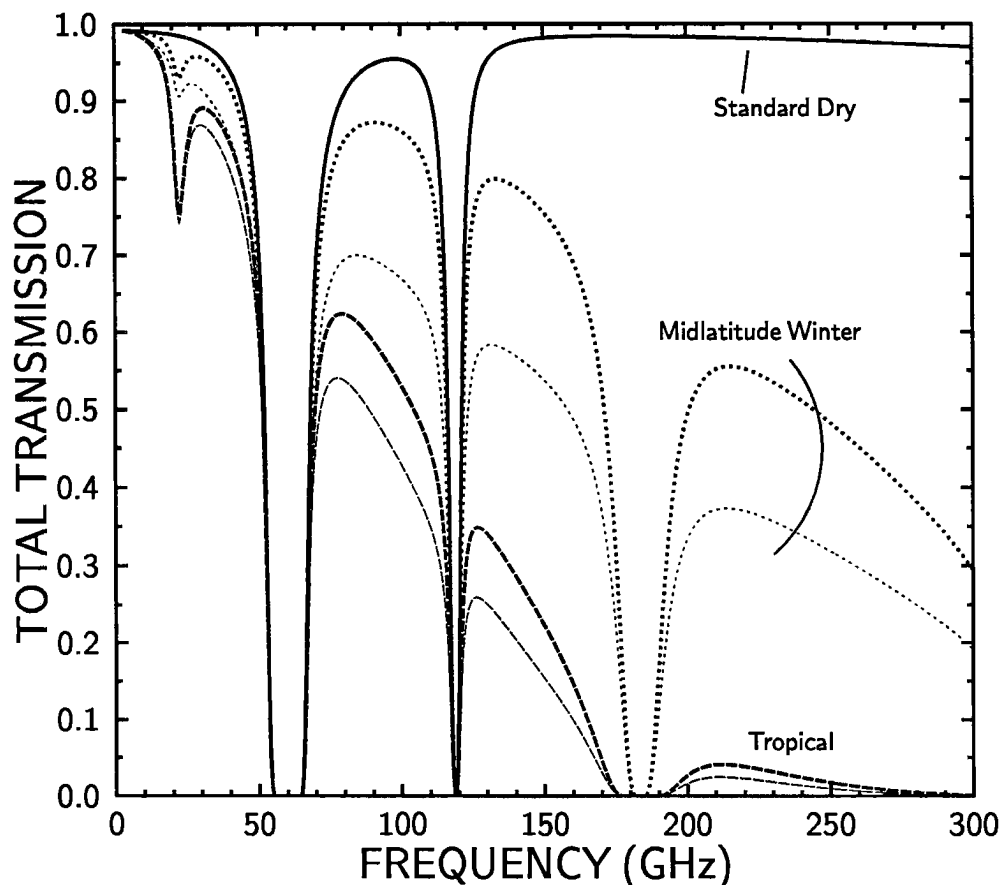


Figure 2.1: Total atmospheric transmission as a function of frequency for different atmospheric conditions. Solid curve is for a completely dry atmosphere using the U.S. standard atmosphere. Dotted curves are for the McClatchey midlatitude winter profile (integrated water vapor of  $8.7 \text{ kg m}^{-2}$ ) and dashed curves are for the tropical profile (integrated water vapor of  $42.3 \text{ kg m}^{-2}$ ). Thin dotted and dashed curves include a nonprecipitating cloud with an integrated liquid water content of  $0.2 \text{ kg m}^{-2}$ .

The microwave spectrum of water vapor also contains several strong absorption lines. The water vapor molecule, with its permanent electric dipole moment, undergoes only rotational motion at microwave frequencies. However, at infrared frequencies the absorption of radiation occurs principally from the vibrating motion of the molecule. The strongest absorption line of water vapor below 300 GHz occurs at 183 GHz (see Figure 2.1). This line is frequently selected for measurements used in determining water vapor profiles. A much weaker absorption line centered at 22.235 GHz (see Figure 2.1) is used to obtain estimates of vertically integrated water vapor. The window regions from 3 to 10 GHz and

between 30 and 40 GHz can be used to remotely sense surface parameters, although the lower frequencies are better suited for this purpose since they can more easily penetrate thick clouds.

Another important but less understood feature of the microwave spectrum is the existence of a water vapor continuum, which also extends throughout much of the infrared region. Several hypotheses have been proposed to explain this phenomenon. For instance, it may be a result of absorption from the far wings of water vapor transition lines in the millimeter and far-infrared regions or possibly due to the transitions resulting from clusters of water vapor molecules, such as dimers (Burch and Gryvnak, 1980). Despite the lack of a coherent theory, the continuum does have certain characteristics that are known from discrepancies between theoretical calculations and observations. For example, the absorption increases predictably with the square of the frequency, decreases with increasing temperature, is greater for pure water vapor than for mixtures of water vapor and other gases, and is larger in window regions than for other more strongly absorbing regions (Stephens and Tsay, 1990; Walter, 1992).

Liquid water is an atmospheric constituent that also contributes significantly to absorption in the microwave spectrum. As opposed to the resonant behavior of water vapor and oxygen, liquid water exhibits nonresonant absorption properties. An example of its influence on the atmospheric transmission is revealed in Figure 2.1. A more detailed description of the optical properties of both pure liquid water and ice is shown in Figure 2.2, which displays the imaginary part of the refractive index as a function of frequency for selected temperatures. The index for water is based on the semi-empirical results of Ray (1972) and that for ice is the measurements of Warren (1984). The high values of this index for liquid water indicates that it is a strongly absorbing substance at microwave wavelengths in which the absorption varies greatly with frequency and temperature. In contrast, the refractive index of ice is also dependent on frequency and temperature but is about 500 to 1000 times smaller than water, which illustrates that the absorption by ice particles is negligible. However, ice can contribute to the extinction of microwave radiation through scattering processes if the size of the ice particles is large compared to the wavelength of the incident radiation.

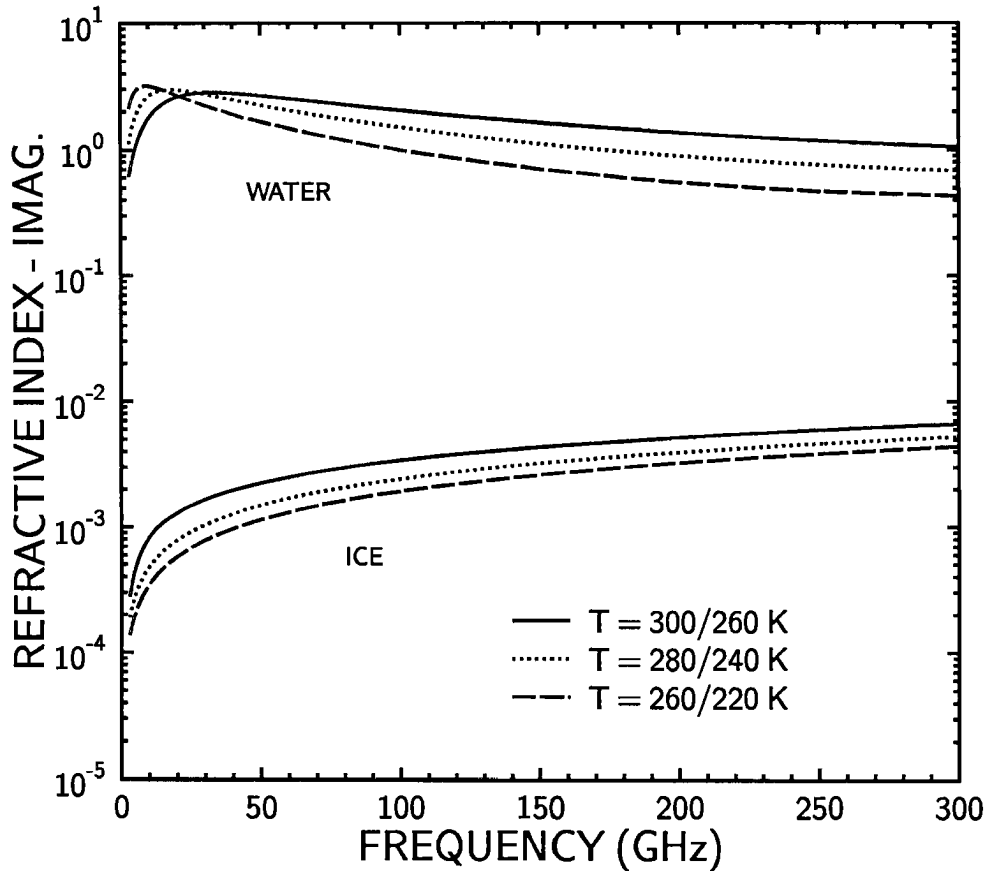


Figure 2.2: Imaginary part of the refractive index of pure ice and water versus frequency (GHz) for different temperatures (K) based on the results of Ray (1972) and Warren (1984). Higher temperatures (300, 280, and 260 K) correspond to water and lower temperatures (220, 240, and 260 K) are for ice.

For cloud droplets, which are traditionally defined as drops of less than  $100 \mu\text{m}$  radius ( $r$ ), the attenuation of microwaves can be described in the Rayleigh limit for frequencies below about 100 GHz (or wavelengths greater than 3 mm). Absorption becomes the dominant process for smaller drops since the absorption efficiency for spheres in the Rayleigh regime, which is proportional to the size parameter  $x^1$  (where  $x < 1$ ), is much greater than the scattering efficiency, which is proportional to the fourth power of  $x$ . One attractive consequence for particles small compared to wavelength is that the mass absorption

---

<sup>1</sup> $x = 2\pi r/\lambda$ , where  $\lambda$  is the wavelength of the incident radiation

coefficient of liquid water can be written in a convenient form as

$$\kappa_\ell = \frac{6\pi}{\rho_\ell \lambda} \text{Im} \left[ \frac{m^2 - 1}{m^2 + 2} \right] \quad (2.1)$$

where  $\rho_\ell$  and  $m$  are the density and complex refractive index, respectively, of liquid water, and  $\lambda$  is wavelength. The obvious advantage of (2.1) is that the absorption characteristics of small drops now become completely independent of dropsize. Figure 2.3 shows the results of calculations of  $\kappa_\ell$  as a function of frequency and temperature using the refractive indices derived by Ray (1972). The absorption coefficient is shown to increase sharply with frequency at lower frequencies and increases at a slower rate at the highest frequencies. It is also a strong function of temperature, increasing with decreasing temperature. These characteristics of the absorption coefficient arise from the strong temperature and

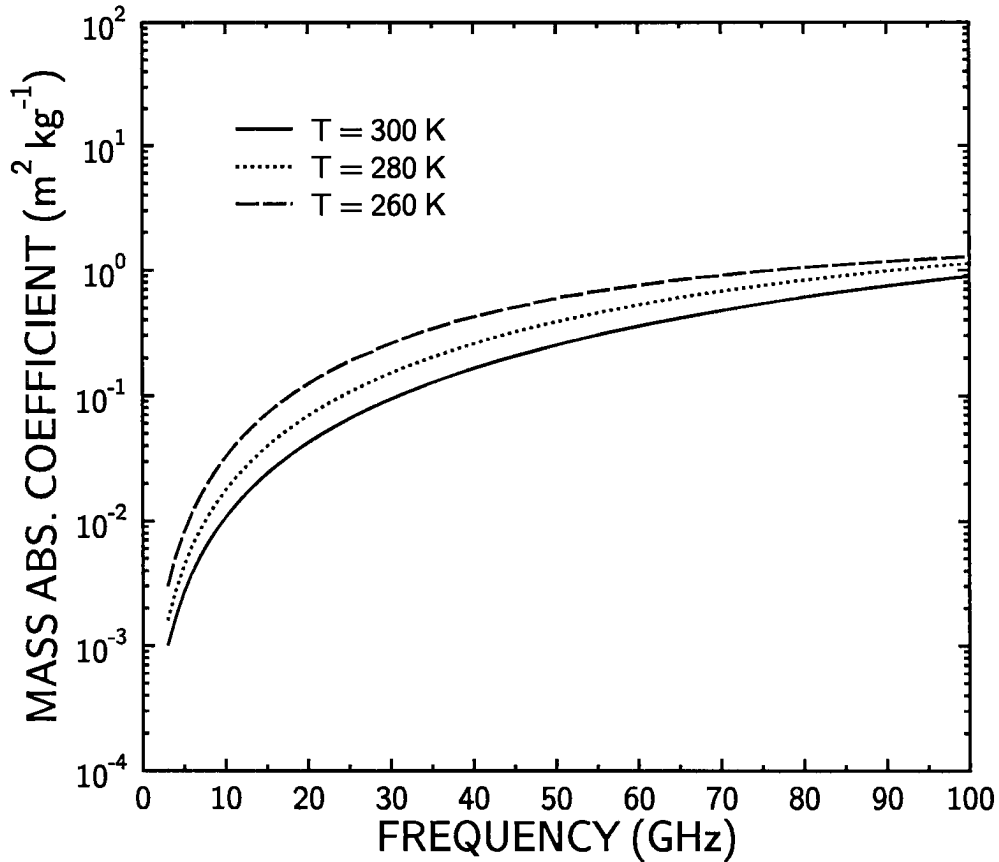


Figure 2.3: Mass absorption coefficient of pure liquid water ( $\text{m}^2 \text{kg}^{-1}$ ) for small drops from 3 to 100 GHz for different temperatures (K).

frequency dependence of the dielectric properties of liquid water.

Raindrops, as well, greatly absorb microwave radiation. A full discussion of these processes, however, is beyond the scope of this research. Briefly, the interaction of liquid precipitation with microwave radiation generally occurs outside of the Rayleigh regime (except perhaps for the smallest raindrops at the lowest frequencies). Thus, scattering is also an important process whose influence is often comparable to absorption. In addition, the absorption characteristics of raindrops also depend much more on the details of the size distribution of the drops.

## 2.2 A Brief History of Cloud Liquid Water Retrieval

The estimation of cloud liquid water and other geophysical quantities (e.g., precipitable water, surface winds, precipitation, and others) over the oceans from space-borne passive microwave instruments has a long history that spans more than two decades. Basharinov et al. (1969) and Akvilonova et al. (1973) were among the first to utilize such measurements to infer information about the water content of the Earth's atmosphere. The measurements were obtained at 3.5, 8.8, 22.235, and 37 GHz from radiometers aboard the Cosmos-243 and Cosmos-384 satellites. Although the microwave instruments on these satellites were short-lived, their measurements provided our first glimpse of the spatial distributions of water vapor and liquid water over the Earth's oceans.

Many other studies followed these pioneering efforts based on observations from different instruments on a variety of satellites. Two such instruments were the Nimbus-E Microwave Spectrometer (NEMS) and the Electrically Scanning Microwave Radiometer (ESMR) on board the Nimbus-5 spacecraft, both of which operated for over two years in the early 1970's. NEMS was strictly a nadir pointing instrument that measured radiation at 22.235, 31.4, 53.65, 54.9, and 58.86 GHz with a coarse spatial resolution of about 190 km. The ESMR was a scanning instrument with a single channel at 19.35 GHz that viewed out to 50° along the satellite cross-track. Its spatial resolution at nadir was 25 km. Despite the limitations in the spatial resolution and coverage of the NEMS measurements, several studies were successful in obtaining useful estimates of liquid water (e.g., Staelin

et al., 1976; Grody, 1976; Chang and Wilheit, 1979; Takeda and Natsuki, 1982). Most of these liquid water algorithms were based on a combination of microwave radiative transfer calculations and multiple regression statistics. Error estimates of the retrievals ranged from 10% for Takeda and Natsuki and  $0.065 \text{ kg m}^{-2}$  for Chang and Wilheit to  $0.1 \text{ kg m}^{-2}$  for Staelin et al.

In the mid-1970's measurements from the Scanning Microwave Spectrometer (SCAMS) aboard the Nimbus-6 satellite were used to derive liquid water and other atmospheric quantities. SCAMS contained two channels located at 22.235 GHz and 31.65 GHz. This instrument, like the ESMR, scanned across the satellite's path to an angle of about  $53^\circ$ . Grody et al. (1980) presented a physical method based on an approximate form of the radiative transfer equation to simultaneously retrieve precipitable water and liquid water over the tropical Pacific. The rms error of the liquid water amounts were shown to be about  $0.13 \text{ kg m}^{-2}$ . In the study of Rosenkrantz et al. (1978) a similar form of the model developed by Grody et al. (1976) was used to extract information about surface winds, liquid water and water vapor for a typhoon.

The space-borne microwave radiometer tradition was continued in 1978 by the Special Multichannel Microwave Radiometer (SMMR), which was flown on both the Nimbus-7 and Seasat satellites. The SMMR on Nimbus 7 provided for the first time a relatively long (4 year) continuous record of microwave measurements. The ability of this satellite to monitor atmospheric water on quasi-long time scales now made it possible to study components of the water cycle in the context of global climate. The Seasat satellite, unfortunately, suffered a mysterious power failure three months after its launch. However, various surface and atmospheric parameters derived from these measurements were presented by Njoku and Swanson (1983).

The SMMR differed in several respects to many of the previous radiometers. Along with the standard frequencies that are used to obtain atmospheric parameters over the ocean (18, 21 and 37 GHz), the SMMR also included channels at 6.6 and 10.7 GHz to measure surface parameters such as sea surface temperature and wind speed. The SMMR also measured radiation at dual-polarization and from a constant viewing angle of  $50^\circ$

due to its conical scan geometry. Although the SMMR represented an advancement in technology, it suffered from calibration problems, which created numerous obstacles in the development of retrieval algorithms. Nevertheless, measurements from the SMMR on Nimbus-7 were invaluable in numerous studies dealing with liquid water in the atmosphere. For example, Wilheit and Chang (1980) and Prabhakara et al. (1983) estimated liquid water on the global scale. Many other studies focused on specific regions, such as in the western North Pacific (Takeda and Liu, 1987), the North Atlantic (Curry et al., 1990), North Pacific (Katsaros and Lewis, 1986), and Indian Ocean (Lojou et al., 1991).

## **2.3 The Special Sensor Microwave/Imager**

### **2.3.1 Instrument characteristics and performance**

The Special Sensor Microwave/Imager, or SSM/I, is a new generation of passive microwave instrument whose measurements are used principally in obtaining atmospheric water and surface parameters. It is presently flown on three Defense Meteorological Satellite Project (DMSP) Block 5D-2 satellites: the F-8, F-10, and F-11. Other instrument packages that are carried aboard these satellites include the Operational Linescan System (OLS), which is a high resolution four-channel visible/infrared imager, the Special Sensor H (SSH), an infrared water vapor, temperature, and ozone sounder, and the Special Sensor Microwave/Temperature sounder (SSM/T). The F-11 has in addition to the SSM/T, the Special Sensor M/T-2 (SSM/T-2), which is a microwave humidity sounder. These satellites travel around the Earth in a sun-synchronous orbit with an inclination angle of roughly  $98.8^\circ$ . The F-8 satellite, for example, is at an average altitude of about 860 km. The primary data used in this study are the brightness temperatures obtained from the SSM/I on board the DMSP F-8 satellite, which was launched June 19, 1987.

The imager consists of 7 channels that measure both vertically and horizontally polarized radiation at 19.35, 37, and 85.5 GHz and strictly vertically polarized radiation at 22.235 GHz. The SSM/I spins at a rate of 32 revolutions/minute about an axis perpendicular to the Earth's surface at a constant pitch, which produces a conical scan. Figure 2.4 is an illustration of the scan geometry of the SSM/I as it sweeps across the surface

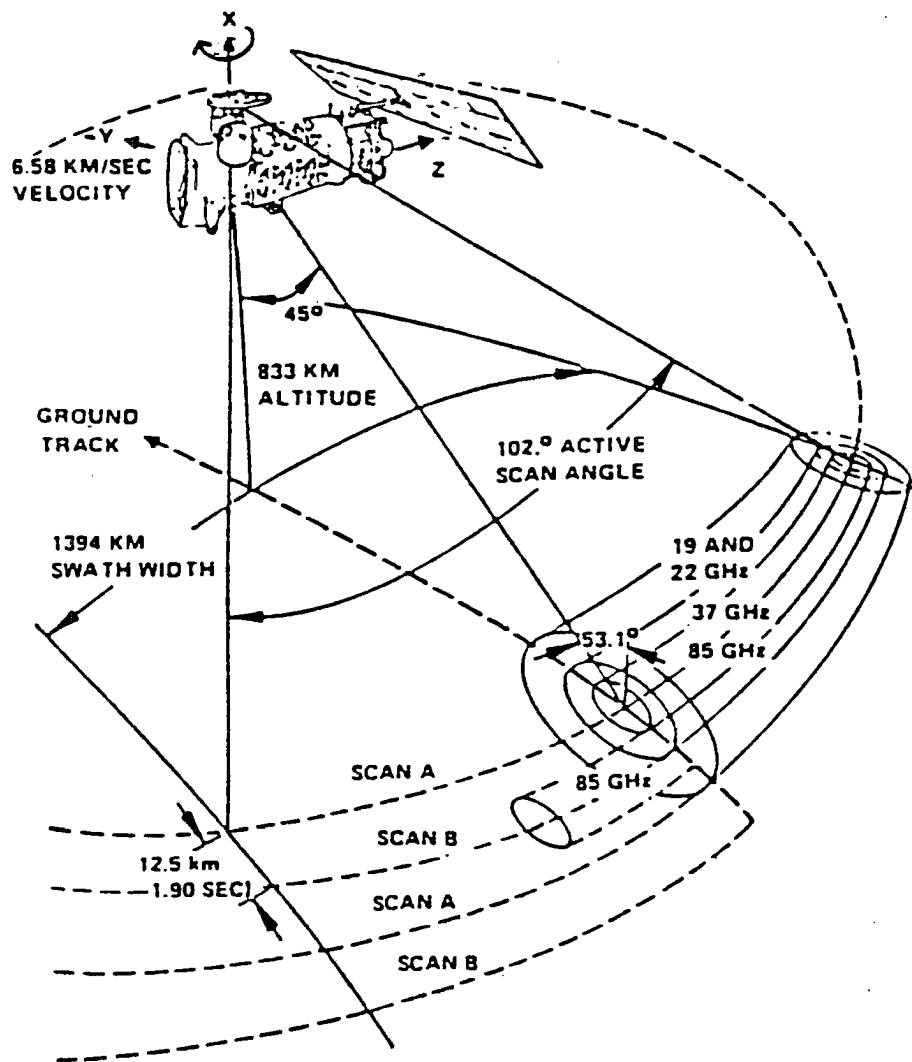


Figure 2.4: Scan geometry of the Special Sensor Microwave/Imager (from Hollinger et al., 1987).

of the Earth. The ellipses in this figure represent the footprint of each of the channels. The SSM/I maintains a relatively constant viewing angle (which is defined as the angle between the line of sight of the instrument and nadir) of approximately  $53^\circ$ . The  $102^\circ$  angular extent of the scan results in a swath width of approximately 1394 km. This is a much wider swath than SMMR (750 km) and results in complete global coverage (except near the poles) in about 2-3 days. The SSM/I samples the 85.5 GHz channels every 12.5 km along the scan for a total of 128 samples. The lower frequency channels, on the other

hand, are only sampled half as frequently (every 25 km for a total of 64 samples). Along the satellite track the 85 GHz channels are sampled for every scan (scans A and B), while the lower frequency channels are observed every other scan (scan A).

The spatial resolution of microwave radiometer measurements at the Earth's surface is typically defined where the antenna gain drops 3 db from its peak value (which is called the beamwidth or field-of-view (FOV) of the instrument). The microwave radiation that impinges on the parabolic reflector produces a diffraction pattern whose angular width of the peak lobe is directly proportional to wavelength. Hence, the spatial resolution of the measurements increases with increasing frequency. Thus the 85 GHz channels have the greatest resolution with along-track and cross-track resolutions of 15 and 13 km, respectively, while the 19 GHz channels have the crudest resolution, being  $69 \times 43$  km (see Table 2.1 for other channels of the SSM/I). It is important to note that these spatial resolutions represent effective FOVs, which include the radiometer's time integration of the measurements.

The SSM/I is more stable and far better calibrated than its predecessor, the Special Multichannel Microwave Radiometer. For each scan the SSM/I goes through an absolute calibration by observing a reference hot load and a cold sky reflector, which directs the background cosmic radiation into the antenna feed. In addition, the long-term stability of the radiometer's receiver is achieved through an Automatic Gain Control (AGC) feature, which steps the gain up or down when needed after sampling the hot load (Hollinger et al., 1989).

The sensitivity of the SSM/I is also much improved over previous microwave radiometers since its signal to noise ratio is greater by a factor of 2 (Hollinger et al., 1987). Table 2.2 shows pre-launch measurements of the radiometer sensitivity or noise equivalent temperature differential ( $NE\Delta T$ ) of the SSM/I for a scene temperature of 300 K. The  $NE\Delta T$  is dependent on the receiver noise temperature, the scene brightness temperature, fluctuation and drift in the radiometer's gain, among several other factors. This quantity varies from about 0.4 to 0.7 K and is highest for the 22.235 and 85 GHz channels. For more details about the SSM/I the reader is referred to Hollinger et al. (1987).

Table 2.1: Effective 3-dB spatial resolution at the Earth's surface of the SSM/I channels (from Hollinger et al., 1987). V and H represent vertical and horizontal, respectively.

Freq. (GHz)	Polariz.	Along-track (km)	Cross-track (km)
19.35	V	69	43
19.35	H	69	43
22.235	V	50	40
37	V	37	28
37	H	37	29
85.5	V	15	13
85.5	H	15	13

Table 2.2: Average pre-launch measurements of  $NE\Delta T$  (K) for the SSM/I at a scene temperature of 300 K (from Hollinger et al., 1987). V and H represent vertical and horizontal, respectively.

Freq. (GHz)	Polariz.	$\Delta T$ (K)
19.35	V	0.45
19.35	H	0.42
22.235	V	0.74
37	V	0.37
37	H	0.38
85.5	V	0.69
85.5	H	0.73

The lower frequency channels of the SSM/I on the F-8 satellite have performed admirably over the last 4–5 years. However, the 85 GHz channels were affected early on by large changes in temperature that were apparently a result of the increased swings in solar illumination during the northern hemisphere winter. As result of these problems, the instrument was shut down beginning December 2, 1987 and ending January 12, 1988. Despite the shutdown, the 85v channel eventually became unusable after January 1989. The 85h channel in contrast had a somewhat longer lifetime. However, it first began experiencing trouble in February 1990 and subsequently failed in February 1991. As of this writing all channels of the SSM/Is on the F-10 and F-11 appear to be functioning normally.

### 2.3.2 Data

The radiation measured by the antenna is commonly expressed in terms of an antenna temperature, which is a measure of the total received radiant power over a solid angle of  $4\pi$  steradians. One way to obtain the radiance or brightness temperature (these two terms can be used interchangeably throughout much of the microwave since they are directly proportional to one another) is to deconvolve the antenna temperatures. In practice, however, this is usually not required since most of the radiant power received by the antenna is over a very narrow solid angle. The brightness temperatures can be directly inverted from the antenna temperatures with sufficient accuracy by assuming a linear relationship between the antenna temperature and the vertical and horizontal polarization brightness temperature components, which works well under a variety of conditions (Wentz, 1991). Included in this relationship is information about the antenna gain patterns, contributions to the brightness temperature from space (referred to as “spillover”), and the effects of cross-polarization. Based on the estimates of Wentz (1991), the precision of the computed brightness temperatures are 0.1 K under most conditions.

Estimates of the absolute errors in the computed brightness temperatures were determined from aircraft underflights and comparisons to model calculations (Hollinger et al., 1989). Flights were made simultaneously with DMSP overpasses over several different scene conditions with radiometers of the same type as the SSM/I mounted on the aircraft. Based on these comparisons, the measurements from the SSM/I on board the DMSP F-8 satellite were found to have an estimated absolute error of roughly  $\pm 3$  K. The 37 and 85 GHz channels exhibited somewhat greater error than the lower frequency channels, and the 37 GHz channels tended to be consistently biased low.

The brightness temperature data used in this study are those computed by Wentz (1991). As discussed earlier, Wentz uses a linear combination of the vertical and horizontal components of the antenna temperatures to represent the brightness temperature. At 22.235 GHz, however, there is no horizontal component. Consequently, Wentz uses model simulations and statistical regression to obtain a relationship between the vertical components of the antenna temperature and brightness temperature. These data also include

an along-scan correction for a cold bias in the brightness temperatures, which reaches a maximum of about 1 K near the edge of the scan. This cold bias is apparently caused by the instrument sensing a portion of the cold space reflector near the end of the scan (Wentz, 1991).

Details of how the latitude and longitude information are determined for each satellite pixel, and the problems that were encountered, are discussed by Wentz (1991). A complete month by month summary of missing SSM/I data from the DMSP F-8 satellite is shown in Appendix A. Excluding July 1987 and the two months in which the instrument was turned off (December 1987 and January 1988), the average missing data for a month is about 13%.

## 2.4 Development of a Physical Method to Estimate Cloud Liquid Water

One objective of this research is to construct a simple physical retrieval scheme for estimating cloud liquid water from SSM/I observations on a global basis over the ice-free oceans. The motivation for creating a new retrieval algorithm is that unlike the retrieval of precipitable water for which much research has been done and several different methods are available (e.g., Schuessel and Emery, 1990; Petty, 1990; Tjemkes et al., 1991), there is a conspicuous lack of rigorously tested cloud liquid water algorithms available for the SSM/I. The algorithms that have been developed thus far have been for the most part statistically based. They range from the purely statistical method of Alishouse et al. (1990) and the semistatistical method of Hargens (1992) to the semiphysical approach of Petty (1990).<sup>2</sup>

What sets the present work apart from these other methods is that every effort has been taken to retain the physics of the problem and to minimize empiricism. The basic philosophy of the present approach consists of using simple, vertically integrated closed forms of the radiative transfer equation. This type of method works well at SSM/I

---

<sup>2</sup>During the course of this research additional liquid water algorithms for the SSM/I have appeared in the literature, including Wentz (1992), which is a physical method conceptually similar to the present one; Liu and Curry (1993), which is a semi-physical approach; and Bauer and Schuessel (1993), which is semistatistical.

frequencies and outside areas of precipitation since the upwelling microwave radiation at the top of the atmosphere originates from a deep layer of the lower troposphere as a result of the very broad weighting functions. The present method is also distinct from the other SSM/I methods in that both water vapor and liquid water are retrieved at the same time, which is analogous to the physical methods that are used in retrieving integrated liquid water and water vapor from ground-based microwave radiometers (e.g., Westwater, 1978).

It is also important to note that the model developed in this study is identical in principal to the dual-frequency physical methods first adopted, for example, by Akvilonova and Kutuza (1979) and others, and later implemented by Grody et al. (1980). Therefore, the present method is a refinement of these previous techniques. The study of Grody et al., which is confined to the tropical and subtropical Pacific, differs from the present method in that the cloud and sea surface properties are held fixed. Another distinction of the present method from this earlier work includes a procedure to calibrate the model.

#### 2.4.1 Model description

The problem of retrieving the total water content (excluding ice) in nonprecipitating clouds from passive microwave measurements can be reduced to one involving only absorption and emission processes. If we invoke the Rayleigh-Jeans Law and assume an isothermal atmosphere, a simple solution to the radiative transfer equation for a purely absorbing/emitting atmosphere can be obtained. The horizontal ( $h$ ) and vertical ( $v$ ) polarized upwelling brightness temperatures at the top of such a hypothetical atmosphere can be expressed as (e.g., Grody, 1976)

$$T_{v,h} = T_s [1 - r_{v,h} \mathcal{T}_\ell^2 \mathcal{T}_w^2 \mathcal{T}_{ox}^2] \quad (2.2)$$

where  $r_{v,h}$  is the surface reflectivity of either vertical ( $v$ ) or horizontal ( $h$ ) polarization,  $T_s$  is the skin temperature of the surface,  $\mathcal{T}_\ell$  is the transmission resulting from cloud liquid water, and  $\mathcal{T}_w$  and  $\mathcal{T}_{ox}$  are the gaseous contributions to the atmospheric transmission from water vapor and oxygen, respectively. The surface reflectivity can be approximated as  $1 - \epsilon_{v,h}$  since the penetration depth of microwaves is very small so that nearly all of the transmitted energy is absorbed.

Despite the simplicity of (2.2) and the gross assumptions that are used to derive it, this model has been found to work surprisingly well in retrieving atmospheric water content over ocean surfaces, where the emissivity is to a certain extent uniform and relatively low ( $\sim 0.3$ – $0.6$ , depending on the frequency, polarization state and surface roughness). Land surfaces, on the other hand, pose a greater challenge in the retrieval of atmospheric parameters because of their large and highly variable emissivities (see, e.g., Jones and Vonder Haar, 1990).

In the development of the physical model, we begin with the water vapor retrieval method of Tjemkes et al. (1991), which uses 19.35 GHz measurements from the SSM/I and is based on (2.2). It is shown here in a slightly different form as

$$W = -\frac{\mu}{2\kappa_{w19}} \ln \left[ \frac{\bar{T}_{19} - T_{19v}}{T_s(1 - \epsilon_{19v})\mathcal{T}_{ox19}^2} \right], \quad (2.3)$$

where  $\mu$  is the cosine of the viewing zenith angle,  $\kappa_{w19}$  is the water vapor mass absorption coefficient that represents the scaling between total water vapor optical depth and integrated water vapor ( $W$ ),  $\epsilon_{19v}$  is the sea surface emissivity at vertical polarization, and

$$\bar{T}_{19} = T_s - \Gamma H_w(1 - \mathcal{T}_{w19})[\mathcal{T}_{ox19} + (1 - \epsilon_{19v})\mathcal{T}_{19}^2], \quad (2.4)$$

where  $\Gamma$  is the temperature lapse rate,  $H_w$  is the scale height of water vapor, and  $\mathcal{T}_{19}$  is the total atmospheric transmittance at 19.35 GHz. The second term on the right-hand side of (2.4) is to account for the change in emission height of water vapor with  $W$  (see Tjemkes et al. for details). One will notice that (2.3) does not include the 19.35h GHz channel, as shown in equation (22) of Tjemkes et al. It can be demonstrated with some algebra that this channel cancels out and the expression reduces to (2.3).

The value of  $\kappa_{w19}$  was slightly modified from the study of Tjemkes et al. to be  $2.58 \times 10^{-3} \text{ m}^2 \text{ kg}^{-1} (300/T_s)^{0.477}$ . This adjustment was necessary in order to provide a better comparison of the water vapor retrievals with radiosonde observations. It can be justified on the grounds that the absorption characteristics of water vapor are not well known; hence the transmission model used to estimate  $\kappa_{w19}$  may be in error. Also, this coefficient is used to indirectly account for biases that might be present in the 19.35 GHz brightness temperatures.

There are basically two reasons for using the 19.35v GHz channel. First, the 22.235 GHz channel, which is directly centered on a water vapor absorption line, has a greatly reduced sensitivity to changes in water vapor for extreme water vapor amounts (i.e., beyond about  $60\text{--}65\text{ kg m}^{-2}$ ), while nearby frequencies do not. Thus, using the 19.35 GHz channels can prevent ambiguities in estimating water vapor in certain regions of the tropics. The disadvantages of using the 19.35 GHz channels is that outside of the tropics they are much less sensitive to changes in water vapor than at 22.235 GHz (since the optical depths are about 3 times smaller) and they tend to result in water vapor retrievals with greater variability (an alternative algorithm that uses the 22.235 GHz channel is described in Appendix B).

Second, the reason for selecting the v-polarization component is that the brightness temperatures at v-polarization becomes relatively insensitive to changes in sea surface roughness (or indirectly wind speed) for viewing angles from about  $50^\circ$  to  $60^\circ$ . This is known from theory (e.g., Stogryn, 1967) and confirmed by observations (e.g., Hollinger, 1971; Sasaki et al., 1987). The h-polarization channels, on the other hand, are greatly sensitive to sea roughness effects but have little incidence angle sensitivity (Sasaki et al., 1987).

To simplify the retrieval of integrated water vapor, Tjemkes et al. assumed  $\bar{T}_{19} \approx T_s$ , which works well for a relatively transparent atmosphere. However, when  $W$  becomes greater than about  $20\text{--}25\text{ kg m}^{-2}$  this approximation breaks down since the contribution by the increasing effective emission height of water vapor becomes important. This is illustrated in Figure 2.5 where retrievals based on simulated brightness temperatures using the method of Tjemkes et al. are shown. The transmission model of Liebe (1981) was used for a sample of 81 radiosonde humidity and temperatures profiles over ocean regions. The simulations are for cloudless conditions and the ocean surface was calm. The results show an underestimation in the retrieved water vapor that sometimes reaches  $5\text{ kg m}^{-2}$  or more.

Due to this deficiency in the algorithm, particularly for higher water vapor amounts, the full expression for  $\bar{T}_{19}$  is used when the retrieved water vapor exceeds  $25\text{ kg m}^{-2}$ . However, additional simulations have shown that (2.4) greatly overestimates the contribution

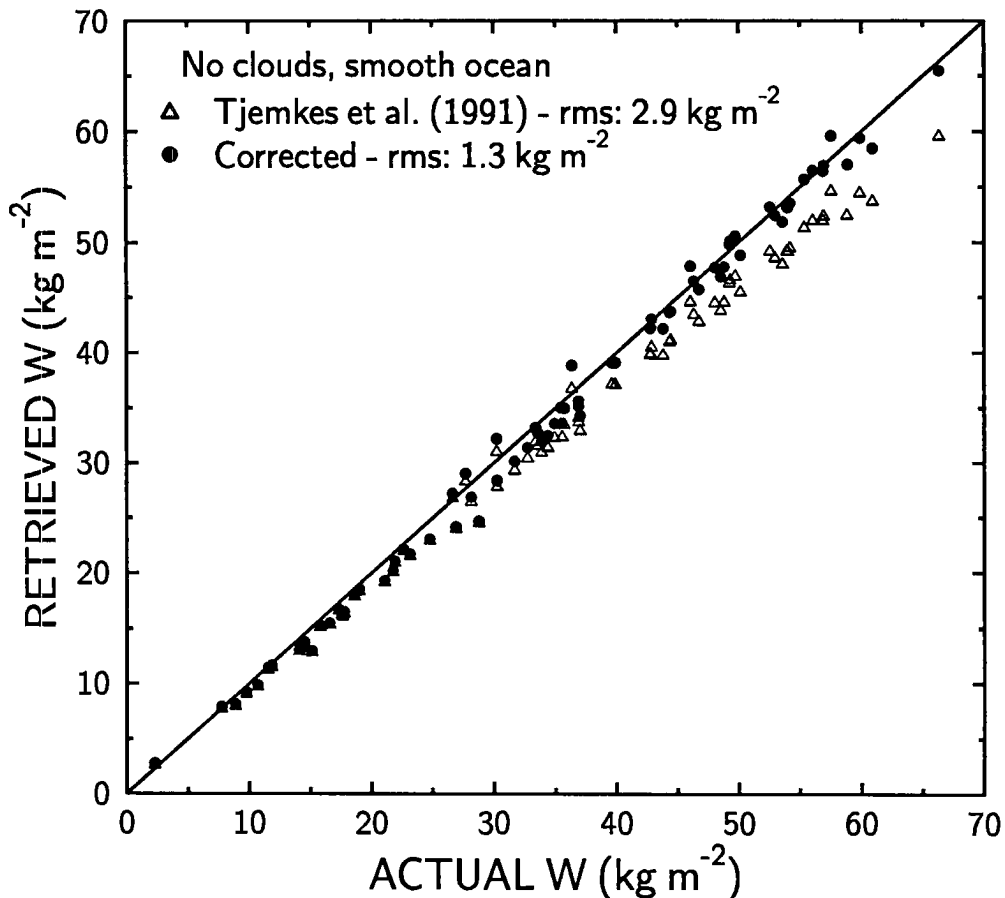


Figure 2.5: Water vapor retrievals for cloudless conditions from the method of Tjemkes et al. (1991) versus actual  $W$  ( $\text{kg m}^{-2}$ ) using simulated brightness temperatures over a smooth ocean from 81 radiosonde profiles over the ocean. Also included is the corrected algorithm (filled circles) and the rms errors. The line of perfect agreement is also shown.

from the water vapor emission height and clearly indicates problems with the formulation by Tjemkes et al. Rather than use statistical regression to correct for this effect, we have chosen instead to modify (2.4) and obtain a pseudo-analytical expression:

$$\bar{T}_{19} = T_s - \Gamma H_w (1 - f T_{w19}^2) \mathcal{T}_{oz19}, \quad (2.5)$$

where  $f = \exp(50\kappa_{w19}/\mu)$ , which is an empirical factor to prevent a discontinuity in the retrievals near  $25 \text{ kg m}^{-2}$  (an improved analytic expression for  $\bar{T}_{19}$  is described in Appendix B). Figure 2.5 shows the results of the retrievals using (2.3) and (2.5).  $\Gamma$  and  $H_w$  are set to typical values of  $5.8 \text{ K km}^{-1}$  and  $2.2 \text{ km}$ , respectively. The corrected algorithm gives

improved results as evidenced by the decrease in rms error from 2.9 to 1.3 kg m<sup>-2</sup> and the lack of any major biases in the retrievals.

It is evident from (2.3) that the obvious effects introduced by clouds are neglected. This is a reasonable assumption for optically thin clouds, which do not significantly alter the 19.35 GHz brightness temperatures. However, as pointed out by Tjemkes et al. (1991), a cloud possessing a moderate water content of 0.25 kg m<sup>-2</sup>, which is typical of thick marine stratocumulus clouds, can cause an error in the instantaneous retrieval of  $W$  of roughly 5 kg m<sup>-2</sup>. If we include the transmittance of a nonprecipitating cloud in (2.3) and assume  $\mathcal{T}_{w19} = \exp(-\kappa_{w19}W/\mu)$  and  $\mathcal{T}_{\ell19} = \exp(-\kappa_{\ell19}L/\mu)$ , we can write

$$\kappa_{w19}W + \kappa_{\ell19}L = -\frac{\mu}{2} \ln \left[ \frac{\bar{T}_{19} - T_{19v}}{T_s(1 - \epsilon_{19v})\mathcal{T}_{ox19}^2} \right], \quad (2.6)$$

where  $\kappa_{\ell19}$  is the liquid water mass absorption coefficient and  $L$  is the vertically integrated liquid water content or liquid water path (LWP) of the cloud.

The other frequency used in the retrieval method is 37 GHz, which lies in a window region and is more responsive to cloud liquid water than 19.35 GHz as seen in Figure 2.3. We may write an expression analogous to (2.6) for the 37v GHz channel as

$$\kappa_{w37}W + \kappa_{\ell37}L = -\frac{\mu}{2} \ln \left[ \frac{\bar{T}_{37} - T_{37v}}{T_s(1 - \epsilon_{37v})\mathcal{T}_{ox37}^2} \right], \quad (2.7)$$

where  $\bar{T}_{37} = T_s + \delta T_{37}$  and  $\delta T_{37}$  is a factor that might represent the contribution by the effective emission height of water vapor or other possible unmodelled effects, and  $\epsilon_{37v}$  and  $\mathcal{T}_{ox37}$  are the sea surface emissivity and oxygen transmittance, respectively, at 37 GHz.

An estimate of  $\delta T_{37}$  can be obtained by comparing the brightness temperatures computed from (2.7) to a more detailed radiative transfer model for clear sky conditions. Figure 2.6 shows the results of these calculations for the 81 profiles discussed earlier. A value of  $\delta T_{37}$  of -1.6 K was determined arbitrarily to give the best agreement. The adjusted temperatures from the simple model are very good for low to intermediate values, but there are noticeable discrepancies at higher brightness temperatures, which become greater with increasing temperature. Thus, there also appears to be a water vapor emission height effect at 37 GHz as well, although it is weaker than at 19.35 GHz. For the

purposes of this study we have chosen not to account for this effect (an improved analytic relationship for 37 GHz is discussed in Appendix B). However, an unfortunate consequence of the high brightness temperatures is to cause small negative biases in the cloud liquid water retrievals in areas of high water vapor.

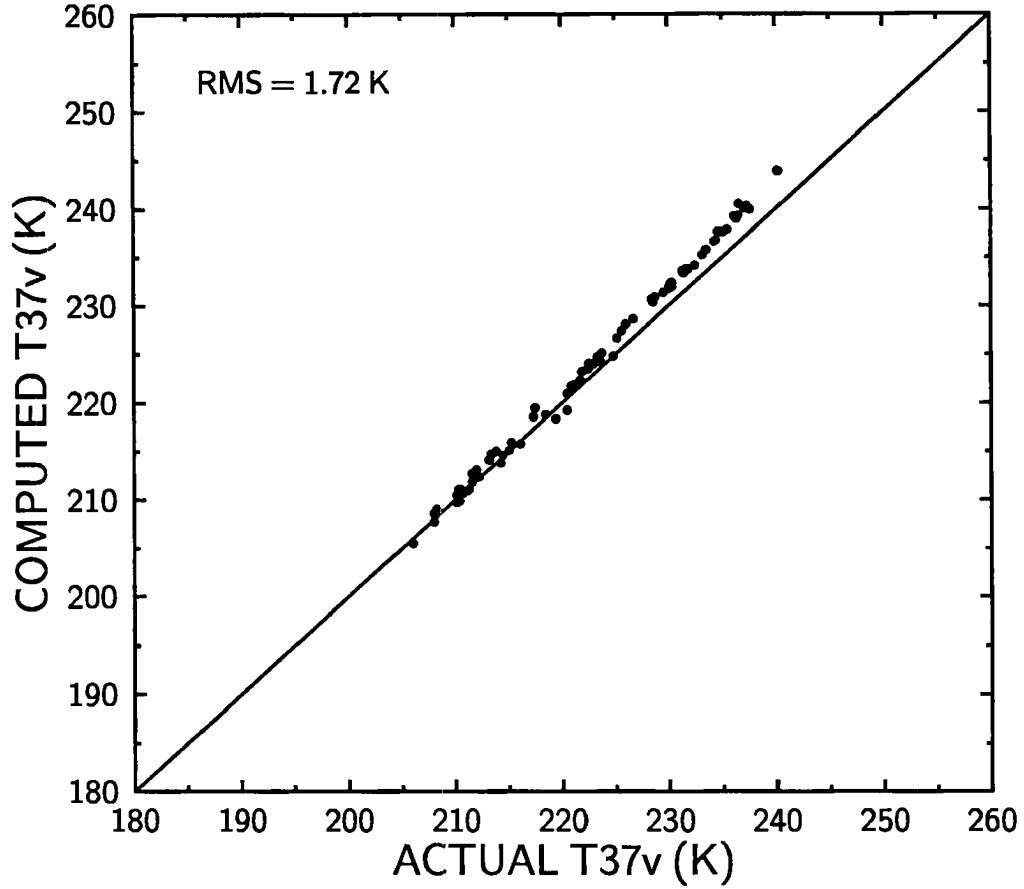


Figure 2.6: Calculations of 37 GHz brightness temperatures from the simple model (2.7) versus more detailed calculations (actual) under clear sky conditions.

Finally, combining (2.6) and (2.7) yields a set of linear equations with the following solutions:

$$W = \frac{\tau_1 \kappa_{\ell 37} - \tau_2 \kappa_{\ell 19}}{\delta} \quad (2.8)$$

$$L = \frac{\tau_2 \kappa_w 19 - \tau_1 \kappa_w 37}{\delta} \quad (2.9)$$

where,

$$\delta = \kappa_w 19 \kappa_{\ell 37} - \kappa_w 37 \kappa_{\ell 19}$$

and  $\tau_1$  and  $\tau_2$  are the right-hand sides of equations (2.6) and (2.7), respectively, which in physical terms represent the optical depths of the total atmospheric water (outside regions of precipitation and excluding ice) at both frequencies. Water vapor optical depths at 19.35 GHz range from about 0.01 to 0.16. Liquid water optical depths at 37 GHz, on the other hand, usually range from less than 0.01 to about 0.1. The procedure for finding  $W$  and  $L$  is to first apply (2.8) and (2.9) using  $\bar{T}_{19} = T_s$ . If  $W \leq 25 \text{ kg m}^{-2}$ , then no further calculations are necessary. On the other hand, if  $W > 25 \text{ kg m}^{-2}$  the retrieved values are used as initial guesses in deriving iterative solutions, where  $\bar{T}_{19}$  is a function of  $W$  as shown in (2.5).

A number of models exist (e.g., Wilheit, 1979; Pandey and Kakar, 1982; Petty, 1990) that may be used to compute the sea surface emissivities in (2.6) and (2.7). In this study the rough emissivity model of Petty (1990) is used since it has been carefully calibrated against SSM/I observations. The formulas of Klein and Swift (1977) are used to compute the dielectric constants for saltwater (a constant value of salinity of 36.5 ppt is adequate since the salinity dependence of the dielectric constant at SSM/I frequencies is nearly negligible), which are then used to calculate the emissivities for a smooth (Fresnel) surface. The dielectric constant of water also depends on temperature and monthly mean SSTs are used for this purpose.

To estimate rough sea surface emissivities, Petty employs a geometric optics approximation. The influences of foam and other related effects on the emissivity are incorporated into the model by assuming a linear weighting of the rough emissivity and foam emissivity based on the foam fraction. In a novel approach, Petty uses SSM/I observations to estimate the dependence of both the effective slope variances of the waves and foam on wind speed for each of the channels. The slope variances are important in determining the rough emissivities. Petty found little or no wind speed dependence of the foam for wind speeds less than  $7 \text{ m s}^{-1}$ . For higher winds a linear relationship was determined between foam fraction and wind speed. In the application of this emissivity model in the present method it is important to set the empirical emissivity bias corrections derived by Petty to zero.

The near surface wind speed, which is required as input to the Petty model, is retrieved from SSM/I measurements using the global statistical method of Goodberlet et al. (1989). The method achieves an accuracy of roughly  $\pm 2 \text{ m s}^{-1}$  over most marine regions based on a comparison to buoy observed winds. A recent study by Bates (1991) suggests that the Goodberlet et al. algorithm may have problems in regions of high SST and  $W$ , such as in the western tropical Pacific. The reason is that the algorithm relies too heavily on the 22.235 and 19.35 GHz channels. In regions of abundant water vapor the algorithm no longer provides a measure of wind speed but instead is coupled to changes in water vapor. Therefore in this study the Bates (1991) algorithm is used in regions that generally have large amounts of water vapor, which we have arbitrarily defined for monthly mean SSTs that reach beyond 300 K. The Bates algorithm is not without its own problems, however. For example, based on simulations, the algorithm shows a tendency for the retrieved wind speed to decrease with increasing water vapor amount (Wentz, personal communication, 1992).

Specification of the sea surface skin temperature is handled by using a monthly mean SST, such as was done by Tjemkes et al. (1991). This is acceptable since the error analysis in Chapter 3 suggests that uncertainties in the skin temperature of up to 3 to 4 K, in most instances, do not result in large retrieval errors. The SST data are those produced operationally by the National Meteorological Center, which are on a  $2^\circ \times 2^\circ$  global grid and consist of ship and buoy observations that are blended with satellite data (Reynolds, 1988).

The oxygen transmittances at 19.35 and 37 GHz ( $\mathcal{T}_{ox19}$  and  $\mathcal{T}_{ox37}$ ) were determined using the transmission model of Liebe (1981) and 81 radiosonde profiles over the ocean. Figure 2.7 shows the oxygen transmittances versus surface air temperature, which is used here as a surrogate for the temperature profile. It can be seen from this figure that the transmission increases at both frequencies as the lower to middle tropospheric temperatures rise. To account for this apparent temperature effect, an equation of the form  $\mathcal{T}_{ox} = a + bT_a + cT_a^2 + dT_a^3$  is fit through the points, where  $T_a$  is the surface air temperature in degrees Celsius, which is replaced by the monthly mean SST. The best fit coefficients are shown in Table 2.3.

The liquid water mass absorption coefficients,  $\kappa_{\ell 19}$  and  $\kappa_{\ell 37}$ , depend strongly on temperature (see Figure 2.3) so one must provide some estimate of the effective cloud temperature  $T_c$ . While these coefficients can be computed from (2.1), we use instead the formulas of Petty (1990), which are statistically fitted to calculations from (2.1), for reasons of computational simplicity. The cubic fit coefficients are shown in Table 2.3 and apply to temperatures in units of degrees Celsius. In the calculation of these absorption coefficients it is assumed that the effective temperature of the cloud is the same at 19.35 and 37 GHz. This is a good assumption since the weighting functions for these two frequencies have nearly the same shape and hence the effective radiating temperatures are very similar. One important point should be made regarding the interpretation of the

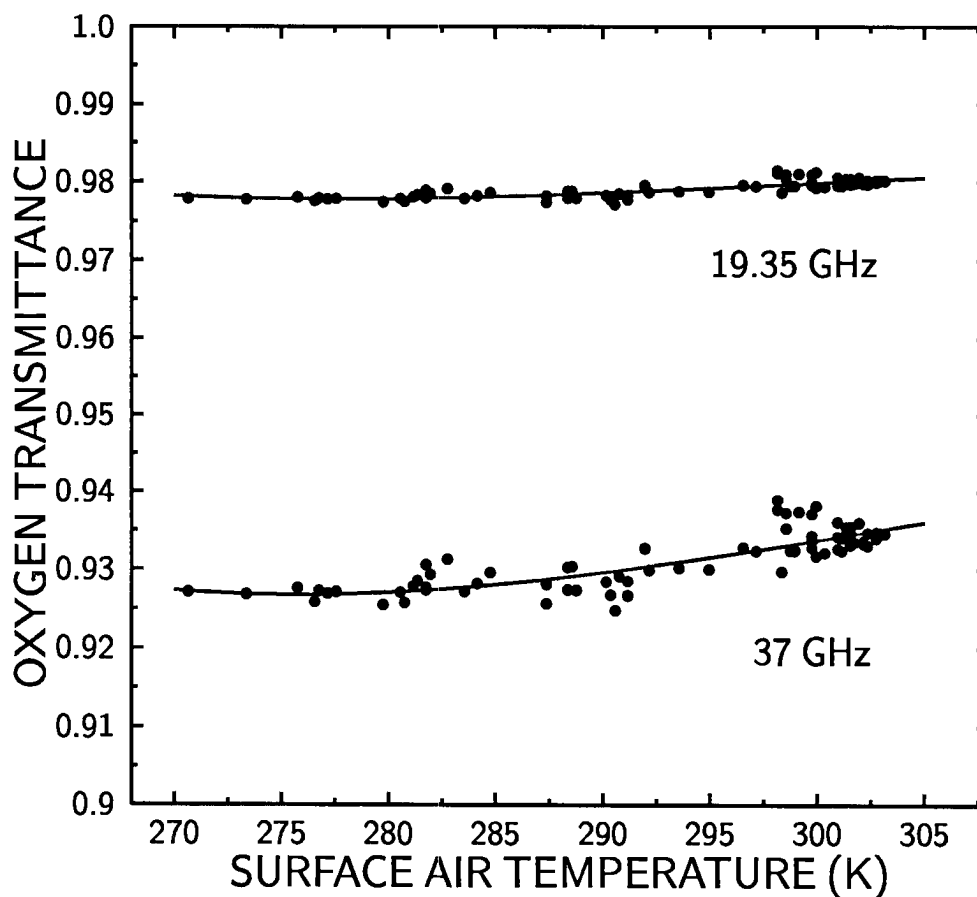


Figure 2.7: Theoretical calculations of oxygen transmission at 19.35 and 37 GHz versus surface air temperature (K) for 81 radiosonde temperature profiles over the ocean. Also indicated are cubic fits to the data points for each frequency, whose coefficients are shown in Table 2.3.

Table 2.3: Cubic fit Coefficients for oxygen transmission  $\mathcal{T}_{ox}$  and liquid water absorption  $\kappa_{\ell}$  (from Petty, 1990) at 19.35 and 37 GHz.

	a	b	c	d
$\mathcal{T}_{ox19}$	0.9779	$-6.314 \times 10^{-5}$	$7.746 \times 10^{-6}$	$-1.003 \times 10^{-7}$
$\mathcal{T}_{ox37}$	0.9269	$-8.525 \times 10^{-5}$	$1.807 \times 10^{-5}$	$-2.008 \times 10^{-7}$
$\kappa_{\ell19}$	0.0786	$-2.30 \times 10^{-3}$	$4.48 \times 10^{-5}$	$-4.64 \times 10^{-7}$
$\kappa_{\ell37}$	0.267	$-6.73 \times 10^{-3}$	$9.75 \times 10^{-5}$	$-7.24 \times 10^{-7}$

liquid water absorption coefficients in the present model. It will be discussed in the next chapter that since the effective emission height of the liquid water is not included in the model, these coefficients also must implicitly account for this effect.

One of the most difficult parameters in the model to estimate is the effective cloud temperature or radiating temperature of the cloud (see Appendix B for a definition of this quantity). Pandey et al. (1983) have shown that it is certainly possible (albeit in a highly statistical way) to infer cloud temperature from multi-channel microwave measurements along with cloud top temperature information from infrared (IR) observations. A much simpler approach is used in this study to specify the cloud temperature. Since we have no a priori knowledge of the height and temperature of the cloud base or the cloud thickness, a climatological effective cloud temperature is estimated based on monthly mean SSTs. The justification is that the temperature of most clouds, in a climatological sense, roughly follows the sea surface temperature. Thus we let  $T_c \approx \text{SST} - 6 \text{ K}$ , which is considered to be representative of most marine boundary layer clouds. A limitation of this crude approximation is that if the cloud is near the sea surface or if a temperature inversion is present, which occurs often at high latitudes, then the retrieved liquid water is likely to be underestimated. For high clouds or clouds with a large vertical extent an overestimation in the retrieval of liquid water will likely result.

As a result of the changes that have been made to the Tjemkes et al. water vapor algorithm, it is appropriate to show a comparison of the water vapor amounts derived from the present method (2.8) to near-coincident radiosonde measurements. The validation is somewhat limited and involves radiosonde measurements of  $W$  over the North Sea during the International Cirrus Experiment (ICE) in 1989 and in the west Pacific during the 1990

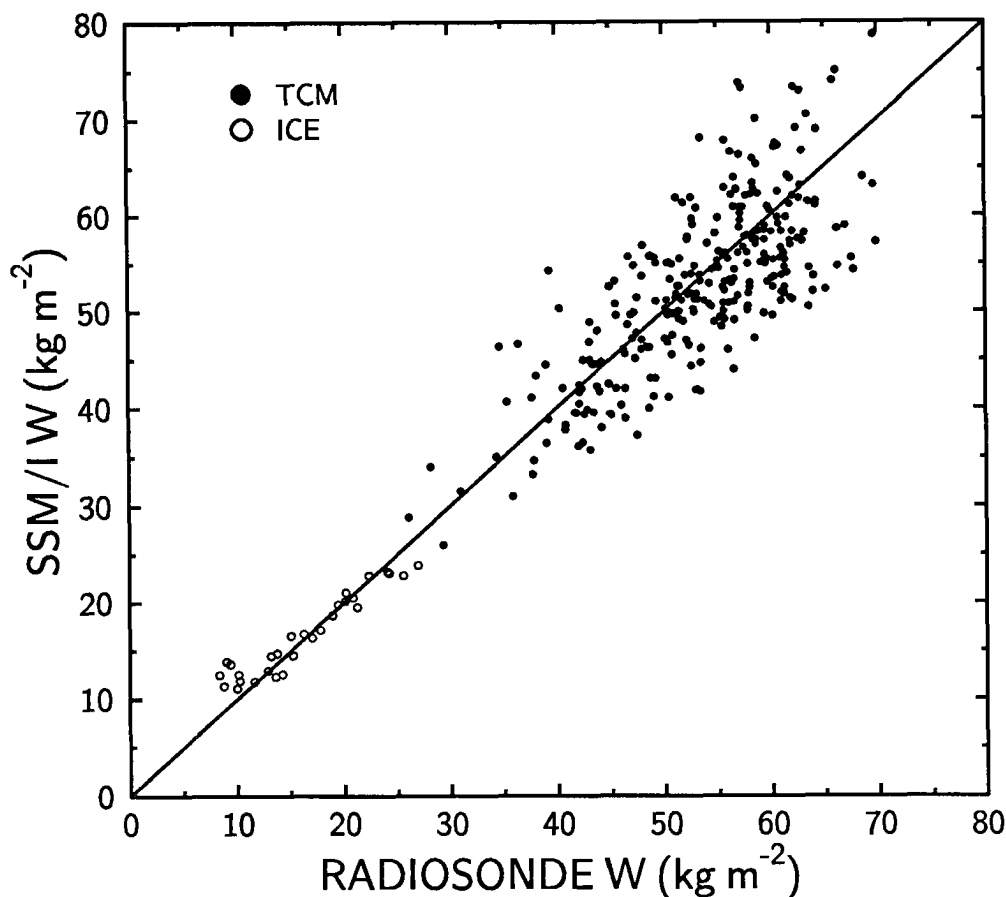


Figure 2.8: Comparison of SSM/I-derived precipitable water ( $W$ ,  $\text{kg m}^{-2}$ ) and radiosonde measurements during the 1989 International Cirrus Experiment (ICE) and the 1990 Tropical Cyclone Motion (TCM) Experiment.

Tropical Cyclone (TCM) Experiment. The ICE measurements were taken on the research vessel Poseiden and consist of 27 cases. These measurements were all within 2 hours of a DMSP overpass and frequently were within half an hour to several minutes. In order to have an adequate sample of radiosonde measurements from the TCM Experiment, the criterion was increased to  $\pm 3$  hours within a satellite overpass, which resulted in a total of 292 observations. These observations originated from both small island stations and ships scattered throughout the west Pacific. Cases where precipitation may have been occurring were eliminated and only SSM/I pixels inside of a 50 km radius of the site were used in the comparison. The results, which are shown in Figure 2.8, are very good for a wide range of water vapor values. The rms difference is  $1.9 \text{ kg m}^{-2}$  for the ICE measurements

and  $5.9 \text{ kg m}^{-2}$  for the TCM measurements, which is slightly larger than other water vapor retrieval algorithms. While Figure 2.8 can be useful in providing an estimate of the uncertainties in the satellite retrievals, it is likely that some of the differences between the radiosonde and satellite measurements may be due to mismatches in time and space.

#### 2.4.2 Model calibration

The main purpose of the calibration process is to arrive at an estimate of the one physical quantity that remains to be specified in the model, namely,  $\kappa_{w37}$ . It also accounts for uncertainties in oxygen and water vapor transmission at 37 GHz, possible biases in the sea surface emissivity model and brightness temperatures, and other unmodeled effects. This procedure is done by using SSM/I measurements in known cloud-free areas. The reason for exploiting such measurements is that three unknown variables, i.e. the liquid water path,  $\kappa_{\ell19}$  and  $\kappa_{\ell37}$ , can be eliminated from the model so as to provide a calibration that is independent of cloud properties (e.g., Petty, 1990). The cloud-free data set consists of 12,287 individual SSM/I pixels that are considered to be, for the most part, free of cloud contamination based on GOES (Geostationary Operational Environmental Satellite) imagery (see Petty, 1990). These observations are located primarily off the east and west coasts of the U.S. for August and September 1987 and January 1988. A number of additional pixels is also included from the North Sea for October 1987. This data set, unfortunately, represents a somewhat limited range of meteorological conditions with surface wind speeds ranging from  $0\text{--}16 \text{ m s}^{-1}$  and water vapor amounts mostly confined to less than  $25 \text{ kg m}^{-2}$  and extending only to about  $50 \text{ kg m}^{-2}$ . However, the monthly mean SSTs have a broad range from 275 to over 300 K.

Since we assume that the cloud liquid water for these observations is at or near zero we can set  $L = 0$  in (2.7) so that the water vapor optical depth at 37 GHz ( $\tau_{w37}$ ) is simply equal to  $\tau_2$ . If  $\tau_{w37}$  derived from the cloud-free data set is plotted against the  $W$  retrieved from (2.3), one can obtain a direct estimate of  $\kappa_{w37}$ . The relationship between  $\tau_{w37}$  and  $W$ , as shown in Figure 2.9, is very distinct and nearly linear. A correction factor of 1.98 K was used in the 37v-GHz channel to correct a constant offset that was evident in the optical depths. This factor is determined specifically for the SSM/I on the DMSP F-8 satellite

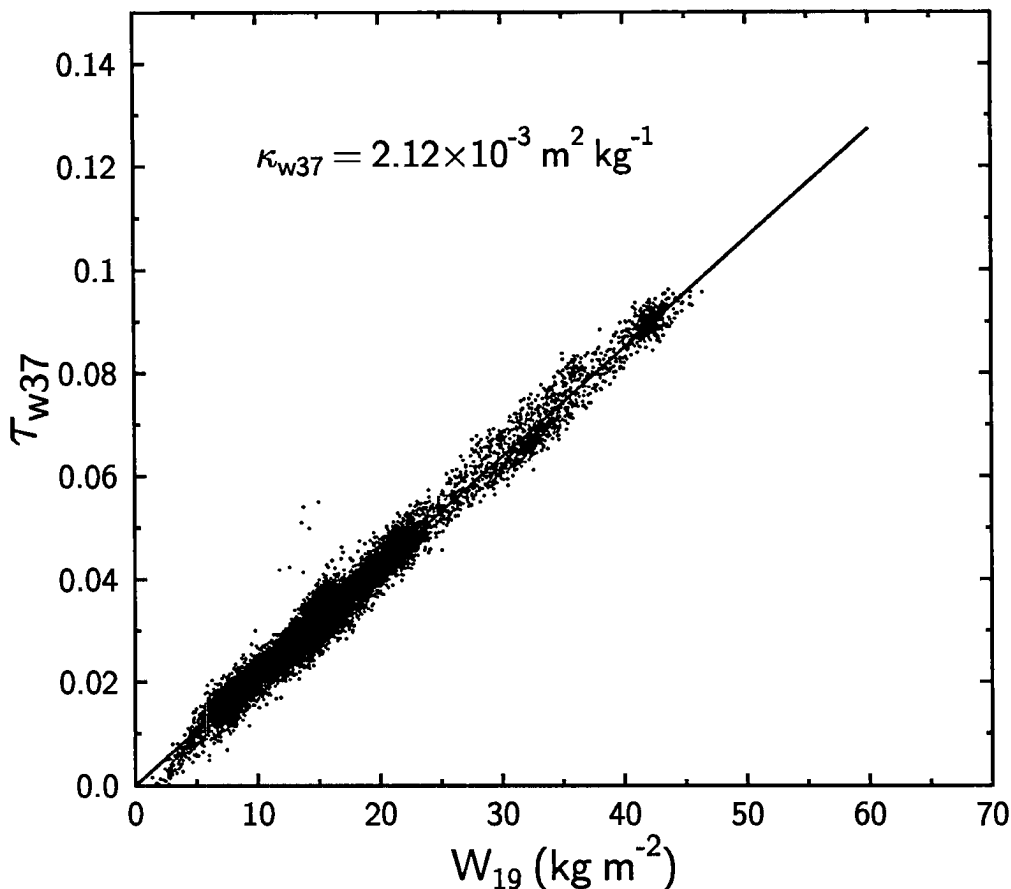


Figure 2.9: Scatter diagram of total water vapor optical depth at 37 GHz ( $\tau_{w37}$ ) versus  $W$  retrieved from 19 GHz measurements ( $W_{19}$ ,  $\text{kg m}^{-2}$ ) for the cloud-free data set. Also shown is a linear least squares fit of the data where the slope corresponds to the water vapor absorption coefficient at 37 GHz ( $\kappa_{w37}$ ).

and a recalibration of the model will be necessary for the SSM/Is on the other satellites. The rationale for adjusting these channels is that it is likely that the biases in the model are largely attributed to systematic biases in the 37-GHz brightness temperatures. This assumption is supported by the study of Petty (1990) where evidence of a cold bias of 2–3 K in 37-GHz observations of melting snow was seen, suggesting it is a sensor calibration error. Petty (1990) also independently derived a similar bias correction for the 37 GHz channels, but expressed it as a correction to the sea surface emissivity. From a linear least squares fit  $\kappa_{w37}$  is determined to be  $2.12 \times 10^{-3} \text{ m}^2 \text{ kg}^{-1}$ . This is in excellent agreement

with the value of  $2.0 \times 10^{-3} \text{ m}^2 \text{ kg}^{-1}$  found by Liu et al. (1992), which was based on transmission calculations for 609 radiosonde soundings.

To illustrate how well the physical model behaves in regions of clear skies, a histogram is presented in Figure 2.10 of the cloud liquid water derived from the cloud-free data set. As expected, the mean LWP is near zero ( $3 \times 10^{-4} \text{ kg m}^{-2}$ ), which is naturally a consequence of the calibration. What is more important, however, is the very small variability of the LWP, which has a standard deviation of  $0.016 \text{ kg m}^{-2}$ . This variability provides an observational measure of the minimum uncertainties that one might expect in the liquid water retrievals. It is significantly smaller than the standard deviations derived by the Petty (1990) and Hargens (1992) algorithms, which are  $0.025$  and  $0.023 \text{ kg m}^{-2}$ , respectively. It should be emphasized that the clear sky data set used in this study is a

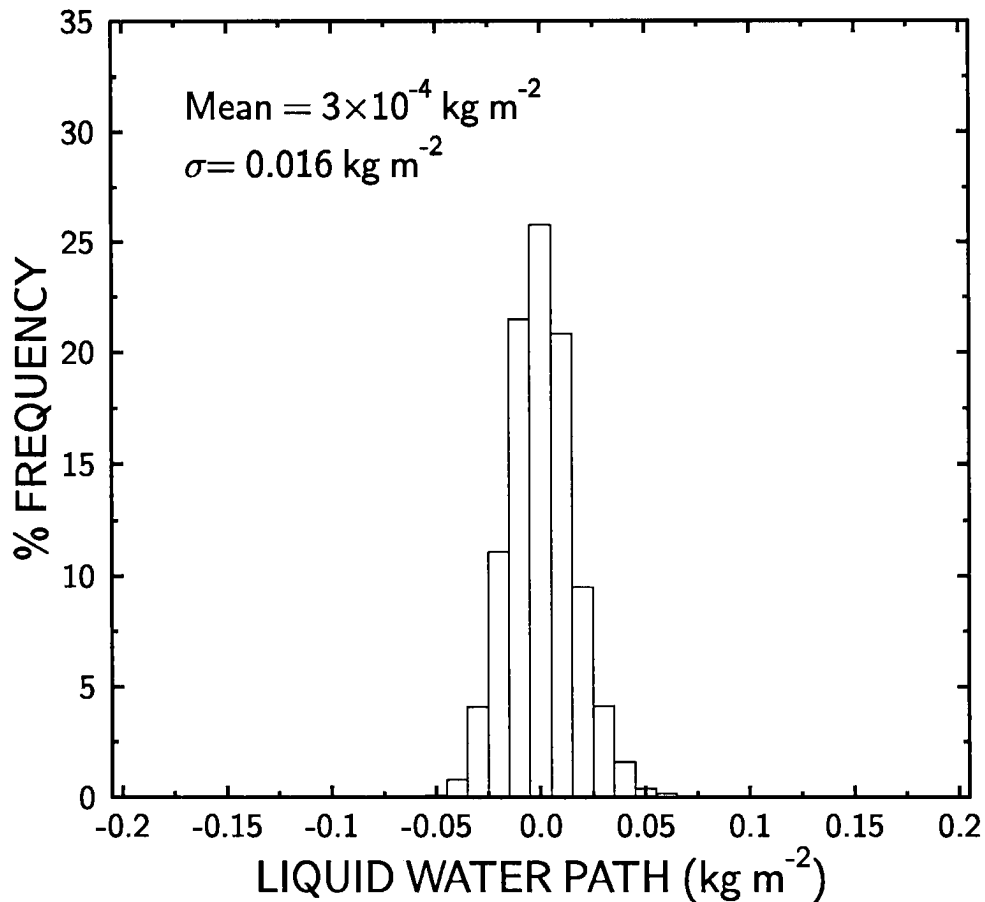


Figure 2.10: Histogram of integrated cloud liquid water ( $\text{kg m}^{-2}$ ) retrieved from the cloud-free data set. The mean and standard deviation are also given.

limited sample of observations and is weighted heavily towards low water vapor amounts. Therefore, in a tropical environment the value of  $\kappa_{w37}$  may require a slight adjustment and, as will be discussed in a subsequent section, the uncertainties in the retrievals are likely to be larger than  $0.016 \text{ kg m}^{-2}$ .

### 2.4.3 Precipitation effects

In regions of precipitating cloud systems the retrieval of cloud liquid water becomes especially difficult because of the dominant influence of absorption and scattering of microwave radiation by precipitation size particles. The upwelling radiation at 19.35 GHz over these cloud systems consists mainly of the strong emission by raindrops below the freezing level (Spencer et al., 1989), while at 37 GHz both absorption and volume scattering effects by raindrops are important. Precipitation in the solid phase has little effect at these frequencies since the absorption by ice is negligible. However, in the presence of large ice particles, radiation at 37 GHz can be scattered as well as polarized (Adler et al., 1990).

Since the present model does not allow for multiple scattering effects or absorption by raindrops, the retrieved cloud liquid water will be overestimated in most cases (the possible exception is during extreme rainfall events where enhanced scattering at 37 GHz by raindrops may lead to underestimates). The overestimation is caused principally by the enhanced absorption by raindrops, which is interpreted by the model as increased cloud liquid water.

There are a number of methods, both scattering and attenuation based, that are available to identify SSM/I pixels suspected of being contaminated by precipitation (e.g., Spencer et al., 1989; Petty, 1990; Liu and Curry, 1992). Rather than applying these techniques we have chosen instead to define a threshold of cloud liquid water of  $0.5 \text{ kg m}^{-2}$  to detect situations where there might be substantial rainfall within the FOV of the instrument. This is based on the notion that the retrieval will in most cases overestimate the cloud liquid water under these conditions. While this criterion may appear to be arbitrary it has support from various studies as being, on average, a value associated with the initiation of rain (e.g., Curry et al., 1990; Liu and Curry, 1992).

As an example of the applicability of using a LWP threshold to detect precipitation, the pixel frequency of LWP retrievals greater than  $0.5 \text{ kg m}^{-2}$  is shown in Figure 2.11 as global distributions for the months of January and July 1990. The spatial characteristics of these distributions are very similar to what might be expected for rainfall rate, as seen, for instance, in the rainfall climatic data presented by Spencer (1993). For example, the highest number of pixels are generally located along the Intertropical Convergence Zone (ITCZ), the South Pacific Convergence Zone (SPCZ), in the tropical west Pacific, and along the midlatitude storm tracks. Also, the lowest pixel frequencies ( $< 40$ ) are common at the highest latitudes and in areas dominated by high pressure systems. One curious feature in these distributions is the probable underestimation of the pixel frequency in the tropical west Pacific and eastern Indian Ocean where intense and extensive convective precipitation occurs. One reason for this may be related to the choice of the LWP threshold. It is likely that a slightly lower threshold is required in these regions. Another possible cause of the underestimation is the low biases in the LWP retrievals in areas of high water vapor as noted earlier in section 2.4.1. These results suggest that while applying a constant LWP threshold in all regions may not be appropriate under every circumstance, it will certainly eliminate pixels that are greatly contaminated by precipitation.

## Chapter 3

### RETRIEVAL ERROR ANALYSIS AND VALIDATION

While countless studies have shown that retrievals of cloud liquid water from satellite microwave measurements are indeed possible and appear to give reasonable results, little has been done to validate the retrievals. Furthermore, a rigorous error analysis of the retrievals has been sorely lacking. This chapter presents the most comprehensive validation to date of cloud liquid water retrievals from space and provides an extensive error analysis under a variety of different atmospheric and surface conditions.

#### 3.1 Error and Sensitivity Analysis

##### 3.1.1 Simulations

The principal objectives of the model simulations are to provide a simple evaluation of the retrieval method and to aid in interpreting certain aspects of the model. One approximation that will be tested is the specification of the effective cloud temperature as  $SST - 6$  K. The retrieval algorithm was applied to forward model calculations of microwave radiances for a typical range of cloud types and atmospheric conditions (see Figure 3.1). A doubling and adding radiative transfer model was used that includes polarization. Gaseous absorption is determined from the empirical transmission model of Liebe (1981). In these calculations the ocean surface is calm, the clouds are plane-parallel, and the zenith angle of the emergent radiation is  $54^\circ$  (which corresponds to the  $53^\circ$  viewing angle of the SSM/I).

The results of the retrievals are shown in Table 3.1 and include the % retrieval error and the change in cloud temperature needed to match the retrieved cloud liquid water with that specified in the model. Note that the oxygen transmission used in these retrievals is computed from the actual temperature profiles so as isolate the uncertainties

resulting from cloud temperature errors. These results indicate that the cloud temperature approximation works surprisingly well for most cloud types except perhaps for thin stratocumulus clouds (labeled cloud 1 in Table 3.1) where the retrieved liquid water is about 14% greater than the actual liquid water in the cloud.

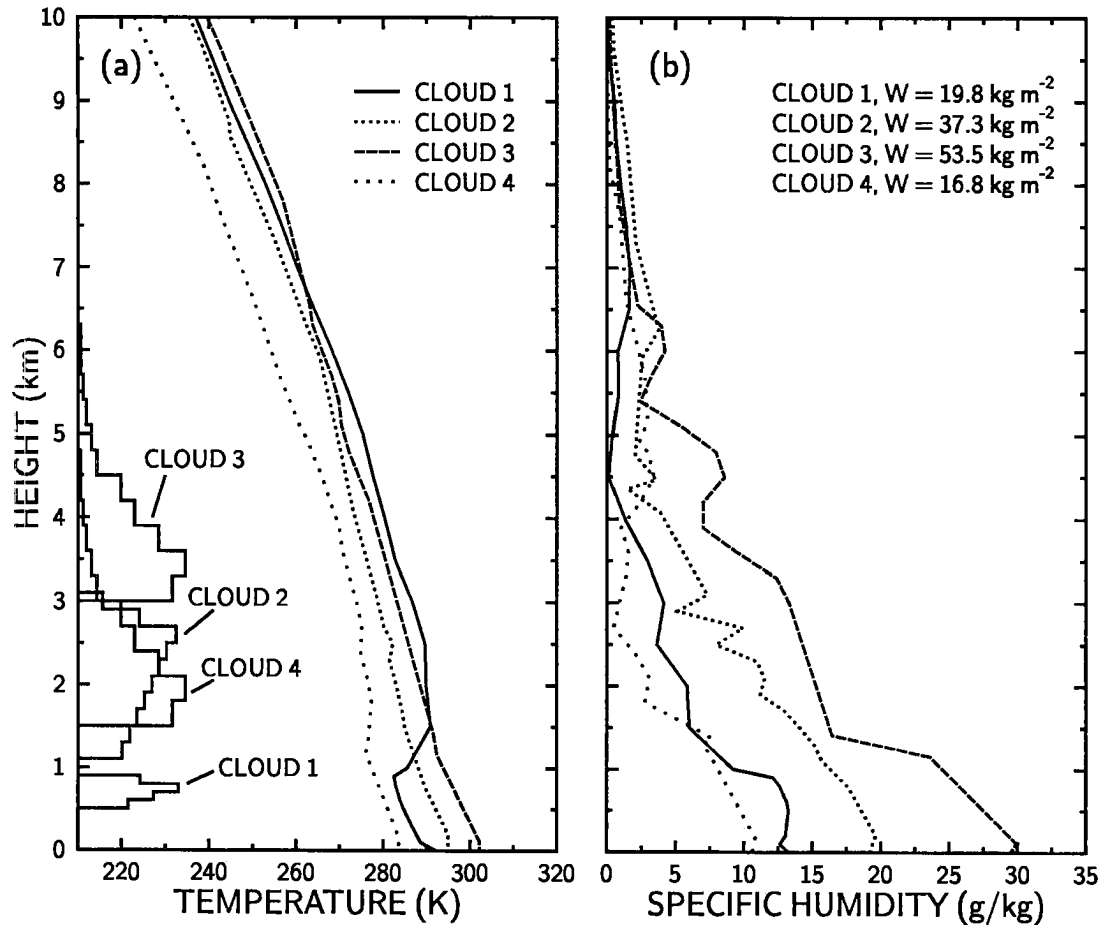


Figure 3.1: Vertical profiles of (a) cloud liquid water and temperature and (b) specific humidity used in the radiative transfer calculations. Also shown is the integrated water vapor ( $W$ ) for each humidity profile.

An unexpected result is that the level at which the cloud temperature is required to match the actual cloud liquid water was in most cases well *below* the cloud base. We conclude that  $\kappa_{\ell 19}$  and  $\kappa_{\ell 37}$ , in the context of this simple one-layer model, cannot be interpreted as merely absorption coefficients. These coefficients are also needed to indirectly account for the contribution from the effective emission height of the liquid

water, which is not considered in the present method. Improved retrieval algorithms that incorporate the liquid water emission height are described in Appendix B.

Table 3.1: Retrieval errors (%) attributed to uncertainties in cloud temperature  $T_c$  based on simulated brightness temperatures for the cloud liquid water profiles in Figure 3.1. Also shown is the change in  $T_c$  ( $\Delta T_c$ , K) necessary to match the retrieved integrated liquid water to the actual cloud liquid water ( $L$ ,  $\text{kg m}^{-2}$ ).

	$L=0.1$		$L=0.2$		$L=0.3$	
	% Err	$\Delta T_c$	% Err	$\Delta T_c$	% Err	$\Delta T_c$
Cloud 1	14	-4.1	9.2	-2.7	7.2	-2.1
Cloud 2	-	-	0.20	-0.04	0.46	-0.12
Cloud 3	-	-	8.9	-2.7	7.2	-2.2
Cloud 4	-4.0	1.2	-3.3	0.95	-3.0	0.9
	$L=0.4$		$L=0.6$		$L=0.8$	
	% Err	$\Delta T_c$	% Err	$\Delta T_c$	% Err	$\Delta T_c$
Cloud 1	-3.9	1.2	-	-	-	-
Cloud 2	-0.6	-0.2	-1.1	0.3	-3.2	1.0
Cloud 3	-4.1	-1.2	-0.3	0.1	-5.3	1.7
Cloud 4	-2.8	0.8	-4.0	1.2	-5.5	1.6

As mentioned in the previous chapter, the present retrieval method is strictly valid only for nonprecipitating cloud systems. One way of expressing the expected range of validity of the method is through a plot of simulated brightness temperatures for different atmospheric conditions. Figure 3.2 shows a scatter diagram of upwelling brightness temperatures at 19.35v GHz versus 37v GHz. The calculations were done over an ocean surface and do not include the effects of wind-induced surface roughness. The clear sky calculations involve the same 81 temperature and humidity profiles that were used for the water vapor retrievals in Figure 2.5. The simulations of nonprecipitating clouds consist of the profiles shown in Figure 3.1 and the integrated liquid water amounts in Table 3.1.

The brightness temperatures determined for precipitating clouds are much more involved and require additional explanation. Rather than use arbitrary profiles of water and ice species to represent hypothetical precipitating clouds we opted instead to use 2-D dynamical model simulations of a tropical mesoscale convective system during EMEX (Equatorial Mesoscale Experiment) as a basis for the profiles. The CSU-RAMS (Regional

Atmospheric Modeling System) was used and details concerning the model simulations are discussed by Wong et al. (1993). The size distributions of the various constituents consisted of the Marshall-Palmer distribution for rain, aggregates, and graupel, and a modified Gamma distribution for cloud drops. The ice crystal distributions were specified from aircraft measurements during FIRE. A more complete description of these distributions is given by Wong et al. (1993). The radiative transfer calculations were performed using the multidimensional model of Evans (1993), which uses the SHSG (Spherical Harmonic Spatial Grid) method of solution. For these calculations, however, the independent pixel approximation mode of the model was used. The calculations are provided at a zenith angle of  $53.13^\circ$ , which is slightly different than the angle of  $54.03^\circ$  for the clear sky and nonprecipitating cloud simulations. Thus, the brightness temperatures for the mesoscale convective system (MCS) were scaled by a ratio of the cosine of the zenith angles (a factor of about 1.02) to be consistent with the other simulations. Another difference in the MCS simulations is that a different gaseous absorption model (Liebe, 1993) was used.

In regions outside of precipitation it can be seen in Figure 3.2 that radiation at both 37v GHz and 19.35v GHz increases monotonically with an increase in either water vapor or cloud liquid water content, as expected. This area is represented by the points contained in the ellipse. The range of brightness temperatures in which the present method can be confidently applied is roughly along a line from 200 K and 170 K, at 37v and 19.35v GHz, respectively, to 260 K and 235 K. Although the effects from sea surface roughness have not been considered the brightness temperatures would also generally fall within the ellipse since the v-polarization component is less sensitive to these effects.

The relationship between 37v GHz and 19.35v GHz for the MCS, on the other hand, exhibits a more complex behavior. The brightness temperatures are in most instances larger than those outside of precipitation, particularly at 19.35v GHz, which is a result of increased absorption by raindrops. However, under certain circumstances the 37v GHz brightness temperatures can be comparable to or lower than that for a clear, very dry atmosphere. These colder 37v GHz brightness temperatures are also associated with 19.35v GHz temperatures that are comparable to those for tropical clear sky conditions.

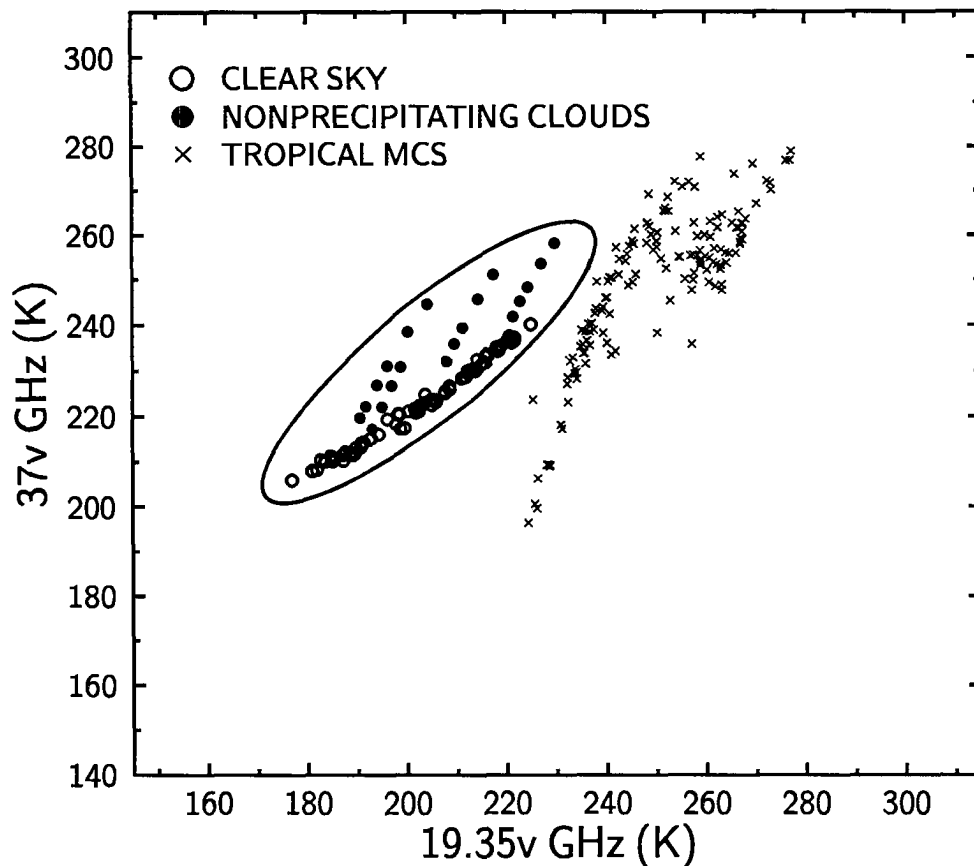


Figure 3.2: Scatter diagram of simulated brightness temperatures at 37v GHz versus those at 19.35v GHz for clear conditions (circles), nonprecipitating clouds (filled circles), and for a tropical mesoscale convective system (crosses). The ellipse illustrates the approximate range of brightness temperatures where the present liquid water retrieval method is valid.

This suggests that the very cold 37v GHz values are probably outside of the core of intense convective rainfall and are the result of scattering effects from large ice particles. This is confirmed from the cloud simulations, which indicated extremely high integrated ice water contents and lower rainfall rates.

While the 19.35v/37v GHz relationship for clear sky and nonprecipitating clouds can be uniquely defined from that for a tropical convective system, the situation might be less clear for other types of precipitating cloud systems. For example, distinguishing between light stratiform precipitation from nonprecipitating regions may be more difficult.

### 3.1.2 Error estimates

In this section the aim is to provide quantitative estimates of the total retrieval errors under different meteorological conditions. The analysis is confined to nonprecipitating

clouds. The approach that is used to determine the errors in (2.9) is one based on propagation of errors, whereby the variance in  $L$  can be expressed as a sum of the uncertainties in a few key atmospheric and surface variables as:

$$\sigma_L^2 \approx \sum_{i=1}^N \sigma_x^2 \left( \frac{\partial L}{\partial x} \right)^2 \quad (3.1)$$

where  $\sigma_x$  represents the standard deviations of the respective variables  $x$ , which include wind speed, the absorption coefficients, surface skin temperature, brightness temperatures, oxygen transmittances, and the cloud temperature. It is assumed in (3.1) that there is little or no correlation among the variables so the covariances are negligible. Uncertainties in the SSM/I viewing angle are neglected because they are less than  $0.1^\circ$ , and their influence on the results is expected to be very small.

The uncertainty in  $L$  will, of course to a large extent, depend on what values are designated for the uncertainties in the various independent variables in (3.1). A pessimistic value of  $\pm 4 \text{ m s}^{-1}$  is assigned to the uncertainty in wind speed, which is a factor of 2 larger than the error quoted by Goodberlet et al. (1989) for the wind speed algorithm. For higher wind speeds (e.g.,  $u = 20 \text{ m s}^{-1}$ ) the uncertainty is increased to  $\pm 8 \text{ m s}^{-1}$ . The error in using a monthly mean SST for the surface skin temperature is assumed to be  $\pm 3 \text{ K}$  for  $W > 20 \text{ kg m}^{-2}$  and  $\pm 4 \text{ K}$  for  $W < 20 \text{ kg m}^{-2}$ . An appropriate cloud temperature error would probably be  $\pm 10 \text{ K}$  if the liquid water absorption coefficients only took into account the temperature dependence of the liquid water drops. However, these coefficients are also used to offset the effects from excluding the effective emission height of the liquid water in the retrieval algorithm. Thus, using the results of Table 3.1 as a guide, a more reasonable uncertainty of  $\pm 5 \text{ K}$  is given to the cloud temperature. The noise in both SSM/I channels is set to a value of  $0.5 \text{ K}$ . Since uncertainties in the water vapor absorption coefficients are difficult to assess, they are given an arbitrary standard deviation of 2.5%. It should be pointed out that the contribution to the total error from the water vapor absorption coefficients is highly dependent on the value of their uncertainties, especially for moderate to high water vapor. The value of 2.5% was chosen because it gave errors that were reasonably consistent with the errors from several of the other variables. Finally, the

errors associated with the oxygen transmittance are based on a 5% uncertainty in the absorption.

Figure 3.3 shows the results of calculations of the standard deviation of the uncertainties in  $L$  ( $\sigma_L$ ) as a function of  $L$  for different water vapor amounts at wind speeds of  $6 \text{ m s}^{-1}$  and  $20 \text{ m s}^{-1}$ . In these calculations the appropriate value for  $T_s$  given a value of  $W$  was determined using the  $W/SST$  relationship of Stephens (1990) and the sea surface roughness model of Petty (1990) was implemented. The trend for the total errors is to increase with increasing  $L$  regardless of the water vapor amount or wind speed. For lower liquid water amounts (less than about  $0.3 \text{ kg m}^{-2}$ ) the errors depend strongly on  $W$  and become larger as  $W$  increases. For example, at  $L = 0.1 \text{ kg m}^{-2}$  the errors increase from  $0.025 \text{ kg m}^{-2}$  to  $0.056 \text{ kg m}^{-2}$  in going from  $W = 5 \text{ kg m}^{-2}$  to  $W = 60 \text{ kg m}^{-2}$  for a wind speed of  $6 \text{ m s}^{-1}$ . At higher values of  $L$  the errors are somewhat less dependent on water vapor and behave in an opposite manner, increasing with decreasing  $W$ . An explanation for these behaviors is given below.

In Figure 3.4 the total errors are represented as a percentage of the amount of liquid water for the results shown in Figure 3.3. When the errors are expressed in this way the smallest percentage errors occur at the largest  $L$ , which range from about 13% to 18%, and increase rapidly for lower values of  $L$ . At  $L = 0.2 \text{ kg m}^{-2}$  the errors can be expected to span from about 15 to 30%, while at  $L = 0.1 \text{ kg m}^{-2}$  the errors increase dramatically from 20 to 56%. In addition, an uncertainty of 100% in the retrievals is usually reached for values of  $L$  from about  $0.02$  to  $0.05 \text{ kg m}^{-2}$  for the driest and wettest atmospheres, respectively.

To examine the relative contribution of each of the variables to the total error, the quantity  $\sigma_x \partial L / \partial x$  was computed for each variable and the results are shown in Figures 3.5 and 3.6. Calculations were carried out for values of  $W$  of 60 and  $10 \text{ kg m}^{-2}$  and for wind speeds of 6 and  $20 \text{ m s}^{-1}$ . It can be seen in both figures that the errors for the highest values of  $L$  are mainly controlled by uncertainties in specifying the effective temperature of the cloud droplets; although uncertainties in  $T_s$  can also contribute significantly to the error. The increase in the error from a dry to moist atmosphere (as observed in Figures

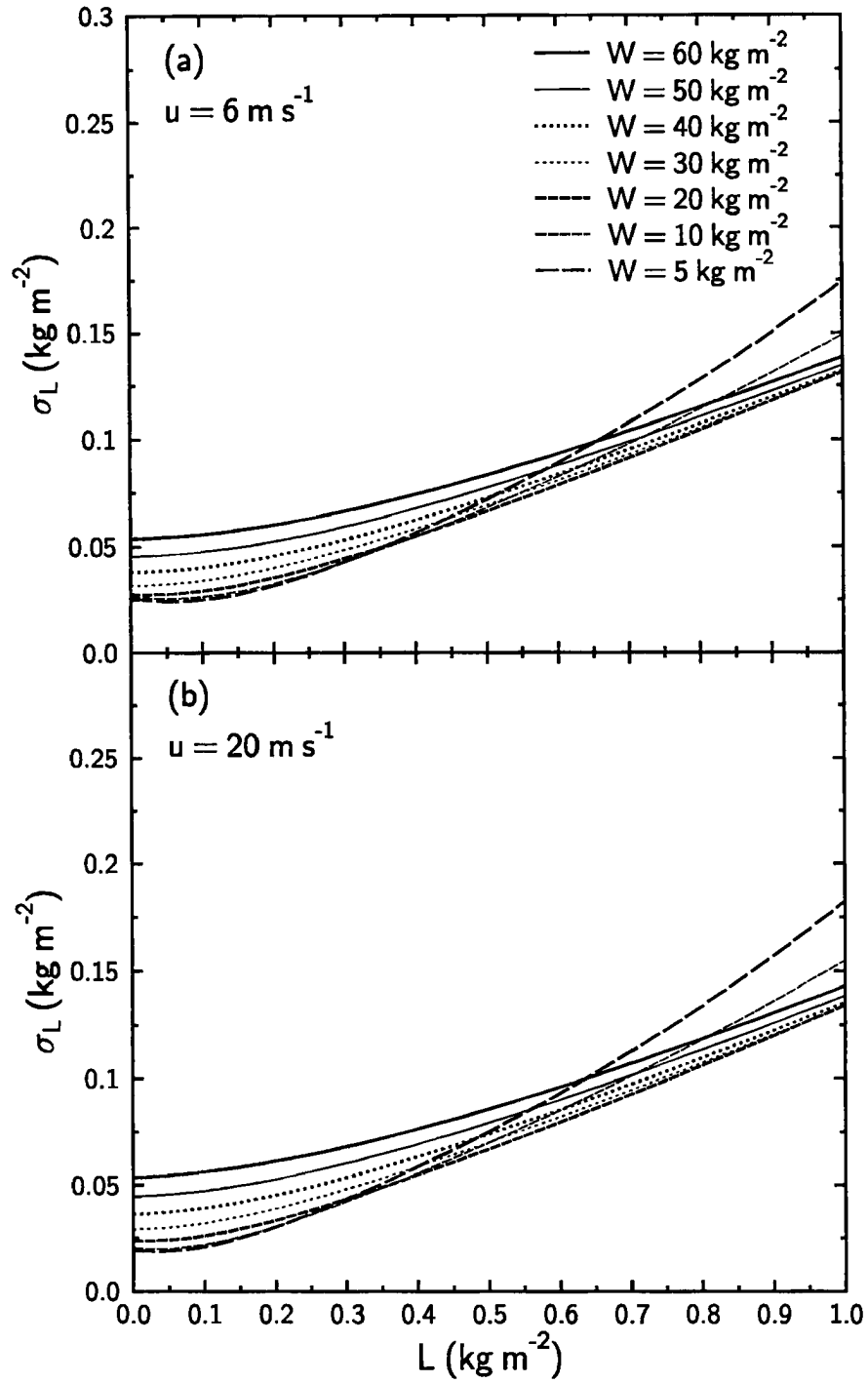


Figure 3.3: Total error estimates of the cloud liquid water retrievals for a wind speed of (a)  $6 \text{ m s}^{-1}$  and (b)  $20 \text{ m s}^{-1}$  as a function of  $L$  ( $\text{kg m}^{-2}$ ) and  $W$  ( $\text{kg m}^{-2}$ ).

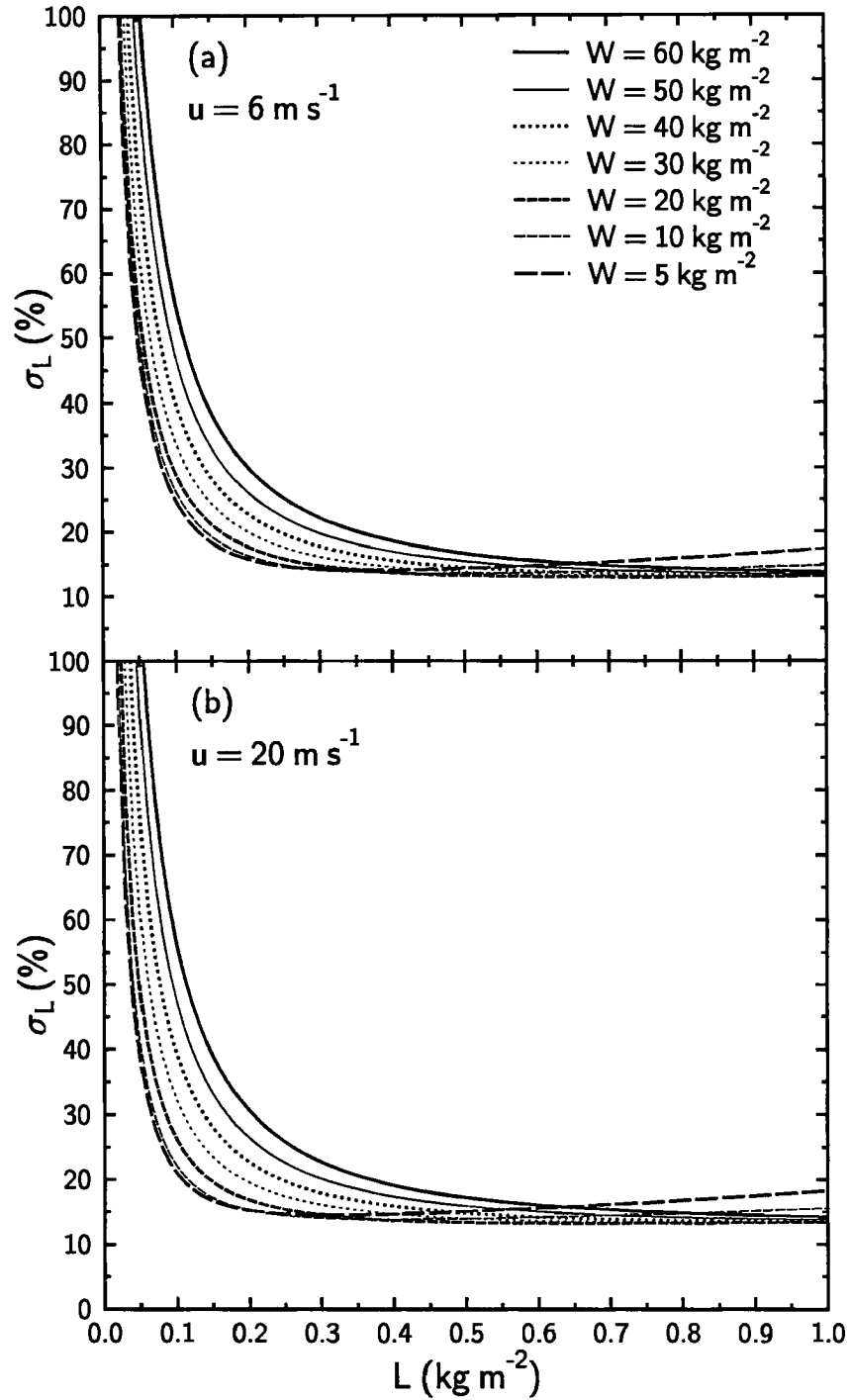


Figure 3.4: Same as Fig. 3.3 except that the error estimates are expressed instead as a percentage of the amount of liquid water  $L$ .

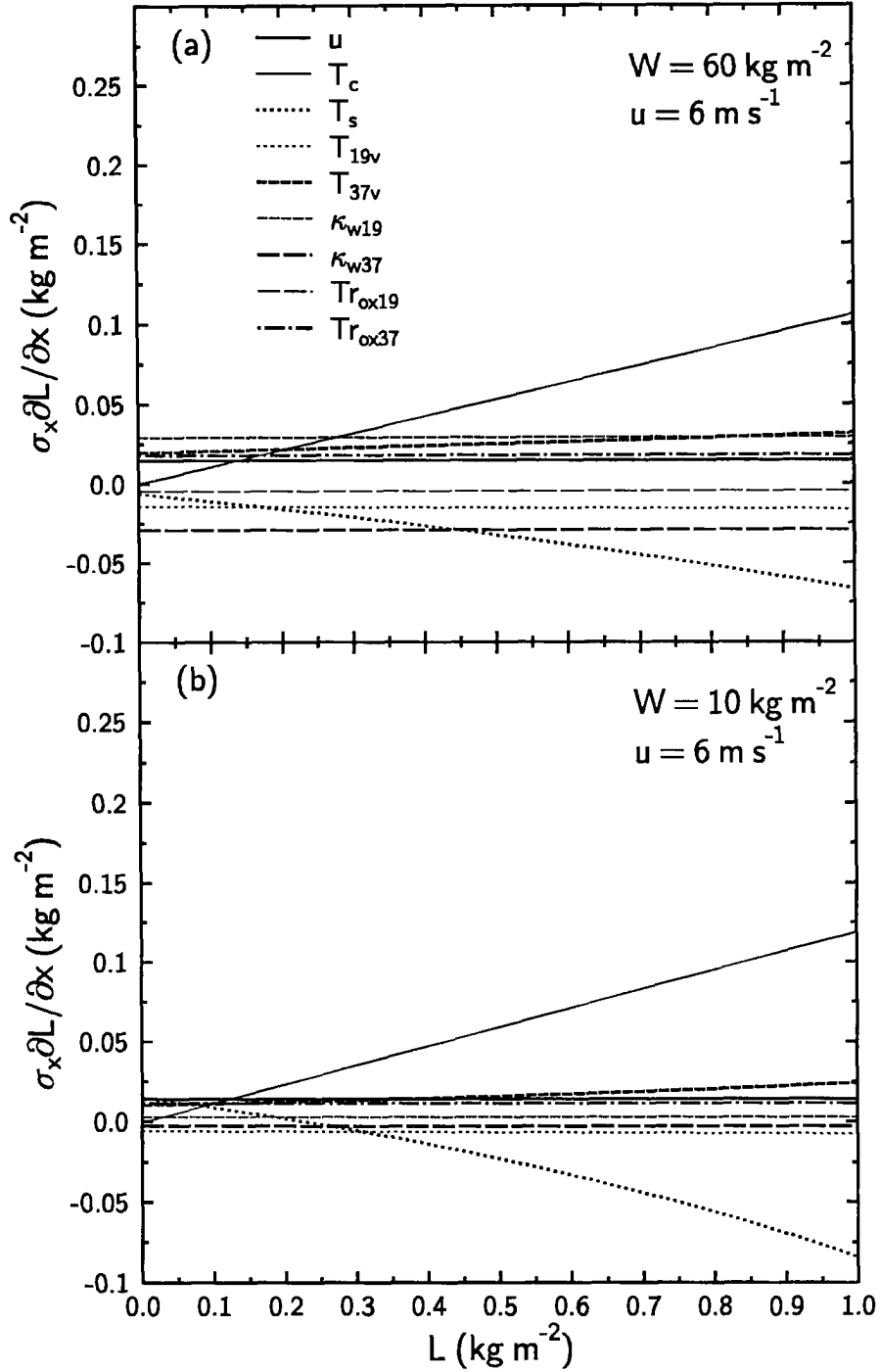


Figure 3.5: Individual error contributions of different variables to the cloud liquid water retrievals for integrated water vapor values ( $W$ ) of (a)  $60 \text{ kg m}^{-2}$  and (b)  $10 \text{ kg m}^{-2}$  as a function of  $L$  ( $\text{kg m}^{-2}$ ), where  $u$  is wind speed,  $T_c$  is cloud temperature,  $T_s$  is sea surface temperature,  $T_{19v}$  and  $T_{37v}$  are brightness temperatures,  $\kappa_{w19}$  and  $\kappa_{w37}$  are the water vapor coefficients, and  $Tr_{ox19}$  and  $Tr_{ox37}$  are the oxygen transmissions. Calculations were done assuming a surface wind speed of  $6 \text{ m s}^{-1}$ .

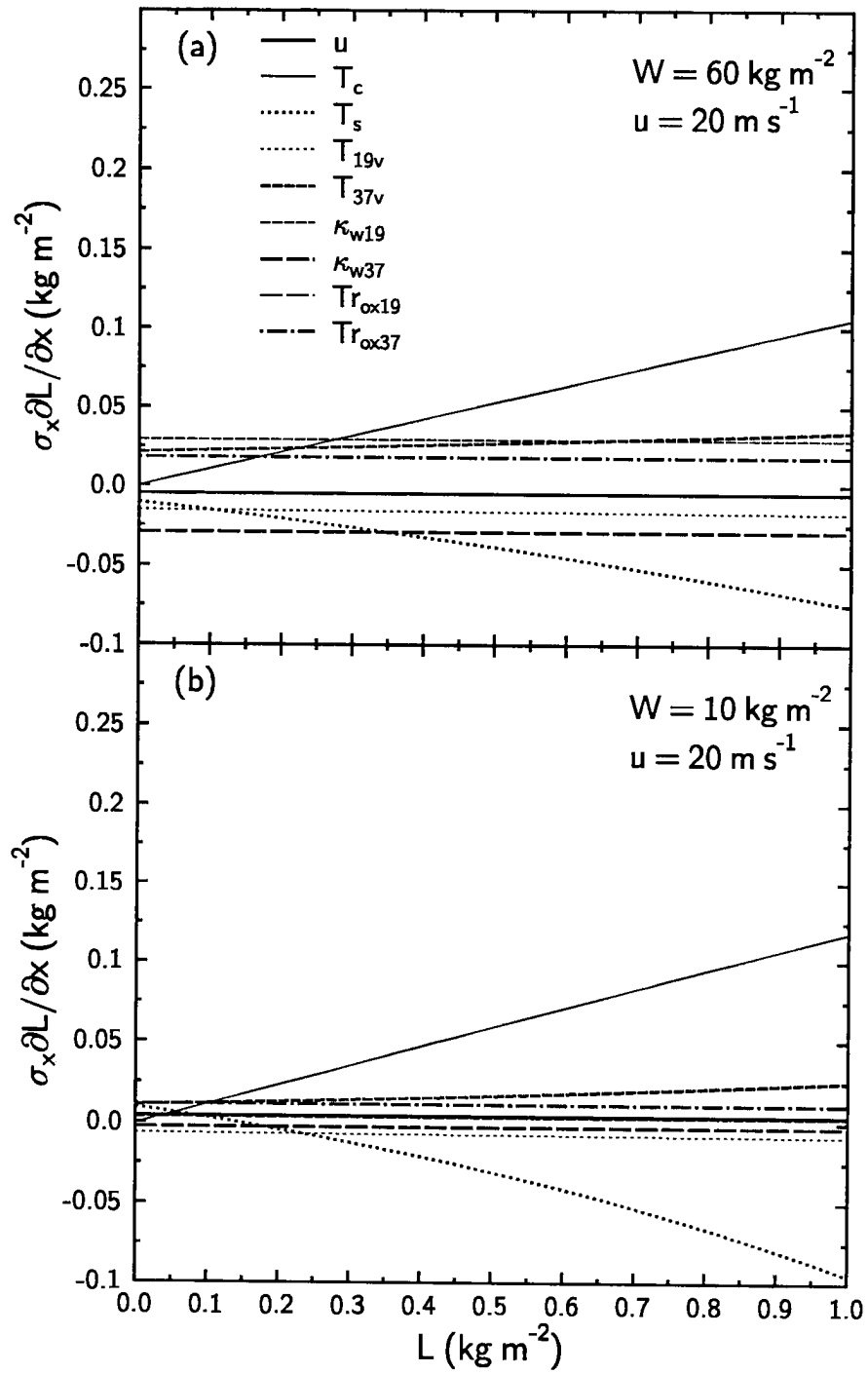


Figure 3.6: Same as Fig. 3.5 except for a near-surface wind speed of  $20 \text{ m s}^{-1}$ .

3.3 and 3.4) can be explained for the most part by an increase in error from the water vapor coefficients. This occurs since the uncertainties in these variables are directly related to the atmospheric optical thicknesses,  $\tau_1$  and  $\tau_2$ . Also, for optically thin clouds under conditions of a dry atmosphere and a wind speed of  $6 \text{ m s}^{-1}$  (Figure 3.5b) the total errors are dictated primarily by errors in  $T_s$  and wind speed (or surface roughness effects). However, for a wind speed of  $20 \text{ m s}^{-1}$  the error in wind speed plays a lesser role. The main conclusion of this analysis is that the total errors in the retrieval appear to vary greatly depending on the surface and atmospheric conditions, where the largest errors occur in a tropical atmosphere.

It is worthwhile to compare the results of the present error analysis to those from Petty (1990), who used a more sophisticated brightness temperature model to determine the minimum theoretical retrieval accuracies that could be achieved from SSM/I measurements. For a value of  $L$  of  $0.1 \text{ kg m}^{-2}$ , errors of 0.031, 0.024, and  $0.015 \text{ kg m}^{-2}$  for water vapor amounts of 50, 30 and  $10 \text{ kg m}^{-2}$ , respectively, were found based on retrievals using all 7 SSM/I channels. A five-channel retrieval (excluding the 85 GHz channels) yielded slightly larger errors of 0.033, 0.03, and  $0.028 \text{ kg m}^{-2}$ . As expected, since the present method involves only two channels, the errors in Figure 3.3 are typically greater than the minimum retrieval accuracies derived by Petty. The biggest differences occur for the largest values of  $W$  and may be an artifact of using only the 19.35v GHz channel to account for water vapor effects in the present method or possibly the values that were chosen for the water vapor absorption coefficient uncertainties in the present error analysis.

There are many other potential sources of error that are not considered in (3.1). These include, for instance, unmodeled effects such as variations in temperature, humidity, and cloud liquid water profiles, although the effect of temperature profile variability on the oxygen transmittance is accounted for in a crude way. Other errors can result from the spatial distribution and structure of the clouds. For example, if the cloud liquid water is vertically distributed in multiple layers or over a single deep layer, an effective cloud temperature alone may be inadequate to represent the cloud(s).

Additional, and possibly more significant, errors can arise from SSM/I footprints that are only partially filled by clouds. Gagarin and Kutza (1983) examined the effect

of broken cloudiness on microwave brightness temperatures at 22 and 37 GHz based on aircraft measurements over the ocean. They reported that an underestimation of the retrieved cloud liquid water occurs, particularly for cumuliform-type clouds, if broken cloudiness within the satellite footprint is not taken into account. Jones and Vonder Haar (1990) investigated the effect of cloudiness on LWP retrieval over land and found that the largest errors are associated with small liquid water amounts and sparse cloudiness. That study, however, involved the 85 GHz channels where nonlinearities caused by partial cloudiness play a more important role in affecting the brightness temperatures than at 37 GHz.

Still other sources of error involve the dielectric constants of water, the rough sea surface emissivity model and possible effects from ice clouds. Because of the lack of observational studies, the influences of wind, foam, and other effects on the surface emissivity are not well known. Therefore, it is not possible to address these errors in this study. As for clouds composed of ice, the optical depths are typically small outside areas of precipitation, so their effect on the brightness temperatures at 19.35 and 37 GHz will likely not be appreciable (Petty and Katsaros, 1992a), although thick anvil cirrus clouds in the tropics may have an impact on the 37 GHz channels.

One final source of error that is of concern is how the different footprint sizes of the measurements at 19.35 and 37 GHz affect the retrieval. A quantitative estimate of this error can be made by using the approach of Robinson et al. (1992) to enhance the 19.35-GHz channels to the resolution of the 37-GHz channels. A segment of a DMSP orbit was arbitrarily selected for this analysis from 1508–1532 UT for July 16, 1987, which extended from about 45°N to 45°S in the eastern Pacific. The rms error between the corrected and uncorrected LWP retrievals was determined for three different  $W$  categories ( $< 15 \text{ kg m}^{-2}$ ,  $25\text{--}35 \text{ kg m}^{-2}$ , and  $45\text{--}55 \text{ kg m}^{-2}$ ) that correspond approximately to several of the atmospheric environments shown in Figures 3.3 and 3.4 (i.e.,  $W = 5$  and  $10 \text{ kg m}^{-2}$ ,  $W = 30 \text{ kg m}^{-2}$ , and  $W = 50 \text{ kg m}^{-2}$ ). The error was found to increase from  $0.012 \text{ kg m}^{-2}$  for the driest atmosphere, to  $0.017 \text{ kg m}^{-2}$  for water vapor ranging from  $25\text{--}35 \text{ kg m}^{-2}$ , and  $0.022 \text{ kg m}^{-2}$  for the tropical atmosphere. A comparison to the results of Figure 3.3

indicates that the error resulting from the spatial disparity between the 19.35- and 37-GHz channels is far less than the errors arising from uncertainties in the atmospheric and surface variables for most values of  $L$ .

Application of the present error analysis to actual retrievals of cloud liquid water using SSM/I observations is displayed in Figure 3.7. These results consist of the average total error for 1990. The analysis was done only for retrievals of  $L$  less than  $0.5 \text{ kg m}^{-2}$  and greater than  $0.025 \text{ kg m}^{-2}$ . The spatial distribution of the error in Figure 3.7a looks very much like the distribution of integrated water vapor. This behavior is expected since the results of Figure 3.3 showed the error in the liquid water to increase systematically with increasing  $W$  over most values of  $L$ . Figure 3.7b shows the zonal average total error as one standard deviation above and below the mean cloud liquid water ( $L > 0.025 \text{ kg m}^{-2}$ ) for 1990. The error relative to the mean is highly dependent on latitude. At the highest latitudes the error is about 20 to 25% of the annual mean, while in the tropics it ranges from 30 to 40%. The largest error occurs in the northern subtropics where it can reach nearly 50%.

### 3.2 Validation

The strategy that has been adopted to verify the retrievals involves a comparison to independent measurements of liquid water from ground-based microwave radiometers. One might say that a comparison of this type is simply an exercise in contrasting one passive microwave sensing technique to another and does not represent a validation. We argue, however, that observations from upward looking dual-frequency microwave radiometers, if they are well calibrated, are sufficient to operate as “ground truth”. Ground-based methods can be, in principle, more accurate than satellite-based methods since the cosmic background is much colder ( $\approx 3 \text{ K}$ ) and more stable than the ocean background emission, which is typically about  $140 \text{ K}$  at  $37 \text{ GHz}$  ( $53^\circ$  zenith angle), for example, and can vary by  $15 \text{ K}$  or more as a result of changes in ocean surface roughening. The theoretical study of Westwater (1978) demonstrated that dual-frequency ground-based microwave systems are able to provide liquid water estimates with errors of less than 15% under a variety

of conditions. Albrecht et al. (1990) showed for marine stratocumulus clouds over San Nicolas Island that ground-based measurements compared exceptionally well to adiabatically-derived liquid water contents. An important point to emphasize, however, is that even ground-based measurements can exhibit significant biases if one does not properly account for the contributions from oxygen and water vapor.

Comparisons of ground-based observations of cloud liquid water to in situ measurements from aircraft have also yielded good results (Hill, 1991; 1992). The measurements of Hill, however, were made under special meteorological conditions in which the clouds were composed entirely of supercooled drops. Petty and Katsaros (1992b) compared in situ aircraft observations of liquid water to coincident measurements obtained from the SMMR on Nimbus 7 during the 1987 Taiwan Area Mesoscale Experiment. The comparison was surprisingly good, but the authors were cautious about making any definite conclusions because of the significant differences in sampling and the potentially large errors. Using aircraft measurements to verify satellite-based LWP retrievals is an intriguing idea but has its own unique problems. The major difficulties include obtaining an adequate vertical sampling of the cloud and the biases that are often associated with liquid water probes (Albrecht et al., 1990).

In addition to the comparison to ground observations, SSM/I-derived cloud liquid water is also compared to liquid water estimated from the visible reflectances of the AVHRR in regions of stratocumulus clouds off the southern coast of California and to other SSM/I LWP algorithms in specific regions. A comparison of LWP derived from visible reflectances to microwave-derived observations has been done by Lojou et al. (1991) with some success using data from the SMMR on the Nimbus 7 and the VISSR (Visible and Infrared Spin-Scan Radiometer) on GOES.

### **3.2.1 Comparison to visible reflectance method**

The technique to estimate integrated cloud liquid water from reflectance measurements in the visible spectrum is based on the shortwave parameterization scheme of Stephens (1978), which relates the albedo of water clouds to their LWP. Coakley and Snider (unpublished manuscript, 1990) obtained a fit to the results of Stephens to yield

a relationship between cloud albedo and LWP. This relationship is inverted to yield an expression for the liquid water path as a function of cloud albedo:

$$L = \frac{\mu_o R A}{1 - RB} \quad (3.2)$$

where  $\mu_o$  is the cosine of the solar zenith angle,  $R$  is the cloud albedo,  $A = 0.0490$ ,  $B = 1.004$ , and the liquid water path  $L$  is in units of  $\text{kg m}^{-2}$ . The standard deviation of the LWP can be approximated as

$$\sigma_L \approx \sigma_R \frac{\partial L}{\partial R} = \frac{\sigma_R \mu_o A}{(1 - RB)^2} \quad (3.3)$$

where  $\sigma_R$  is the cloud albedo standard deviation.

Visible reflectance measurements were obtained from the AVHRR aboard the NOAA-9 and NOAA-10 satellites. The channel of the AVHRR relevant to this study (channel 1) has a bandwidth ranging in the visible from 0.58–0.68  $\mu\text{m}$  and a spatial resolution of 1 km at nadir. The AVHRRs on these satellites have exhibited a loss in sensitivity over the course of their lifetimes. The calibration factors used to correct this degradation are discussed by Coakley and Snider.

Table 3.2: Selected cases for the AVHRR and SSM/I cloud liquid water comparison over San Nicolas Island

	NOAA-10		DMSP	
Case	Date	UT	Date	UT
1	July 10	1537	July 10	1320
2	July 16	1647	July 16	1348
	NOAA-9		DMSP	
Case	Date	UT	Date	UT
3	July 15	2256	July 16	0226
4	July 16	2246	July 17	0213

The comparison is confined to subtropical stratocumulus clouds under overcast conditions so as to minimize cloud brokenness and spatial inhomogeneity effects and to minimize influences on the albedo by ice particles. The cases chosen for the comparison are those taken from the study of Coakley and Snider for stratocumulus over San Nicolas Island for

July 1987. In each of these cases there is no precipitation, the clouds are for the most part single-layered, and the cloud cover is complete over the island. Table 3.2 shows the NOAA-9, NOAA-10, and DMSP satellite overpass times for the cases used in this study. Only DMSP overpasses within about 4 hours of the NOAA overpasses are used, which is reasonable since marine stratocumulus cloud decks are relatively persistent features over the course of a few hours. The measurements from the NOAA satellites are taken within a 90 km radius of San Nicolas Island. Since the spatial resolution of the SSM/I is far cruder than the AVHRR, a radius of 65 km is used instead for the SSM/I observations.

Figure 3.8 shows a scatter plot of the SSM/I-derived LWP versus that estimated from the AVHRR. The error bars refer to the spatial variability of the measurements in terms of one standard deviation above and below the data points. The standard deviations for the AVHRR-derived LWP are calculated using (3.3). From this figure it can be seen that the two methods give consistent results, with the SSM/I LWPs being offset generally higher than the AVHRR-derived LWPs. The rms difference is about  $0.08 \text{ kg m}^{-2}$ . This offset is most likely due to the choice of the calibration factor that is used for the AVHRR reflectances and presumably dominates over the effect of the disparity in the spatial resolutions of the two instruments. Apart from the bias, the differences between the two methods might be caused by changes in the microphysics of the cloud that may have occurred between the DMSP and NOAA satellite overpasses.

### 3.2.2 Comparison to surface-based measurements

The ground radiometer measurements used in this study are taken from three island sites and one ship location. Although this is a very small sample of sites, they do represent different seasons and climate regimes. One disadvantage of using island locations is that they might contaminate the retrieval. Fortunately, most of the islands are comparatively small and the satellite footprints are large enough so that they produce a small to negligible effect on the SSM/I brightness temperatures. The possible exception is San Nicolas Island, which may cause a non-negligible increase in the 37 GHz channels if the island is within a large fraction of the FOV.

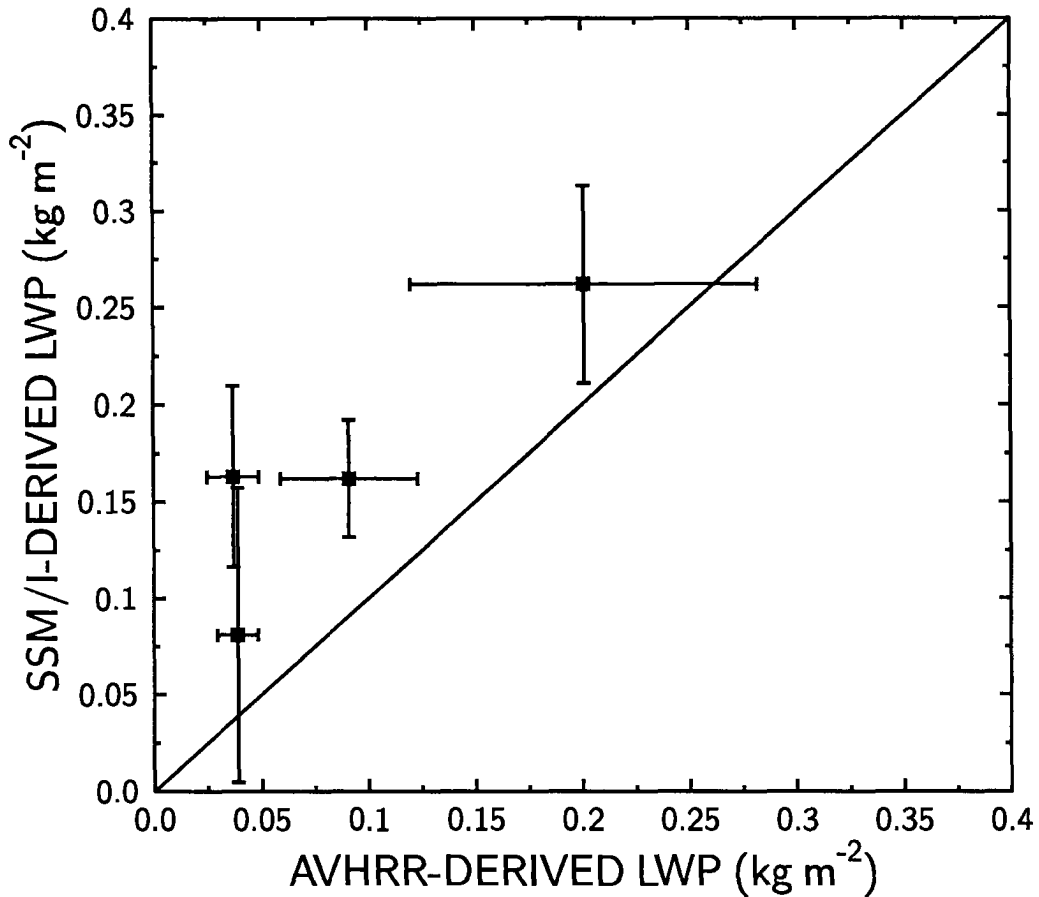


Figure 3.8: Scatter diagram of cloud liquid water path ( $\text{kg m}^{-2}$ ) derived from the present method (SSM/I) versus the visible reflectance retrievals (AVHRR) over San Nicolas Island. Error bars represent the spatial variability of the measurements and are one standard deviation above and below the points.

The major obstacle in directly comparing ground observations to satellite observations is of course the significant differences in sampling of the two measurement systems. In our opinion, the most useful way of comparing these measurements is through the use of histograms. For the SSM/I data, spatial histograms are constructed from pixels that are within 50 km of the site. Unless otherwise noted, temporal histograms are derived from the ground observations over a 1-hour time period centered on the time of the satellite overpass. It should be mentioned that from July 1987 through 1988 the DMSP F-8 satellite suffered from occasional geolocation problems, which are traced to errors in the spacecraft ephemeris (Poe and Conway, 1990). As a result, the position of some SSM/I pixels may

be in error in certain regions by as much as 30 km. A correction is not applied to the data since the navigation problem would affect only the San Nicolas Island and Kwajalein Island sites, and it was felt it would not greatly impact the results of the analysis.

In the first comparison, measurements of integrated liquid water are used from a microwave radiometer on San Nicolas Island (33.25°N, 119.6°W) during the First ISCCP Regional Experiment (FIRE). The radiometer has three channels at 20.6, 31.65, and 90 GHz. The integrated water vapor and liquid water are estimated simultaneously from a statistical retrieval algorithm discussed by Hogg et al. (1983) and are conservatively estimated at 20%. However, based on a study by Albrecht et al. (1990), the accuracy of the liquid water amounts may be far better than this estimate. Both types of observations were made from July 2 to July 19, 1987, and consist of one minute averages.

The San Nicolas Island comparison involves nine cases. All but two cases consist of overcast conditions as determined from ceilometer measurements (Schubert et al., 1987). The July 13 case is free of clouds, while the July 18 case has broken cloud conditions. As presented in Figure 3.9, the agreement between the two independent sets of observations is remarkable. In order to provide a rough quantitative estimate of the disparity between these data sets, the temporal mean value for the ground observations and the spatial mean value for the SSM/I data are computed for each case. It is found that the overall rms difference between the surface-based and SSM/I mean values is  $0.036 \text{ kg m}^{-2}$ . It is possible that the underestimation by the SSM/I for the July 16 case is in part linked to an error in the cloud temperature, which becomes increasingly important for higher liquid water amounts. Ceilometer measurements indicate during this time that the cloud deck was low, with a cloud base at about 200 m. This fact supports the idea that the specified cloud temperature may be too cold. The July 18 case has the SSM/I generally overestimating the liquid water for a thin, broken cloud deck. Under these conditions one would expect the SSM/I to underestimate the cloud water. The likely explanation is that several of the outermost pixels are sensing a thicker portion of the cloud deck that was evident earlier in the ground observations from 1145–1245 UT.

The second set of ground-based measurements originate from Kwajalein Island (8.7°N, 167.75°E) in the west Pacific, which are made up of twelve cases from March 24 to April

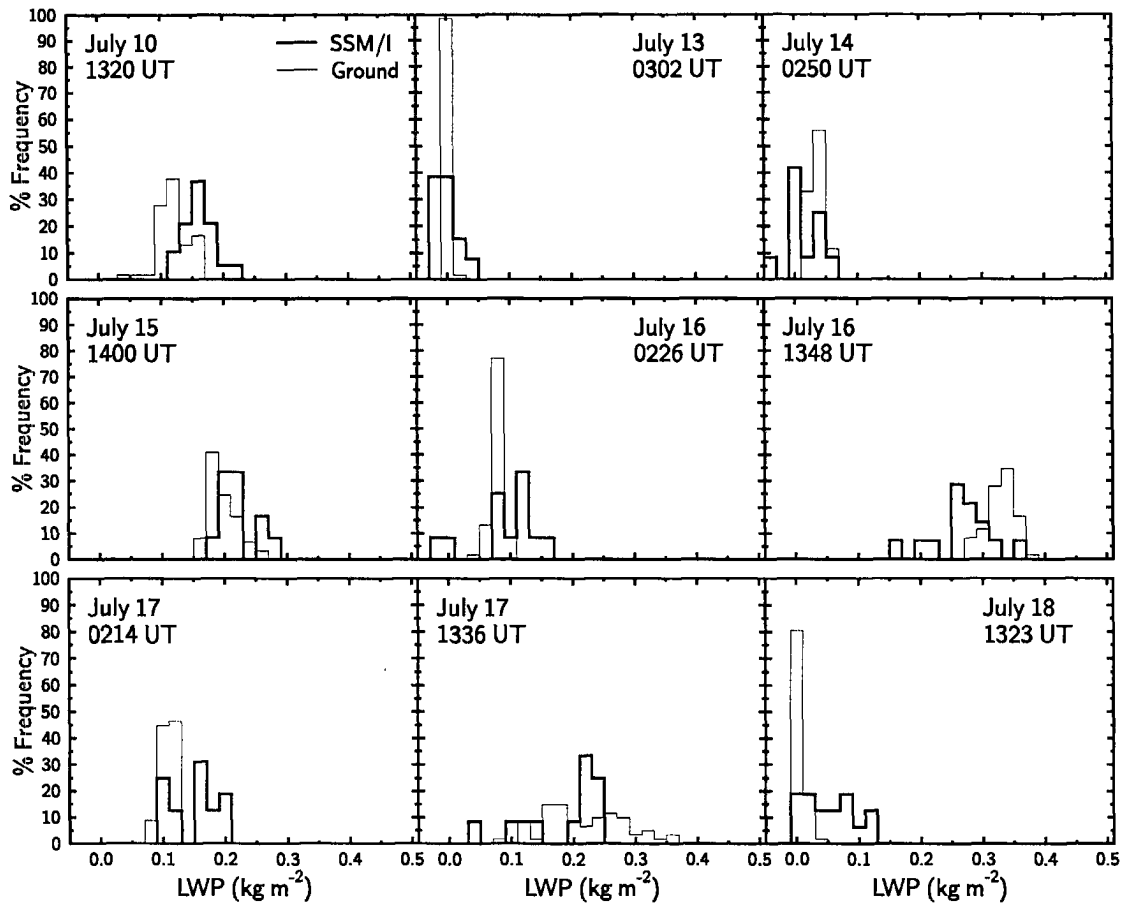


Figure 3.9: Comparison of histograms of LWP ( $\text{kg m}^{-2}$ ) from the SSM/I and ground observations for cases in July 1987 over San Nicolas Island.

7 of 1988. These measurements were estimated from two different microwave radiometers: the University of Massachusetts autocorrelation radiometer (CORRAD) that measures downwelling radiation at 31 channels from 20.5 to 23.5 GHz (Ruf and Swift, 1988), and an additional radiometer that only senses radiation at 37 GHz. The method of retrieving both water vapor and cloud liquid water involves the 21, 22.2 and 37 GHz channels based on a statistical minimum error technique (Alishouse et al., 1990). Observations were taken every 10 minutes.

The most consistent feature of the comparison in Figure 3.10 is that the SSM/I frequently underestimates the liquid water, with the worst case occurring at 1830 UT on March 29. The rms difference between the mean values is  $0.13 \text{ kg m}^{-2}$ . These differences are too great to be caused entirely by errors in cloud temperature because a temperature

much warmer than the surface temperature would be needed to bring the two observations into agreement. Uncertainties in modeling the surface or the geolocation errors discussed earlier may also contribute to this difference. Another possibility is that if the cloudiness is patchy, this would cause the SSM/I to underestimate the LWP. Since the ground LWP observations are of somewhat low resolution in time (10 min.) and because there are no available surface observations of the sky conditions, it is not possible to determine whether

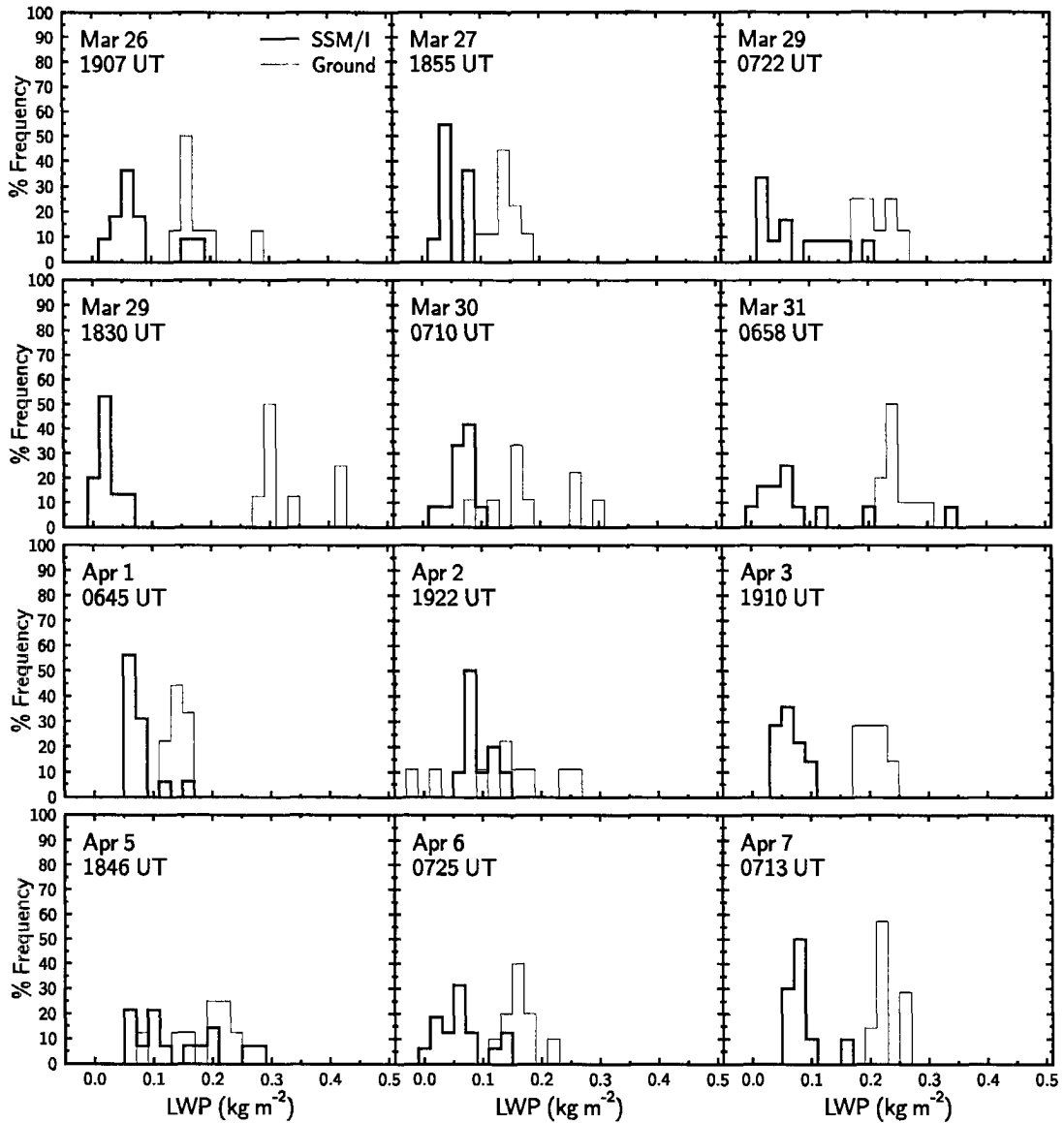


Figure 3.10: Comparison of histograms of LWP ( $\text{kg m}^{-2}$ ) from the SSM/I and ground observations for cases in March and April 1988 over Kwajalein Island.

cloudiness effects play a role. Thus, it is unclear why the comparison is relatively poor at this particular site, although it is possible that the ground observations may be suspect.

For the March 26 Kwajalein Island case, a qualitative comparison is made in Figure 3.11 of the cloud liquid water field derived from the SSM/I to visible satellite imagery. The visible image is taken from the AVHRR on board the NOAA-10 satellite, which passed over the island at roughly 2000 UT. Also shown is the liquid water field on a pixel scale for a portion of the DMSP orbit at 1907 UT. Values of LWP greater than  $0.5 \text{ kg m}^{-2}$  are portrayed as a gray tone. The most distinctive feature in both the satellite imagery and cloud liquid water field is the long band of convection located south of the island near the equator. Many LWPs in this region extend beyond  $0.5 \text{ kg m}^{-2}$  and indicate possible heavy and widespread rainfall. In other areas, a good correspondence can be seen between other smaller individual cloud systems and the liquid water field. The majority of the cloud liquid water amounts are  $0.1 \text{ kg m}^{-2}$  or less.

The third group of measurements were made in the North Sea in October of 1989 during the International Cirrus Experiment (ICE) on the R/V Poseiden. The microwave radiometer was supplied by the University of Hamburg in Germany and operates at a frequency of 33 GHz. Measurements are made up of 1-minute averages. The method used to determine liquid water is based on a difference between the observed brightness temperature and an estimated background clear sky temperature (Hargens, 1992). The minimum errors are roughly  $0.06 \text{ kg m}^{-2}$ .

At this site, cases that were suspected of being contaminated by precipitation were excluded from the comparison. As seen in Figures 3.12 and 3.13, the agreement between the two data sets is generally very good, with the tendency of the SSM/I to slightly overestimate the LWP, especially for higher amounts. The rms difference for these cases is  $0.046 \text{ kg m}^{-2}$ . It is not known whether these differences are a consequence of improper specification of the sea surface and/or cloud temperature. For higher cloud water amounts the cause may be related to the cloud temperature.

The final set of measurements was carried out during the TCM experiment in August and September of 1990 on Saipan Island in the west Pacific. These measurements were

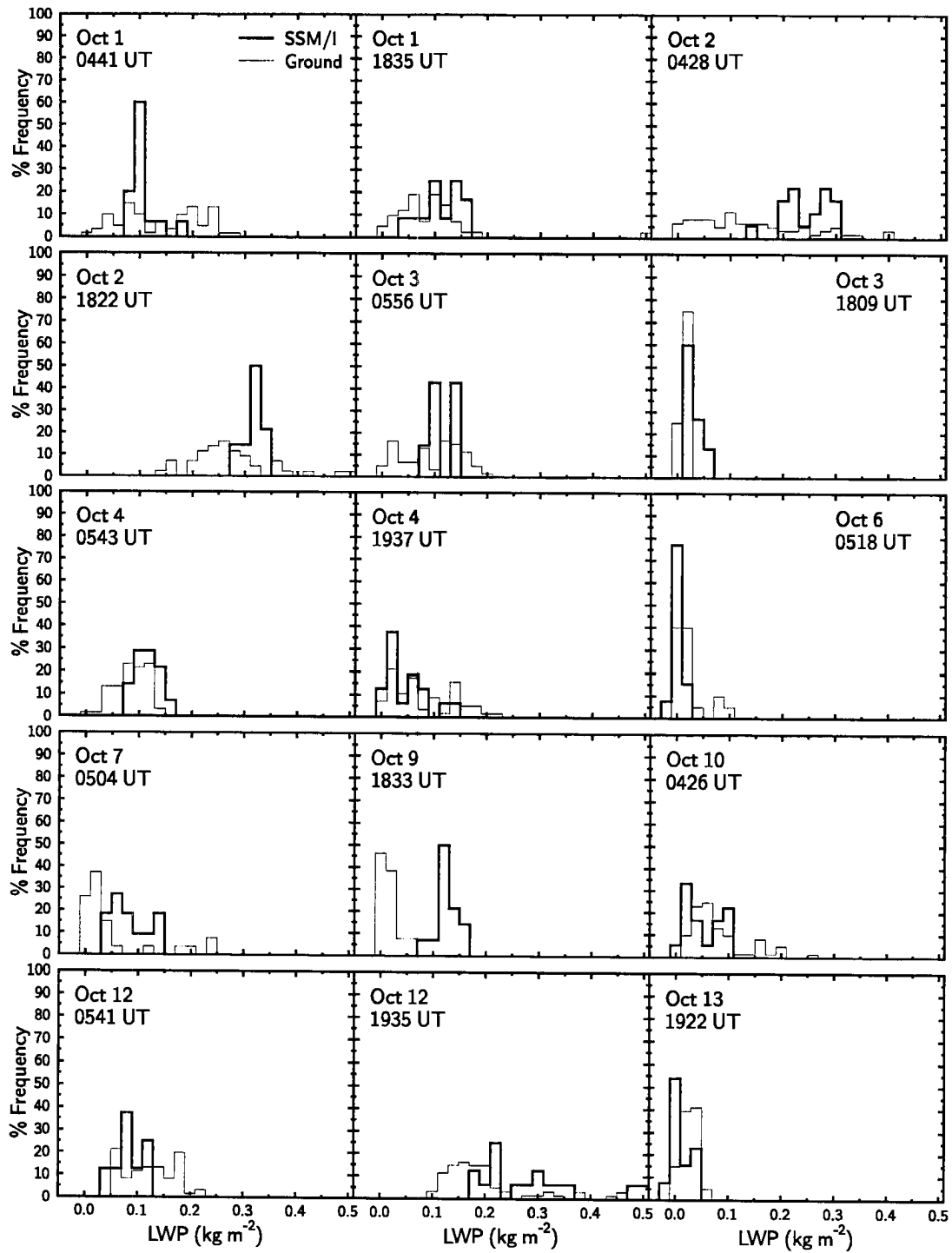


Figure 3.12: Comparison of histograms of LWP ( $\text{kg m}^{-2}$ ) from the SSM/I and ground observations for cases in October 1989 in the North Sea.

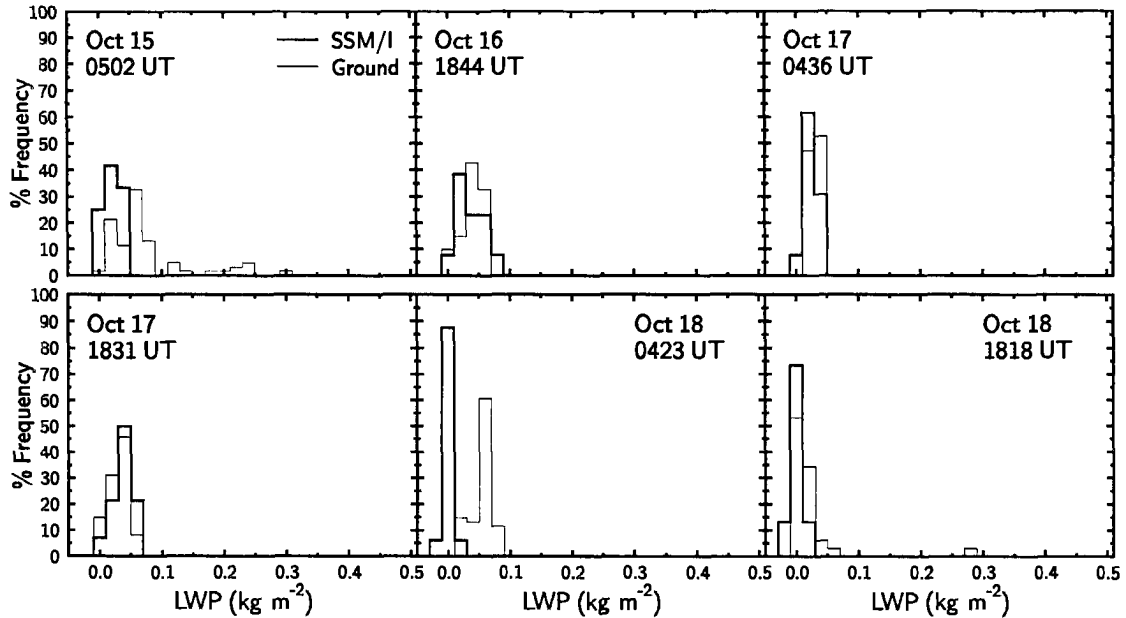


Figure 3.13: Fig. 3.12 continued.

provided by the Penn State 9-channel microwave radiometer located on Saipan Island (15.2°N, 145.8°E). The radiometer has six channels operating from 50.4 to 61.2 GHz, two channels near the water vapor resonance line at 22.2 and 24.1 GHz, and one channel at 37 GHz (Wassenberg, 1989). Measurements consist of 5-minute averages. The retrieval of liquid water involves a physical inversion method (Westwater, 1978) and includes ceilometer measurements of cloud base height to help improve estimates of the cloud absorption (Han and Thomson, 1994). The retrieval errors are estimated to be about 5% based on theoretical calculations (Han, personal communication, 1992).

The results of the analysis are presented for August and September in Figures 3.14 and 3.15. Ceilometer measurements are used to exclude cases where precipitation is occurring since both surface and satellite-based methods are sensitive to moderate and heavy rain. For this set of ground observations the histograms are created from a 2-hour time interval centered about the satellite overpass time. This figure reveals that nearly all cases are restricted to low liquid water amounts. Those situations where there are higher LWPs

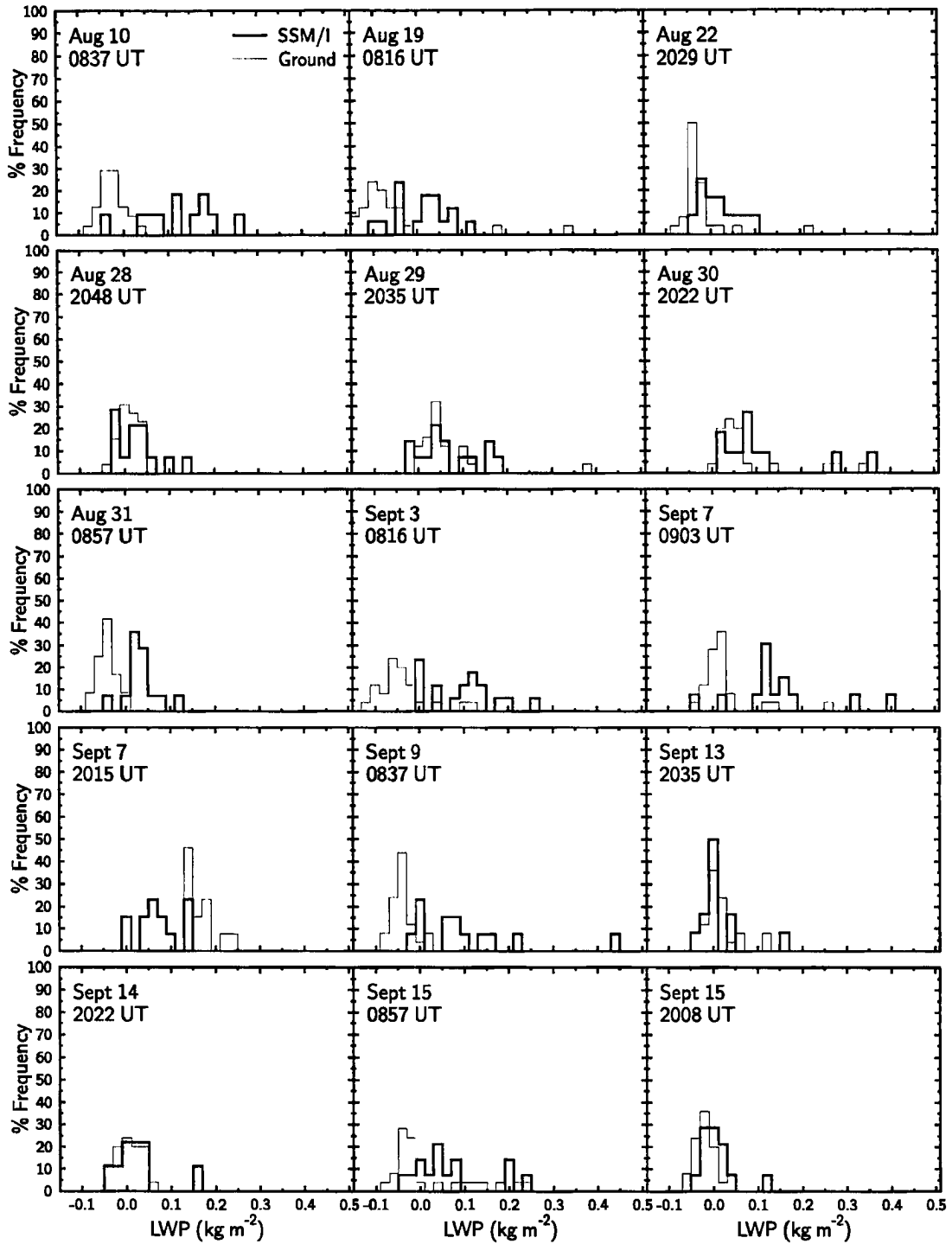


Figure 3.14: Comparison of histograms of LWP ( $\text{kg m}^{-2}$ ) from the SSM/I and ground observations for cases in August and September 1989 over Saipan Island.

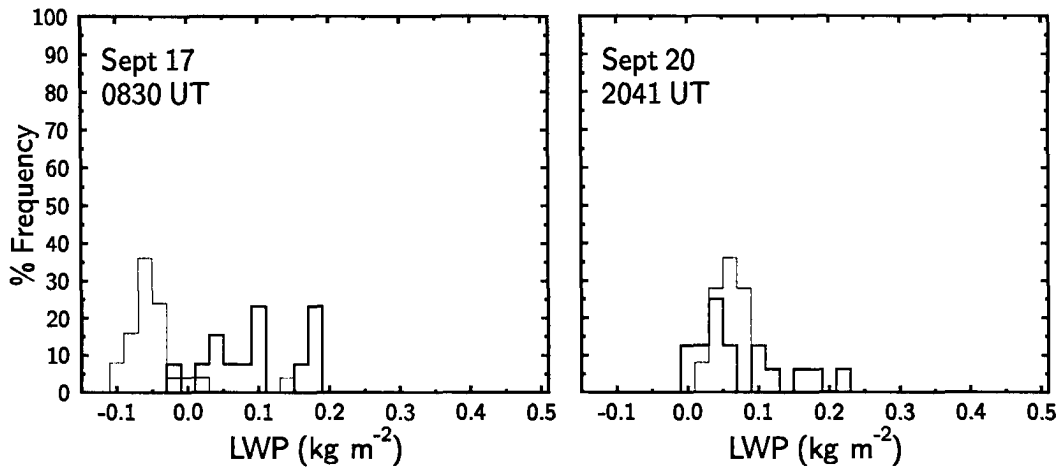


Figure 3.15: Fig. 3.14 continued.

are nearly always associated with precipitation. With the exception of three or four cases, there appears to be a qualitative consistency between the two data sets, although it is difficult to evaluate this agreement because of the greater variability of the SSM/I-derived LWPs.

A comparison of specific interest is the September 7 morning case (2015 UT). During this time it is likely that a thin stratiform-type cloud deck is overlaying the island since a time series of the surface observations shows that the cloud liquid water is relatively uniform ( $0.15\text{--}0.2\text{ kg m}^{-2}$ ) over a period of five hours. Unfortunately, measurements of the cloud base height are not available to confirm that these clouds are stratiform in nature. The more or less homogeneous structure of these clouds allows us to examine the true accuracy of the SSM/I liquid water estimates at this site. As shown in Figure 3.14, both sets of measurements appear to be in reasonable agreement with one another, where the SSM/I slightly underestimates the LWP.

One characteristic of the surface measurements of liquid water on Saipan Island that prevents a more thorough analysis of the two data sets is the existence of an obvious negative bias. For instance, on August 31 where the skies are mostly clear, the ground observations show a mean LWP of  $-0.047\text{ kg m}^{-2}$ . In another case on September 17, where mid-level clouds are present (the ceilometer measurements indicate cloud bases at 2 and

3.5 km), the ground observations have a mean LWP of  $-0.055 \text{ kg m}^{-2}$ . Unfortunately, the bias does not appear to be systematic and its cause is largely uncertain. One can conclude from this comparison that it is extremely difficult to get reliable estimates of LWP from either satellite and ground observations in the tropics. Thus, there is a need for obtaining other types of measurements of cloud liquid water in areas such as the tropical west Pacific in order to validate the satellite retrievals.

### 3.3 Comparison to Other Microwave Methods

The present method is now compared to other cloud liquid water retrieval schemes that have been developed for the SSM/I and to previous results obtained from SMMR. The SSM/I comparison involves the algorithms of Petty (1990), Alishouse et al. (1990), and Hargens (1992) in two specific regions. These regions were chosen because ground measurements were also available.

Our first area of interest is the stratocumulus cloud decks that regularly form off the west coast of North America. We confine the analysis to an area bounded from 25–40°N latitude and 118–130°W longitude over the time period July 16–18, 1987. The semi-physical method of Petty (1990) consists of the following expression

$$L = -1.42 \ln(P_{37}) \quad (3.4)$$

where the normalized polarization difference  $P_{37}$  is defined as

$$P_{37} = \frac{\Delta T_{37}}{\Delta T_{37clr}} \quad (3.5)$$

where

$$\frac{1}{\Delta T_{37clr}} = \exp(0.0151u + 0.00607W - 4.40) \quad (3.6)$$

and  $\Delta T_{37clr}$  is the 37 GHz polarization difference under clear sky conditions, and  $u$  is the near surface wind speed. The expression in (3.6) is simply a parameterization based on the cloud-free data set described in Chapter 2. The coefficients that appear in (3.6) were determined specifically from the water vapor algorithm given in Petty (1990) and for the wind speed algorithm of Goodberlet et al. (1989). This method is intended for use with

spatially smoothed fields of  $W$  and wind speed, although this was not done in the present comparison. An alternative four-channel algorithm to the one presented in Alishouse et al.'s 1990 paper is also used in the comparison, where the 37h channel is used in place of the 85h channel (J. C. Alishouse, personal communication, 1991). The algorithm is given as:

$$L = -2.838 + 0.00843T_{19h} - 0.00759T_{22v} + 0.0201T_{37v} - 0.00531T_{37h}. \quad (3.7)$$

The results of the comparison, which were done on a pixel basis, are displayed in Figure 3.16. A cloud temperature of 285 K was specified for both the Petty algorithm and the present method. Good agreement can be seen in Figure 3.16a between the physical methods. The rms difference is only  $0.027 \text{ kg m}^{-2}$ , but there is some disagreement for lower liquid water amounts. In the comparison to Alishouse et al. in Figure 3.16b, more significant differences are evident. The statistical method has an rms difference of  $0.074 \text{ kg m}^{-2}$  and severely underestimates the LWP by roughly a factor of 2 for all values. Although the method of Alishouse et al. appears to have the ability to at least partially detect a cloud liquid water signal, the primary reason for the discrepancy is that the influence of water vapor has not been fully separated from the effects of clouds. This fact is confirmed by Petty (1990) who observed that the Alishouse et al. LWPs were highly correlated with  $W$ .

The next region for comparison is the North Sea from October 1 to 18, 1989, during the ICE. The area that is defined is from  $54.5\text{--}58^\circ\text{N}$  and from Greenwich to  $5.7^\circ\text{E}$ . The LWP retrieval method of Hargens is based on theoretical calculations for roughly 3000 radiosonde profiles in the North Sea and Atlantic Ocean. Multiple regression is then used to relate the computed brightness temperatures to the cloud liquid water prescribed in the model. The resultant expression is

$$L = 0.3996 \ln(280 - T_{22v} - \delta T_{22v}) - 1.407 \ln(280 - T_{37v} - \delta T_{37v}) + 4.299, \quad (3.8)$$

where  $\delta T_{22v}$  and  $\delta T_{37v}$  are the brightness temperature bias factors determined by Wentz (1992) to be  $-1.3 \text{ K}$  and  $+1.6 \text{ K}$ , respectively.

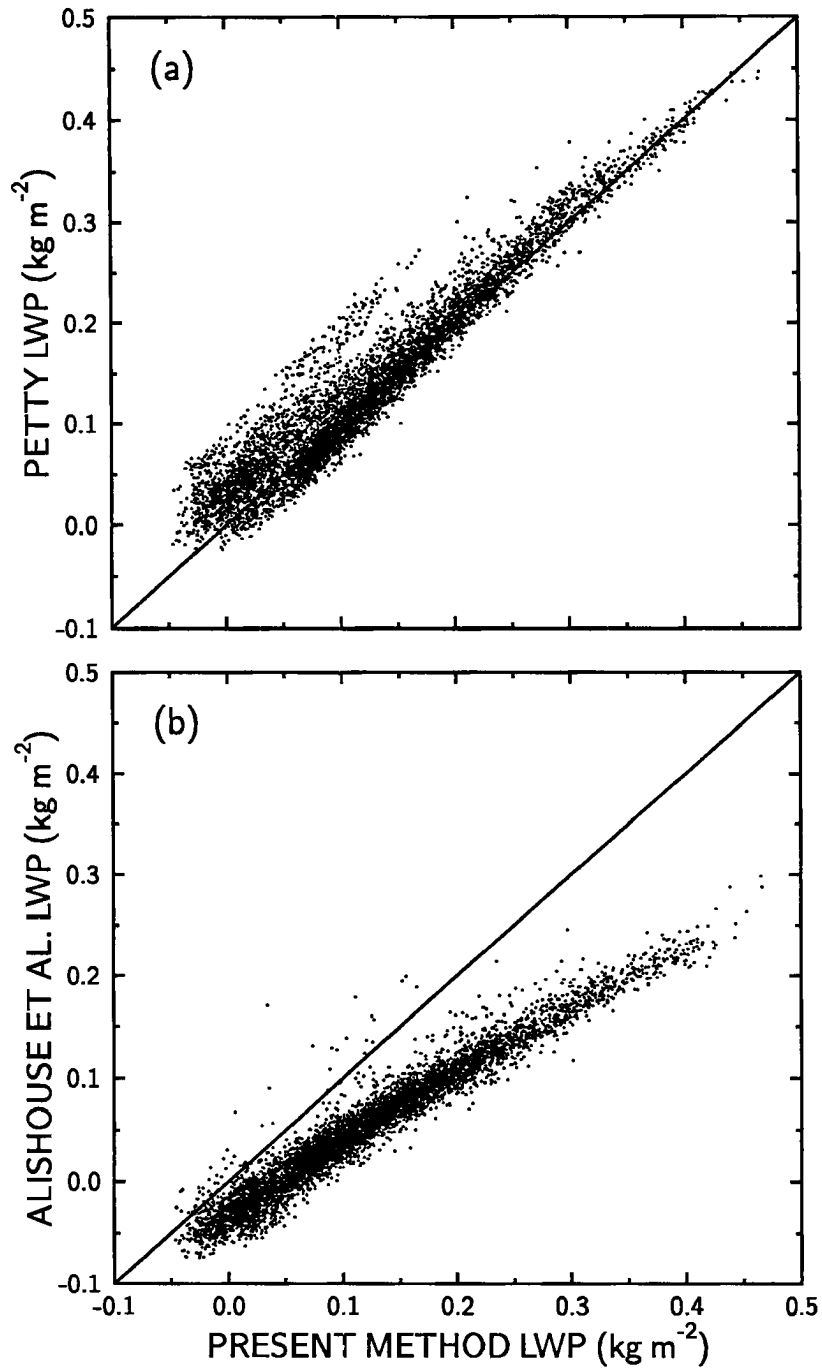


Figure 3.16: Scatter diagrams of LWP ( $\text{kg m}^{-2}$ ) derived from the method of (a) Petty (1990) and (b) Alishouse et al. (1990) versus the present method for stratocumulus clouds off the west coast of California from July 16 to 18, 1987.

The comparison between the present model and (3.8) for the North Sea is shown in Figure 3.17a. Excellent agreement can be seen except that the LWPs derived from the present retrieval method are offset slightly higher. The rms difference between these data sets is extremely small at  $0.019 \text{ kg m}^{-2}$ . The small differences may be explained by a small negative bias of about  $0.02\text{--}0.025 \text{ kg m}^{-2}$  in the LWPs from the method of Hargens, which was determined from the cloud-free data set for the North Sea observations. The algorithm of Alishouse et al. in Figure 3.17b again underestimates the LWP with a large fraction of values less than zero.

The final comparison involves zonal average distributions of liquid water derived from the SMMR based on previously published results. Figure 3.18 shows the latitudinal distribution of SSM/I cloud liquid water for August 1987, and liquid water from the study of Njoku and Swanson (1983) for July 11–August 10, 1978, and the method of Prabhakara et al. (1983) for August 1979. Some of the more distinct features of the SSM/I LWP distribution include the maximum in the northern midlatitudes, which is mainly a result of abundant stratus cloudiness, the maximum in the southern midlatitudes, caused by cyclonic weather systems, minima in the subtropics, and a distinct maximum at the ITCZ.

There is a surprisingly good correlation in the latitudinal behavior of the liquid water between the present method and the results of Njoku and Swanson. The method used by Njoku and Swanson is based on SMMR observations made from the Seasat and consists of a slightly modified form of the statistical regression method of Wilheit and Chang (1980). The magnitude of the SMMR results in the tropics and subtropics appears to be biased slightly lower than the SSM/I cloud liquid water, which shows greater values in the ITCZ region. It is not known whether these differences are caused by the interannual variability of cloud liquid water, differences in temporal and spatial sampling between the SSM/I and SMMR, or simply by biases in either method. We speculate that some of these differences may be accounted for by the retrieval of cloud liquid water in areas of precipitation where the retrievals are less reliable. As documented by Lipes (1981), the liquid water retrieved by the Wilheit and Chang algorithm in these areas occasionally became negative, thus

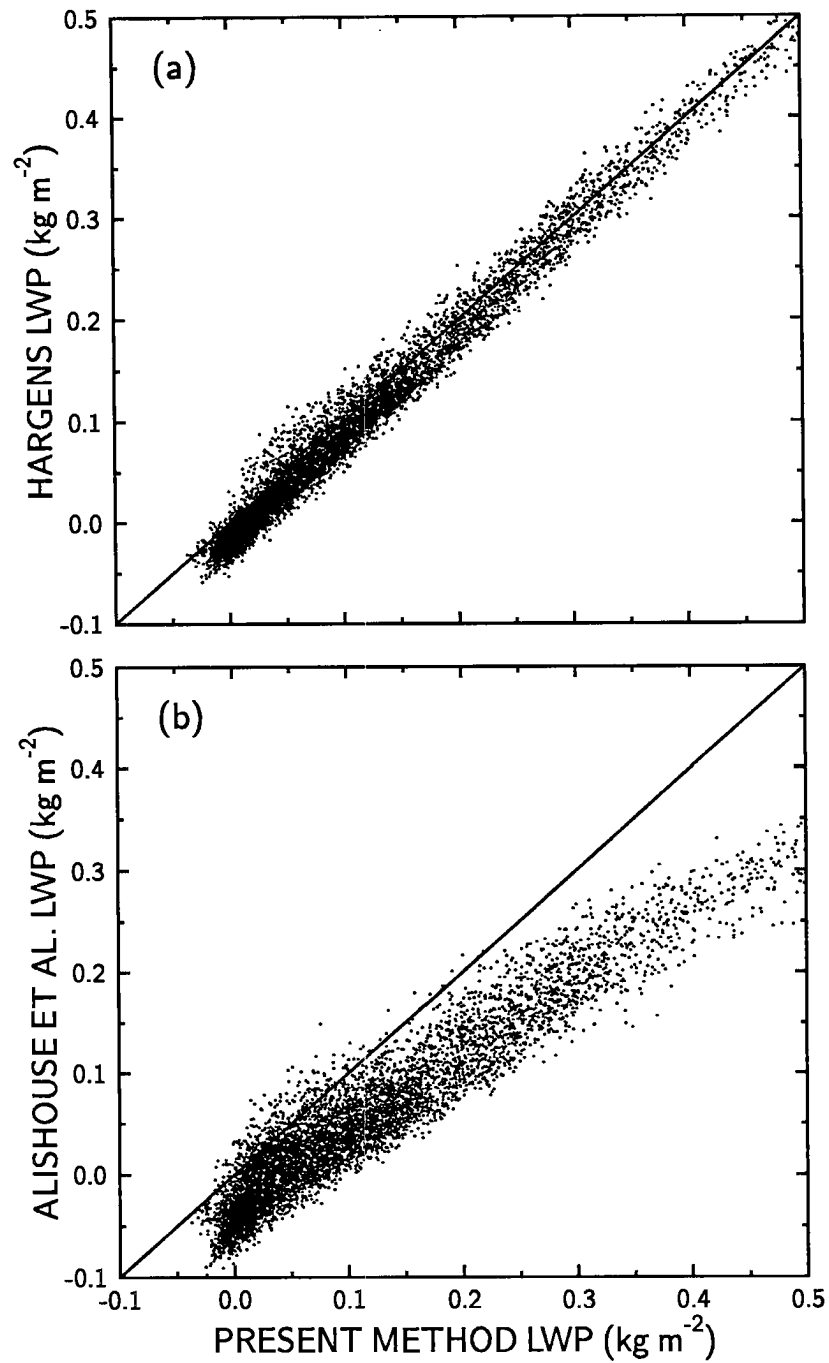


Figure 3.17: Scatter diagrams of LWP ( $\text{kg m}^{-2}$ ) derived from the method of (a) Hargens (1992) and (b) Alishouse et al. (1990) versus the present method over the North Sea from October 1 to 18, 1989.

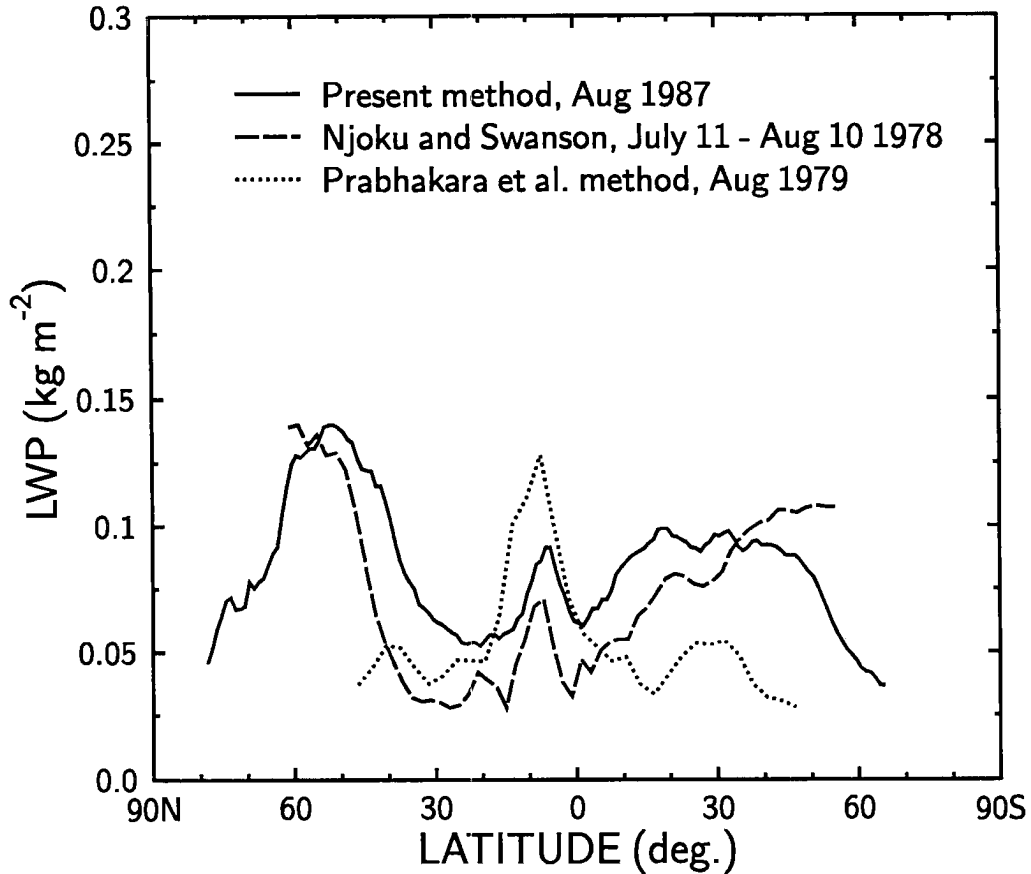


Figure 3.18: Zonal distributions of liquid water ( $\text{kg m}^{-2}$ ) derived from the present method for August 1987 (solid), Seasat Special Multichannel Microwave Radiometer (SMMR) results from the study of Njoku and Swanson (1983) for July 11 to August 10, 1978 (dashed), and Nimbus 7 SMMR results from the method of Prabhakara et al. (1983) for August 1979 (dotted).

requiring an ad hoc correction. In any case, these differences are most likely within the errors associated with the SSM/I retrievals.

The comparison to the liquid water derived from the method of Prabhakara et al. reveals a better correspondence in the equatorial region, but far less agreement at higher latitudes. The close agreement in the tropics is perhaps accidental because Prabhakara et al. actually estimate the total liquid water content of the atmosphere, which includes contributions from both cloud water and precipitation. Their physically-based approach is based on measurements at 6.6 and 10 GHz from the Nimbus 7 SMMR. These frequencies are primarily sensitive to high amounts of liquid water, which are in the form of raindrops

in the precipitating convective systems of the tropics. Thus, the liquid water amounts retrieved from this method are more likely representative of rain water than cloud water. This idea may explain why the liquid water has a significant maximum in the equatorial region and steadily decreases towards the poles, with relative maxima in the mid-latitudes caused by the precipitation in cyclonic storms (the low values in the subtropics and mid-latitudes are also caused by the inability of the algorithm to estimate liquid water in regions of low-level divergence, where marine stratocumulus clouds commonly form). Further evidence for this interpretation is supported by the rainfall study of Prabhakara et al. (1986) where these same liquid water fields were used to derive climatic rainfall data.

## Chapter 4

### GLOBAL CHARACTERISTICS OF MARINE CLOUD LIQUID WATER

#### 4.1 Data Description

When producing cloud liquid water data sets for climate studies, it is a common and simple practice to include all pixels in the averaging process, whether they are clear or cloudy. Obviously, how one averages the data depends on the application that is of interest to the scientist. For example, when comparing observations to cloud liquid water fields generated by GCMs, one might want to include clear pixels in the average. However, if one is specifically interested in cloud properties, then it might be better to exclude clear pixels. Thus, it is highly recommended that both types of data sets be produced.

Unless specifically mentioned, the cloud liquid water results presented in this study include only cloudy pixels. Gridbox averages were done by taking the average of all cloudy pixels over a month within a given gridbox. Despite the limitations of using microwave measurements alone to identify clear pixels, a reasonable guess can be made by using a cloud liquid water threshold. For the purposes of this study we have chosen values of cloud liquid water greater than  $0.025 \text{ kg m}^{-2}$  to represent cloudy pixels since this threshold is a rough estimate of the limit of detectability of cloud liquid water. This value is consistent with clear sky retrievals done in Chapter 2 where the standard deviation was found to be  $0.016 \text{ kg m}^{-2}$ .

Several other details should be noted regarding the processing of the data. For example, since the retrieval algorithm depends somewhat on SST it was discovered that using the nearest monthly mean SST value (on a  $2^\circ$  grid) would cause spurious oscillations in the retrieved fields of both water vapor and liquid water. This was a particular problem in the midlatitudes where the SST gradients can be very large. To solve this problem, the

SST that was used as input into the retrieval model was bilinearly interpolated based on the four nearest SST gridpoints. Another problem to consider is eliminating pixels that are contaminated by sea ice and land. Detection of sea ice was done using a simple version of the AES/YORK algorithm that was developed for the SSM/I Cal/Val effort (Hollinger et al., 1991). A  $0.5^\circ \times 0.5^\circ$  land mask was used to avoid retrievals over land regions. Pixels that were within  $0.5^\circ$  of land were also eliminated since sidelobe contributions from the emission by nearby land areas can greatly influence the brightness temperatures, particularly at the lowest resolution 19.35 GHz channels. Lastly, it should be emphasized that an enormous amount of time and effort was spent carefully processing the cloud liquid water and water vapor data from the SSM/I radiance measurements. The total amount of data processed was about 53 GB for the 4.5-year period.

The major limitation of the cloud liquid water data sets, as with all microwave-derived cloud liquid water data sets, is the large uncertainties in the estimates in tropical regions. The tropics present special problems in retrieving cloud liquid water as a result of the abundant water vapor and extensive regions of heavy rainfall. Cloud liquid water cannot be reliably retrieved when rainfall and other precipitation is widely distributed within the field-of-view of the instrument since emission from raindrops and scattering effects by raindrops and large ice particles (at 37 GHz) become important. For the purpose of minimizing biases in the monthly mean cloud liquid water amounts, which would probably occur if cloud liquid water was neglected in precipitating cloud systems, the LWP is set to a constant value of  $0.5 \text{ kg m}^{-2}$  for SSM/I pixels in which the LWP retrieval is greater than  $0.5 \text{ kg m}^{-2}$ .

Another difficulty with retrievals in the tropics is that biases in estimating  $W$  can have a large effect on the estimation of  $L$ . This effect may be at least as significant as precipitation contamination since Jackson and Stephens (1994) show that the largest disagreement among current water vapor algorithms occurs in regions of high water vapor. Additional problems with cloud liquid water retrieval in the tropics might include saturation of the 37v GHz channel or even scattering effects (at 37 GHz) from thick anvil cirrus clouds containing large ice particles that completely fill the satellite footprint.

## 4.2 Spatial Distribution and Temporal Statistics

Figure 4.1 shows the annual mean SSM/I cloud liquid water for the 53 monthly averages.<sup>1</sup> This figure illustrates that much of the horizontal distribution of cloud liquid water is closely tied to large-scale dynamical patterns since to a significant extent cloud droplets are tracers of atmospheric motion. These include, for instance, the high values (greater than  $0.14 \text{ kg m}^{-2}$ ) in the North Pacific and Atlantic, which are in part a result of the rising motion in baroclinic storm systems, and the signatures of the ITCZ in the Pacific and Atlantic which arise through upward motion from intense convection. In addition, high cloud liquid water values of over  $0.14 \text{ kg m}^{-2}$  are common in the Indonesian area. In other regions of interest, the SPCZ is well represented by a relative maximum and there is a hint of the southern hemisphere storm track in the southern Indian Ocean. In areas typically dominated by subtropical highs and subsidence, the cloud liquid water is generally lower except in those regions off the west coasts of the major continents, particularly near North and South America, where extensive and persistent stratocumulus reside. The lowest cloud liquid water (less than  $0.08 \text{ kg m}^{-2}$ ) is associated with areas of subsidence and generally concentrated near land masses except perhaps in the central Pacific.

The zonal average characteristics of oceanic cloud liquid water are shown in Figure 4.2. These calculations do not reflect the fact that there is more ocean relative to land in the southern oceans than for the northern oceans. As a result, features in the northern hemisphere will be emphasized. The annual mean relationship in Figure 4.2a is represented as three distinct peaks. The maximum in the southern midlatitudes is mainly a result of baroclinic storm systems while the slightly broader northern midlatitudes maximum is caused by storminess and increased stratiform cloudiness during the summer. The maximum at about  $5^\circ\text{N}$  is due to intense convection associated with the ITCZ. Convective activity in the southern hemisphere is indicated as a slight secondary maximum at about

---

<sup>1</sup>Strictly speaking, this is not the annual mean since the months of July through November include one more year than the other months, which causes these five months to be weighted slightly higher when computing the mean. However, in a practical sense the differences in the mean between including and excluding the months of July 1987 through November 1987 are extremely small.

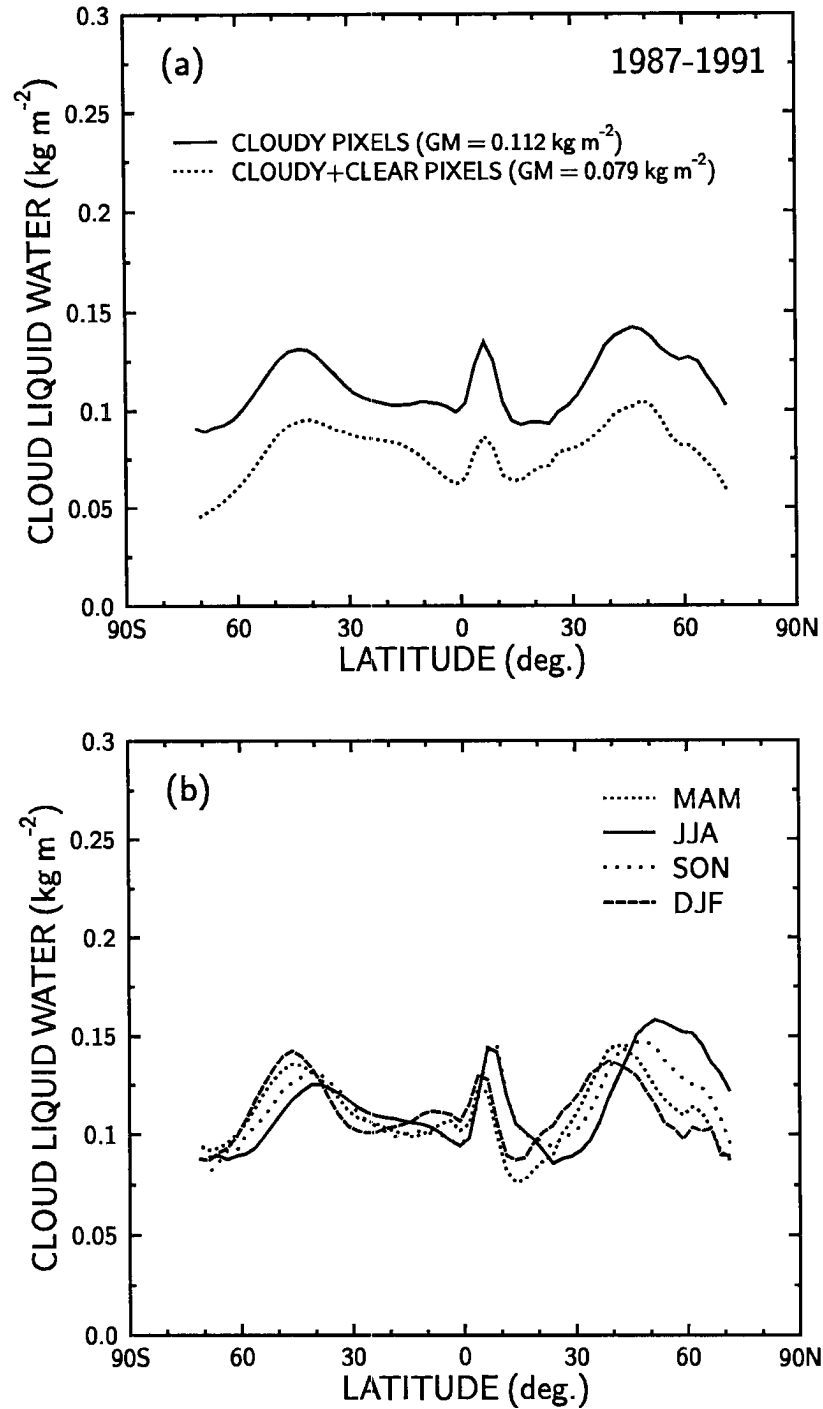


Figure 4.2: (a) Zonal average cloud liquid water ( $\text{kg m}^{-2}$ ) averaged from July 1987 to December 1991. Solid curve includes only cloudy pixels in the average while dotted curve include cloudy and clear pixels in the average. Areally weighted global means (GM) for each data set are also shown. (b) Seasonal zonal averages of cloud liquid water over the same 53-month period.

10°S. Regions of minima are located in the subtropics. There is also an overall decline in the cloud liquid water as one approaches the highest latitudes.

Also depicted in Figure 4.2a is the annual mean cloud liquid water when clear pixels are included in the average. As expected, the values are lower (typically about 20–30%) relative to the cloudy pixel average but at certain latitudes the differences are much larger. Some of the larger differences may be a direct result of small clear sky biases. On a zonal average basis these biases amount to no more than about  $-0.01 \text{ kg m}^{-2}$  in the tropics and at the highest latitudes relative to the midlatitudes. In specific locations in the tropics, however, most notably in areas of extremely high water vapor, the clear sky biases can reach  $-0.03 \text{ kg m}^{-2}$ . It is also somewhat surprising that the differences between the clear-plus-cloudy pixels and the cloudy-only pixels seem to be regular. One might expect the differences between the two to be a measure of cloud amount. There is some evidence to suggest that the LWP threshold used to separate clear from cloudy pixels may be too low, which might be a partial explanation for these results.

The seasonal character of the spatial distribution of cloud liquid water is shown in Figures 4.3 and 4.4. The highest cloud liquid water is almost exclusively confined to the northern hemisphere except during DJF. One feature that appears regularly from season to season in the southern hemisphere is the maximum cloud liquid water (greater than  $0.14 \text{ kg m}^{-2}$ ) in the southern Indian Ocean near 45°S. It appears to be a consequence of baroclinic storms since it corresponds qualitatively with regions of maximum transient eddy kinetic energy computed by James and Anderson (1984) and high frequency variances of geopotential height derived by Trenberth (1991). A distinct maximum, which coincides well with the principal track of cyclones (see, e.g., Wallace et al., 1988), is clearly visible over the northern oceans during the DJF, MAM, and SON seasons. The large production of cloud liquid water mass off the east coasts of China and the United States, especially during DJF and MAM, is due to the significant fluxes of latent and sensible heat and subsequent convective instabilities that occur as a result of the advection of cold, dry continental air over the warmer ocean.

One of the most striking features in the seasonal maps is the broad region of high cloud liquid water (from  $0.14 \text{ kg m}^{-2}$  to more than  $0.16 \text{ kg m}^{-2}$ ) during JJA in the North

Pacific and Atlantic. The conditions responsible for the formation of cloud liquid water during the summer in this region are vastly different than in other seasons. At this time of the year there is diminished storm activity and a far greater occurrence of stratus clouds. The specific cause of the increased stratus cloudiness is not well understood; however, Klein and Hartmann (1993) have shown that the stratus cloudiness is well correlated with the presence of low-level temperature inversions and high stability in the lower troposphere.

To investigate further the relationship between cloud liquid water and cloudiness, we show in Figure 4.5 a scatter diagram of monthly mean cloud liquid water versus total cloud amount derived from ISCCP for the summer months from July 1987 to June 1991 over the North Pacific ( $50^{\circ}$ – $35^{\circ}$ N;  $155^{\circ}$ – $125^{\circ}$ W). Each data point represents a  $2.5^{\circ}$  gridbox. A well-defined and nonlinear relationship is clearly evident from this figure. These results support the idea that the significant rise in cloud liquid water can be attributed principally

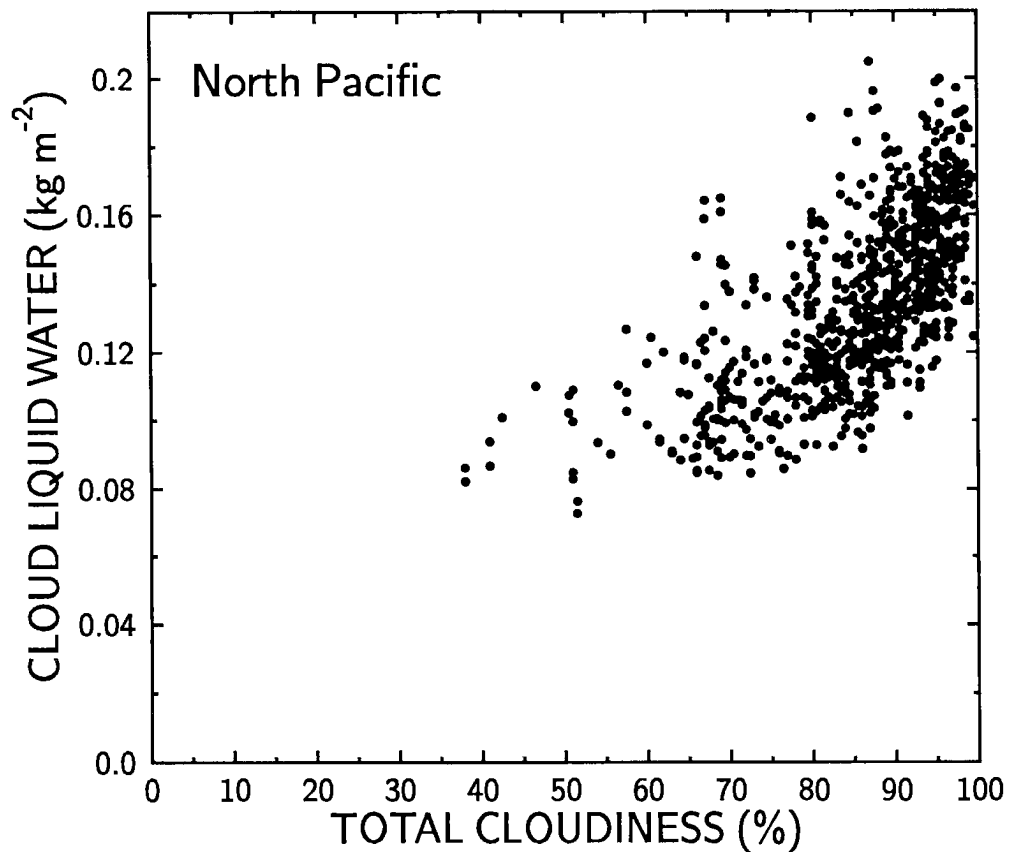


Figure 4.5: Scatter diagram of monthly mean SSM/I cloud liquid water ( $\text{kg m}^{-2}$ ) versus ISCCP total cloudiness (%) for the summer months from July 1987 to June 1991 over the North Pacific.

to increases in cloudiness. However, we cannot completely rule out that some of the observed increase in cloud liquid water in certain regions may be caused by an enhanced geometric thickness of the clouds.

Another distinguishing phenomenon in the seasonal maps is the zonal shift of the maximum cloud liquid water along the ITCZ. While the absolute cloud liquid water estimates along the ITCZ are in all likelihood dubious, the relative changes from one season to another may be fairly realistic. The most salient feature in the eastern Pacific is the movement of the cloud liquid water maximum to the west during the MAM season. This result is consistent with similar shifts in rainfall maxima that were seen from the rainfall climatology observed by Spencer (1993) based on measurements from the Microwave Sounding Unit (MSU) on the NOAA satellites.

Aside from the obvious maximum of the ITCZ, other prominent characteristics in the tropics can be seen for JJA in Figure 4.3a. For example, evidence of the southern Asian monsoon is observed as liquid water maxima exceeding  $0.15 \text{ kg m}^{-2}$  on the western side of India and along the coast of Burma. In contrast, the cloud liquid water is a minimum (less than  $0.06 \text{ kg m}^{-2}$ ) in this same region during DJF, which is attributed to the reversal of the monsoonal flow and a dominance of the descending branch of the Hadley circulation. There is also an indication of a cloud liquid water maximum in the west Pacific where the convection is known to be most vigorous. During DJF when the greatest convective activity advances to the southern parts of Indonesia and just north of Australia, the cloud liquid water values are greater than  $0.14 \text{ kg m}^{-2}$  and sometimes reach  $0.16 \text{ kg m}^{-2}$ . We should stress that the magnitude of the cloud liquid water in these regions should be treated with some suspicion since the retrievals are less reliable where precipitating cloud systems prevail.

The variation of cloud liquid water with season in terms of zonal mean profiles is shown in Figure 4.2b. All seasons retain a basic trimodal structure as seen earlier for the annual mean. In both hemispheres, particularly in the north, the equatorward push of cloud liquid water during the winter is observed. The greatest seasonal variation appears in the northern subtropics and midlatitudes. The ITCZ shows little seasonal variation in

its position and remains confined to the northern hemisphere. The summertime convection in the southern hemisphere tropics can also be seen during DJF and MAM near 5° and 10°S.

Further information about the temporal variation of cloud liquid water can be gathered by calculating the sample interannual and intra-annual standard deviations, which for this study are defined, respectively, at each gridbox as

$$\sigma_{inter} = \left[ \frac{1}{52} \sum_{j=1}^{12} \sum_{i=1}^N (L_{ij} - \bar{L}_j)^2 \right]^{1/2} \quad (4.1)$$

$$\sigma_{intra} = \left[ \frac{1}{52} \sum_{i=1}^{53} (L_i - \bar{L})^2 \right]^{1/2} \quad (4.2)$$

where  $N$  is 4 or 5 depending on the month,  $\bar{L}_j$  is the average observation for a particular month  $j$ , and  $\bar{L}$  is the average observation over all 53 months.

Calculations of  $\sigma_{inter}$  and  $\sigma_{intra}$  are shown as global distributions in Figure 4.6a and 4.6b, respectively. Regions of maximum interannual variation in Figure 4.6a of over 0.025 kg m<sup>-2</sup> occur near the China coast and Japan and in the tropical convective areas in the West Pacific and Indian Ocean. Other relative maxima are evident along the eastern North American coast, in the SPCZ, and near southern Brazil. The most extreme interannual variability occurs in the Timor Sea off the northwest coast of Australia, where it reaches 35–40% of the annual mean. Minimal year-to-year variability (less than 0.015 kg m<sup>-2</sup>) is seen in areas where high pressure systems typically occur and in the high latitude southern oceans. On a zonal average basis the year-to-year variations range from about 10 to 17% of the annual mean, where the highest variability occurs in the tropics and subtropics and diminishes at higher latitudes. This is probably an overestimate of the true interannual variation since a low sample of 4–5 years of data was used in the analysis.

The intra-annual variability shown in Figure 4.6b, in many ways, resembles the interannual variability but there are important differences. For instance, an area of high variability (as large as 0.05 kg m<sup>-2</sup>) exists in the tropical Atlantic, which is a result of the significant meridional excursions of the ITCZ. There are also large seasonal changes in the far eastern Pacific ITCZ. The Asian and Australian monsoons are exhibited as regions of

very high seasonal swings in cloud liquid water, sometimes as great as 50% of the annual mean. Another region of large (greater than  $0.035 \text{ kg m}^{-2}$ ) and widespread variability extends along the Asian eastern coast into the far North Pacific and Bering Sea. The behavior is similar on the eastern side of North America, though to a lesser degree. Much of the large seasonal variability in these regions is likely a result of continental influences. This is in contrast to the middle and high latitudes of the southern hemisphere where the impact of land masses is far less and the seasonal variability is smaller (less than  $0.02 \text{ kg m}^{-2}$ ). The lowest intra-annual variability, on the other hand, is generally located in regions whose climate is influenced by high pressure systems, with the exception of a few areas west of northern South America and the relative maximum west of southern Africa. When zonally averaged, the intra-annual variability varies from 15% to about 25% of the annual mean and peaks along the ITCZ where it is over 30% of the annual mean. The northern hemisphere also shows greater variability than the southern hemisphere.

Global and hemispheric average values of marine cloud liquid water over the 53-month period are shown in Figure 4.7 as a function of the month of the year. These quantities were derived by weighting the equal-angle gridboxes according to their area. The gray shading in the figure represents the interannual standard deviation. Over the globe the mean cloud liquid water has a minimum of  $0.110 \text{ kg m}^{-2}$  in April and steadily increases to a maximum of  $0.114 \text{ kg m}^{-2}$  in December. When separated into hemispheric means, the northern hemisphere has a seasonal behavior similar to the global mean except that it exhibits far greater seasonal change, with a low value of  $0.105 \text{ kg m}^{-2}$  in April and reaches a peak value of about  $0.118 \text{ kg m}^{-2}$  in November. In the southern hemisphere the seasonal variability is far less and the nature of the seasonal cycle is very different than the northern hemisphere, aside from the obvious phase shift. For example, the lowest values of cloud liquid water are spread out over a 4 to 5-month period and gradually increase to a maximum of  $0.115 \text{ kg m}^{-2}$  in March. However, both hemispheres share similar behavior in terms of year-to-year variability where it is usually greatest in the late summer and fall.

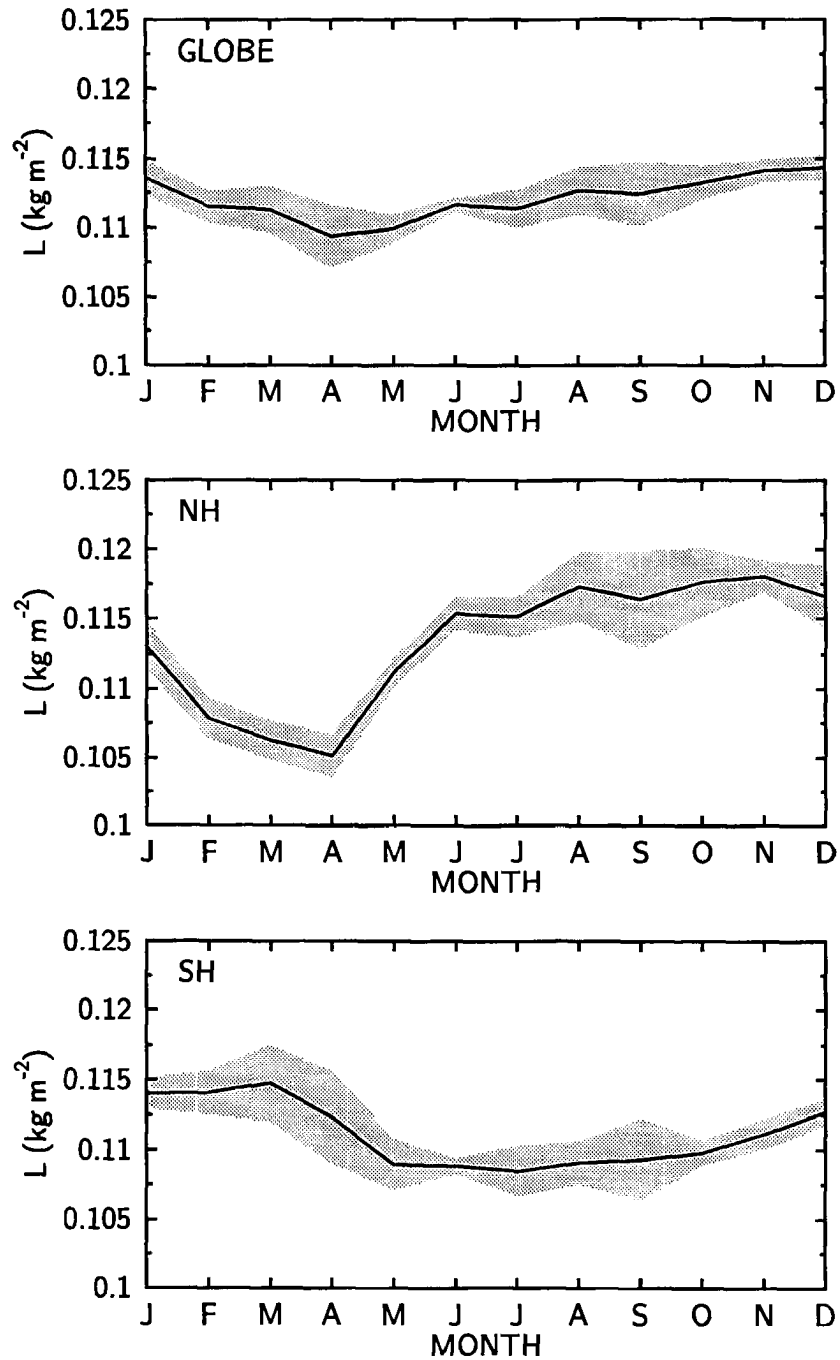


Figure 4.7: Areal weighted averages of cloud liquid water ( $L$ ) for the globe (top), northern hemisphere (middle), and southern hemisphere (bottom) as a function of month. Gray shading represents interannual variation as one standard deviation above and below the data points.

### 4.3 Cloud Liquid Water-Temperature Sensitivity Analysis

It was shown in the previous section that the spatial distribution of cloud liquid water over the oceans takes on a variety of distinctive characteristics, many of which are related to known general circulation patterns. The focus of this section is to quantify the relationship between cloud liquid water and the atmospheric temperature field and to describe its seasonal and regional qualities, with the analysis being restricted to low-lying clouds. Further, we also explore the relationship of cloud liquid water to sea surface temperature.

#### 4.3.1 Data and analysis method

Cloudiness and other related cloud data are obtained from the products derived by the International Satellite Cloud Climatology Project (ISCCP). The ISCCP is a multiyear effort, started in July 1983, whose goals include, but are not limited to, providing a reliable global climatology of cloudiness and cloud properties based on existing weather satellites and to make available a well-calibrated, global radiance data set (Schiffer and Rossow, 1983).

The source of data used in the following analyses are the ISCCP Stage C1 data products, which are on an equal area grid and are given every 3 hours (0, 300, 600, 900, 1200, 1500, 1800, and 2100 UT). The data are subsequently mapped to a 2.5 equal-angle grid. The cloud products include cloud fraction, cloud top pressure and temperature, visible optical depth for seven different cloud types, among other statistical information. These cloud types are arbitrarily defined according to their cloud top pressure and optical depth as shown in Figure 4.8. More general definitions of low, middle, and high cloudiness in this figure are determined using IR measurements only.

The cloud properties are determined based on a three-step process. First, spatial and temporal statistics of the shortwave and longwave radiances are gathered over the course of a month to determine the best estimate of the clear sky radiances for each region and time (Rossow and Schiffer, 1991). Then a given pixel is classified as either cloudy or clear based on a bispectral radiance threshold technique using information about the variability

of the clear sky radiances derived previously. Once a pixel has been determined to be cloudy, the second step is to use a “table look-up” approach to infer the cloud optical properties of the cloudy pixel. That is, radiative transfer calculations are first done at two frequencies (0.6 and 11  $\mu\text{m}$ ) for different solar angles, satellite viewing geometries, surface reflectances, and atmospheric conditions. Then given the clear sky radiances, satellite geometry, ozone abundance, etc., the surface visible reflectance and temperature can be estimated from the table of precalculated values. Once the surface properties have been determined, the cloud optical depth and cloud top temperature can be derived from a similar table which also includes calculations for different cloud optical depths and cloud top pressures. The clouds are modeled as a single layer consisting of water droplets with an average radius of 10  $\mu\text{m}$ . Multiple scattering is also accounted for in the model. The final step consists of a space/time averaging of the pixel-level cloud products and transferring the data to an equal area grid. This process also involves combining the data from different

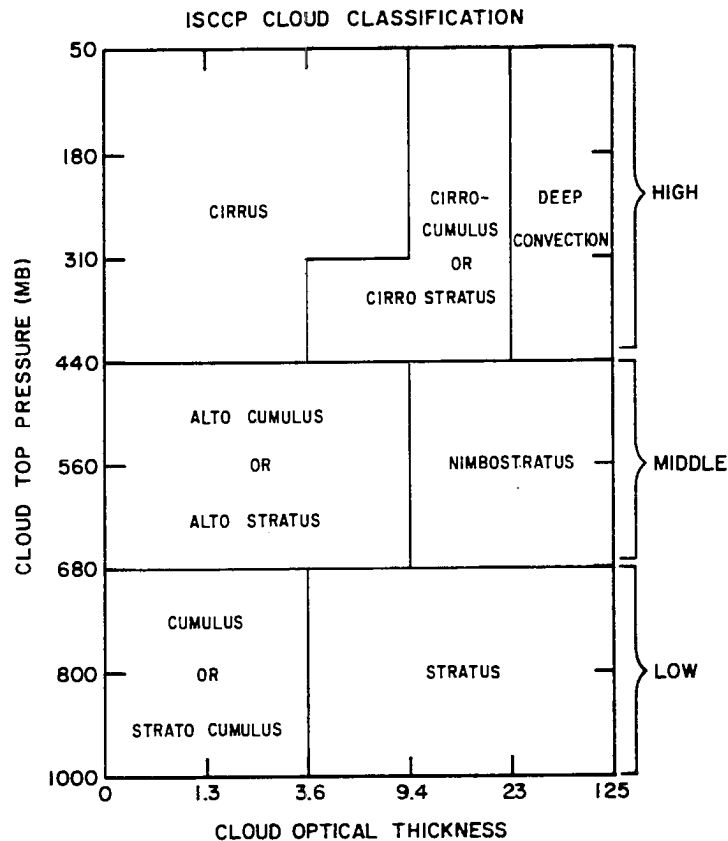


Figure 4.8: Cloud types as defined by ISCCP (from Rossow and Schiffer, 1991).

geostationary and polar orbiting satellites into one product. More details about these data sets is supplied by Rossow and Schiffer (1991).

The comparisons are made with daily mean cloud top pressure and cloud liquid water data on a  $2.5^\circ$  grid. We define low clouds the same as ISCCP, which are clouds with cloud top pressures between 680 and 1000 mb. One difficulty with using daily mean gridded data is that although the mean cloud top pressure may be greater than 680 mb a large fraction of the gridbox, in some instances, might be covered by higher level cloudiness. As an attempt to ensure that the majority of clouds within the gridbox are low level, we include only gridboxes where the low cloudiness (determined by ISCCP) exceeds 40%.

The atmospheric temperature data used in this study are also obtained from the ISCCP products, which are based on TOVS (TIROS Operational Vertical Sounder) satellite retrievals. Temperatures are given at seven pressure levels: 115, 245, 375, 500, 620, 740, and 900 mb, and at the surface. Ideally, one would want to compare the cloud temperature to the cloud liquid water data. Unfortunately, the cloud temperature is difficult to estimate since the cloud base temperature is unknown and since there is likely to be a mixture of different cloud base heights within the gridbox. Thus the cloud liquid water data are compared instead to a layer mean atmospheric temperature, which consists of the average temperature from 680 mb to the surface. Other data used in the analyses are the monthly mean sea surface temperature data described by Reynolds (1988).

The method of analyzing the cloud liquid water-temperature relationship is very similar to that of Tselioudis et al. (1992), so as to facilitate a comparison of the results of that study with the present one. The daily mean cloud liquid water and temperature data are collected together over specified time periods and/or latitudinal zones and sorted into temperature intervals, each with a width of 15 K. The lower bound of the first interval occurs at  $-25^\circ\text{C}$  and each successive interval is shifted by 5 K. For the SSTs the width of the temperature intervals is changed to 9 K and the intervals are shifted by 3 K, with the lowest bound occurring at  $-3^\circ\text{C}$ . The temperature representing each interval is simply the average of the temperature data within the interval. The logarithm of  $L$  is correlated to temperature using linear least squares regression, and the significance of the fit is determined from an F test.

### 4.3.2 Results

Figure 4.9 shows the zonal average cloud liquid water of low clouds for JJA and DJF 1990. The global mean values are comparable, with the liquid water content of clouds during JJA being slightly greater than those during DJF ( $0.088 \text{ kg m}^{-2}$  versus  $0.084 \text{ kg m}^{-2}$ ). The largest seasonal change in cloud liquid water occurs throughout the subtropics and poleward of about  $45^\circ\text{N}$ . Also, our analysis seems to indicate that wintertime low-level clouds over the middle to high latitude oceans tend to be less optically thick than during the summer, while the behavior is the opposite in the subtropics.

The seasonal changes in cloud liquid water between about  $40^\circ\text{N}$  and  $40^\circ\text{S}$  are consistent with the variation in cloud optical depth reported by Tselioudis et al. (1992), which consisted of clouds with cloud top pressures from 680 to 800 mb over both land and ocean (see their Fig. 3). At higher latitudes, however, the discrepancies between the present results and those of Tselioudis et al. are substantial during DJF in the northern hemisphere and for both seasons in the southern hemisphere. During the winter season, especially at middle to high northern latitudes, the higher optical depths observed by ISCCP are most likely resulting from ice clouds over land and to a smaller degree over the ocean. During the winter, temperatures often fall to  $-10^\circ\text{C}$  or colder at relatively low levels such as 750 mb. Although many of the clouds at these temperatures are composed of supercooled drops, there is also a greater chance of the presence of ice clouds.

The relation between cloud liquid water and temperature can be characterized by the sensitivity parameter defined by Somerville and Remer (1984):

$$f = \frac{1}{L} \frac{dL}{dT} = \frac{d \ln L}{dT} \quad (4.3)$$

where for our application  $L$  is the vertically integrated liquid water content of clouds below the 680 mb level and  $T$  is the average temperature of the atmosphere below this level.

The results of the global sensitivity analysis using data from JJA and DJF 1990 are given in Figure 4.10. The quantity  $d \ln L/dT$  is plotted as a function of the mean temperature of the 680-1000 mb layer for data extending from  $70^\circ\text{N}$  to  $70^\circ\text{S}$ . Also shown for reference is the range in the sensitivity relationship one would expect based purely on

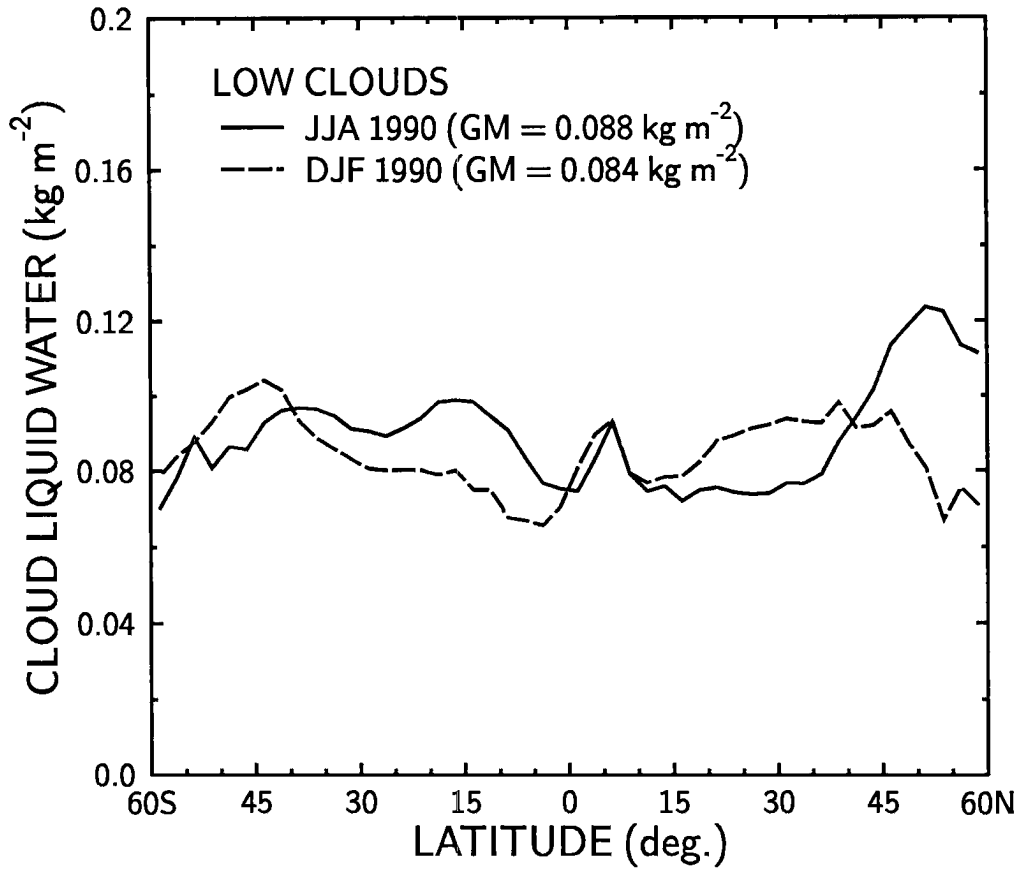


Figure 4.9: Zonal average distributions of the liquid water ( $\text{kg m}^{-2}$ ) of low clouds (cloud top pressures from 680–1000 mb) for JJA 1990 (solid curve) and DJF 1990 (dashed curve). Areal weighted global means (GM) are also given.

adiabatic arguments for clouds of different thickness and height below the 680 mb level, where the temperature is also the layer mean. These results are based on Table 1 of the analysis of Betts and Harshvardhan (1987). The filled symbol represents a correlation that is not statistically significant beyond the 99% confidence level. The results in Figure 4.10 indicate that the observed sensitivities for low clouds vary significantly with temperature. A quasi-adiabatic behavior is observed for temperatures below about  $0^{\circ}\text{C}$ , with sensitivities at roughly  $0.03\text{ deg}^{-1}$ . For temperatures greater than  $3^{\circ}\text{C}$ , the sensitivity becomes negative and is as low as  $-0.04\text{ deg}^{-1}$  for temperatures near  $17^{\circ}\text{C}$ .

Comparisons of cloud liquid water to sea surface temperature are illustrated as scatter diagrams in Figure 4.11. Each data point represents a  $2.5^{\circ}$  gridbox. Figure 4.11a shows the annual mean cloud liquid water data of Figure 4.1 plotted against the annual mean SSTs determined over the same time period. The results reveal a distinctly coherent relationship.

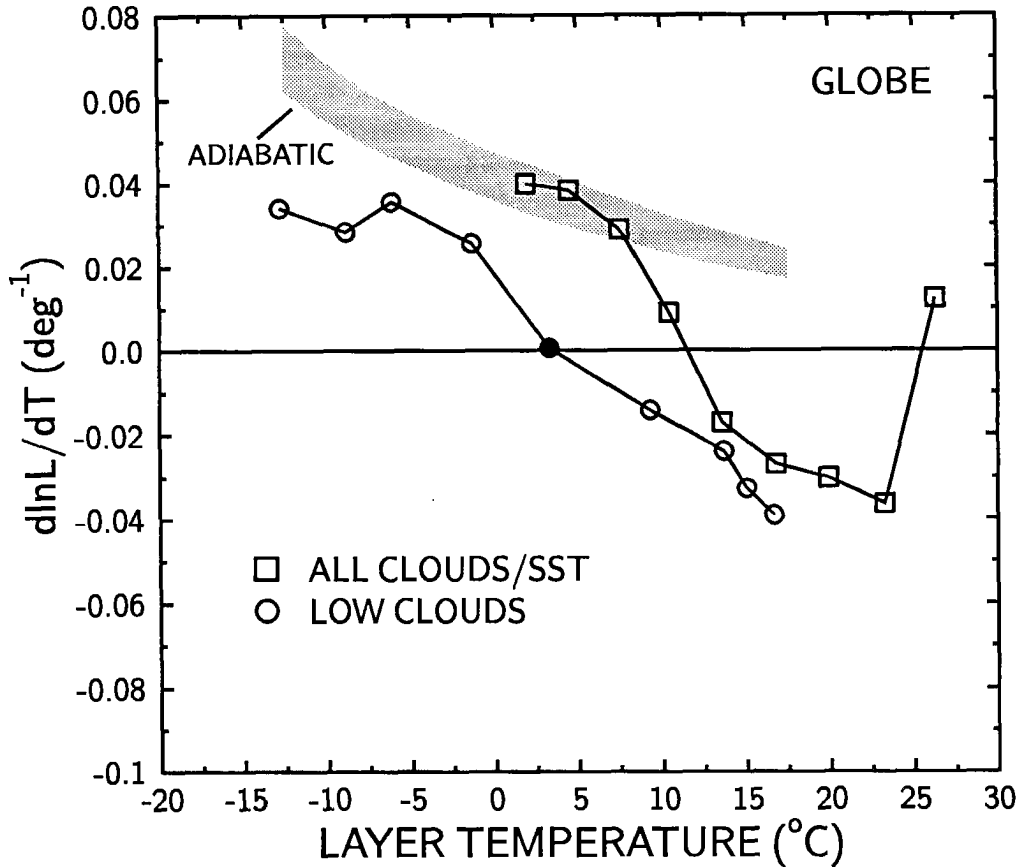


Figure 4.10: Global relationship between  $d\ln L/dT$  ( $\text{deg}^{-1}$ ) for low clouds versus the temperature ( $^{\circ}\text{C}$ ) of the atmospheric layer from 680 mb to the surface. Each circle represents a temperature interval of width 15 K. Filled circle has a correlation below the 99% significance level. Light shading indicates the range of the relationship derived from an adiabatic assumption for clouds of varying thickness and height from 680 to 1000 mb. Also illustrated as squares is the sensitivity relationship using sea surface temperatures (SSTs) for the cloud liquid water data (all clouds) shown in Figure 4.1 as a function of SST. For these calculations the temperature interval is 9 K.

Cloud liquid water increases gradually from the lowest SSTs until a maximum is attained at roughly  $12^{\circ}$  to  $15^{\circ}\text{C}$ . This maximum is presumably a result of increased cloudiness from midlatitude baroclinic storms. The liquid water values then begin a steady descent towards warmer SSTs and reach a minimum at about  $27^{\circ}\text{C}$ , which is a consequence of lower cloudiness in the subtropics. At the warmest SSTs the cloud liquid water increases abruptly, which is brought about by tropical convective activity. When these data are analyzed in terms of the sensitivity parameter  $d\ln L/dT$  and plotted versus SST (see Figure 4.10), the relationship has a similar behavior and magnitude of sensitivities as seen

for low clouds. The major difference is the sudden rise to a positive value of  $d \ln L/dT$  at the warmest temperatures.

Figure 4.11b shows the liquid water of low clouds averaged for the two seasons and plotted as a function of SST. The relationship for low clouds is much different than that for all clouds in Figure 4.11a. The liquid water is only weakly dependent on SST with a minor indication of a maximum near  $15^\circ \text{ C}$  and no discernible peak is observed at the warmest SSTs. A scatterplot of the liquid water of low clouds versus the layer temperature (not shown) also shows very nearly the same type of behavior. These results demonstrate that while statistically significant correlations are indeed found between cloud liquid water and temperature, these relationships are exceedingly weak.

The relationship of  $d \ln L/dT$  to temperature for low clouds also undergoes sizeable variations on both seasonal and regional scales. Figure 4.12 presents the results of an analysis for the same data sets but separated into different latitude zones of midlatitude ( $35^\circ\text{--}55^\circ$ ), subtropics ( $15^\circ\text{--}35^\circ$ ), and tropics ( $0^\circ\text{--}15^\circ$ ) for each of the two seasons. In the northern hemisphere in Figure 4.12a, all regions have negative values of  $d \ln L/dT$  except for temperatures less than about  $-5^\circ \text{ C}$  (and an anomalous point near  $7^\circ \text{ C}$ ) for the midlatitudes during DJF. The northern midlatitudes show little change with temperature but exhibit large seasonal differences with values near  $-0.025 \text{ deg}^{-1}$  during DJF and values as low as  $-0.07 \text{ deg}^{-1}$  during JJA. The tropics, on the other hand, show a much greater sensitivity of  $d \ln L/dT$  to temperature with values ranging from about  $-0.025 \text{ deg}^{-1}$  to  $-0.1 \text{ deg}^{-1}$ .

Comparing these results to those obtained by Tselioudis et al. (1992) reveals many quantitative similarities. Their results show that the sensitivities for midlatitude clouds over the ocean are positive (though statistically insignificant) at the coldest temperatures but somewhat smaller than the results in Figure 4.12a. The differences might be attributed to the effect of ice clouds in the observations of cloud optical depth. The sensitivities eventually crossover into negative values at higher temperatures, which are as low as  $-0.04 \text{ deg}^{-1}$ . These negative values are comparable to the values of  $-0.04$  to  $-0.075 \text{ deg}^{-1}$  seen in Figure 4.12a. The results of Tselioudis et al. also give average subtropical

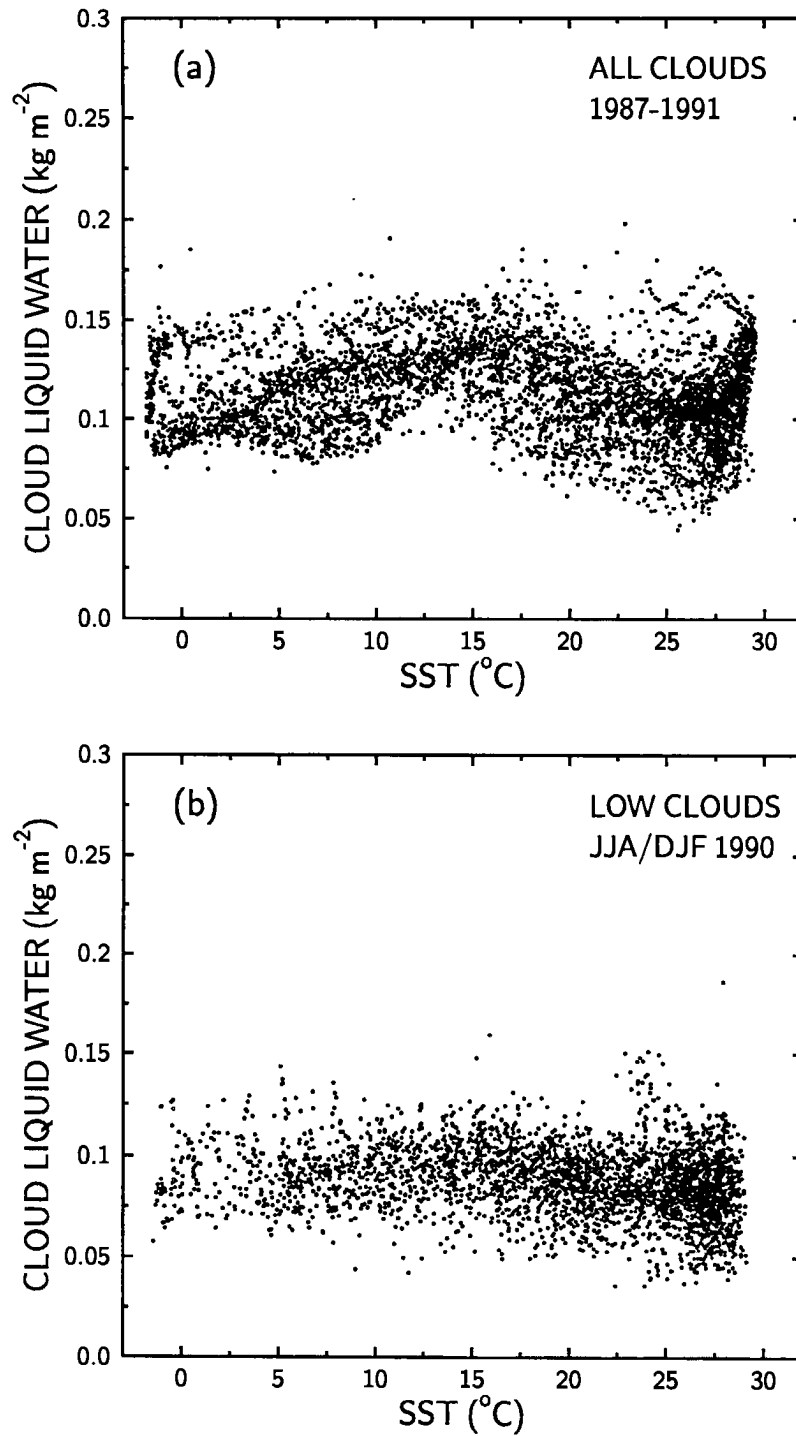


Figure 4.11: Scatter diagrams of the (a) annual mean cloud liquid water data from Figure 4.1 and (b) the cloud liquid water of low clouds averaged for the JJA and DJF seasons in 1990 versus sea surface temperature ( $^{\circ}\text{C}$ ).

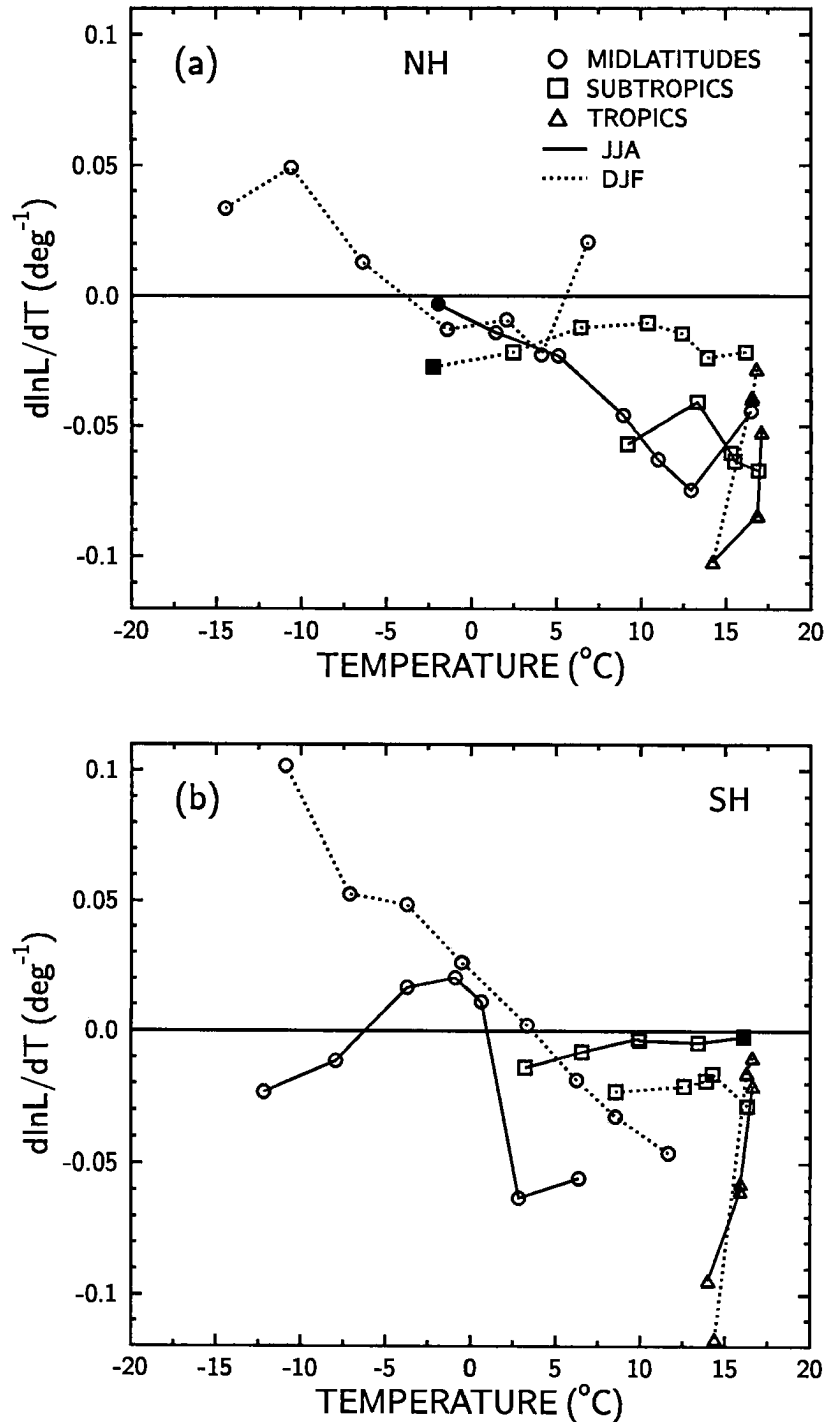


Figure 4.12: Scatter diagrams of  $d\ln L/dT$  ( $\text{deg}^{-1}$ ) for low clouds as a function of temperature ( $^{\circ}\text{C}$ ) separated into midlatitude ( $35^{\circ}$ – $55^{\circ}$ ), subtropical ( $15^{\circ}$ – $35^{\circ}$ ), and tropical ( $0^{\circ}$ – $15^{\circ}$ ) latitude regions and the seasons of JJA and DJF for the (a) northern hemisphere and (b) southern hemisphere. Filled symbols are data points with correlations below the 99% significance level.

and tropical values of about  $-0.05 \text{ deg}^{-1}$ , which are generally consistent with the average of the seasonal results in Figure 4.12a.

The results for the southern hemisphere in Figure 4.12b yield a somewhat different behavior in the temperature dependence and magnitudes of  $d \ln L/dT$ . While the warmest oceans of both hemispheres are associated with negative values of  $d \ln L/dT$ , the subtropical values are smaller in the southern hemisphere (on average about  $-0.01 \text{ deg}^{-1}$ ) and the tropical values are more sensitive to temperature, ranging from  $-0.01$  to  $-0.12 \text{ deg}^{-1}$ . Furthermore, the seasonal change in the southern midlatitudes at the coldest temperatures is far more dramatic than in the northern latitudes.

Because of the relatively coarse resolution of the measurements, it is difficult to isolate the cloud liquid water-temperature relationship completely from other factors that determine the amount of cloud liquid water over the gridbox, such as changes in cloud thickness and cloud amount. The effects of variations in cloud thickness are reduced by using low clouds. To minimize the influence of cloudiness on the sensitivity relationships the data were analyzed again but using only gridboxes where ISCCP total cloudiness exceeded 80%. For the global analysis the differences in the results obtained for these conditions with those presented in Figure 4.10 are fairly small. The data become shifted systematically towards positive values of  $d \ln L/dT$  relative to the curve in Figure 4.10 by about  $0.01 \text{ deg}^{-1}$ . However, for the regional and seasonal analyses in Figure 4.12 the differences are more significant. For example, although the basic temperature dependence of  $d \ln L/dT$  is retained for most regions, the differences in magnitude of the sensitivities are sometimes as great as  $0.05 \text{ deg}^{-1}$ .

In summary, these results indicate that the change in liquid water of low clouds in the tropics and subtropics tends to decrease with increasing temperature, while the relationship becomes quasi-adiabatic at higher latitudes. Tselioudis et al. (1992) proposed a microphysical explanation for the negative correlations they found between optical depth and temperature, ascribing them to more efficient precipitation processes. An important point to emphasize is that the correlations between cloud liquid water and temperature, though statistically significant, do not imply a causal link between these two quantities.

On large spatial scales, changes in temperature may not necessarily produce direct changes in cloud liquid water. Since atmospheric dynamics apparently plays a dominant role in determining the global distribution of cloud liquid water, further research is required to establish whether these processes help to create the correlations we observe between cloud liquid water and temperature.

#### 4.4 Comparisons to General Circulation Models

The final task of this chapter is to provide simple comparisons of the observations to the results from two GCMs that predict cloud liquid water. They include direct comparisons of the cloud liquid water distributions and an analysis of how one of the models performs in terms of cloud liquid water-temperature sensitivities.

##### 4.4.1 Model descriptions

One of the climate models used in the comparisons is the Colorado State University General Circulation Model (CSU GCM). The CSU GCM was built upon the UCLA GCM (see, e.g., Randall et al.; 1989, 1991) and is a gridpoint model that uses a modified  $\sigma$ -coordinate in the vertical direction. The simulations discussed here consist of spinning up the model over a three month's time and then running it over an annual cycle. A diurnal cycle is also included in the model. These calculations involved a horizontal resolution of  $4^\circ$  latitude by  $5^\circ$  longitude and 17 vertical levels. Further information regarding the computational details of the simulations is given by Fowler et al. (1994). In the present version of the model, a gridbox is considered either clear or overcast. If the sum of the cloud liquid water, cloud ice, and snow is different from zero, then the gridbox is considered overcast. Plans are currently underway to incorporate cloud amount into the model by specifying subgrid-scale cloudiness.

The cloud microphysical processes in the CSU GCM are governed by a family of bulk water budget continuity equations. These equations are those used in several existing mesoscale cloud models (e.g., Rutledge and Hobbs, 1983). These equations predict the mixing ratios, at each level, of 5 basic water constituents: water vapor, cloud liquid water, cloud ice, rain, and snow. The quantity of interest to this study, namely cloud liquid water,

is created either through large-scale condensation processes, from the melting of cloud ice, or from the detrainment of moist air at the tops of cumulus clouds. Supercooled liquid water is allowed to exist down to a temperature of  $-20^{\circ}\text{C}$ . In addition, the Bergeron-Findeisen mechanism operates when liquid water and ice coexist.

The second set of model simulations comes from the European Center Hamburg (ECHAM) climate model, which is a modification of the European Center for Medium-range Weather Forecast model. The ECHAM model is a spectral model with a hybrid vertical coordinate consisting of 2nd order finite differences. The model also includes a diurnal cycle. The simulations supplied for this study were done in conjunction with the Atmospheric Model Intercomparison Project (AMIP). AMIP was created to provide a means of intercomparing and validating the results of existing climate models based on simulations over a specific test period, from 1979–1988 (Gates, 1992). The boundary conditions for these model simulations are monthly mean distributions of SST and sea ice. The ECHAM simulations were done over an 11-year period from 1979 to 1989. Each month consists of an ensemble average of 119 realizations. The horizontal resolution used in the simulations was T42.

The prediction of cloud water in the ECHAM model is based on a single cloud water prediction equation to represent all condensed water species. This approach follows the work of Sundquist (1978). In addition, the cloud amount within a gridbox can be determined since subgrid-scale condensation and cloud formation are taken into account. It is important to mention that the cloud water results from the ECHAM simulations represent only liquid water from stratiform clouds. In the tropics, however, contributions to the cloud water mass also include ice from anvil clouds.

#### 4.4.2 Results

The spatial distributions of the annual mean cloud liquid water observations and the annual mean simulations from the CSU GCM and the ECHAM model are presented in Figures 4.13a, 4.13b, and 4.13c, respectively. The observations are averaged over 53 months and include clear and cloudy pixels. The ECHAM results represent only the average of the July and January runs. Both model simulations show high values of cloud

liquid water along the storm track regions in the North Pacific and Atlantic and in the southern hemisphere midlatitudes. The magnitude of the cloud water values from the ECHAM model are much larger than the observations and the CSU GCM. Indications of an ITCZ are also seen in the simulations but are less clearly defined than in the observations. In the equatorial west Pacific the observations indicate very little cloud liquid water. This is caused by the clear sky biases noted earlier and are estimated to be about  $0.03 \text{ kg m}^{-2}$  in this region. One major problem with the simulations is that stratus clouds, which are known to form in subtropical subsidence regions, are nearly nonexistent, particularly for the ECHAM model. This is an indication of possible problems with the boundary layer cloud parameterization in the ECHAM model. The current version of the liquid water diagnostics in the CSU GCM, on the other hand, does not include boundary layer clouds, such as marine stratocumulus.

Zonal averages of the annual mean cloud water distributions in Figure 4.13 are shown in Figure 4.14. The magnitude and latitudinal behavior of the CSU GCM cloud liquid water is remarkably similar to the observations, although the observations are systematically higher at most latitudes. The differences in the subtropics can be attributed in part to the absence of marine stratocumulus in the simulations. Also, the positions of the maxima in the midlatitudes are offset about  $10^\circ$  poleward of the observations. It is possible that some of this discrepancy may actually be a result of biases in the observations themselves. For example, the position of the storm track may be in error simply due to a combination of low biases at higher latitudes and high biases in the subtropics. Note that the differences are within the estimated errors of the retrievals (see Figure 3.7b). Comparing the results from the ECHAM model is difficult in the tropics since the cloud water is primarily ice. However, the cloud liquid water values in the midlatitudes are far too large and are sometimes a factor of 2 greater than the observations.

When the zonal average data are separated into their respective JJA and DJF seasonal components (Figure 4.15), larger differences are revealed between the CSU GCM and the observations at certain locations. For instance, during JJA in the northern midlatitudes the CSU GCM shows small liquid water amounts of about  $0.05 \text{ kg m}^{-2}$ , while the

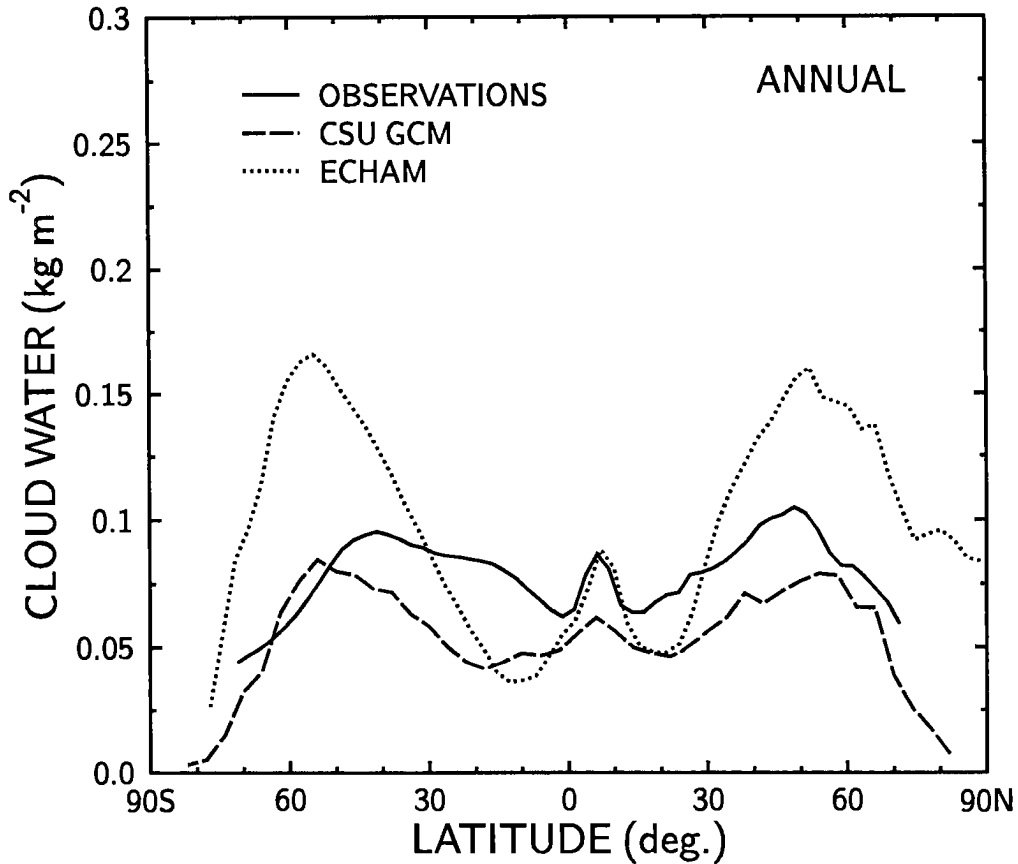


Figure 4.14: Zonal means of the global distributions of cloud liquid water shown in Figure 4.13.

observations indicate  $0.1 \text{ kg m}^{-2}$  or more. The high liquid water values in this region were shown to be associated with increased stratiform cloudiness (see Figure 4.5). As stated previously, the exclusion of boundary layer cloud liquid water in the CSU GCM is likely responsible for most of the disagreement. The ECHAM model results, on the other hand, which are only July and January means, show similar behavior to that seen previously in Figure 4.13.

An additional test of the model-simulated cloud liquid water is to determine how the relationship between cloud liquid water and SST compares to observations. Figure 4.16 shows a scatter diagram of the annual mean cloud liquid water derived from the CSU GCM versus SST. The observations, which include clear and cloudy pixels, were averaged in 3 K SST bins, where the filled squares are the midpoints of the intervals and the average liquid water in a given interval. The gray shading is to symbolize the variability of the

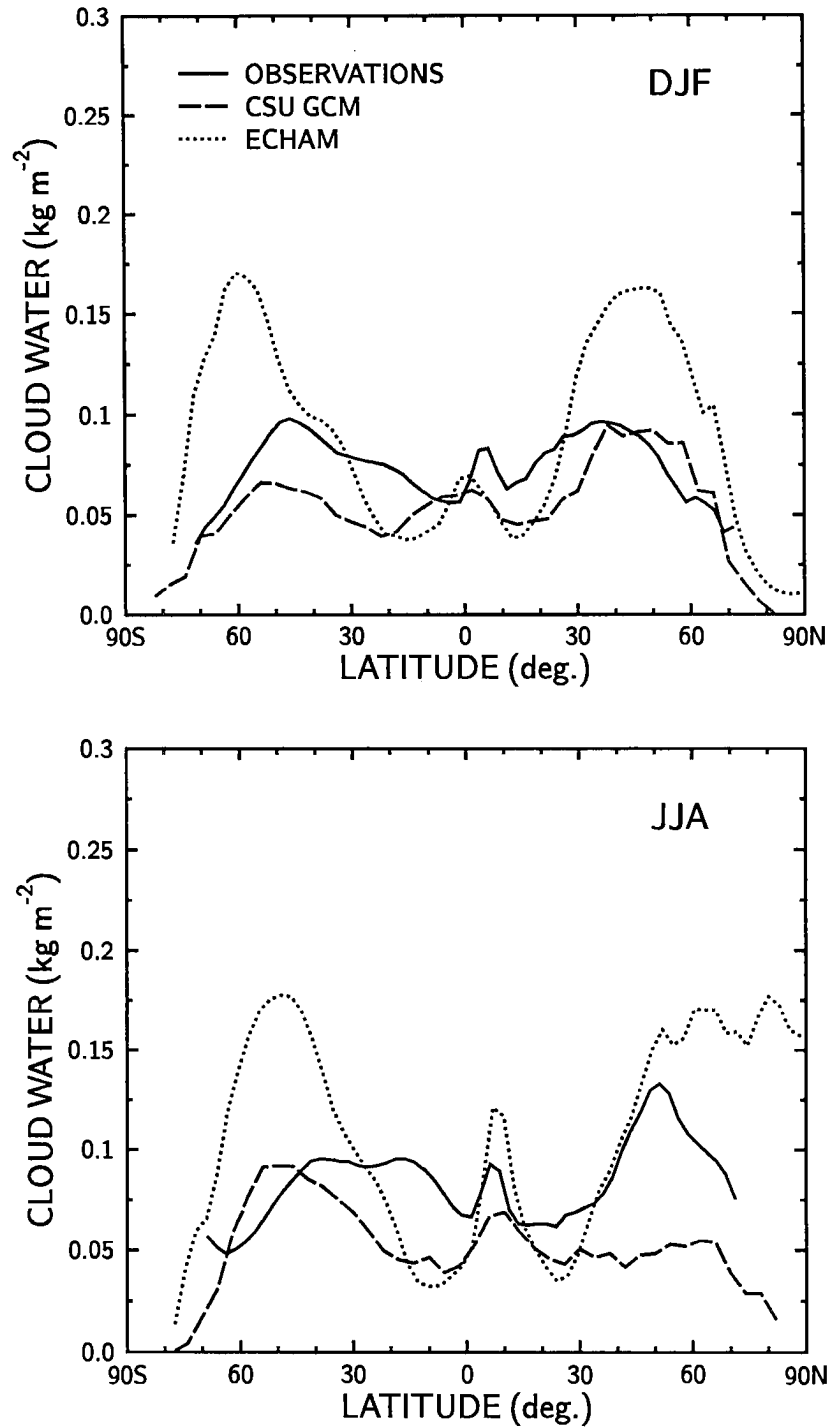


Figure 4.15: Seasonal zonal means of the cloud liquid water observations and model simulations for (a) DJF and (b) JJA (Note: ECHAM results are only January and July averages, respectively).

observed liquid water within the bin and is one standard deviation above and below the points. The principal difference between the model simulations and the observations is the location of the maximum, which is a marker of the midlatitude storm tracks. The observations show it to occur at about  $14^{\circ}$  C, while for the model it is at far lower SSTs of between  $2^{\circ}$  and  $10^{\circ}$  C. These results demonstrate that small differences in the latitudinal position of the storm tracks can lead to large differences in the cloud liquid water-SST relationship, which is a result of the high SST gradients in the midlatitudes.

The next comparison involves the CSU GCM and how well it reproduces the observed cloud liquid water-temperature sensitivities from the previous section. There are several drawbacks in attempting to directly compare the temperature sensitivities computed from the model simulations to the observations. First, unlike the observations, which were daily

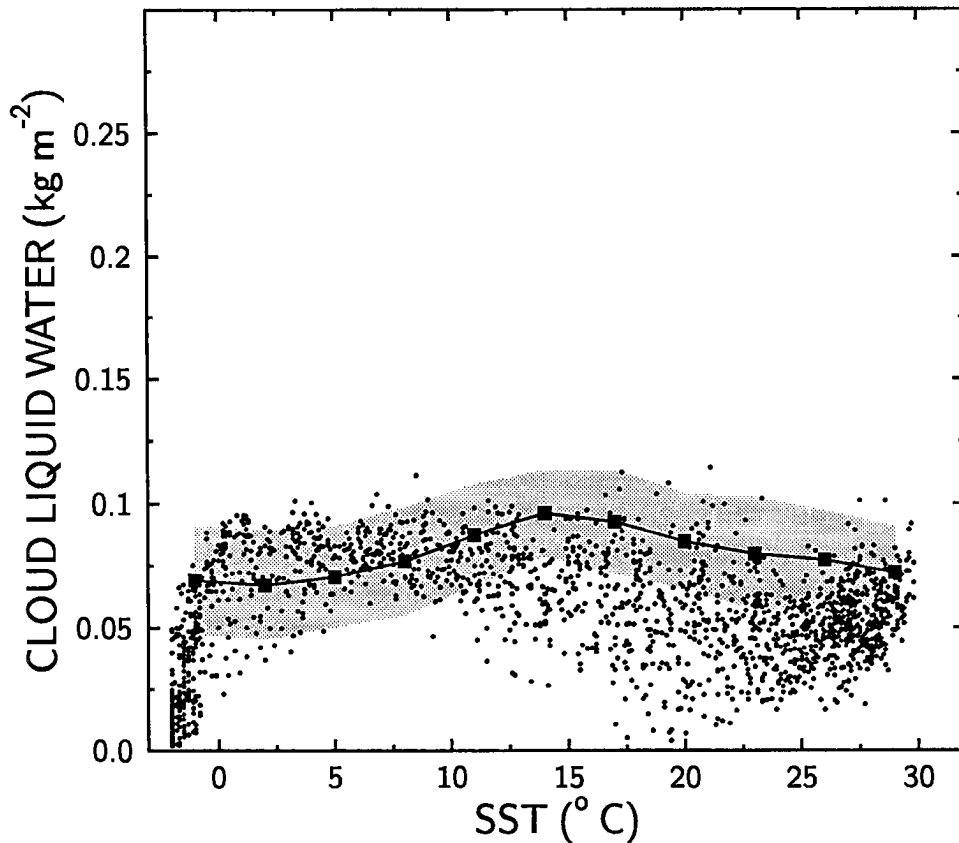


Figure 4.16: Scatter diagram of annual mean cloud liquid water ( $\text{kg m}^{-2}$ ) versus SST (K) for the CSU GCM. The observations are represented as the average liquid water within a 3 K SST bin, where the SST is the midpoint of the bin (filled squares). The gray shading shows the standard deviation of the observed liquid water within a given bin.

averaged quantities, only monthly mean cloud liquid water and temperature data from the GCM were available. Second, the simulations include cloudy and clear situations in the average. Also, the GCM gridboxes are much larger than the  $2.5^\circ$  gridboxes used in the observational analyses. These differences must be kept in mind when comparing the two different sets of data.

The results of the temperature sensitivity analysis are presented in Figure 4.17. The CSU GCM results are for clouds below the 700 mb level. The temperature and liquid water mixing ratio were given at three different levels: 700, 850, and 1000 mb. The integrated cloud liquid water was determined by taking the average liquid water content at, for example, 700 and 850 mb and then multiplying this quantity by the layer depth of 150 mb. Similar calculations were done for the layer between 850 and 1000 mb. The cloud liquid water for these two layers was subsequently added together to arrive at the total amount. The mean temperature of the layer was determined by taking the average of the temperatures at the three levels.

Over the ocean, in Figure 4.17a, the model gives sensitivities as a function of temperature that are surprisingly comparable to the observations. Sensitivities are about  $-0.07$  to  $-0.05 \text{ deg}^{-1}$  for the warmest temperatures and gradually become positive as the temperature decreases. However, at the coldest temperatures the sensitivities are much greater than the observations and are similar to the relationship that is expected for adiabatic clouds. The difference in the temperature which separates the negative and positive sensitivities between the model and the observations is about  $8^\circ\text{C}$ . This is likely a result of the differences in the position of the storm tracks, as discussed earlier. The analysis for the model over land in Figure 4.17b shows similar behavior as seen over the ocean except that the sensitivities are much lower ( $-0.1 \text{ deg}^{-1}$ ) at the warmest temperatures and increase at a smaller rate as a function of temperature. When compared to the satellite observations of Tselioudis et al. (1992), the model results are quantitatively very close except at the coldest temperatures.

Another evaluation of the CSU GCM simulations of cloud liquid water is in terms of their seasonal variability. Figure 4.18 shows the latitudinally averaged intra-annual

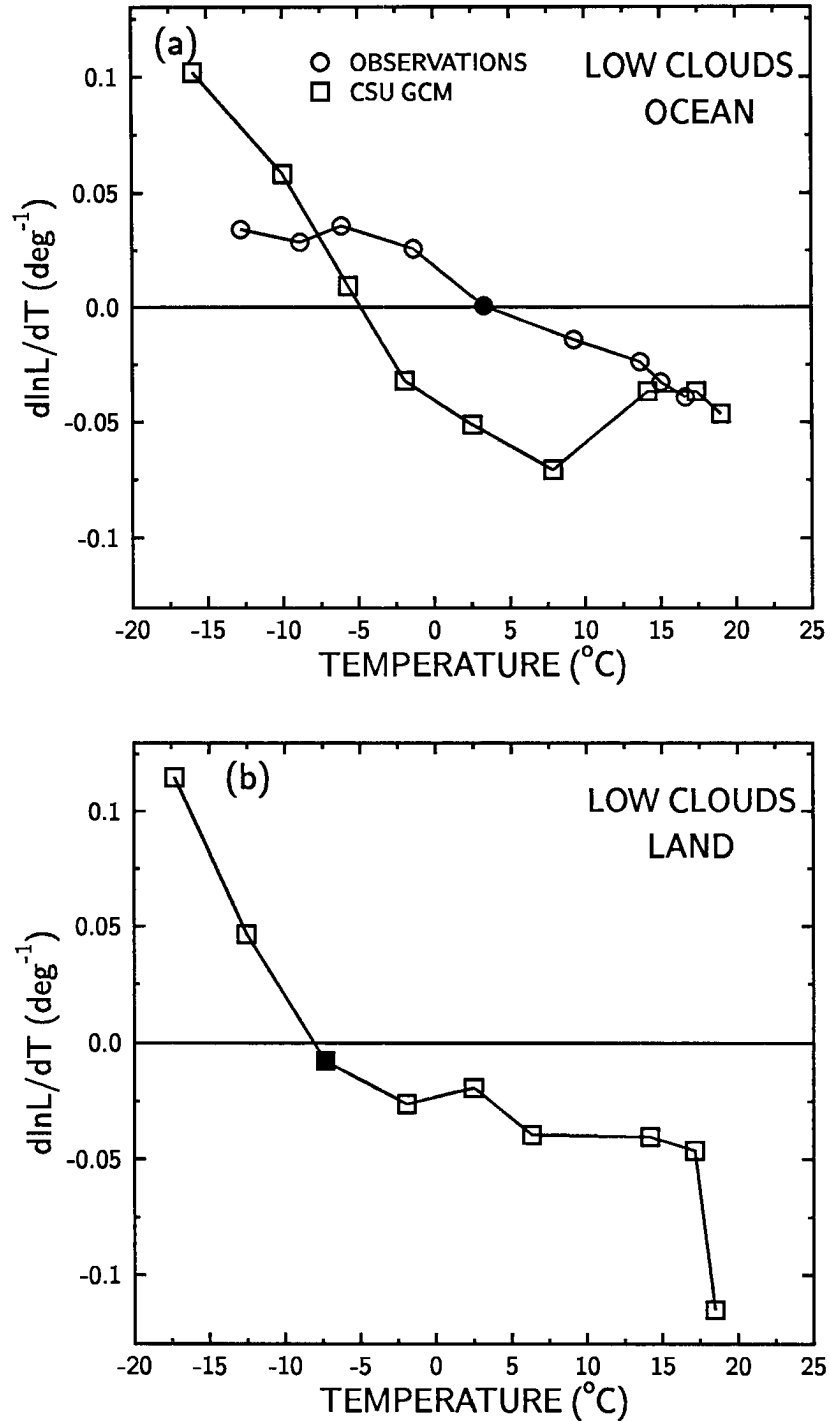


Figure 4.17: Scatter diagram of  $d\ln L/dT$  (deg<sup>-1</sup>) versus the layer temperature for low clouds (700 mb–1000 mb) for the CSU GCM over the (a) ocean and (b) land. The analysis method is the same as that described in section 4.3.1. Also shown for comparison is the relationship deduced from observations. Filled symbols are correlations that are not significant beyond the 99% confidence limit.

standard deviation for the observations and the model over the oceans. Both show a trend of increasing seasonal variability as one moves from the south pole towards the north pole. However, the model exhibits substantially greater seasonal variation than the observations, being larger by about 50%. This higher variability may be a result of the fact that a single year was used in analysis, while the observations are the mean intra-annual variation over a nearly five-year period. To provide a more consistent comparison, the intra-annual standard deviation for the year of 1990 is also shown in Figure 4.18. The seasonal variability for 1990 is similar to the longer term mean and confirms that the CSU GCM seasonal variation in cloud liquid water is too high.

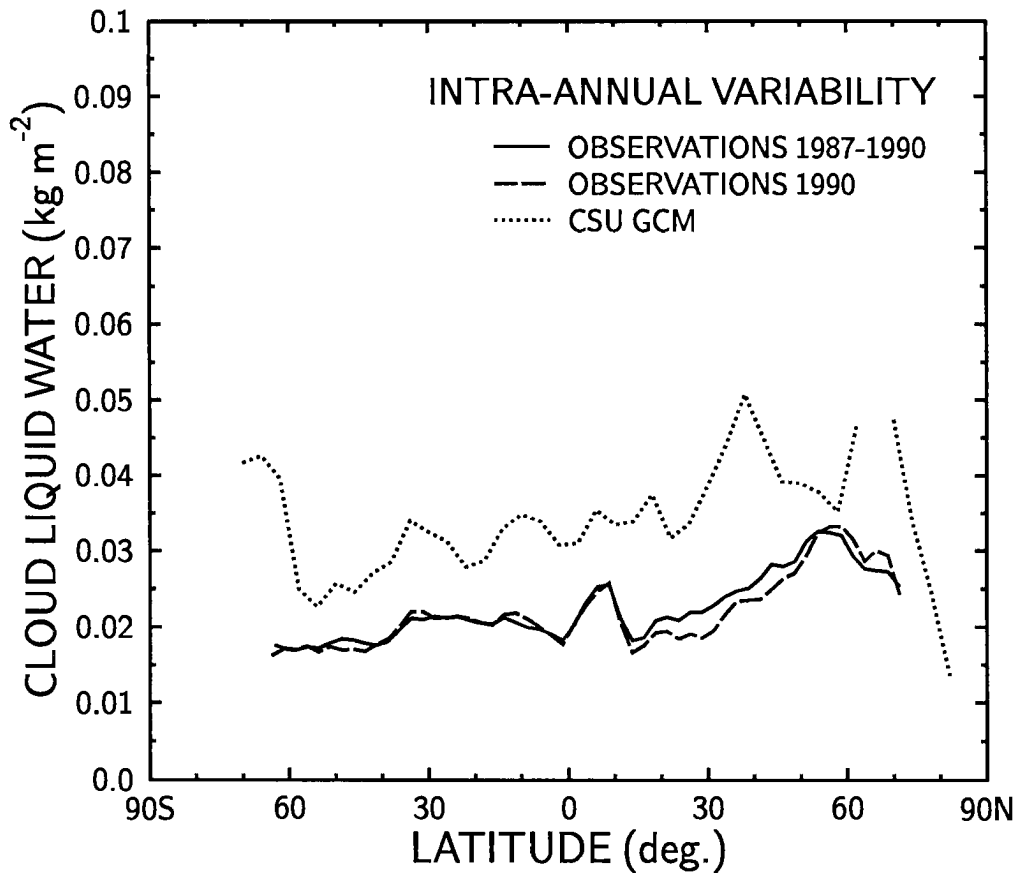


Figure 4.18: Zonal averages of the intra-annual standard deviation for the CSU GCM (dotted curve) and observations from 1987–1991 (solid curve) and for the year 1990 (dashed).

## Chapter 5

### OBSERVED RELATIONSHIPS BETWEEN CLOUD LIQUID WATER AND THE EARTH'S RADIATION BUDGET

Although understood from an ideal theoretical perspective, the actual nature of the large-scale interactions between cloud liquid water and the Earth's radiation budget is largely unknown. Determining the association between these variables is likely to contribute significantly to studies of the global climate and possibly climate change. In the first part of this chapter we attempt to characterize the gross climatic relationships between cloud liquid water and the radiation budget using monthly mean data sets. The emphasis is on the seasonal aspects of these relationships, and several specific regions were chosen for more detailed analyses. In the final section we explore the connection between cloud albedo and cloud liquid water in more detail using nearly coincident observations in areas dominated by summertime stratus in the northern midlatitudes. Comparisons are also made to plane-parallel theory and several ideas are proposed to explain the apparent discrepancies between observations and theory.

#### 5.1 Radiation Budget Data

The Earth radiation budget data used in the following analyses are derived from the Earth Radiation Budget Experiment (ERBE), a NASA project begun in the mid-1980s to provide continuous, long-term monitoring of the global radiation budget from a system of multiple satellites (for an overview of the ERBE see Barkstrom, 1984 and Barkstrom and Smith, 1986). The ERBE mission consists of three satellites: the NOAA-9 and NOAA-10, which are sun-synchronous weather satellites, and the low inclination ( $57^\circ$ ) Earth Radiation Budget Satellite (ERBS), each of which carry scanner and nonscanner instrument packages. Data that are of interest to this study are those that overlap the

cloud liquid water data set (July 1987–December 1991), which include measurements from the NOAA-10 satellite and the ERBS. The comparison is restricted to ERBS measurements since they provide the longest period of overlap, a 31-month period from July 1987 to February 1990.

High spatial resolution (or narrow FOV) measurements of the radiation budget, which are used in this study, are made by the ERBE scanning instrument. This instrument has three channels that measure broadband radiances over different spectral regions, consisting of the total spectrum (0.2–200  $\mu\text{m}$ ), the longwave (5–50  $\mu\text{m}$ ) and the shortwave (0.2–5  $\mu\text{m}$ ). A more detailed account of the spectral response of these channels is described by Smith et al. (1986). The redundant total channel is useful as an additional consistency check for the other channels and can help in improving the correction for the nonflat spectral response of the sensor (Kidder and Vonder Haar, 1994).

Each channel of the scanner undergoes a series of tests for absolute calibration. The internal calibration consists of two reference blackbody sources which are used for the longwave (LW) and total channels. Solar calibration of shortwave (SW) channel is done using an illuminated integrating sphere. Additional tests include a look at cold space for all channels and a solar view for the SW and total channels (Kopia, 1986).

The instrument, in its normal mode of operation, scans across (i.e., perpendicular to) the track of the satellite from horizon to horizon. The instantaneous FOV of the scanner is  $4.5^\circ$  along the track and  $3^\circ$  in the cross-track direction. For the ERBS, with an average altitude of 610 km, this translates to footprint dimensions at nadir of  $32 \times 48$  km. The scanner instrument on the ERBS provided measurements from November 1984 until its failure at the end of February 1990. A more complete description of the scanner instrument, including its operation and calibration, is discussed by Kopia (1986).

Conversion of the satellite observed radiances to hemispheric fluxes involves an inversion process. A summary of these inversion methods is given by Smith et al. (1986). Since the ERBE scanner measurements for a given scene consist of a single radiance measurement, additional information must be supplied regarding the complete angular distribution of the radiation in order to estimate the hemispheric fluxes. This angular information is

often referred to as a bidirectional reflection function (BDRF) or angular directional model (ADM). This function describes the amount of anisotropy of the reflected and/or scattered radiation. It is usually grouped into azimuthal and zenith angle bins and depends on the type of scene that is being viewed (surface type, degree of cloudiness, etc.) and the solar zenith angle (for SW radiation). The estimation of longwave hemispheric fluxes, unlike the SW fluxes, is far less complicated since the LW BDRFs are independent of azimuth and solar zenith angle, and generally need only account for such effects as limb darkening.

The BDRFs used in the processing of ERBE fluxes were obtained from scanner measurements on the Nimbus-7 satellite (Taylor and Stowe, 1984). The Nimbus-7 scanner had the unique ability to scan in five different patterns, which allowed a scene to be viewed at a number of different zenith and azimuth angles (Jacobowitz et al., 1984). Since investigators in past studies of the ERB were often forced to assume an idealized radiation field (such as isotropy and a Lambertian surface), these measurements were invaluable in providing a description of the anisotropic characteristics of the upwelling radiation.

An important step in determining the SW and LW fluxes is proper identification of the scene. A scene is made up of the surface and the cloud conditions. ERBE surface types are determined over a  $2.5^\circ \times 2.5^\circ$  geographic region and consist of five categories: ocean (> 67% water), land (> 67% land), snow/ice, desert, and mixed ocean-land or coastal (33-67% water). The ocean, land, and coastal surface categories are further divided into three cloudiness types: clear (0-5%), partly cloudy (5-50%), and mostly cloudy (50-95%). Other scene types consist of clear snow/ice, clear desert, and overcast (95-100%). This gives a total of twelve different scene types. The most probable cloudiness type is estimated for each scanner measurement from bispectral radiance plots using a maximum likelihood estimator (MLE) technique, which depends on the solar zenith angle, the viewing angle, surface type, and season (Wielicki and Green, 1989). Each scene type is assigned a different BDRF. Thus, misidentifying a scene will result in applying an incorrect BDRF, which may lead to errors in the flux retrieval.

Once the instantaneous fluxes and shortwave albedos have been computed, the diurnal variation of albedo (for time averaging purposes) is determined using albedo directional

models that account for the variation of albedo with solar zenith angle. A description of these models is given by Brooks et al. (1986). There are only nine basic scene types for the directional models. The three coastal scene types are based on an areally weighted average of the land and ocean models. Figure 5.1 shows the ERBE albedo directional models for an ocean surface for the four cloudiness classes, where albedo is a function of the cosine of the solar zenith angle (Brooks et al., 1986).

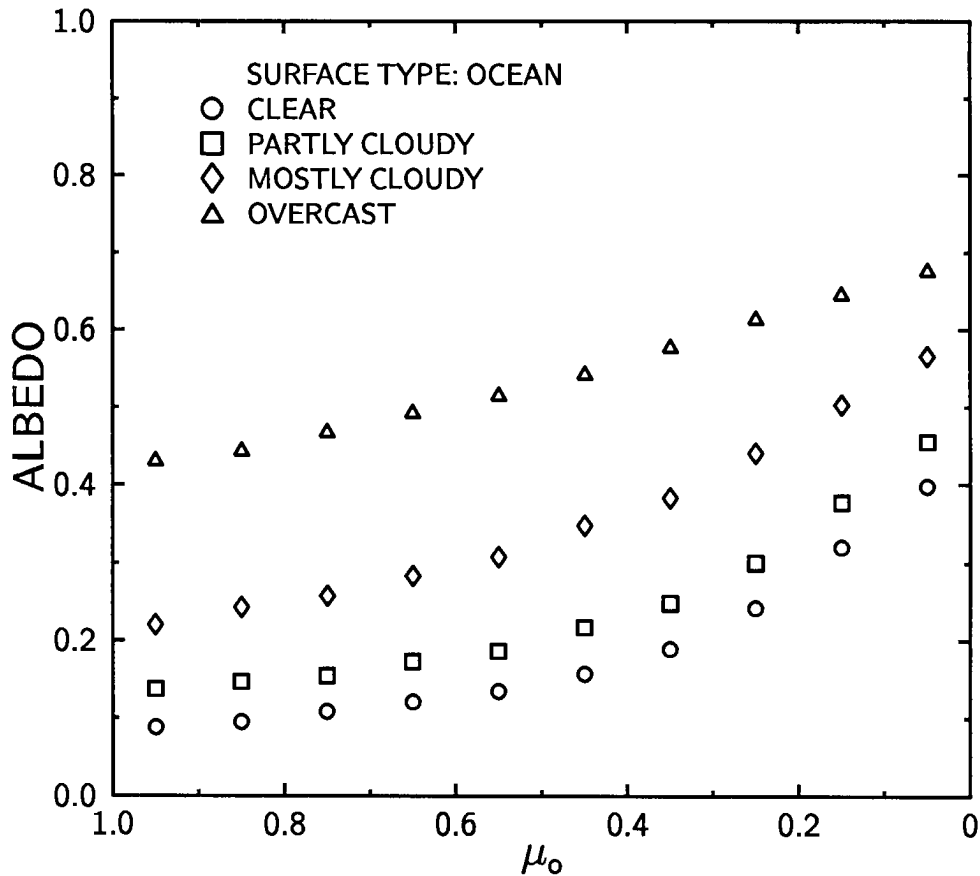


Figure 5.1: ERBE albedo directional models for different cloudiness types over an ocean surface, which are expressed as the albedo versus the cosine of the solar zenith angle  $\mu_0$ .

The uncertainties in the processed ERBE fluxes are a subject of ongoing research. Wielicki and Green (1989) used simulations to show that the MLE method for identifying scenes gave SW flux errors of  $5.6 \text{ W m}^{-2}$  and LW errors of less than  $1 \text{ W m}^{-2}$ . They also concluded that uncertainties in specifying the anisotropy of the radiation field are most likely the largest contributor to the rms error in the instantaneous flux retrievals. While

scene misclassification can also contribute additional error to the retrievals, it is generally of secondary importance.

Preliminary assessments of the flux uncertainties have been shown on a regional basis to be about  $5 \text{ W m}^{-2}$  for the SW fluxes and  $3 \text{ W m}^{-2}$  for the LW fluxes. The clear sky fluxes in contrast are found to have systematic high biases of about  $4 \text{ W m}^{-2}$  for the LW and  $1 \text{ W m}^{-2}$  for the SW on a monthly mean regional scale (Harrison et al., 1990). Barkstrom et al. (1989) estimate the errors in instantaneous fluxes averaged over a  $2.5^\circ$  gridbox as  $5 \text{ W m}^{-2}$  for the LW and  $15 \text{ W m}^{-2}$  for the SW. Apart from errors resulting from BDRFs and scene misclassification, there is also the possibility of systematic biases in the radiances themselves. However, this is unlikely since the measurements are highly calibrated (in an absolute sense). The errors in the radiances have been estimated at 1% for the LW and 2–3% for the SW.

The comparisons shown in the next section require an estimation of the cloud albedo from the satellite albedo measurements. Here, the cloud albedo is determined using the method of Stephens and Greenwald (1991). It is based on multiple scattering theory for a two-layer atmospheric-surface system. By considering only quadratic or lower terms in the cloud albedo (i.e. eliminating higher order reflections) and assuming that the cloud absorption,  $a$ , is directly proportional to the cloud albedo, a quadratic equation of the following form was found:

$$\alpha_{cld}^2 A + \alpha_{cld} B + C = 0 \quad (5.1)$$

where

$$A = \alpha_{clr}(c + 1)^2 - 2\alpha_{clr}^2(c + 1)$$

$$B = (\alpha_{clr} - 1)^2 - 2c\alpha_{clr}$$

$$C = \alpha_{clr} - \alpha_{obs}$$

and  $\alpha_{clr}$  is the clear sky albedo,  $\alpha_{cld}$  is the cloud albedo,  $\alpha_{obs}$  is the albedo observed by the satellite, and  $c$  is the constant of proportionality between the cloud absorption and the cloud albedo. Stephens and Greenwald (1991) found that the estimated cloud albedo is not very sensitive to the expected range of values of  $c$ . A typical value for  $c$  is 0.1, which

is used in this study. There are naturally two possible solutions to (5.1) and the solution of physical significance is

$$\alpha_{cld} = \frac{-B + \sqrt{B^2 - 4AC}}{2A} \quad (5.2)$$

For the monthly mean analyses, monthly mean observations of albedo and clear sky albedo are used to derive the cloud albedo.

One goal of the comparison is to isolate how gross changes in cloud albedo are related to gross changes in cloud liquid water. This relationship, however, can be obscured by the strong solar geometry dependence of the albedo. One way to eliminate this effect is to use albedo directional models (such as in Figure 5.1) to adjust the clear sky and total sky albedo measurements to a common solar zenith angle. While this was not possible with previous ERB data sets, ERBE provides a sufficient array of statistics to allow this type of normalization.

The ERBE S-9 data products, which are data averaged over a  $2.5^\circ$  gridbox and collected into hourly bins, are used in the albedo normalization procedure. For each observation gridbox, a vector of data is given regarding the mean albedo and fraction of pixels for each of the four cloudiness conditions (i.e. clear, partly cloudy, mostly cloudy, and overcast). The normalized albedo for a given gridbox over the ocean is determined by adjusting the albedo measurements to that which would be observed for a near-overhead sun for each cloudiness condition. The reference solar zenith angle is the first  $\mu_o$  bin of the albedo directional model, which is centered at 0.95, and corresponds to a solar zenith angle of about  $18^\circ$ . The adjusted albedos are then averaged to yield a gridbox mean. Figure 5.2 shows an example of the normalized albedo for total sky and clear sky compared to their unadjusted counterparts on a zonal average basis for August 1987. The albedos at higher latitudes undergo a greater adjustment since they have larger solar zenith angles than at lower latitudes. The clear sky albedos required the greatest relative adjustment and are about 0.075–0.085 for a nearly overhead sun.

To be consistent with the cloud liquid water data sets, we also use only cloudy ERB pixels in the seasonal, monthly mean analysis. The ERBE S-9 data products provide the necessary information to easily compute the albedo for cloudy pixels. Unfortunately, the

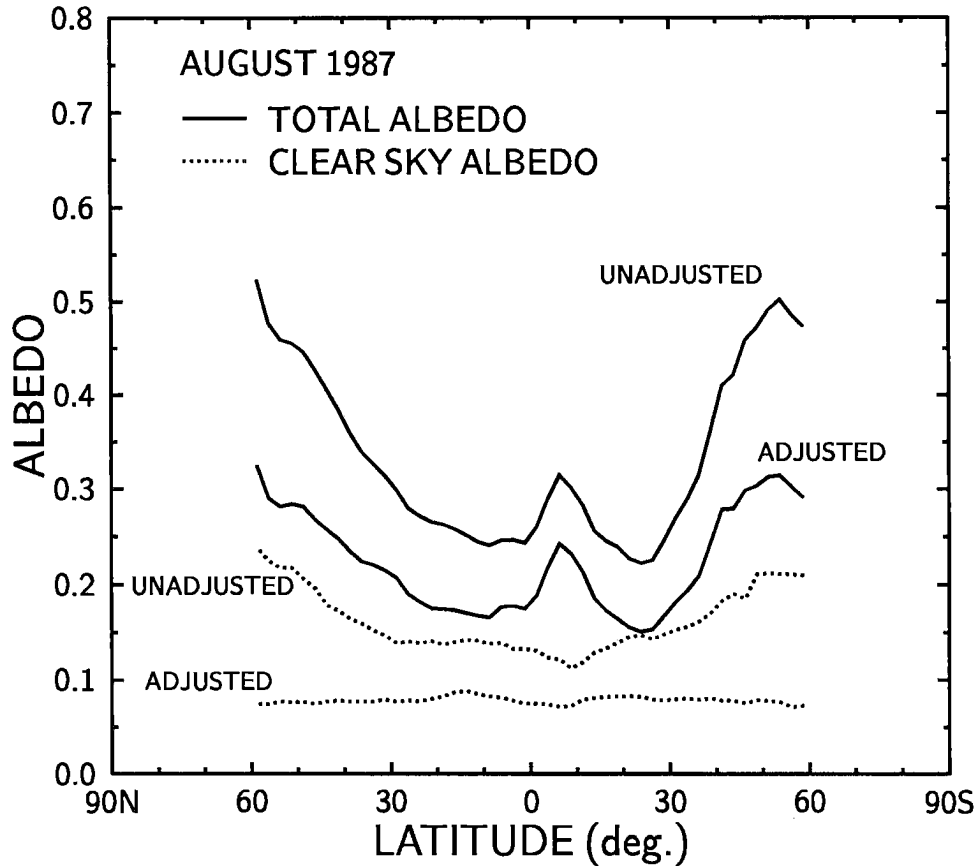


Figure 5.2: Zonal averages of the total (solid) and clear sky (dotted) albedo for August 1987 (unadjusted) from ERBS. Also shown is the albedo normalized to a solar zenith angle of  $18^\circ$  or  $\mu_0 = 0.95$  (adjusted) using the directional models in Fig. 5.1.

LW measurements are accompanied by insufficient information to determine the LW fluxes for cloudy pixels. Thus, the monthly mean cloudy LW fluxes were estimated by excluding data where the cloud amount within the gridbox was less than 20% (cloud amount is a by-product of the ERBE analyses). On occasion the cloud liquid water data sets were missing data for an entire day or for several days over the course of a month, due to either instrument malfunction, low data quality, or problems at the receiving station. For these cases, the same days that were missing data in the liquid water data sets were also excluded from the monthly average of the ERB observations.

One difficulty with correlating monthly mean ERBE albedo data and SSM/I cloud liquid water data is the lack of simultaneity of the two sets of measurements. The DMSP satellite is sun-synchronous and samples only in the early morning and late afternoon.

The ERBS, on the other hand, due to its  $57^\circ$  inclination orbit, precesses through many different local times over a month and thus provides superior diurnal sampling.

A few words need to be said concerning the data processing in this part of the research. The original ERBE S-9 data products were stored on large optical platters. Since this is an inconvenient storage medium to work with, the data were transferred to EX-ABYTE tapes, which involved about 3 GB of data over the 31-month period. These data were subsequently processed from the tapes to produce the normalized albedos and other quantities.

## 5.2 Seasonal Aspects of the Relationships

Figure 5.3 shows the global distribution of the annual mean normalized cloud albedo and its intra-annual standard deviation over the 31-month period. In Figure 5.3a the mean albedo exhibits many features observed in previous studies. Although the albedos have been adjusted to a common solar zenith angle, the brightest clouds (greater than 0.22) still occur primarily in the mid-latitudes. This is mainly a result of increased cloudiness but may also be due in part to greater cloud optical depths as suggested from ISCCP analyses (e.g., Tselioudis et al., 1992).

A qualitative comparison of the annual mean albedo distribution to the mean cloud liquid water in Figure 4.1 reveals many similarities but also some differences (the 31-month average cloud liquid water distribution is nearly identical to Figure 4.1). For example, in areas of tropical convection and in many areas of the subtropics the two fields coincide very well. In certain regions of the subtropics, however, there are noticeable differences. For instance, the cloud albedo maximum located west of Mexico and the U.S. is nearer to the coast than the same feature in the liquid water field. In addition, the liquid water values appear to be somewhat too high in a few areas in the subtropics that are dominated by low-level clouds, such as in certain regions of the southern Pacific and Atlantic, where we might expect a reasonable correspondence between the cloud albedo and cloud liquid water. These differences might be caused by either spatial and/or temporal sampling deficiencies or possible biases in the cloud liquid water measurements. In some areas at

higher latitudes there are further discrepancies, which are likely attributed to the effects of ice clouds.

Figure 5.3b shows the intra-annual deviations in cloud albedo, which are independent of seasonal changes in solar insolation. As expected, very large seasonal variability of greater than 0.065 occurs in the Asian and Australian monsoon regions, along the ITCZ in the eastern Pacific and Atlantic, and in the northern midlatitude storm track regions. Low variabilities of less than 0.035 are generally seen in regions of subtropical high pressure systems and throughout the southern midlatitudes. Areas of maximum variation are also evident in specific areas dominated by stratocumulus; for example, along the western South American coast and west of southern Africa.

To explore how the seasonal variations in cloud albedo relate to the seasonal variations in cloud liquid water, correlations were computed at each gridbox based on the following expression:

$$R = \frac{1}{30\sigma_{intra,L}\sigma_{intra,\alpha}} \sum_{i=1}^{31} (L_i - \bar{L})(\alpha_i - \bar{\alpha}) \quad (5.3)$$

where  $\bar{L}$  and  $\bar{\alpha}$  are the mean cloud liquid water and cloud albedo, respectively, averaged over all 31 months and  $\sigma_{intra,L}$  and  $\sigma_{intra,\alpha}$  are the cloud liquid water and cloud albedo intra-annual standard deviations computed from (4.2). The statistical significance of the correlations could be estimated based on a lag correlation analysis described by Weare (1993). Unfortunately, the present data sets do not contain a sufficient number of years to make this type of analysis meaningful. One must also bear in mind that these correlations ignore the effects of ice water path on the cloud albedo so that poor correlations in certain regions may reflect the impact of ice clouds.

As observed in Figure 5.4a, broad regions of correlations of 0.7 or more occur where the seasonal variability is generally the highest. This is seen over most of the tropics, parts of the subtropics, and in the northern midlatitude storm tracks. The largest correlations of 0.9 or higher are limited exclusively to the tropics, which include the monsoon regions, the ITCZ, and the stratocumulus region west of southern Africa. Thick ice clouds that form at the tops of tropical convective systems are the primary regulators of the radiation budget at the top of the atmosphere in many regions of the tropics. Therefore, the observed

high correlations are not the result of seasonal changes in cloud liquid water directly causing changes in cloud albedo. Rather the connection is indirect; that is, these regions are also associated with large seasonal variations in precipitation which are reflected as large fluctuations in cloud liquid water. However, changes in albedo for the clouds west of southern Africa are more directly a result of changes in cloud liquid water since ISCCP climatic data suggest that ice clouds are less prevalent in this region.

The same type of correlation analysis was also done for cloud liquid water and total cloudiness data from ISCCP, and the results are presented in Figure 5.4b. Some of the same regions of high correlations that were seen in Figure 5.4a are also observed in Figure 5.4b, although the magnitudes are somewhat reduced. These areas include the monsoon regions, along the northern midlatitude storm tracks, and the stratocumulus cloud systems west of Africa just south of the equator. Other characteristics of the correlations that are of interest are the extremely low (and sometimes negative) correlations throughout the southern midlatitudes. The objective of these results is to simply show that the highest correlations between seasonal variations in cloud albedo and cloud liquid water in many regions are largely caused by the seasonal changes in the cloudiness within the  $2.5^\circ$  gridboxes.

The lowest correlations in Figure 5.4a are typically associated with regions of lower seasonal variability, such as west of North America, in the southeastern Pacific, in parts of the southern Atlantic and in the southern midlatitudes. Although the correlations are small, both cloud liquid water and cloud albedo exhibit low variability in these areas. In most of these same regions, particularly in the southern midlatitudes, the intra-annual standard deviations of total cloudiness also display very little seasonal variability.

The zonal mean characteristics of the intra-annual standard deviations of cloud albedo and cloud liquid water are presented in Figure 5.5. Also included is the variability of the flux difference quantity  $C_{LW}$ , which is defined as  $C_{LW} = F_{clr} - F_{tot}$ , and often referred to as LW cloud forcing, where  $F_{clr}$  is the clear sky LW flux and  $F_{tot}$  is the total LW flux. The latitudinal behavior of both cloud albedo and cloud liquid water variability follow one another surprisingly well. The highest seasonal variation occurs in the tropics at approximately  $10^\circ\text{N}$ . As mentioned previously, the good correspondence in the tropics

is mainly due to indirect effects. Reasonable agreement also exists at higher latitudes in both hemispheres. For example, both variables indicate a maximum near  $30^{\circ}\text{S}$ , which is caused by the SPCZ and the high variability over the southern Atlantic near Brazil. In the north, a maximum at about  $35^{\circ}\text{--}40^{\circ}\text{N}$ , which is a marker of midlatitude storminess, is observed for both variables. The LW cloud effect shows basically the same behavior but has far greater variation in the tropics since the clouds in this region experience the largest seasonal changes in height. Another distinguishing feature, which is common to all three variables, is the steady increase from the southern latitudes to the northern latitudes. Greater influences from land may be the primary cause of this behavior.

The next part of the comparison involves an examination of the mean characteristics of cloud liquid water and the separate components of the radiation budget in specific

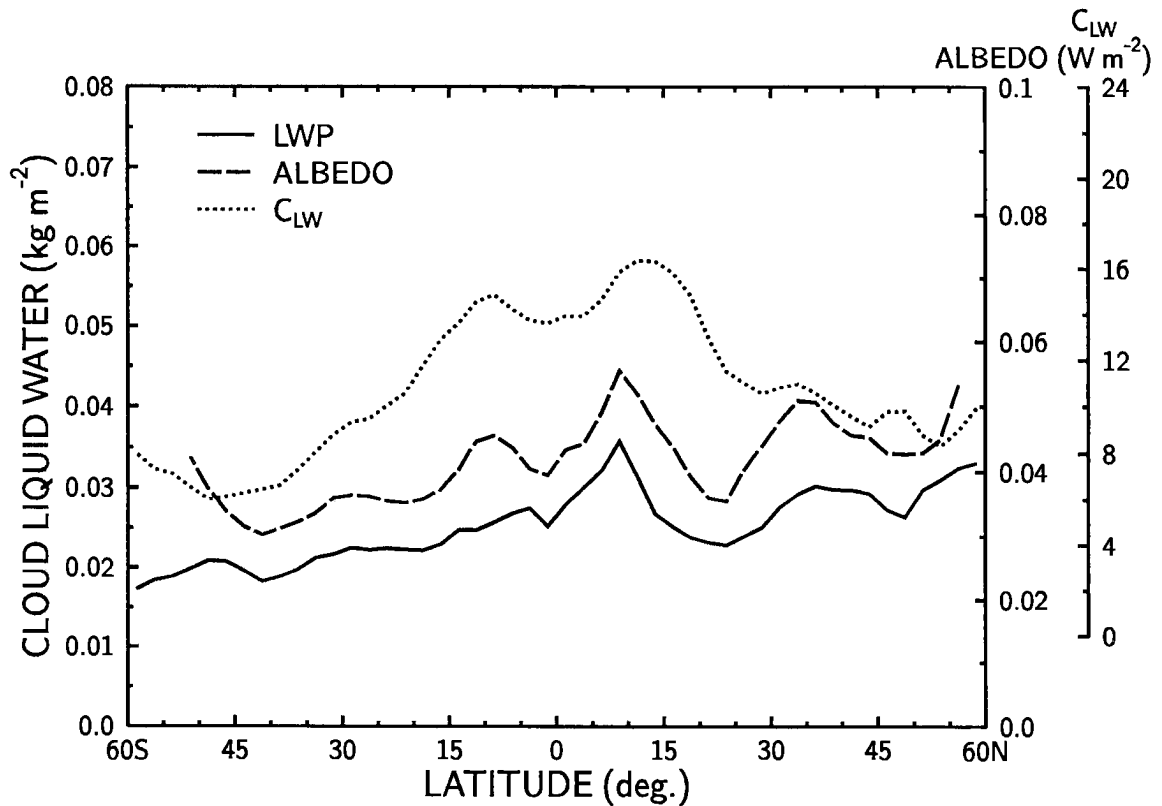


Figure 5.5: Zonal mean characteristics of the intra-annual standard deviations of cloud liquid water path (LWP) (solid curve), cloud albedo (dashed curve) and  $C_{LW}$  (dotted curve) over the period from July 1987 to February 1990.

locations. Six  $10^\circ \times 10^\circ$  regions, labeled A-F in Figure 5.6, were chosen to represent a number of different climate regimes. The region off the coast of China was included because of the extraordinary seasonal changes in cloud liquid water and albedo that occur there. The clouds of the North Pacific and Atlantic are of interest since they have a significant effect on the net radiation budget during the summer. Subtropical stratocumulus clouds, as well, have a large impact on the radiation budget and are represented in Region D near the Peruvian coast. We also focus on the clouds of the SPCZ since this region is not often studied and is poorly understood. A region in the southern Indian Ocean was chosen because it is an area of maximum transient eddy activity. The convectively active portions of the tropics have been excluded since the cloud liquid water retrievals are less accurate in these regions.

The results of the analyses are depicted in Figures 5.7–5.9. Each figure includes the average cloud liquid water, cloud albedo, total cloud amount (obtained from the ISCCP C2 data sets), and  $C_{LW}$  as a function of the month of the year. Each data point consists of a spatial average of the  $2.5^\circ$  gridboxes within a given region, which is then averaged over 2 or 3 years depending on the month. For the East China Sea (Region A), shown in Figure 5.7a, there are enormous seasonal swings in albedo and cloud liquid water, as seen previously in Figures 5.3b and 4.6b, respectively. The largest liquid water paths and albedos occur in the first five months of the year, while a minimum occurs in July. It is highly likely that the magnitude of the liquid water is overestimated during this time period as a result of precipitation since Figure 2.11a indicates a large number of retrievals with  $LWP > 0.5 \text{ kg m}^{-2}$  in this region for January 1990.

Table 5.1 gives the linear correlations between cloud liquid water and the three other variables based on the complete 31-month-long time series. Correlations beyond the 99% confidence level using the F test are also indicated. From this table the average cloud liquid water and cloud albedo for region A are highly correlated, but so are cloud liquid water and cloudiness. Obviously, it cannot be concluded that cloud liquid water is the main factor in controlling the SW radiative budget of the clouds in this region because of the effects of changes in cloudiness. In addition, it is not known the extent of the influence of ice water path on the cloud albedo.

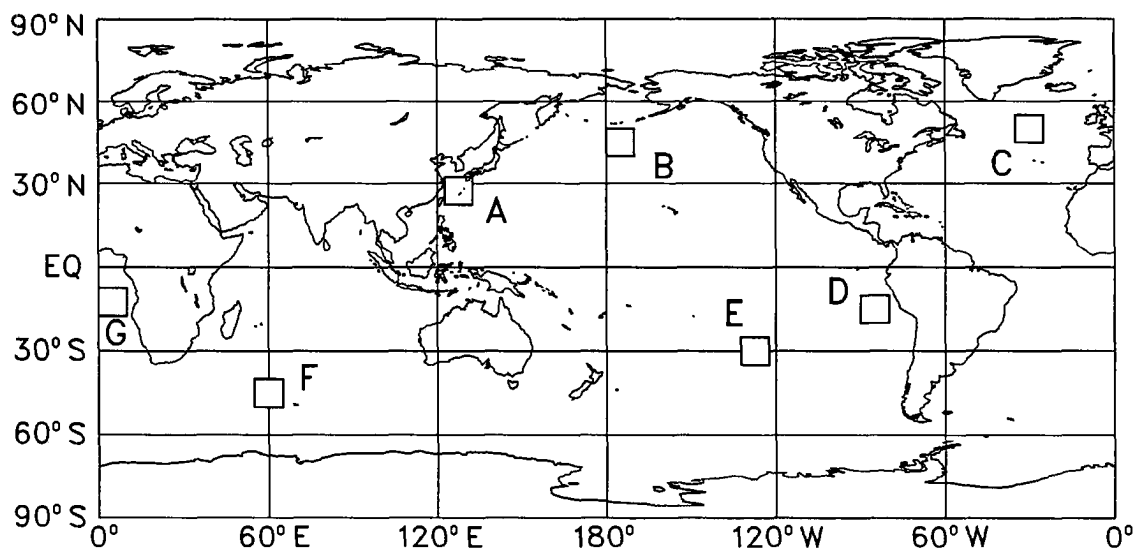


Figure 5.6: Global map depicting the six  $10^\circ \times 10^\circ$  regions (A–F) used in the seasonal analyses of cloud liquid water and the Earth radiation Budget. Also shown is an additional area (Region G) included in the comparison involving the net radiative fluxes.

Region B in the North Pacific (Figure 5.7b) consists of weaker, but statistically significant, correlations between liquid water, cloud albedo, and cloudiness. As in Region A, cloudiness appears to be a major contributor in determining the cloud albedo, although changes in the optical depth of the clouds may also play a role. All three variables reach a peak during the summer months where the total cloudiness averages nearly 100%. With the exception of June,  $C_{LW}$  remains virtually constant throughout the year at roughly  $40 \text{ W m}^{-2}$ , which indicates a dominance of low to middle-level clouds.

The North Atlantic region in Figure 5.8a, in contrast, shows drastically different behavior. The cloudiness remains extremely high year-round between 90 and 95%. A surprising result is that the liquid water and cloud albedo are essentially uncorrelated. Even more curious, the liquid water and cloudiness are negatively correlated. During the summer months when low clouds are most common, the cloud liquid water increases while the albedo decreases. It is difficult to conceive of a situation that would result in this type of relationship. Therefore, the cloud liquid water values in this region may be suspect or possibly the retrievals are overestimated due to precipitation effects (see, e.g., Figure

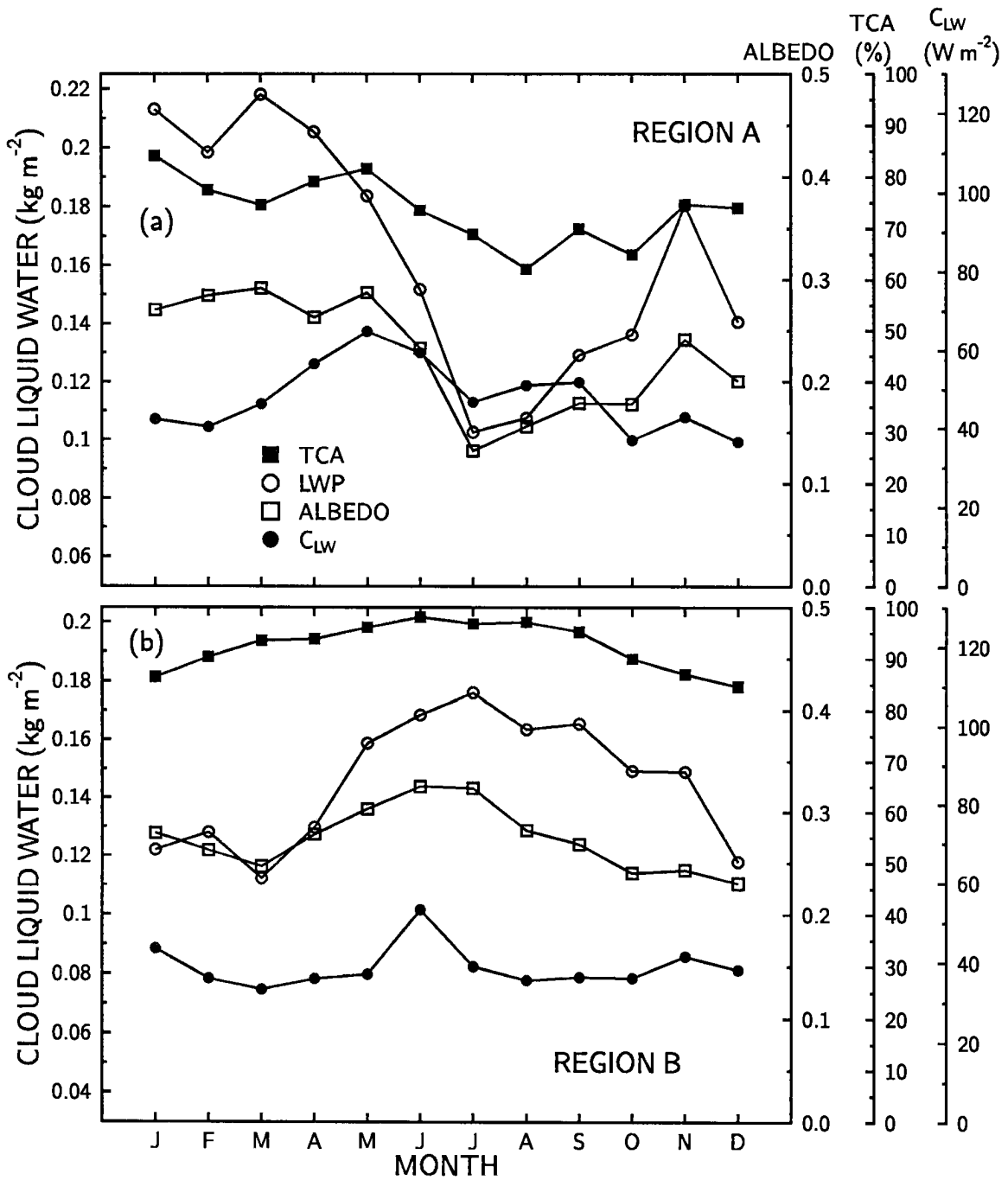


Figure 5.7: Seasonal time series of cloud liquid water path (LWP) (circles), cloud albedo (squares), total cloud amount (filled squares), and  $C_{LW}$  (filled circles) averaged from July 1987 to February 1990 for regions (a) A and (b) B depicted in Figure 5.6. Each point represents a spatial average of the  $2.5^\circ$  gridboxes within the  $10^\circ \times 10^\circ$  region, which are then averaged in time.

2.11b). Lastly, the high cloudiness associated with wintertime storms is seen as large values of  $C_{LW}$ , which can reach as high as  $50 \text{ W m}^{-2}$  during January and December.

Table 5.1: Linear correlations between cloud liquid water ( $L$ ) and cloud albedo ( $\alpha_{cld}$ ), total cloud amount (TCA), and longwave cloud effect ( $C_{LW}$ ) for the six regions defined in Fig. 5.6 from July 1987 to February 1990. Correlations beyond the 99% significance level are denoted by an asterisk.

REGION	$L, \alpha_{cld}$	$L, \text{TCA}$	$L, C_{LW}$
A	0.882*	0.750*	0.167
B	0.559*	0.572*	0.157
C	0.0565	-0.426*	-0.0391
D	0.836*	0.877*	-0.390*
E	0.888*	0.732*	0.802*
F	0.502*	0.480*	0.0742

In the southern hemisphere the region of subtropical stratocumulus off the coast of Peru (Region D) yields a very close agreement and high correlations between cloud liquid water, cloud albedo, and cloudiness as expected (see Figure 5.8b and Table 5.1). These correlations indicate, again, the strong role that cloudiness has in determining the amount of cloud liquid water and hence the cloud albedo over these large areas. The time of maximum cloudiness occurs during the spring (SON) and agrees well with the results of Klein and Hartmann (1993). These clouds remain relatively close to the sea surface all year long as evidenced by the very small values of  $C_{LW}$  of about  $20 \text{ W m}^{-2}$ .

The SPCZ is represented by Region E in Figure 5.9a. This region is unique in that both components of the radiation budget are strongly correlated with cloud liquid water (see Table 5.1). The annual cycle of all four variables consists of a minimum in January, a steady rise until about May, and then little change or a slight decline throughout the rest of the year. The effects of cloudiness can be proposed as the main cause of the high correlations between cloud liquid water and the SW radiative budget, but this is less likely to be entirely the case for the cloud liquid water and the LW component. Instead, the cause of the high correlations between  $C_{LW}$  and cloud liquid water may be related to limited convective activity. That is, convective clouds, which are associated with higher cloud tops and hence larger values of  $C_{LW}$ , usually contain more intense precipitation than

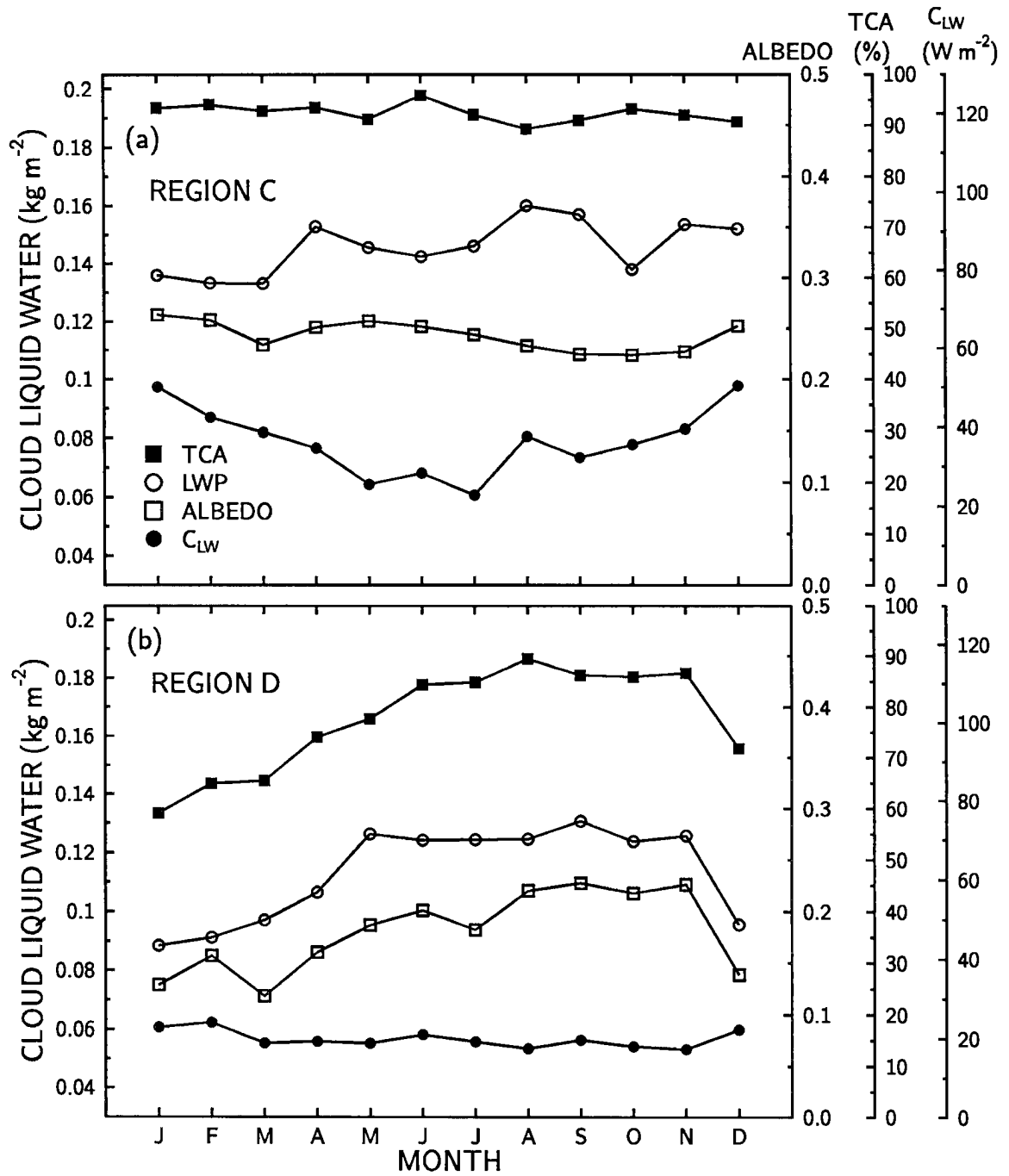


Figure 5.8: Same as Fig. 5.7 except for regions C and D.

stratiform clouds, which in turn is correlated with higher values of cloud liquid water.

The final region of consideration is Region F shown in Figure 5.9b, which is located in the path of southern hemisphere storms in the Indian Ocean. All variables display weak seasonal variability, with the exception of perhaps  $C_{LW}$ , which indicates slightly higher values during the winter. The cloudiness, especially, is nearly constant at about 85%. The weak correlations suggest the probable effects of ice clouds.

The next step is to arrive at a quantitative assessment of the net radiative impact of cloud liquid water. For this analysis we have chosen Region E and the region of subtropical stratus near Angola (Region G in Figure 5.6). The net radiative cloud effect is defined simply as the sum of the SW and LW cloud effects:

$$C_{net} = -F_o\alpha_{cld} + C_{LW} \quad (5.4)$$

where  $F_o$  is the solar flux, which is set to a constant value of  $400 \text{ W m}^{-2}$ , and  $\alpha_{cld}$  is the normalized cloud albedo.

The results of the comparison for Region G are exhibited in Figure 5.10a. Each data point signifies a  $2.5^\circ$  gridbox and monthly mean value. An estimate of the sensitivity of the net radiative cloud effect to a change in cloud liquid water, that is  $dF_{net}/dL$ , is obtained by applying a linear least squares fit to the data. The results of the fit, which are significant beyond the 99% confidence level, are shown in Figure 5.10a. Thus for low-lying subtropical stratus clouds there is about a  $15.4 \text{ W m}^{-2}$  loss in the net cloud effect for every  $0.02 \text{ kg m}^{-2}$  increase in cloud liquid water. This result is similar to the sensitivity of the SW cloud effect alone ( $-15.2 \text{ W m}^{-2}$  per  $0.02 \text{ kg m}^{-2}$ ) since the LW cloud effect is a small contributor to the net radiative flux for these types of clouds.

In contrast, the relationship of the net cloud effect to cloud liquid water for clouds of the SPCZ in Figure 5.10b takes on a much different character. Linear regression fits were done for liquid water values less than  $0.11 \text{ kg m}^{-2}$  and greater than  $0.11 \text{ kg m}^{-2}$ . Both fits are significant beyond the 99% confidence level. As seen in Figure 5.10b, two different sensitivities emerge. For smaller cloud liquid water values, there is a  $10.4 \text{ W m}^{-2}$  decrease in  $C_{net}$  for a  $0.02 \text{ kg m}^{-2}$  increase in cloud liquid water, which is comparable but slightly

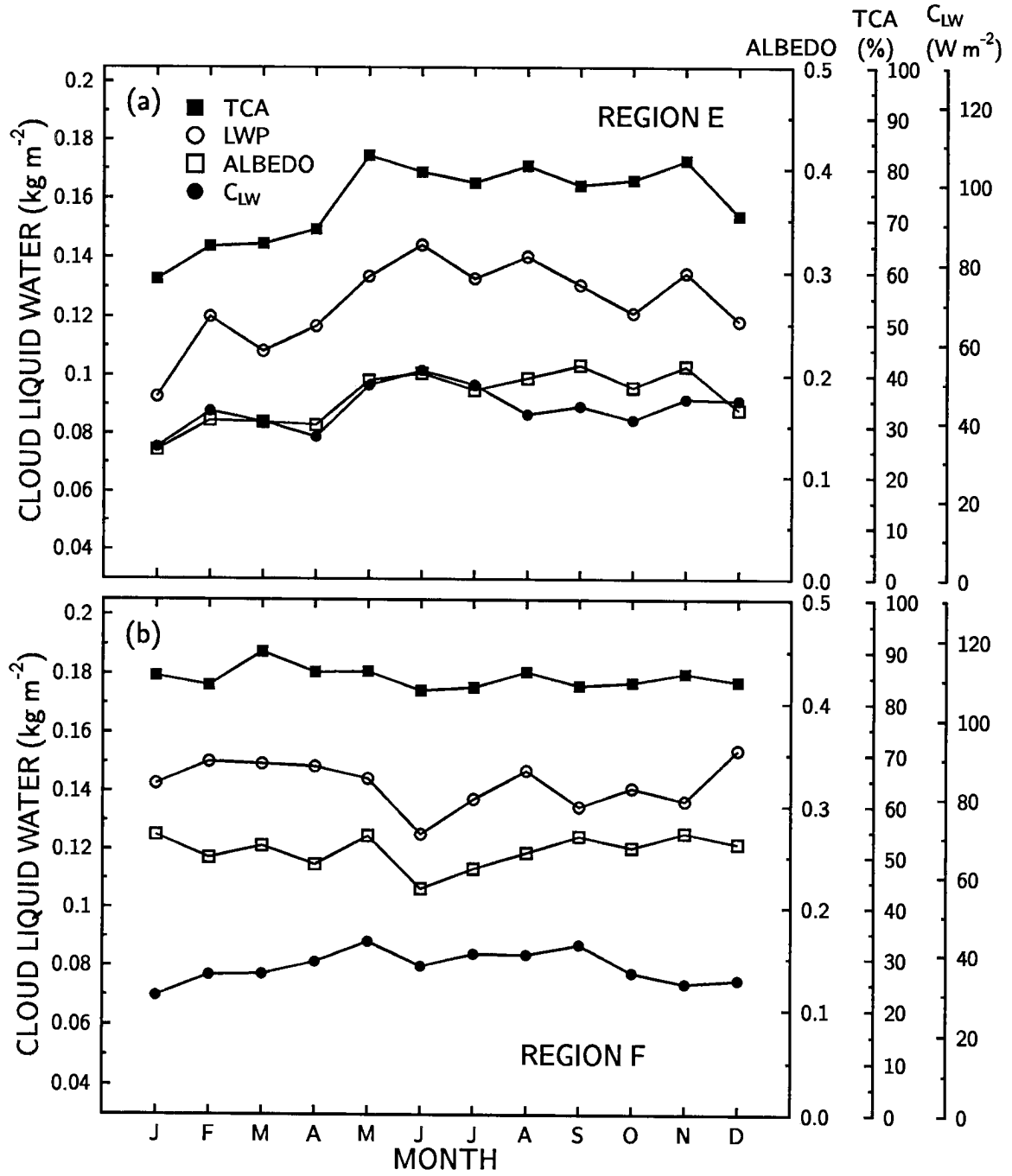


Figure 5.9: Same as Fig. 5.7 except for regions E and F.

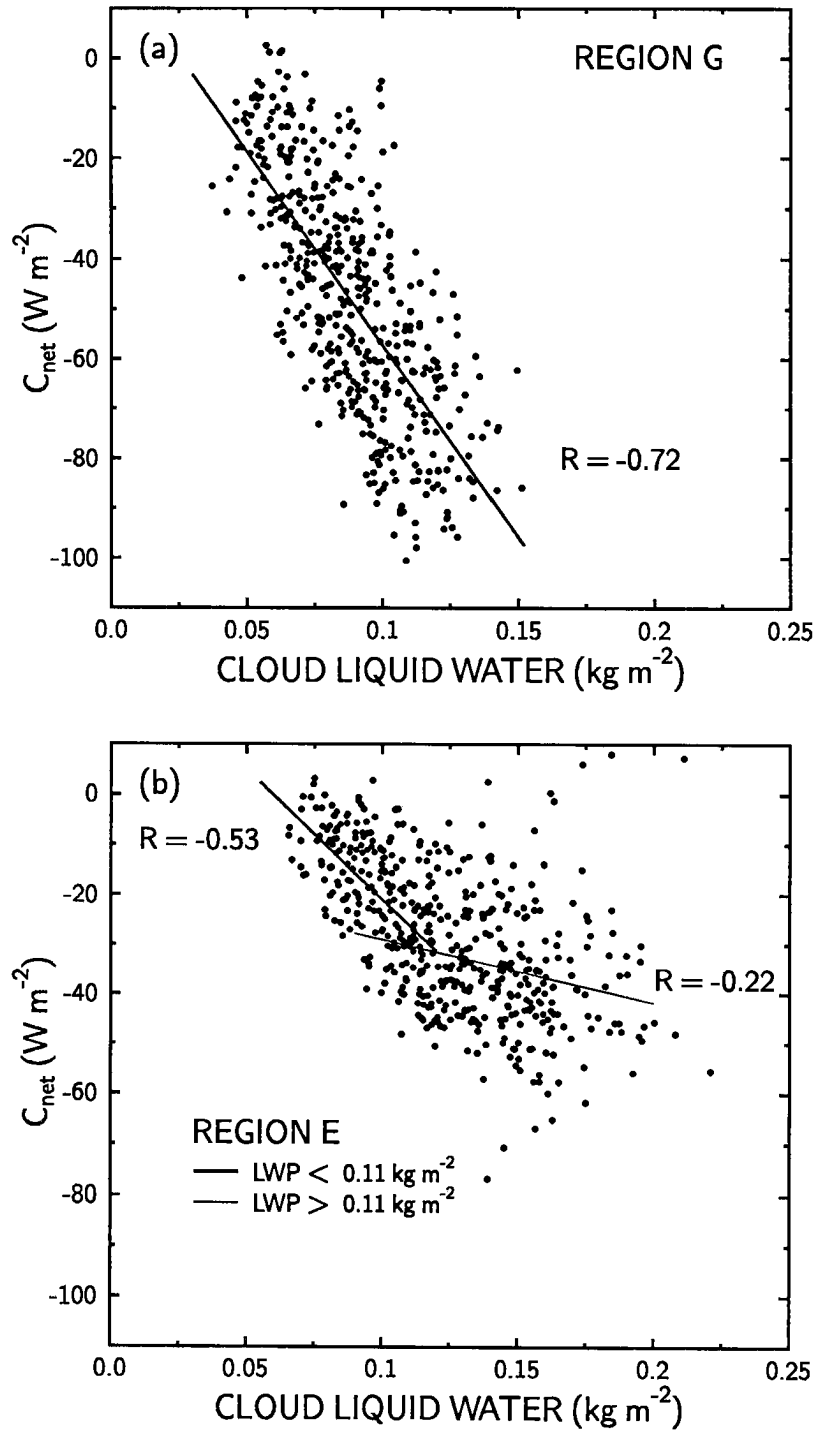


Figure 5.10: (a) Scatter plot of the monthly mean net radiative cloud effect ( $C_{net}$ ) versus cloud liquid water for Region G. Each point is a  $2.5^\circ$  gridbox average. Also shown is a least squares linear fit and the resultant correlation coefficient. (b) Scatter plot of  $C_{net}$  versus cloud liquid water for Region E. Linear fits and their respective correlations are shown separately for cloud liquid water less than and greater than  $0.11 kg m^{-2}$ .

lower than the  $C_{SW}$  sensitivity of  $-13.3 \text{ W m}^{-2}$  per  $0.02 \text{ kg m}^{-2}$ . On the other hand, clouds with greater liquid water amounts have a greatly reduced impact on  $C_{net}$ . For these clouds a  $0.02 \text{ kg m}^{-2}$  increase in cloud liquid water results in a net loss of only  $2.5 \text{ W m}^{-2}$ . Apparently, the LW component of the radiation budget greatly reduces the effectiveness of the cloud liquid water to alter  $C_{net}$  but only for the optically thickest clouds.

A crucial limitation of this analysis is that one important effect has not been considered; that is, changes in cloudiness. Since cloud liquid water has been shown in earlier analyses to be also a measure of cloudiness on the spatial scale of the data sets, then it follows that the derived net radiative flux sensitivities are expected to be mainly a result of variations in cloudiness. This is confirmed by scatter diagrams of  $C_{net}$  versus total cloudiness for the regions shown in Figure 5.10 (not shown), which indicate similar relationships. Therefore, in order to determine the true sensitivity of  $C_{net}$  to changes in cloud liquid water, future analyses will require one to eliminate or at least minimize the effects of cloudiness.

### 5.3 Cloud Liquid Water and Cloud Albedo

The purpose of this section is to provide a more detailed analysis of the large-scale relationships between cloud liquid water path and cloud albedo using near-coincident satellite observations. As in the previous section, the data involve  $2.5^\circ$  gridbox averages and only albedo measurements from the ERBS. The comparison is limited to three areas in the northern hemisphere during the summer where extensive stratiform cloud systems are known to exist, so as to minimize the effects of ice clouds. These regions are indicated in Figure 5.11. They include the broad region west of North America (Region 1), the North Pacific near the Aleutian Islands (Region 2), and the North Atlantic near Greenland (Region 3).

Several criteria were used to select suitable cases. First, the time difference between the DMSP and ERBS overpasses was arbitrarily chosen as 1.5 hours from the center of the ERBE hourly bins. Since there is a half hour uncertainty in the ERB measurements the difference in time is actually between 1 and 2 hours. This time difference is thought to

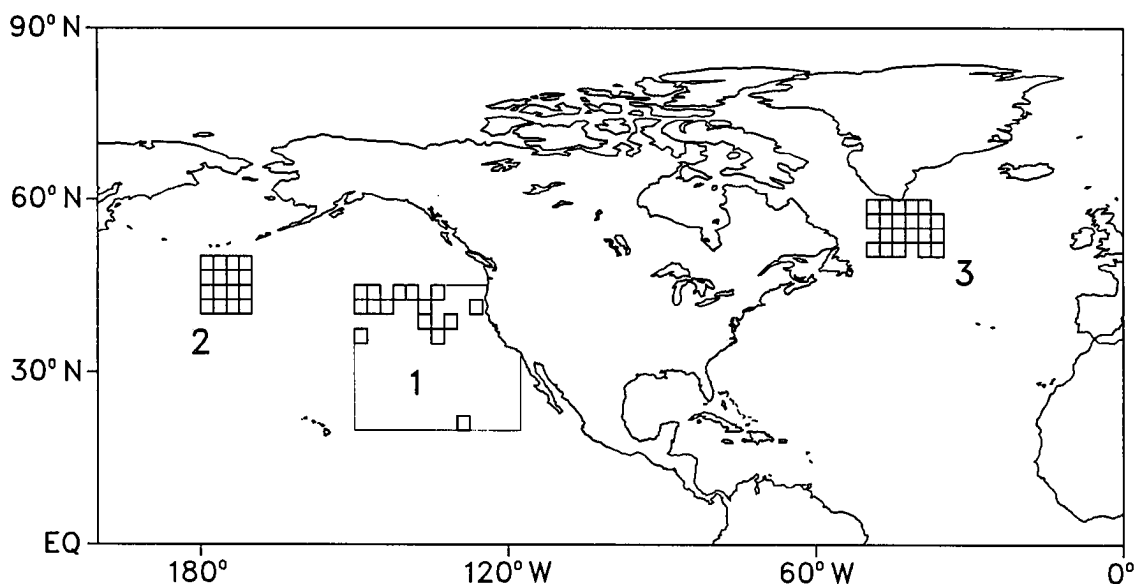


Figure 5.11: Locations of the  $2.5^\circ$  gridboxes used in the cloud albedo and cloud liquid water comparison, which are separated into three general regions. The thin solid line indicates the boundaries of region 1.

be adequate for the relatively large gridboxes that are used in the comparison. In addition, application of a smaller time interval would produce far fewer cases.

Second, we want to minimize the effects of cloud amount on the albedo and cloud liquid water by restricting the comparison to mostly overcast conditions. Thus, the percentage of ERBS pixels determined to be overcast (i.e., 95–100% cloudiness) must be greater than 90% within the gridbox. Only overcast albedos are used in the gridbox average. As an added measure to ensure that the gridbox is mostly overcast, the closest (in time) ISCCP-derived total cloud amount must be greater than 80%. This was necessary since the ERBE scene identification process might have difficulty distinguishing between overcast and mostly cloudy conditions for low-lying clouds. Also, for large viewing zenith angles the scene may be misidentified as overcast since the satellite footprint becomes larger and the scene is viewed at an oblique angle.

Third, only solar zenith angles at the time of the observations of less than  $80^\circ$  are used. The reason is that at extremely low sun angles the highly anisotropic nature of the radiation field may not be properly specified, thus compromising the reliability of

the estimated SW fluxes. Another problem to consider is the undersampling that might arise when, for example, only a portion of the swath (from either instrument) covers the gridbox. Thus, the number of SSM/I and ERBS pixels in a gridbox must be at least 10.

Further criteria are applied to the estimates of cloud liquid water from the SSM/I. As discussed in previous chapters, the effects of precipitation can overestimate the retrievals of cloud liquid water. If a large portion of the gridbox is covered by precipitating cloud systems, the cloud albedo-LWP relationships might become biased. The test that we use to exclude these situations is to apply a LWP threshold to the retrievals and flag pixels that may be contaminated by precipitation. If more than 20% of the pixels in the gridbox have LWP values greater than  $0.4 \text{ kg m}^{-2}$ , then the gridbox is considered to be contaminated by precipitation and is excluded from the comparison. This threshold value is slightly lower than that used in the global analysis of cloud liquid water so as to ensure that significant precipitation is not present in the retrievals. If the retrieved cloud liquid water exceeds  $0.4 \text{ kg m}^{-2}$ , then its value is set to  $0.4 \text{ kg m}^{-2}$ . An additional criterion to lessen the impact of ice clouds is to provide a rough estimate of cloud amount for water clouds using the liquid water observations. Pixels are determined to be cloudy if the retrieved liquid water is greater than  $0.025 \text{ kg m}^{-2}$ . If the cloud amount calculated in this way falls below 80%, the gridbox is not included in the comparison. Although this criterion might eliminate cases where there are only ice clouds in certain regions of the gridbox, it does not preclude the possibility of ice clouds occurring above the water clouds.

Applying these criteria to the months of June, July, and August from 1987 to 1989 results in a total of 118 cases. Broken down into their respective regions gives 18, 59, and 41 cases for regions 1, 2 and 3. The locations of these near-coincident cases are shown in Figure 5.11. As seen from this figure, the stratocumulus region off the coast of the southern U.S. and Mexico is not well represented. This is due to data gaps that occur for the SSM/I in the subtropics, which greatly reduces the chances of finding a match. Using ERB data from the NOAA-10 satellite might help to provide more cases in these regions (NOAA-10 is also a polar orbiting early morning/late afternoon satellite). Since gridboxes in the middle and higher latitudes usually have at least two measurements per day, the chances of finding a match are much greater.

The cloud albedo is estimated from the ERB albedo measurements using the method of Stephens and Greenwald (1991), which was described earlier. Unfortunately, the clear sky albedo is not known due to the overcast conditions in the comparisons. However, it can be estimated assuming an albedo of 0.075 at nadir (see, e.g., Dlhopsky and Ccss, 1993). Then using the solar zenith angle and ERBE directional albedo model for a clear ocean (Figure 5.1), this value can be scaled to give the appropriate clear sky albedo. Most of the solar zenith angles for the comparison cases are found to range from about  $60^\circ$  to  $80^\circ$ . Consequently, the cloud albedos are divided into three different solar zenith angle categories, from  $55^\circ$  to  $65^\circ$ ,  $65^\circ$  to  $75^\circ$ , and  $75^\circ$  to  $80^\circ$ .

Separate scatter plots of cloud albedo versus cloud liquid water for the three regions and solar zenith angle categories are shown in Figures 5.12–5.16. In each figure theoretical plane-parallel calculations are also indicated for various cloud droplet effective radii ( $r_e$ ) and for solar zenith angles of  $60^\circ$ ,  $70^\circ$ , and  $80^\circ$  that correspond to the solar angle categories. The SW broadband ( $0.25\text{--}4\ \mu\text{m}$ ) parameterization scheme developed by Slingo (1989) was used in these calculations. We implemented the four-band version of the parameterization. Using a more sophisticated radiative transfer model was deemed unnecessary since the parameterization compares well with more detailed calculations and with observations (Slingo, 1989). The values of  $r_e$  that were chosen, that is 5, 10, 15, and  $20\ \mu\text{m}$ , are thought to represent a typical range for most stratiform-type clouds, although  $20\ \mu\text{m}$  is probably an extreme value. In situ measurements of  $r_e$  in marine stratocumulus (e.g., Slingo et al., 1982; Stephens and Platt, 1987; Albrecht et al., 1988) and arctic stratus clouds (Herman and Curry, 1984) have been shown to range from about  $5\text{--}10\ \mu\text{m}$ . Also, remote sensing studies of stratocumulus have derived values of  $r_e$  of between 10 and  $15\ \mu\text{m}$ , which sometimes reached  $18\ \mu\text{m}$  (Nakajima et al., 1991).

There are several characteristics of the observed albedo-LWP relationships that are generally common to all regions and solar zenith angles. For example, there is a fair amount of scatter in the relationships. This may be caused by variations in droplet size, time mismatches between the measurements, and possibly the impact from ice clouds, among other reasons. There is also little indication of a clear relationship between cloud

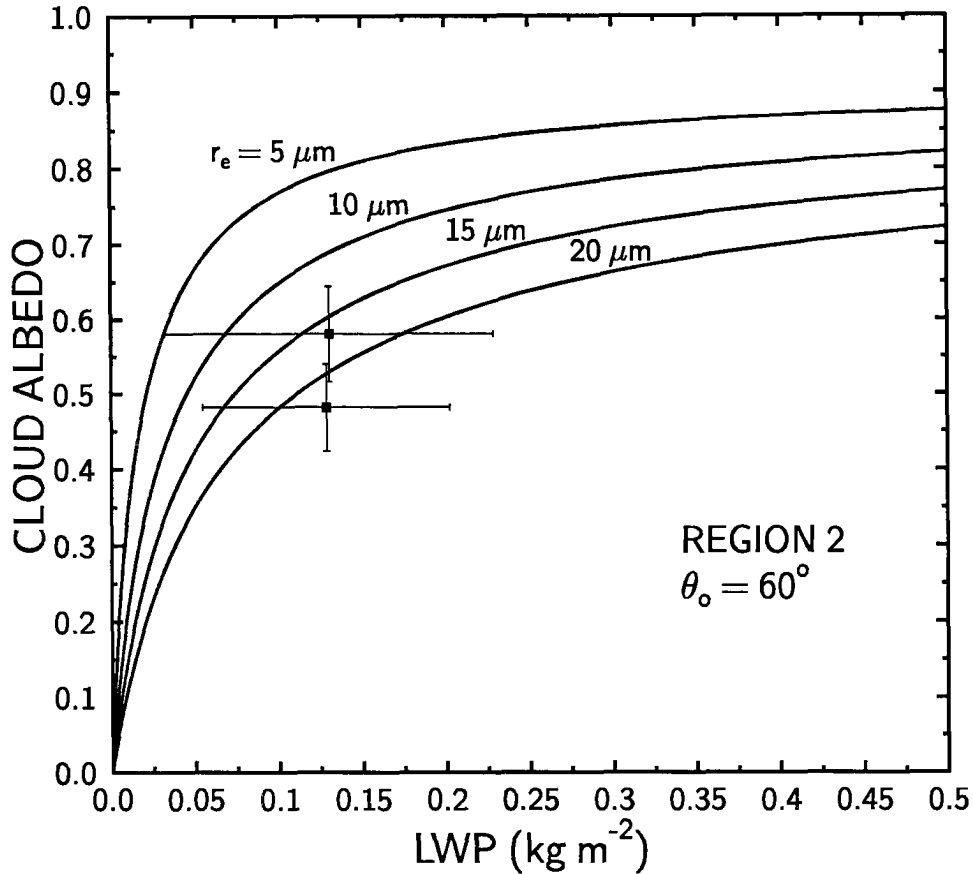


Figure 5.12: Scatter plot of cloud albedo versus cloud liquid water path for solar zenith angles from  $55^\circ$  to  $65^\circ$  for Region 2. Curves represent theoretical calculations at a solar zenith of  $60^\circ$  for plane-parallel clouds with various effective radii ( $r_e$ ) using the parameterization of Slingo (1989).

albedo and LWP in many of the comparisons. However, for the cloud albedos, liquid water amounts and droplet sizes considered in these comparisons, the theoretical calculations show that there is not expected to be a great deal of sensitivity of cloud albedo to changes in LWP, as compared to small  $r_e$  and very small LWP. A more unexpected behavior in the comparisons is that most of the observations agree with effective radii that are much larger (i.e., greater than  $20 \mu\text{m}$ ) for these types of clouds. There are cases where the observations fall within expected limits for this relationship; however, they are much less common and usually occur for the lowest LWPs.

ISCCP cloud analyses reveal that for nearly all of the cases the percentage of low clouds (i.e., below 680 mb) is about 30%. This fact is somewhat misleading because

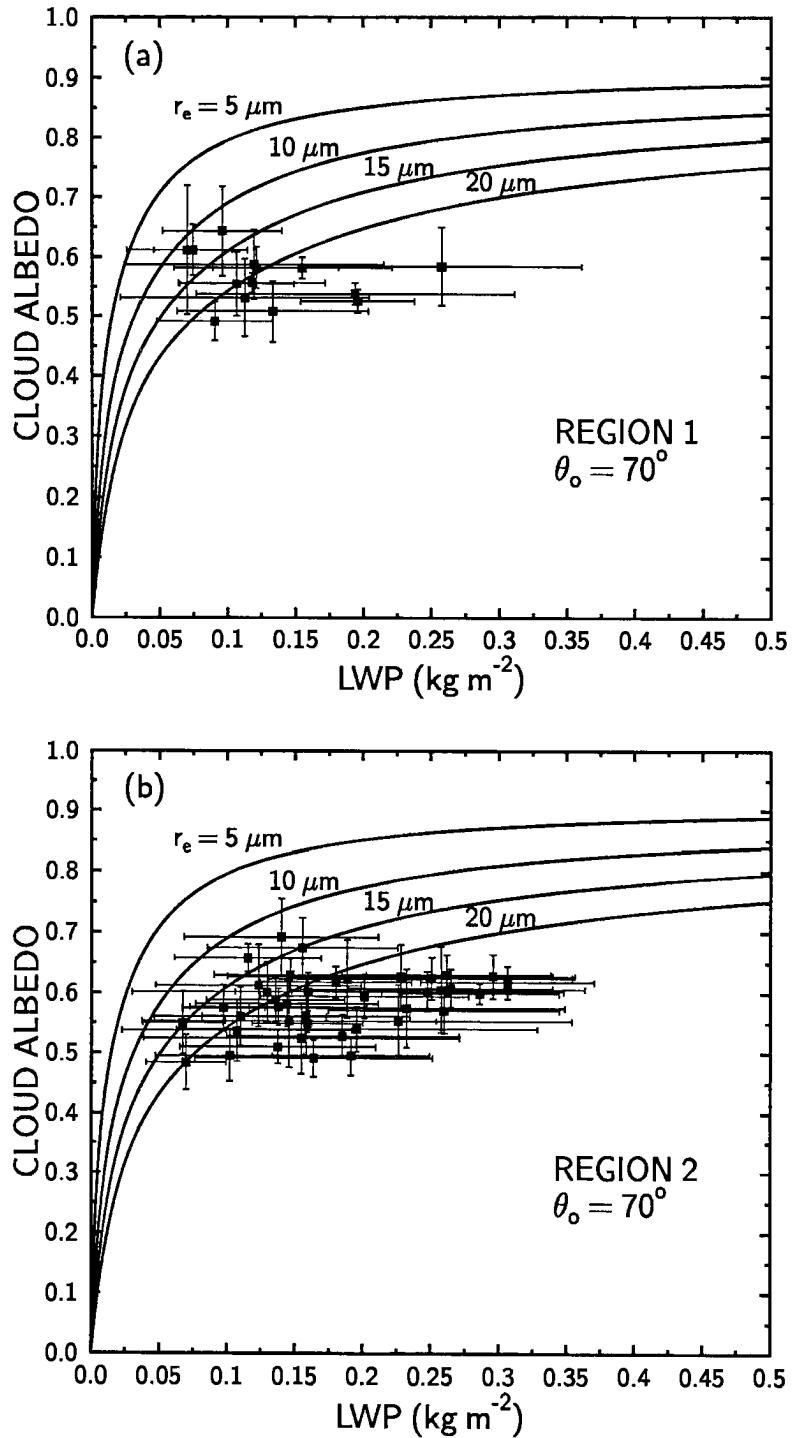


Figure 5.13: Scatter plot of cloud albedo versus cloud liquid water path for solar zenith angles from  $65^\circ$  to  $75^\circ$  for regions (a) 1 and (b) 2. Curves represent theoretical calculations at a solar zenith angle of  $70^\circ$ .

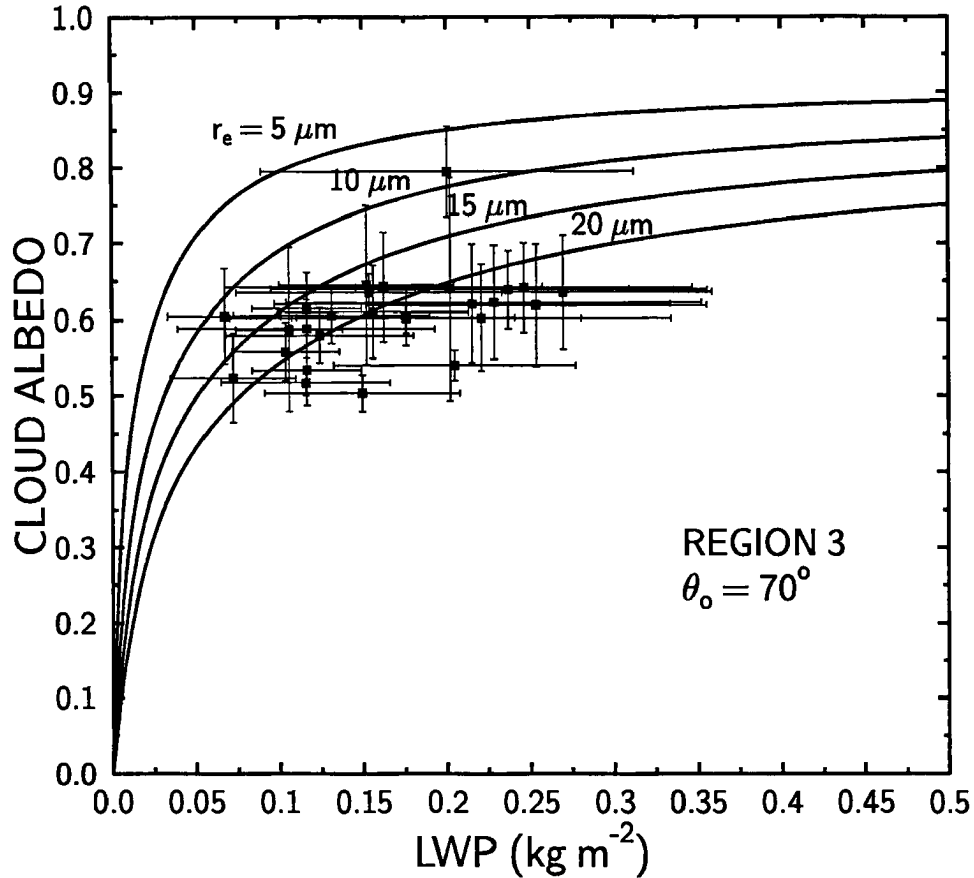


Figure 5.14: Same as Fig. 5.13 except for region 3.

satellite measurements of cloud amount only involve the uppermost portions of the cloud systems. Therefore, it is possible that many more low clouds exist below the higher level cloudiness. At any rate, it is clear that there may be other cloud types that are influencing the albedo.

One cloud type that might bias the albedo-LWP relationship is ice clouds. If large numbers of ice clouds were in fact present, one might expect the observations of cloud albedo to be too high and result in lower values of  $r_e$  than expected. However, the results indicate just the opposite. Thus, the effect of ice clouds on the albedos do not appear to be large in general, although a few anomalous points with high albedos in Figures 5.14 and 5.16 suggest the impact of extensive ice clouds.

The comparisons in Figures 5.12-5.16 also include the standard deviations of the albedo and cloud liquid water measurements within the gridbox (which are represented

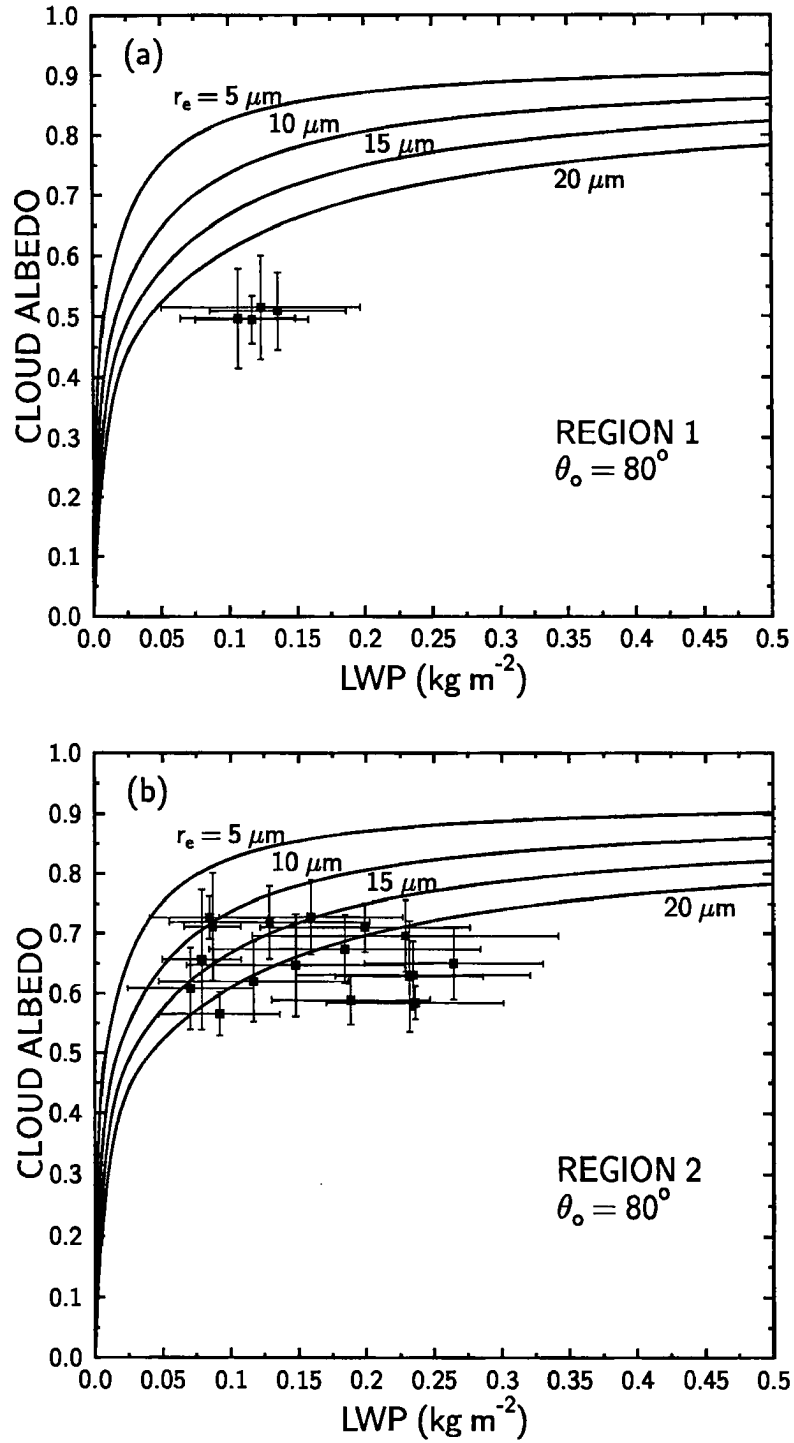


Figure 5.15: Scatter plot of cloud albedo versus cloud liquid water path for solar zenith angles from  $75^\circ$  to  $80^\circ$  for regions (a) 1 and (b) 2. Curves represent theoretical calculations at a solar zenith of  $80^\circ$ .

as the vertical and horizontal error bars). The variability of the cloud albedo is typically 10% of the mean value and is usually much less. In contrast, the cloud liquid water observations are surprisingly highly variable, often being 50% or more of the mean LWP. The high spatial variability of cloud liquid water underscores one of the major difficulties in comparing these measurements with albedo measurements over a relatively large region, such as a  $2.5^\circ$  gridbox.

The most likely explanations for the discrepancies that we observe between theory and observations can be divided into three basic categories. First, the albedo measurements may be systematically too low. An increase in the cloud albedo of about 15 to 25% would be needed to match the observations with reasonable values of  $r_e$  in the theoretical calculations. This requires rather large increases in SW reflected fluxes of roughly 25 to  $45 \text{ W m}^{-2}$ . As discussed before, the errors in the instantaneous SW fluxes averaged over

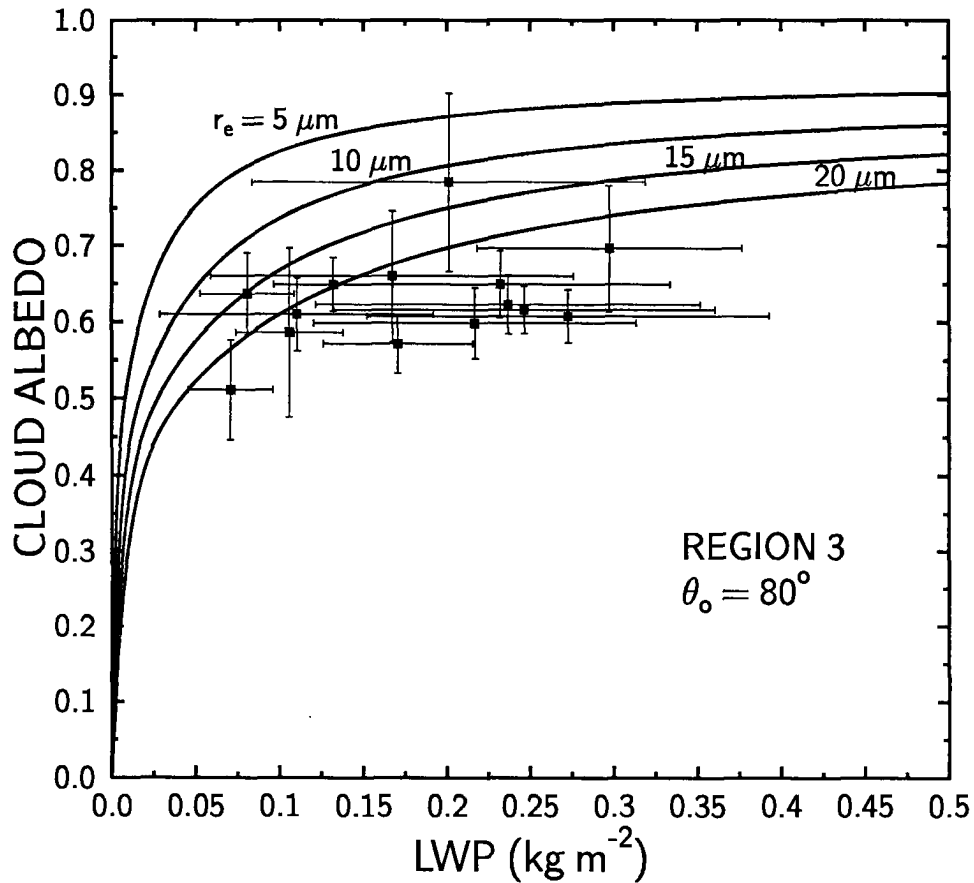


Figure 5.16: Same as Fig. 5.15 except for region 3.

the gridbox are estimated to be about  $15 \text{ W m}^{-2}$ . Thus, possible systematic biases in the SW fluxes alone are not large enough to account for these differences. In fact, if one does a “back-of-the-envelope” calculation assuming an incoming solar flux of  $300 \text{ W m}^{-2}$ , a  $10 \text{ W m}^{-2}$  uncertainty in the solar flux measurement, and a cloud albedo of 0.6, the uncertainty in the albedo is about 0.05, which is comparable to the standard deviation of the albedos within the gridbox.

To aid in interpreting how the satellite geometry might affect the albedo observations, we show in Figure 5.17 frequency histograms of the gridbox average viewing zenith angle and relative azimuth angle of the measurements. An azimuth angle of  $0^\circ$  corresponds to the forward scattering direction. This figure shows that the majority of the observations are taken at large zenith angles and at azimuth angles away from the forward and backscattering directions. As mentioned before, the scanner footprint size is much greater at larger zenith angles than it is at smaller angles. For example, at a zenith angle of  $60^\circ$  the footprint size is rather large, covering an area about four times that of the footprint at nadir. Thus, the fact that most of the albedo measurements are much larger than the SSM/I footprint might explain why the albedo standard deviations are generally smaller than the cloud liquid water standard deviations.

The second explanation concerns possible systematic biases in the cloud liquid water measurements. An analysis of the retrieval errors in Chapter 3 suggested that the errors are expected to range from about 20 to 30% for the average liquid water and water vapor amounts represented in these comparisons. In a scatter plot of cloud albedo versus LWP for the data in Figures 5.13 and 5.14 where the LWP values have been systematically reduced by 30% (not shown), it appears that systematic biases in the retrievals are large enough to account for much of the discrepancy for many of the lowest LWPs. In comparison, the albedo-LWP relationship for higher LWPs are still in disagreement with plane-parallel theory. In fact, an inspection of Figures 5.12–5.16 shows that the LWPs would need to be reduced by about a factor of 3 in order to agree with reasonable values of  $r_e$ . For larger LWPs it is possible that precipitation contaminated pixels may be contributing to the greater disagreement, although these effects have been largely mitigated by the

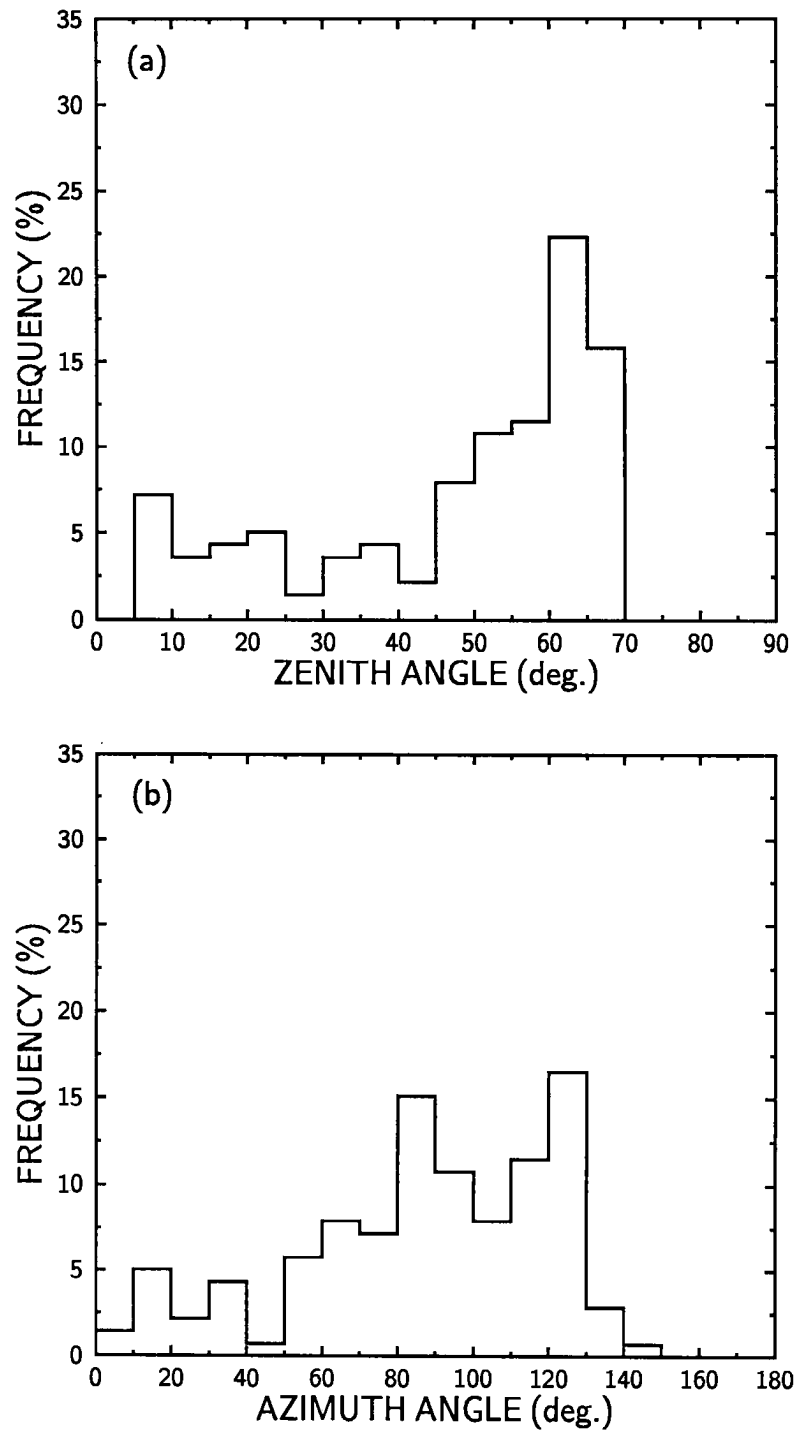


Figure 5.17: Histograms of the % occurrence of the average (a) zenith angle and (b) azimuth angle of the ERB measurements for the cloud albedo-LWP comparison.

screening procedure described earlier.

Even if one does not consider systematic biases in the retrievals, the discrepancies between theory and observations are in most cases within the variability associated with the cloud liquid water in the gridbox. Thus, a smaller scale comparison may be necessary to reduce this variability and provide a more reliable comparison of cloud albedo and cloud liquid water. In summary, it is very probable that high estimates in the cloud liquid water retrievals are the main cause of at least some of the disagreement. However, future comparisons will require validation of the cloud liquid water retrievals to confirm this.

The last explanation is based on the idea that the disagreement between plane-parallel theory and the observations may be real and is caused instead by the macrophysical structure of the clouds. Since we have chosen situations that are mostly overcast, broken cloudiness effects will likely have only a small effect on the SW measurements. Another more likely candidate is that inhomogeneities within the clouds can lead to a low bias in the cloud albedo. Recent work by Cahalan et al. (1994) has demonstrated that the albedos of fractal stratocumulus clouds are roughly 10% lower than that expected from plane-parallel theory for the optical depths and solar zenith angles typical of the present comparisons. Of course, those results are for a specific type of cloud and it is not known to what extent the inhomogeneities in other cloud types will affect the albedo. However, the results of Cahalan et al. (1994) show that cloud inhomogeneities may potentially have a significant influence on the albedo of the cloud. This effect is probably not large enough to completely close the gap between theory and observations in our comparisons, but it may at least partly account for the discrepancies.

## Chapter 6

### CONCLUSIONS AND FUTURE WORK

Satellite passive microwave measurements from the SSM/I and Earth radiation budget measurements from the ERBS have been used to study the large-scale characteristics and radiative effects of integrated cloud liquid water over the oceans. A method of simultaneously estimating both integrated cloud liquid water and water vapor is presented. The technique consists of a simple physical model, which in part derives from the physical water vapor scheme of Tjemkes et al. (1991), and exploits measurements at 19.35 and 37 GHz from the SSM/I. There are several novel aspects of the model when compared with other physical algorithms of its type. For example, it attempts to account for sea surface roughness effects and changes in cloud temperature. In addition, a means of calibrating the model is provided.

The results of a preliminary validation of cloud liquid water determined from satellites have shown the retrievals to be consistent with coincident estimates of liquid water from independent ground-based measurements in the subtropics and middle to high latitudes. The rms differences ranged from 0.036 to 0.046  $\text{kg m}^{-2}$ . The comparisons at the tropical sites were generally disappointing, which was mainly a result of the difficulty in estimating liquid water from either satellite or ground-based systems in the tropical Pacific. A comparison to near-coincident LWP inferred from visible reflectances for California marine stratus clouds showed reasonable agreement. Further comparisons in specific regions and under limited conditions to other SSM/I liquid water algorithms gave mixed results, with generally good agreement for the Petty (1990) and Hargens (1992) algorithms (rms differences of 0.03 and 0.02  $\text{kg m}^{-2}$ , respectively) but large discrepancies for the Alishouse et al. (1990) method (rms differences of 0.07  $\text{kg m}^{-2}$ ).

For nonprecipitating clouds it was shown from a simple error analysis that the degree of confidence in the retrieved liquid water depends on the type of atmospheric and surface conditions and on the amount of liquid water. The total retrieval errors are anticipated to range from about 15 to 35% for a liquid water path of  $0.2 \text{ kg m}^{-2}$  and 20 to 60% for a value of  $0.1 \text{ kg m}^{-2}$ , where the error increases with increasing water vapor. The greatest contribution to the error for higher liquid water paths is uncertainties in the effective cloud temperature. Wind induced changes in surface roughness typically introduce small errors in the retrieval, except for the lowest liquid water amounts under relatively dry atmospheric conditions. The largest percentage errors occur for environments with an abundance of water vapor and for low cloud liquid water. In average conditions consisting of a surface wind speed of  $6 \text{ m s}^{-1}$ , a water vapor amount of  $30 \text{ kg m}^{-2}$ , and a cloud liquid water amount of  $0.1 \text{ kg m}^{-2}$ , the retrieval error is about 30%. Retrievals for a limited number of SSM/I observations in known clear sky regions resulted in a standard deviation of  $0.016 \text{ kg m}^{-2}$ , which is an estimate of the minimum retrieval errors. Differences in the footprint sizes of the 19.35 and 37 GHz channels are shown to contribute errors that are smaller than errors caused by imprecise knowledge of the state of the atmosphere and sea surface.

The retrieval method was applied to 53 months (July 1987 to December 1991) of SSM/I measurements to produce global, monthly mean climatic data sets of cloud liquid water and water vapor. The observed cloud liquid water data exhibited many outstanding spatial characteristics. Some of the largest liquid water amounts observed (greater than  $0.015 \text{ kg m}^{-2}$ ), apparently caused by prolific stratus cloudiness, were located in the North Pacific and Atlantic during the summer when these regions are under the controlling influence of high pressure systems and strong static stability. In subtropical subsidence regions stratocumulus clouds were a conspicuous and persistent feature in the cloud liquid water fields, containing somewhat less liquid water on average, which ranged from about 0.09 to  $0.12 \text{ kg m}^{-2}$ . Surprisingly, the subtropical stratus formations near the northern coast of South America and west of Africa displayed large seasonal variability while the North American stratocumulus showed little seasonal change. In the northern hemisphere during

fall, winter, and spring the eastward progression of midlatitude weather systems produced a narrow belt of elevated cloud liquid water values. Extensive and large cloud liquid water amounts, often more than  $0.14 \text{ kg m}^{-2}$  and sometimes exceeding  $0.2 \text{ kg m}^{-2}$ , occurred along these storm pathways. The magnitude of the cloud liquid water within the southern hemisphere storm track was generally less than in the north, though still significant, ranging from  $0.12$  to  $0.14 \text{ kg m}^{-2}$ . Finally, in areas of the tropics where moisture convergence and convection is especially strong and widespread the cloud liquid water values were expectedly high ( $0.014$ – $0.18 \text{ kg m}^{-2}$ ). These areas included the ITCZ in the Pacific and Atlantic and the intense convection in the western equatorial Pacific and Indian Ocean.

The zonal distribution of cloud liquid water is made up of three primary maxima. The peaks in the midlatitudes are thought to be associated with cyclonic storm activity. A slightly wider maximum in the northern latitudes is the result of increased stratus cloudiness during the summer. Another maximum in the tropics is an indicator of tropical convection, which is caused mainly by the ITCZ in the Pacific.

The observations were also compared to simulated fields of cloud liquid water generated by the ECHAM model and the CSU GCM. In terms of the spatial characteristics of cloud liquid water, both models were able to capture the storm track regions, which appeared as maxima, but severely underestimated stratus liquid water in areas of large-scale subsidence. On a zonal mean basis the CSU GCM compared well in terms of magnitude with the observations, differing only with respect to the latitudinal position of the storm tracks. Although the mean cloud liquid water from the CSU GCM was reasonable, its seasonal variability was found to be about 50% greater than the observations.

The important conclusions of this work can be summarized as follows:

- (1) This study has demonstrated that adequate estimates of integrated cloud liquid water can be obtained from SSM/I measurements over the oceans and outside regions of precipitation. Retrievals appear to be most accurate in areas of persistent stratocumulus clouds and least accurate in the tropics. Despite the good performance of the simple retrieval model over many regions, the physics of the model is oversimplified for a tropical atmosphere, which leads to small negative biases in the retrievals. Improvements to the

model that overcome this and other problems are described in the appendix. Further research efforts are needed to monitor oceanic cloud liquid water over long periods of time at various sites, especially in the tropics, to provide reliable “ground truth” data sets to validate methods such as described in this research.

(2) The spatial distribution of integrated cloud liquid water over the oceans is consistent with the proposition that it is largely controlled by large-scale dynamics. The average amount of marine cloud liquid water over the globe is estimated to be  $0.112 \text{ kg m}^{-2}$ , while low clouds have an average of about  $0.086 \text{ kg m}^{-2}$ . The seasonal departures of cloud liquid water are on average 15% to 30% of the annual mean and are largest in the tropics and northern midlatitudes.

(3) The liquid water path of low clouds is determined to be negatively correlated with temperature throughout most of the tropics and subtropics, which is in general agreement with previously published results based on observations of cloud optical depth. At higher latitudes the correlations are reversed and assume a quasi-adiabatic behavior. This result is also consistent with the sensitivities deduced by Somerville and Remer (1984) based on aircraft measurements of high latitude clouds over Russia. These relationships also exhibit significant variability on both seasonal and regional scales. Comparisons of cloud liquid water to SSTs also show strong relationships that reflect the impact of different dynamical regimes in determining these sensitivities. These results cannot be used to imply a global cloud-climate feedback given that the observed sensitivities can change sign depending on latitude and since the correlations between cloud liquid water and temperature, excluding the coldest clouds, are thought to be largely a result of dynamical processes.

(4) In a comparison that has never been done before, seasonal changes in cloud albedo and cloud liquid water are found to be well correlated over most regions of the globe, particularly for specific regions in the tropics. This is primarily a result of cloud liquid water being strongly related to the amount of cloudiness within the relatively large  $2.5^\circ$  gridboxes. With few exceptions, the mean cloud liquid water is shown to coincide well with the mean cloud albedo in selected regions. Again, these relationships occur mainly because of cloudiness effects. These results suggest that the mean cloud liquid water alone

may be adequate in many cases to characterize the mean cloud albedo, at least in areas of extreme cloudiness. However, it is important to emphasize that this is true only in areas dominated by water clouds. In regions where ice clouds are prevalent these albedo-LWP relationships are not expected to be as useful. Clearly, more work is required to establish the separate influences of cloudiness, cloud type, and cloud particle size on the observed albedo-LWP relationships and to determine how these relationships vary from region to region.

(5) Another important result is that the sensitivity of the net radiative cloud effect to changes in cloud liquid water is radically different for subtropical stratus clouds and for clouds with greater vertical extent. Whereas the low-lying stratus clouds exhibit a large and nearly constant sensitivity as a function of cloud liquid water, deeper clouds undergo a substantial reduction in sensitivity for higher liquid water amounts due to enhanced LW effects. However, it should be noted that the usefulness of these results is limited since the effects of changes in cloudiness have not been accounted for.

(6) A detailed examination of near-coincident observations of cloud liquid water and cloud albedo observations for stratiform clouds revealed large discrepancies with relationships expected from plane-parallel theory. The observed albedo-LWP relationships were found to correspond to clouds with effective radii much larger than is typical of stratiform clouds. It is proposed that the differences may be due to a combination of possible systematic high biases in the liquid water retrievals and macrophysical cloud effects which act to reduce the observed cloud albedo.

There are several exciting avenues of research that could be pursued in the future which are related to the work presented in this study. For instance, since atmospheric dynamics evidently plays an important role in characterizing the large-scale patterns of oceanic cloud liquid water, additional work will need to be done to understand and quantify the scope of these dynamical processes. One example might be to investigate the interannual variability of cloud liquid water and its relationship to the ENSO (El Niño-Southern Oscillation).

A more rigorous way of comparing the albedo observed from the ERBS and the cloud liquid water observations is to collocate the data at the pixel level. One major

problem with this approach is that a smaller time interval would be required between the observations than what was used for the gridbox analyses, thus greatly reducing the number of cases. Additional cases can be obtained from ERB measurements on board the NOAA-10 satellite. Future projects such as TRMM will solve the problem of noncoincident measurements by providing both ERB and microwave radiometers on board the satellite platform.

Further improvements in the physical retrieval model might be undertaken by increasing the accuracy of certain variables in the model. For instance, information about the vertical temperature structure of the atmosphere based on SSM/T retrievals might improve estimates of the oxygen transmission, particularly at 37 GHz. One might add other types of ancillary information, such as IR data, to help in estimating the effective cloud temperature. This would consist of using collocated IR data at the pixel level, possibly from the OLS, to input into the model rather than what is currently done by others, which is to use near-coincident spatially sampled IR data (e.g., Liu and Curry, 1993). Also, retrievals of SST and better estimates of surface wind speeds using lower frequency channels of future instruments, such as the HIMSS (High Resolution Microwave Spectrometer Sounder), proposed for the EOS (Earth Observing System) satellites and the TRMM Microwave Imager can help to provide more accurate retrievals.

Another potential use for the model is the retrieval of cloud liquid water and water vapor over land and ice surfaces. Retrievals are possible since the surface emissivity can be determined using a combination of IR and microwave data based on an approach outlined by Jones and Vonder Haar (1990). The retrieval of water vapor over land and sea ice has never been done using SSM/I frequencies. However, it needs to be demonstrated whether it can be accomplished with sufficient accuracy. It would certainly have one advantage over IR moisture retrievals in that retrievals can also be attempted in cloudy regions. Despite the advancements that can be achieved in the types of retrieval methods described in this research (i.e., two and three-channel algorithms) it is anticipated that the most accurate methods over both land and water surfaces will undoubtedly use all available spectral information and be at least semi-physical in nature.

## REFERENCES

- Adler, R. F., R. A. Mack, N. Prasad, H.-Y. M. Yeh, and I. M. Hakkarinen, 1990: Aircraft microwave observations and simulations of deep convection from 18 to 183 GHz, Part I: Observations, *J. Atmos. Oceanic Tech.*, **7**, 377–391.
- Akvilonova, A. B., A. Y. Basharinov, A. K. Gorodetskiy, A. S. Gurvich, M. S. Krylova, B. G. Kutuza, D. T. Matveyev, and A. P. Orlov, 1973: Cloud parameters measured from the Cosmos-384 satellite, *Atmos. Oceanic Phys.*, **9**, 187–189.
- Akvilonova A. B., and B. G. Kutuza, 1979: Microwave radiation of clouds, *Radio Eng. Elect. Phys.*, **24**, 12–24.
- Albrecht, B. A., C. W. Fairall, D. W. Thomson, A. B. White, J. B. Snider, W. H. Schubert, 1990: Surface-based remote sensing of the observed and the adiabatic liquid water content of stratocumulus clouds, *Geophys. Res. Letters*, **17**, 89–92.
- Albrecht, B. A., D. A. Randall, and S. Nicholls, 1988: Observations of marine stratocumulus clouds during FIRE, *Bull. Amer. Meteor. Soc.*, **69**, 618–626.
- Alishouse, J. C., J. B. Snider, E. R. Westwater, C. T. Swift, C. S. Ruf, S. A. Snyder, J. Vongsathorn, and R. R. Ferraro, 1990: Determination of cloud liquid water content using the SSM/I, *IEEE Trans. Geosc. Rem. Sensing*, **28**, 817–822.
- Barkstrom, B. R., 1984: The Earth Radiation Budget Experiment (ERBE), *Bull. Am. Meteorol. Soc.*, **65**, 1170–1185.

- Barkstrom, B. R., E. Harrison, G. Smith, R. Green, J. Kibler, R. Cess, and the ERBE Science Team, 1989: Earth Radiation Budget Experiment (ERBE) archival and April 1985 results, *Bull. Amer. Meteor. Soc.*, **70**, 1254–1262.
- Barkstrom, B. R., and G. L. Smith, 1986: The Earth Radiation Budget Experiment: Science and Implementation, *Rev. Geophys.*, **24**, 379–390.
- Basharinov, A. Y., A. S. Gurvich, and S. T. Yegorov, 1969: Determination of geophysical parameters from data on thermally-induced radio emission obtained with the Cosmos 243 satellite, *Dokl. Akad. Nauk. SSSR*, **188**, 1273–1276.
- Bates, J. J., 1991: High-frequency variability of Special Sensor Microwave/Imager derived wind speed and moisture during an intraseasonal oscillation, *J. Geophys. Res.*, **96**, 3411–3423.
- Bauer, P., and P. Schluessel, 1993: Rainfall, total water, ice water, and water vapor over sea from polarized microwave simulations and Special Sensor Microwave/Imager Data, *J. Geophys. Res.*, **98**, 20,737–20,759.
- Betts, A. K., and Harshvardham, 1987: Thermodynamic constraint on the cloud liquid water feedback in climate models, *J. Geophys. Res.*, **92**, 8483–8485.
- Brooks, D. R., E. F. Harrison, P. Minnis, and J. T. Suttles, 1986: Development of algorithms for understanding the temporal and spatial variability of the earth's radiation budget, *Rev. Geophys.*, **24**, 422–438.
- Burch, D. E., and D. A. Gryvnak, 1980: Continuum absorption by H<sub>2</sub>O vapor in the infrared and millimeter regions, In: *Atmospheric Water Vapor*, Eds. A. Deepak, T. Wilkerson and L. Ruhnke, Academic Press.

- Cahalan, R. F., W. Ridgway, W. J. Wiscombe, T. L. Bell, and J. B. Snider, 1994: The albedo of fractal stratocumulus clouds, *J. Atmos. Sci.*, **51**, 2434–2455.
- Chang, A. T. C., and T. T. Wilheit, 1979: Remote sensing of atmospheric water vapor, liquid water, and wind speed at the ocean surface by passive microwave techniques from the Nimbus 5 satellite, *Radio Science*, **14**, 793–802.
- Charlock, T. P., 1982: Cloud optical feedback and climate stability in a radiative-convective model, *Tellus*, **34**, 245–254.
- Curry, J. A., C. D. Ardeel, and L. Tian, 1990: Liquid water content and precipitation characteristics of stratiform clouds as inferred from satellite microwave measurements, *J. Geophys. Res.*, **95**, 16,659–16,671.
- Dlhopsky, R., and R. D. Cess, 1993: Improved directional models for clear sky ocean derived from earth radiation budget satellite shortwave radiances, *J. Geophys. Res.*, **98**, 16,713–16,721.
- Evans, K. F., 1993: Two-dimensional radiative transfer in cloudy atmospheres: The spherical harmonic spatial grid method, *J. Atmos. Sci.*, **50**, 3111–3124.
- Fowler, L. D., D. A. Randall, and S. A. Rutledge, 1994: Liquid and ice cloud microphysics in the CSU general circulation model. Part I: Model description and simulated microphysical processes, submitted to *J. Climate*.
- Gagarin, S. P., and B. G. Kutuza, 1983: Influence of sea surface roughness and atmospheric inhomogeneities on microwave radiation of the atmosphere-ocean system, *IEEE J. Ocean. Eng.*, **OE-8**, **2**, 62–70.
- Gates, W. L., 1992: AMIP: The Atmospheric Model Intercomparison Project, *Bull. Amer. Meteor. Soc.*, **73**, 1962–1970.

- Goodberlet, M. A., C. T. Swift, and J. C. Wilkerson, 1989: Remote sensing of ocean surface winds with the Special Sensor Microwave/Imager, *J. Geophys. Res.*, **94**, 14,547–14,555.
- Grody, N. C., 1976: Remote sensing of atmospheric water content from satellites using microwave radiometry, *IEEE Trans. Antenn. Propag.*, **AP-24**, 155–162.
- Grody, N. C., A. Gruber, and W. C. Shen, 1980: Atmospheric water content over the tropical Pacific derived from the Nimbus-6 scanning microwave spectrometer, *J. Appl. Meteor.*, **19**, 986–996.
- Han, Y., and D. W. Thomson, 1994: Multichannel microwave radiometric observations at Saipan during 1990 Tropical Cyclone Motion experiment, *J. Atmos. Ocean. Techn.*, **11**, 110–121.
- Hargens, U., 1992: Remote sensing of cloud liquid water during ICE'89, *Proceedings Third Specialists Meeting on Microwave Radiometry and Remote Sensing Applications*, NOAA Environ. Res. Lab, Boulder, Colorado, 27–31.
- Harrison, E. F., P. Minnis, B. R. Barkstrom, V. Ramanathan, R. D. Cess, and G. G. Gibson, 1990: Seasonal variation of cloud radiative forcing derived from the Earth Radiation Budget Experiment, *J. Geophys. Res.*, **95**, 18,687–18,703.
- Herman, G. F., and J. A. Curry, 1984: Observational and theoretical studies of solar radiation in arctic stratus clouds, *J. Clim. Appl. Meteor.*, **23**, 5–24.
- Hill, G., 1991: Comparison of simultaneous airborne and radiometric measurements of supercooled liquid water, *J. Appl. Meteor.*, **30**, 1043–1046.
- Hill, G., 1992: Further comparisons of simultaneous airborne and radiometric measurements of supercooled liquid water, *J. Appl. Meteor.*, **31**, 397–401.

- Hogg, D. C., F. O. Guiraud, J. B. Snider, M. T. Decker, and E. R. Westwater, 1983: A steerable dual-channel microwave radiometer for measurement of water vapor and liquid in the troposphere, *J. Clim. Appl. Meteor.*, **22**, 789–806.
- Hollinger, J. P., 1971: Passive microwave measurements of sea surface roughness, *IEEE Trans. Geosci. Electron.*, **GE-9**, 165–169.
- Hollinger J. P., and the DMSP SSM/I Cal/Val team, 1989: DMSP Special Sensor Microwave/Imager Calibration/Validation final report, Vol. I, Space sensing branch, Naval Research Laboratory, Washington, D.C., 176 pp.
- Hollinger J. P., and the DMSP SSM/I Cal/Val team, 1991: DMSP Special Sensor Microwave/Imager Calibration/Validation final report, Vol. II, Space sensing branch, Naval Research Laboratory, Washington, D.C., 277 pp.
- Hollinger J. P., R. Lo, G. Poe, R. Savage, and J. Peirce, 1987: Special Sensor Microwave/Imager user's guide, Naval Research Laboratory, Washington, D.C., 177 pp.
- Jackson, D. L., and G. L. Stephens, 1994: A Study of SSM/I derived columnar water vapor over the global oceans, submitted to *J. Climate*.
- Jacobowitz, H., H. V. Soule, H. L. Kyle, F. B. House, and the NIMBUS 7 ERB experiment team, 1984: The Earth Radiation Budget (ERB) experiment: An overview, *J. Geophys. Res.*, **89**, 5021–5038.
- James, I. N., and D. L. T. Anderson, 1984: The seasonal mean flow and distribution of large-scale weather systems in the southern hemisphere: the effects of moisture transports, *Quart. J. R. Met. Soc.*, **110**, 943–966.

- Jones, A. S., and T. H. Vonder Haar, 1990: Passive microwave remote sensing of cloud liquid water over land regions, *J. Geophys. Res.*, **95**, 16,673–16,683.
- Katsaros, K. B., and R. M. Lewis, 1986: Mesoscale and synoptic scale features of north Pacific weather systems observed with the Scanning Multichannel Microwave Radiometer on Nimbus 7, *J. Geophys. Res.*, **91**, 2321–2330.
- Kidder, S. Q., and T. H. Vonder Haar, 1994: *Satellite Meteorology: An introduction*, Academic Press, in press.
- Klein, L. A., and C. T. Swift, 1977: An improved model for the dielectric constant of sea water at microwave frequencies, *IEEE Trans. Antennas Propagat.*, **AP-25**, 104–111.
- Klein, S. A., and D. L. Hartmann, 1993: The seasonal cycle of low stratiform clouds, *J. Climate*, **6**, 1587–1606.
- Kopia, L. P., 1986: Earth radiation budget experiment scanner instrument, *Rev. Geophys.*, **24**, 400–406.
- Liebe, H. J., 1981: Modeling attenuation and phase of radio waves in air at frequencies below 1000 GHz, *Radio Sci.*, **16**, 1183–1199.
- Liebe, H. J., G. A. Hufford, and M. G. Cotton, 1993: Propagation modeling of moist air and suspended water/ice particles at frequencies below 1000 GHz, Atmospheric propagation effects through natural and man-made obscurants for visible to MM-wave radiation, AGARD Conference Proceedings, No. 542, 3.1–3.10.
- Lipes, R., Ed., 1981: SMMR mini-workshop IV, Publ. 622-234, Jet propulsion laboratory, Pasadena, CA, 135 pp.

- Liu, G., and J. A. Curry, 1992: Retrieval of precipitation from satellite microwave measurements using both emission and scattering, *J. Geophys. Res.*, **97**, 9959–9974.
- Liu, G., and J. A. Curry, 1993: Determination of characteristic features of cloud liquid water from satellite measurements, *J. Geophys. Res.*, **98**, 5069–5092.
- Liu, W. T., W. Tang, and F. J. Wentz, 1992: Precipitable water and surface humidity over global oceans from Special Sensor Microwave Imager and European Center for Medium Range Weather Forecasts, *J. Geophys. Res.*, **97**, 2251–2264.
- Lojou, J.-Y., R. Frouin, and R. Bernard, 1991: Comparison of Nimbus-7 SMMR and GOES-1 VISSR atmospheric liquid water content, *J. Appl. Meteor.*, **30**, 187–198.
- McClatchey, R. A., R. W. Fenn, J. E. A. Selby, F. E. Volz, J. S. Garing, 1972: Optical properties of the atmosphere, 3rd Ed., AFCRL-72-0497, 108 pp.
- Nakajima, T., M. D. King, and J. D. Spinhirne, 1991: Determination of the optical thickness and effective particle radius of clouds from reflected solar radiation measurements. Part II: Marine stratocumulus observations, *J. Atmos. Sci.*, **48**, 728–750.
- Njoku, E. G., and L. Swanson, 1983: Global measurements of sea surface temperature, wind speed, and atmospheric water content from satellite microwave radiometry, *Mon. Weath. Rev.*, **111**, 1977–1987.
- Paltridge, G. W., 1980: Cloud-radiation feedback to climate, *Q. J. R. Meteorol. Soc.*, **106**, 895–899.
- Pandey, P. C., and R. K. Kakar, 1982: An empirical microwave emissivity model for a foam covered sea, *IEEE J. Oceanic Eng.*, **OE-7(3)**, 135–140.

- Pandey, P. C., E. G. Njoku, and J. W. Waters, 1983: Inference of cloud temperature and thickness by microwave radiometry from space, *J. Clim. Appl. Meteor.*, **22**, 1894–1898.
- Petty, G. W., 1990: On the response of the Special Sensor Microwave/Imager to the marine environment - Implications for atmospheric parameter retrievals, Ph.D. dissertation, University of Washington, 291 pp.
- Petty, G. W., and K. B. Katsaros, 1992a: The response of the SSM/I to the marine environment. Part I: An analytic model for the atmospheric component of observed brightness temperatures, *J. Atmos. Ocean. Technol.*, **9**, 746–761.
- Petty, G. W., and K. B. Katsaros, 1992b: Nimbus 7 SMMR precipitation observations calibrated against surface radar during TAMEX, *J. Appl. Meteor.*, **31**, 489–505.
- Poe, G. A., and R. W. Conway, 1990: A study of the geolocation errors of the Special Sensor Microwave/Imager (SSM/I), *IEEE Trans. Geosc. Remote Sens.*, **28**, 791–799.
- Prabhakara, C., D. A. Short, W. Wiscombe, and R. S. Fraser, 1986: Rainfall over oceans inferred from Nimbus 7 SMMR: Application to 1982-83 El Niño, *J. Clim. Appl. Meteor.*, **25**, 1464–1474.
- Prabhakara, C., I. Wang, A. T. C. Chang, and P. Gloerson, 1983: A statistical examination of Nimbus-7 SMMR data and remote sensing of sea surface temperature, liquid water content in the atmosphere and surface wind speed, *J. Clim. Appl. Meteor.*, **22**, 2023–2037.
- Randall, D. A., 1989: Cloud parameterization for climate modeling: Status and prospects, *Atmos. Res.*, **23**, 341–361.

- Randall, D. A., and D. A. Dazlich, 1991: Diurnal variability of the hydrologic cycle in a general circulation model, *J. Atmos. Sci.*, **48**, 40–62.
- Ray, P. S., 1972: Broadband complex refractive indices of ice and water, *Appl. Optics*, **11**, 1836–1843.
- Reynolds, R. W., 1988: A real-time global sea surface temperature analysis, *J. Climate*, **1**, 75–86.
- Robinson, W. D., C. Kummerow, and W. S. Olson, 1992: A technique for enhancing and matching the resolution of microwave measurements from the SSM/I instrument, *IEEE Trans. Geosci. Remote Sens.*, **30**, 419–429.
- Rosenkranz, P. W., D. H. Staelin, and N. C. Grody, 1978: Typhoon June (1975) viewed by a scanning microwave spectrometer, *J. Geophys. Res.*, **83**, 1857–1868.
- Rossow, W. B., and R. A. Schiffer, 1991: ISCCP cloud data products, *Bull. Am. Meteorol. Soc.*, **72**, 2–20.
- Ruf, C. S., and C. T. Swift, 1988: Atmospheric profiling of water vapor density with a 20.5–23.5 autocorrelation radiometer, *J. Atmos. Ocean. Tech.*, **5**, 539–546.
- Rutledge, S. A., and P. V. Hobbs, 1983: The mesoscale and microscale structure and organization of cloud bands and precipitation in midlatitude cyclone. VIII: A model for the "Seeder Feeder" process in warm-frontal bands, *J. Atmos. Sci.*, **40**, 1185–1206.
- Sasaki, Y., I. Asanuma, K. Muneyama, G. Naito, and T. Suzuki, 1987: The dependence of sea-surface microwave emission on wind speed, frequency, incidence angle, and polarization over the frequency range from 1 to 40 GHz, *IEEE Trans. Geosci. Remote Sens.*, **GE-25**, 138–146.

- Schiffer, R. A., and W. B. Rossow, 1983: The International Satellite Cloud Climatology Project (ISCCP): The first project of the World Climate Research Programme, *Bull. Am. Meteorol. Soc.*, **64**, 779–784.
- Schluessel, P., and W. J. Emery, 1990: Atmospheric water vapour over oceans from SSM/I measurements, *Int. J. Remote Sens.*, **11**, 753–766.
- Schubert, W. H., S. K. Cox, P. E. Ciesielski, and C. M. Johnson-Pasqua, 1987: Operation of a ceilometer during the FIRE marine stratocumulus experiment, Colo. St. Univ., Dept. Atmos Sci. paper no. 420, 28 pp.
- Slingo, A., 1989: A GCM parameterization for the shortwave radiative properties of water clouds, *J. Atmos. Sci.*, **46**, 1419–1427.
- Slingo, A., S. Nicholls, and J. Schmetz, 1982: Aircraft observations of marine stratocumulus during JASIN, *Quart. J. Roy. Meteor. Soc.*, **108**, 833–856.
- Smith, G. L., R. N. Green, E. Raschke, L. M. Avis, J. T. Suttles, B. A. Wielicki, and R. Davies, 1986: Inversion methods for satellite studies of the Earth's radiation budget: Development of algorithms for the ERBE mission, *Rev. Geophys.*, **24**, 407–421.
- Somerville, R. C. J., and L. A. Remer, 1984: Cloud optical thickness feedbacks in the CO<sub>2</sub> climate problem, *J. Geophys. Res.*, **89**, 9668–9672.
- Spencer, R. W., 1993: Global oceanic precipitation from the MSU during 1979-91 and comparisons to other climatologies, *J. Climate*, **6**, 1301–1326.
- Spencer R. W., H. M. Goodman, and R. E. Hood, 1989: Precipitation retrieval over land and ocean with the SSM/I: Identification and characteristics of the scattering signal, *J. Atmos. and Oceanic Tech.*, **6**, 254–273.

- Staelin, D. H., K. F. Kunzi, R. L. Pettyjohn, R. K. L. Poon, R. W. Wilcox, and J. W. Waters, 1976: Remote sensing of atmospheric water vapor and liquid water with the Nimbus 5 microwave spectrometer, *J. Appl. Meteor.*, **15**, 1204–1214.
- Stephens, G. L., 1978: Radiation profiles in extended water clouds, II: Parameterization schemes, *J. Atmos. Sci.*, **35**, 2123–2132.
- Stephens, G. L., 1990: On the relationship between water vapor over the oceans and sea surface temperature, *J. Climate*, **3**, 634–645.
- Stephens, G. L., and T. J. Greenwald, 1991: The Earth's radiation budget and its relation to atmospheric hydrology, 2. Observations of cloud effects, *J. Geophys. Res.*, **96**, 15,325–15,340.
- Stephens, G. L., and C. M. R. Platt, 1987: Aircraft observations of the radiative and microphysical properties of stratocumulus and cumulus cloud fields, *J. Clim. Appl. Meteor.*, **26**, 1243–1269.
- Stephens, G. L., and S.-C. Tsay, 1990: On the cloud absorption anomaly, *Q. J. R. Meteorol. Soc.*, **116**, 671–704.
- Stogryn, A., 1967: The apparent temperature of the sea at microwave frequencies, *IEEE Trans. Ant. Propag.*, **AP-15**, 278–286.
- Sundqvist, H., 1978: A parameterization scheme for non-convective condensation including prediction of cloud water, *Quart. J. R. Meteor. Soc.*, **104**, 677–690.
- Takeda, T., and G. Liu, 1987: Estimation of atmospheric liquid water amount by Nimbus 7 data – A new method and its application to the western north-Pacific region, *J. Meteor. Soc. Japn.*, **65**, 931–946.

- Takeda, T., and S. Natsuki, 1982: Estimation of liquid water amount in an extended cloud by Nimbus 5 microwave data, *J. Meteor. Soc. Japn.*, **60**, 1153–1164.
- Taylor, K. E., and S. J. Ghan, 1992: An analysis of cloud liquid water feedback and global climate sensitivity in a general circulation model, *J. Climate*, **5**, 907–919.
- Taylor, V. R., and L. L. Stowe, 1984: Reflective characteristics of uniform earth and cloud surfaces derived from NIMBUS 7 ERB, *J. Geophys. Res.*, **89**, 4987–4996.
- Tjemkes, S. A., G. L. Stephens, and D. L. Jackson, 1991: Spaceborne observation of columnar water vapor: SSMI observations and algorithm, *J. Geophys. Res.*, **96**, 10,941–10,954.
- Trenberth, K. E., 1991: Storm tracks in the southern hemisphere, *J. Atmos. Sci.*, **48**, 2159–2178.
- Tselioudis, G, W. B. Rossow, and D. Rind, 1992: Global patterns of cloud optical thickness variation with temperature, *J. Climate*, **5**, 1484–1495.
- Twomey, S., 1991: Aerosols, clouds and radiation, *Atmos. Environ*, **25A**, 2435–2442.
- Wallace, J. M., G.-H. Lim, and M. L. Blackmon, 1988: Relationship between cyclone tracks, anticyclone tracks and baroclinic waveguides, *J. Atmos. Sci.*, **45**, 439–462.
- Walter, S., 1992: The tropospheric microwave water vapor spectrum: Uncertainties for remote sensing, *Proceedings Third Specialists Meeting on Microwave Radiometry and Remote Sensing Applications*, NOAA Environ. Res. Lab, Boulder, Colorado, 203–210.
- Warren, S. G., 1984: Optical constants of ice from the ultraviolet to the microwave, *Appl. Optics*, **23**, 1206–1225.

- Wassenberg, C. A., 1989: Development of a multi-frequency microwave radiometer for the measurement of atmospheric water vapor and temperature profiles, M. S. Thesis, 101 pp.
- Weare, B. C., 1993: Multi-year statistics of selected variables from the ISCCP C2 data set, *Q. J. R. Meteorol. Soc.*, **119**, 795–808.
- Wentz, F. J., 1991: User's manual SSM/I antenna temperature tapes, Remote Sensing Systems, Santa Rosa, CA, 70 pp.
- Wentz, F. J., 1992: Measurement of oceanic wind vector using satellite microwave radiometers, *IEEE Trans. Geosci. Remote Sens.*, **30**, 960–972.
- Westwater, E. R., 1978: The accuracy of water vapor and cloud liquid determination by dual-frequency ground-based microwave radiometry, *Radio Science*, **13**, 677–685.
- Wielicki, B. A., and R. N. Green, 1989: Cloud identification for ERBE radiative flux retrieval, *J. Appl. Meteorol.*, **28**, 1133–1146.
- Wilheit, T. T., 1979: A model of the microwave emissivity of the ocean's surface as a function of wind speed, *IEEE Trans. Geoscience Electron.*, **GE-17**, 244–249.
- Wilheit, T. T., and A. T. C. Chang, 1980: An algorithm for retrieval of ocean surface and atmospheric parameters from the observations of the Scanning Multichannel Microwave Radiometer, *Radio Science*, **15**, 525–544.
- Wong, T., G. L. Stephens, and P. W. Stackhouse, 1993: The radiative budgets of a tropical mesoscale convective system during the EMEX-STEP-AMEX experiment, 2., Model Results, *J. Geophys. Res.*, **98**, 8695–8711.

Wu, S.-C., 1979: Optimum frequencies of a passive microwave radiometer for tropospheric path-length correction, *IEEE Trans. Antennas Propag.*, **AP-27**, 233–239.

## Appendix A

### INVENTORY OF MISSING SSM/I DATA

Table A.1: Monthly summary of missing SSM/I data for the DMSP F-8 satellite

Year	Month	Missing Days	Missing Data (%)	Year	Month	Missing Days	Missing Data (%)
1987	7	1-8	46	1989	10	23	16
1987	8	25,26	11	1989	11	–	5.4
1987	9	–	6.6	1989	12	–	6.3
1987	10	6,7	16	1990	1	–	4.7
1987	11	–	6.1	1990	2	–	8.9
1987	12	1-31	100	1990	3	–	6.7
1988	1	1-12	45	1990	4	–	7.9
1988	2	–	3.5	1990	5	–	6.7
1988	3	–	6.7	1990	6	–	5.9
1988	4	–	3.4	1990	7	–	4.8
1988	5	6-8	20	1990	8	13,25,26	29
1988	6	–	2.8	1990	9	–	9.5
1988	7	–	3.0	1990	10	–	38
1988	8	–	4.3	1990	11	–	33
1988	9	23	11	1990	12	22-26	36
1988	10	23	1.9	1991	1	–	15
1988	11	–	4.9	1991	2	–	19
1988	12	25-27	19	1991	3	–	25
1989	1	19	11	1991	4	–	19
1989	2	–	5.0	1991	5	–	23
1989	3	–	9.9	1991	6	–	24
1989	4	–	6.3	1991	7	–	21
1989	5	–	4.1	1991	8	–	19
1989	6	7	20	1991	9	–	20
1989	7	23,24	26	1991	10	–	22
1989	8	–	7.3	1991	11	5-8	20
1989	9	–	5.2	1991	12	19,27	48

## Appendix B

### IMPROVED RETRIEVAL ALGORITHMS

Modified and improved water vapor/cloud liquid water retrieval algorithms using the method described in Chapter 2 are now presented. A more suitable analytic form for the upwelling (+) vertical polarization brightness temperature at the top of the atmosphere and the downwelling (-) brightness temperature at the surface, based on a reworking of the results of Tjemkes et al. (1991), can be expressed at frequency  $\nu$  as

$$T_{\nu,\nu}^+ = T_s[1 - (1 - \epsilon_{\nu,\nu})\mathcal{T}_\nu^2] - \Gamma[Z^+ + (1 - \epsilon_{\nu,\nu})Z^-\mathcal{T}_\nu] + T_{cos}(1 - \epsilon_{\nu,\nu})\mathcal{T}_\nu^2 \quad (\text{B.1})$$

$$T_\nu^- = T_s(1 - \mathcal{T}_\nu) - \Gamma Z^+ + T_{cos}\mathcal{T}_\nu \quad (\text{B.2})$$

where

$$Z^+ = \frac{1}{\mu}(\mathcal{T}_{ox,\nu}H_w\tau_{w,\nu} + H_\ell\tau_{\ell,\nu}\mathcal{T}_{\ell,\nu}) \quad (\text{B.3})$$

$$Z^- = \frac{\mathcal{T}_\nu}{\mu}[\mathcal{T}_{ox,\nu}H_w(\tau_{w,\nu} + f\tau_{w,\nu}^2/\mu) + H_\ell\tau_{\ell,\nu}\mathcal{T}_{\ell,\nu}] \quad (\text{B.4})$$

are the atmospheric terms,  $\mathcal{T}_\nu$  is the total transmission of the atmosphere ( $\mathcal{T}_{w,\nu}\mathcal{T}_{\ell,\nu}\mathcal{T}_{ox,\nu}$ ),  $\tau_{w,\nu}$  is the water vapor optical depth ( $\kappa_{w,\nu}W$ ),  $\Gamma$  is the temperature lapse rate ( $\approx 5.8$  deg/km),  $H_w$  is the water vapor scale height ( $\approx 2$  km), and  $T_{cos}$  is the cosmic background brightness temperature ( $\approx 2.7$  K). The transmission terms for water vapor, oxygen and liquid water are defined, respectively, as  $\mathcal{T}_{w,\nu} = \exp(-\tau_{w,\nu}/\mu)$ ,  $\mathcal{T}_{ox,\nu} = \exp(-\tau_{ox,\nu}/\mu)$ , and  $\mathcal{T}_{\ell,\nu} = \exp(-\tau_{\ell,\nu}/\mu)$ , where  $\tau_{\ell,\nu}$  is the liquid water optical depth ( $\kappa_{\ell,\nu}L$ ) and  $\tau_{ox,\nu}$  is the oxygen optical depth. The contribution to the brightness temperatures from the effective height of the liquid water is included as the second term in (B.3) and third term in (B.4)

by assuming that the cloud is a delta function, whereby the liquid water is concentrated at a height  $H_\ell$ . The contribution from the cosmic background is included as the last term in (B.1) and third term in (B.2), although in practical terms it adds very little to the upwelling radiation, being typically less than 1 K. Finally, the quantity  $f\tau_{w,\nu}^2/\mu$  is a second order term in the expansion of  $Z^-$  that was required as a result of discrepancies at 22 GHz between the analytic expression and more detailed calculations of  $T_{v,\nu}^+$ . The expansion gives a value for  $f$  of 0.25; however, a value of 3.2 was found to provide the best results, which was used for all three frequencies.

Figures B.1 and B.2 illustrate how well the simplified model performs relative to more detailed brightness temperature calculations of  $T_\nu^-$  under clear sky and cloudy conditions, respectively, at 19.35, 22.235 and 37 GHz. The humidity and temperature profiles used in these cases are the 81 profiles used previously in Chapter 2. The cloudy simulations, on the other hand, are based on the cloud liquid water and atmospheric profiles shown in Figure 3.1 and the integrated liquid water values in Table 3.1. The values of  $H_\ell$  assumed in these calculations were 750 m, 2.4 km, 4 km, and 2.5 km for cloud 1–cloud 5, respectively, labeled in Figure 3.1. An additional cloud type was also included in these calculations ( $W = 8.7 \text{ kg m}^{-2}$  and  $L = 0.1, 0.2, 0.3, 0.4, 0.6 \text{ kg m}^{-2}$ ) in which  $H_\ell$  was 2 km.

The brightness temperatures computed from (B.2) are in very good agreement, with rms differences of less than 1 K except at 22.235 GHz where it is about 1.2 K. It should also be noted that the 37 GHz brightness temperatures were systematically too high. As a result it was necessary to add a factor of  $-1.2$  K to the brightness temperatures. It is thought that this discrepancy may be caused by the second term in (B.2).

The results of the clear and cloudy comparisons for  $T_{v,\nu}^+$  are shown in Figures B.3 and B.4, respectively. As seen earlier for  $T_\nu^-$ , the brightness temperatures computed from (B.1) also compare very well to the more accurate calculations, again except at 22.235 GHz where the rms difference is 1.4 K. A slightly higher offset of  $-1.5$  K, in contrast to  $T_{37}^-$ , was needed for  $T_{37v}^+$ .

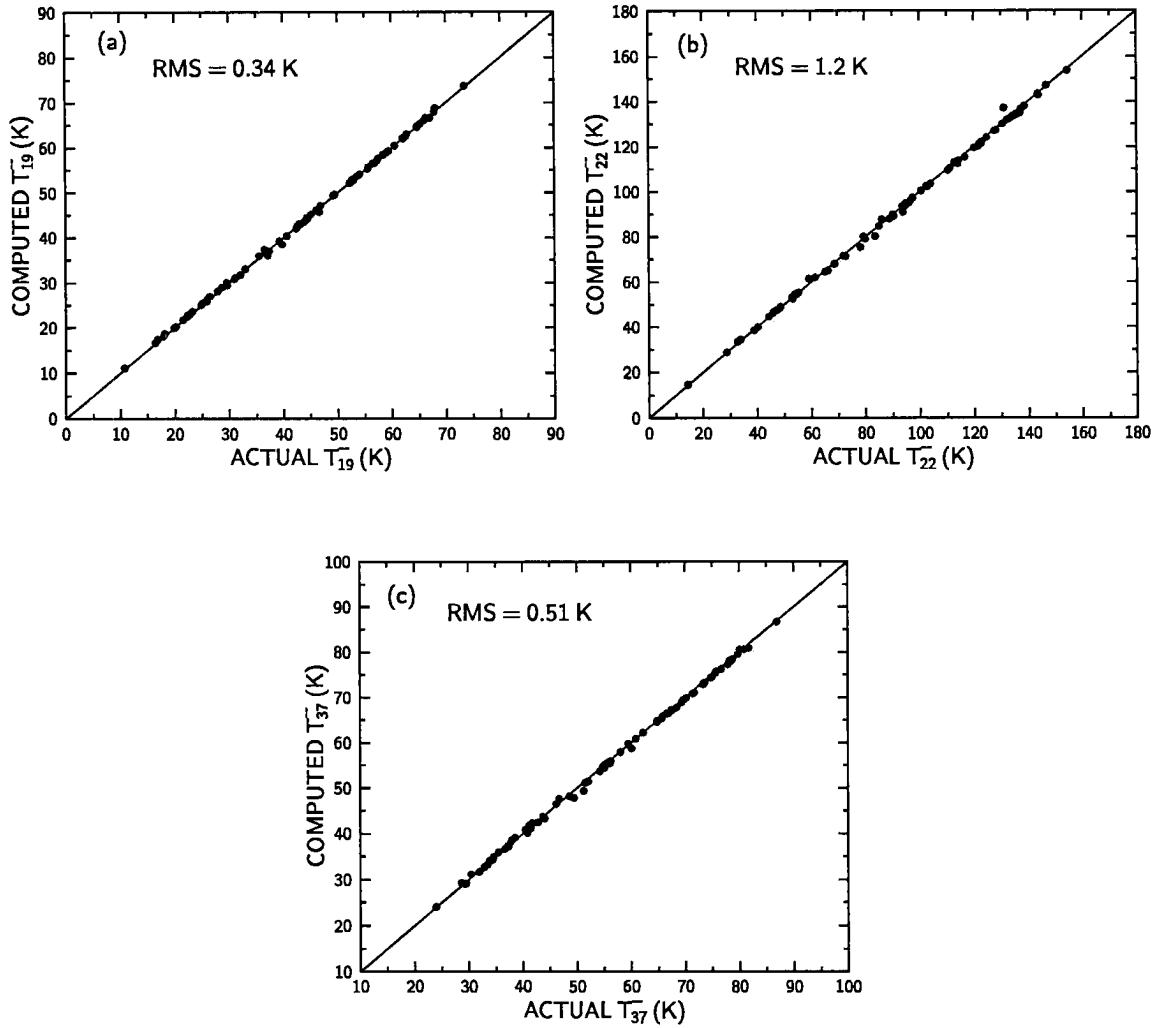


Figure B.1: Scatter diagram of downwelling brightness temperatures ( $T^-$ ) at the surface under clear sky conditions for the simplified model (computed) versus the detailed calculations (actual) at (a) 19.35 GHz, (b) 22.235 GHz, and (c) 37 GHz. Also shown are the line of perfect agreement and the rms differences.

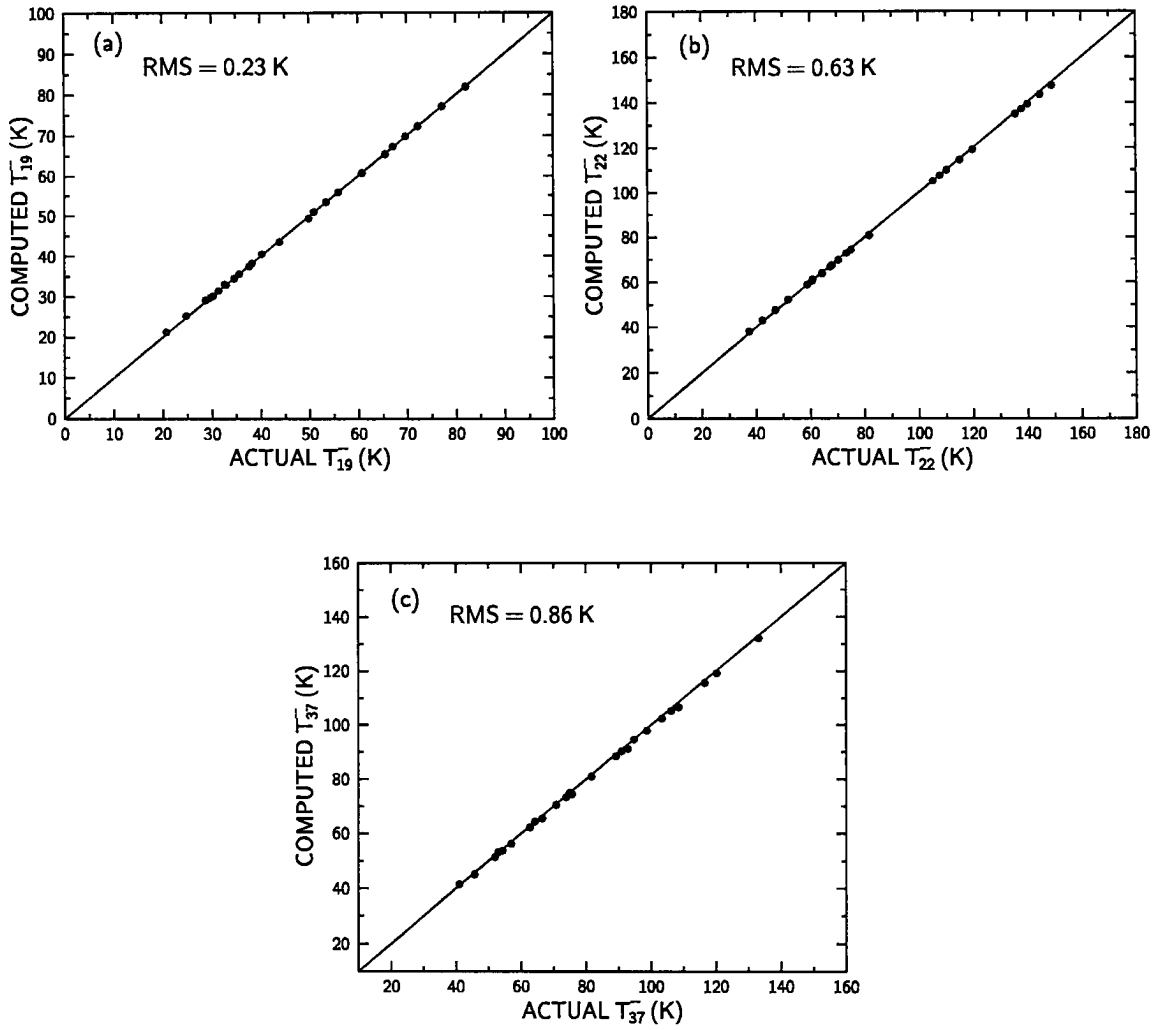


Figure B.2: Same as Fig. B.1 except for cloudy cases.

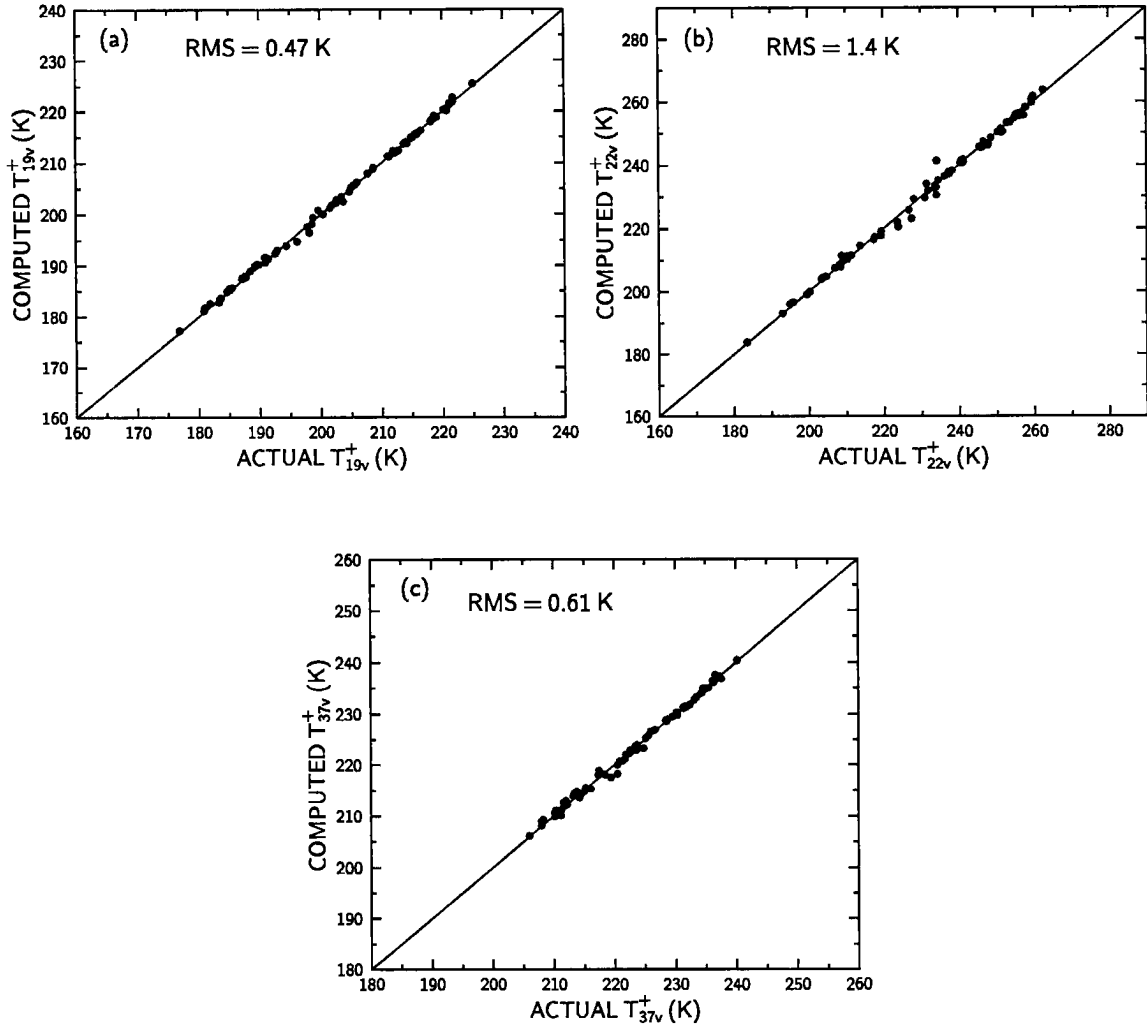


Figure B.3: Scatter diagram of upwelling brightness temperatures at vertical polarization ( $T_v^+$ ) under clear conditions for the simplified model (computed) versus the detailed calculations (actual) at (a) 19.35 GHz, (b) 22.235 GHz, and (c) 37 GHz. Also shown are the line of perfect agreement and the rms differences.

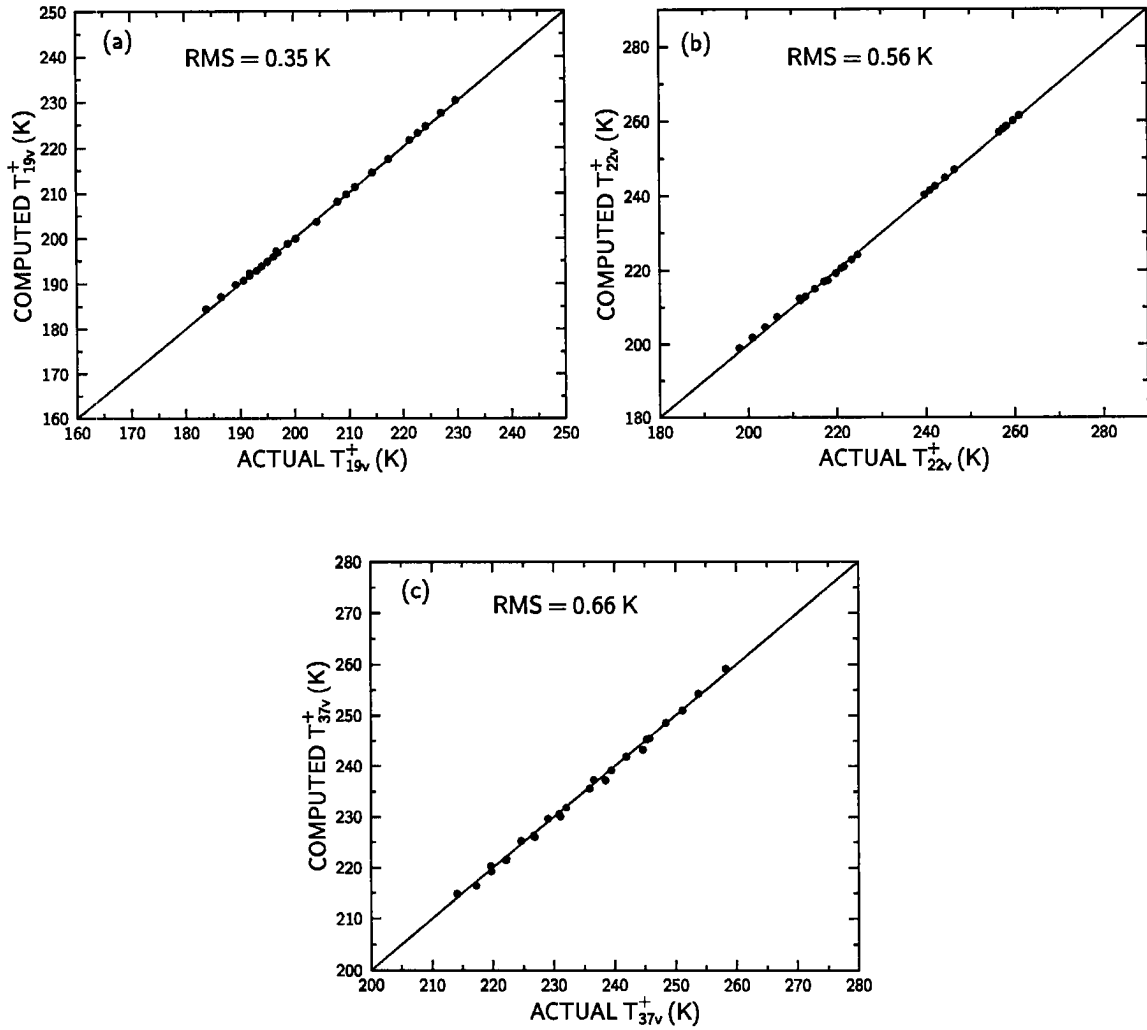


Figure B.4: Same as Fig. B.3 except for cloudy cases.

As discussed in Chapter 2, the oxygen transmittance was found to depend on the surface air temperature ( $T_a$ ). Here we have allowed the oxygen optical depth ( $\tau_{ox,\nu}$ ) to vary as a function of temperature. Figure B.5 shows a scatter diagram of  $\tau_{ox}$  at 19.35, 22.235, and 37 GHz versus  $T_a$  for the 81 temperature profiles. Table A.1 indicates the fit coefficients for cubic fits of the form  $\tau_{ox,\nu} = c_{1,\nu} + c_{2,\nu}T_a + c_{3,\nu}T_a^2 + c_{4,\nu}T_a^3$  for  $T_a \geq 0^\circ\text{C}$ , where the monthly mean SST in degrees Celsius is substituted for  $T_a$ . When  $T_a < 0^\circ\text{C}$ , then  $\tau_{ox,\nu} = c_{1,\nu}$ .

The water vapor coefficients,  $\kappa_{w19}$  and  $\kappa_{w22}$ , are determined to be  $2.36 \times 10^{-3} \text{ m}^2 \text{ kg}^{-1}$  and  $6.40 \times 10^{-3} \text{ m}^2 \text{ kg}^{-1}$ , respectively, using the millimeter wave transmission model of Liebe (1981) and the 81 radiosonde temperature and humidity profiles. These values were slightly adjusted to values of  $2.3 \times 10^{-3} \text{ m}^2 \text{ kg}^{-1}$  and  $6.19 \times 10^{-3} \text{ m}^2 \text{ kg}^{-1}$  to provide a better match to near-coincident radiosonde measurements. Again, adjustments such as these are inevitable given the uncertainties in water vapor transmission at microwave wavelengths.

Based on the calibration procedure described in Chapter 2,  $\kappa_{w37}$  was determined to be  $2.04 \times 10^{-3} \text{ m}^2 \text{ kg}^{-1}$  for the 19 GHz water vapor retrievals and  $1.93 \times 10^{-3} \text{ m}^2 \text{ kg}^{-1}$  for the 22 GHz water vapor retrievals. The results are illustrated in Figure B.6. Also, the bias corrections in the 37v GHz brightness temperature ( $\Delta T_{37v}$ ) were estimated to be 1.31 and 0.95 K for the 19 and 22 GHz retrievals, respectively. The calibration gives slightly different values for  $\kappa_{w37}$  and  $\Delta T_{37v}$  at the two frequencies since it also accounts for other effects (i.e., unmodeled effects, surface emissivity biases, etc.), which may differ at 19 and 22 GHz. It is also important to note that these corrections are only for the measurements

Table B.1: Cubic fit coefficients for oxygen optical depths ( $\tau_{ox}$ ) at 19.35, 22.235, and 37 GHz.

$\nu$ (GHz)	$c_1$	$c_2$	$c_3$	$c_4$
19.35	0.0134	$3.86 \times 10^{-5}$	$-4.74 \times 10^{-6}$	$6.12 \times 10^{-8}$
22.235	0.0155	$4.46 \times 10^{-5}$	$-5.57 \times 10^{-6}$	$7.33 \times 10^{-8}$
37	0.0453	$1.33 \times 10^{-4}$	$-1.67 \times 10^{-5}$	$2.26 \times 10^{-7}$

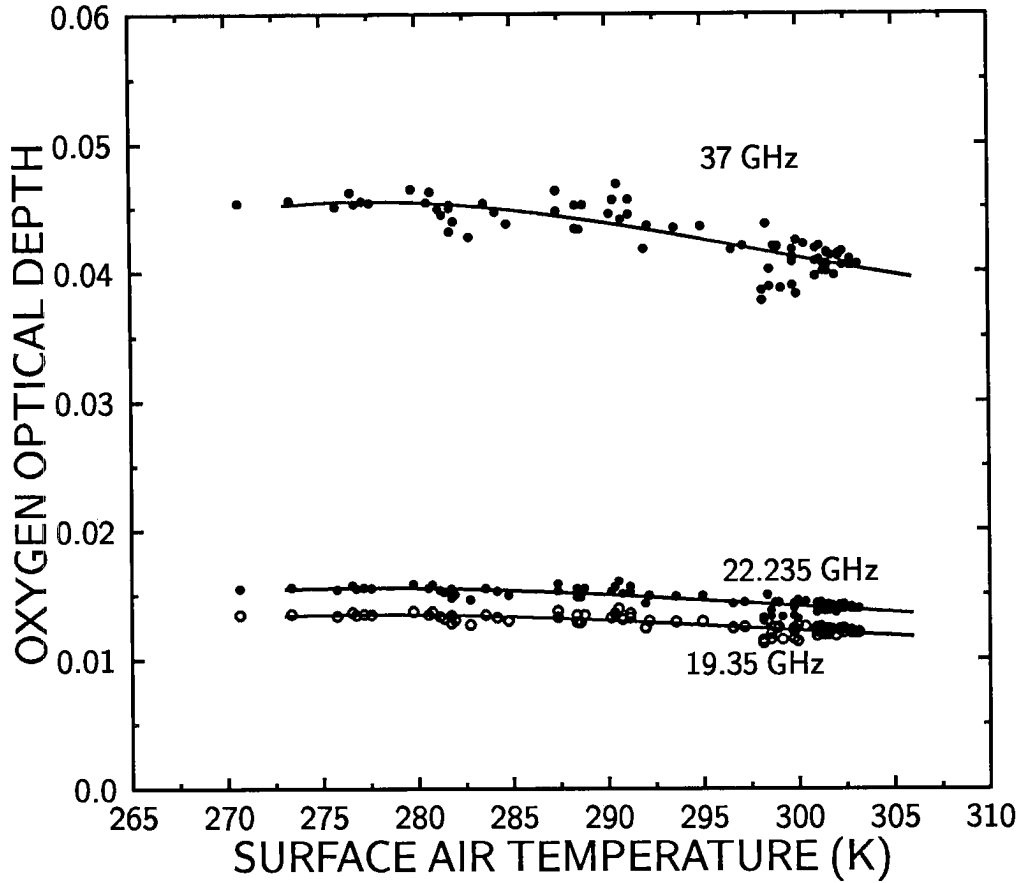


Figure B.5: Scatter diagram of oxygen optical depth versus surface air temperature (K) at 19.35 (open circles), 22.235 and 37 GHz.

from the SSM/I on the F-8 satellite and applying the Petty (1990) roughness emissivity model.

Following the same convention as in Chapter 2, the optical depths for the modified method can be written as:

$$\tau_1 = -\frac{\mu}{2} \ln \left[ \frac{T_s - T_{19v,22v} + T_{19,22}(W, L) - \Delta T_{19v,22v}}{(T_s - T_{cos})(1 - \epsilon_{19v,22v})T_{ox19,22}^2} \right] \quad (\text{B.5})$$

$$\tau_2 = -\frac{\mu}{2} \ln \left[ \frac{T_s - T_{37v} - 1.5 + T_{37}(W, L) - \Delta T_{37v}}{(T_s - T_{cos})(1 - \epsilon_{37v})T_{ox37}^2} \right] \quad (\text{B.6})$$

where  $\tau_1$  is defined for either the 19.35v or 22.235v channels, the factor 1.5 is the offset for  $T_{37v}$  in order for the simple model to agree with the more detailed calculations as discussed earlier, and  $T_v(W, L)$  consists of the terms containing  $\Gamma$  in (B.1), which is a function of  $W$  and  $L$ . The quantities  $\Delta T_{19v}$ ,  $\Delta T_{22v}$ , and  $\Delta T_{37v}$  account for possible sources of bias,

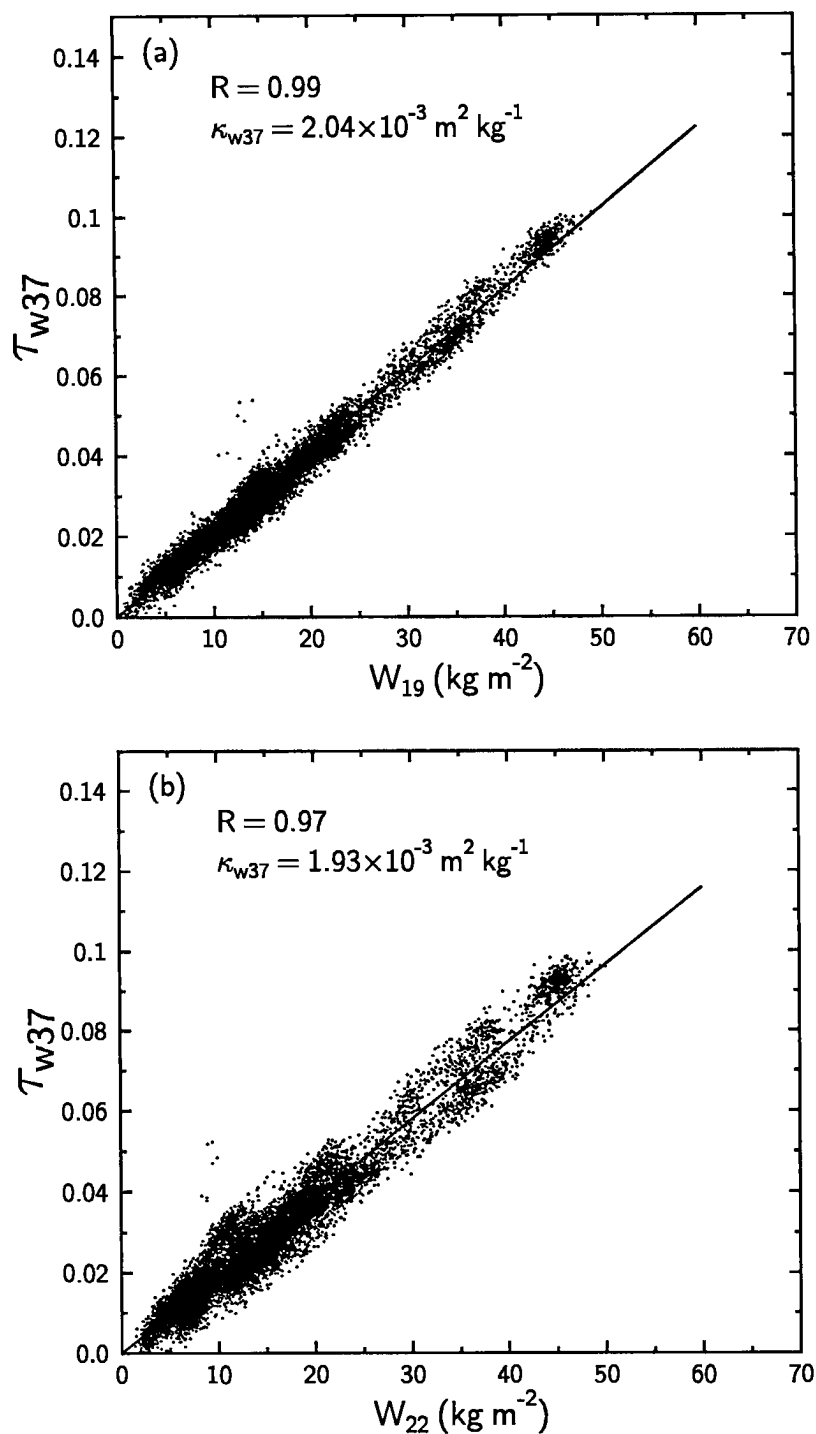


Figure B.6: Scatter diagrams of total water vapor optical depth at 37 GHz ( $\tau_{w37}$ ) versus water vapor retrieved at (a) 19.35 GHz ( $W_{19}$ ,  $\text{kg m}^{-2}$ ) and (b) 22.235 GHz ( $W_{22}$ ,  $\text{kg m}^{-2}$ ) derived from the cloud-free data set. Also shown are linear least squares fit of the data where the slope corresponds to the water vapor absorption coefficient at 37 GHz ( $\kappa_{w37}$ ) and the linear correlation coefficient of the fit ( $R$ ).

including systematic biases in the brightness temperatures, uncertainties in gaseous absorption, biases in the sea surface emissivities, among others. For the SSM/I on the F-8 satellite  $\Delta T_{19v}$  and  $\Delta T_{22v}$  are estimated to be  $-2.2$  and  $-2.6$  K, respectively. These corrections were determined through a comparison of the water vapor retrievals to radiosonde observations of  $W$ .

Retrievals of  $W$  and  $L$  are obtained by an iterative process. First, initial guesses are found by setting  $T_\nu(W, L) = 0$  in (B.5) and (B.6) and then directly computing  $W$  and  $L$  from (2.8) and (2.9). The initial guesses require an estimate of the surface wind speed ( $u$ ), which is used as input into the roughness emissivity model. For this step, we use the algorithm described by Goodberlet et al. (1989). To obtain solutions for  $W$  and  $L$ , one simply uses the initial guesses to compute  $T_\nu(W, L)$  and a new wind speed from the following preliminary expression (personal communication, Grant Petty, 1993)

$$u' = u - 2.130 + 0.220W - 4.008 \times 10^{-3}W^2, \quad (\text{B.7})$$

which corrects for biases in the Goodberlet et al. algorithm that are known to exist for low and, especially, high water vapor. This process is repeated until adequate convergence is achieved.

Retrievals of  $L$  using the new model for the clear sky data set are shown in Figure B.7. The standard deviation for the 19.35/37 GHz retrievals is  $0.016 \text{ kg m}^{-2}$ , which is the same as the model described in Chapter 2, while the 22/37 GHz retrievals are more variable at  $0.022 \text{ kg m}^{-2}$ . It is recommended that the 19.35 and 37 GHz channels be used for retrievals of  $L$ , but further work is needed to determine the extent of the differences between these two retrieval methods.

For retrievals of  $W$ , on the other hand, the combination of the 22.235 and 37 GHz channels gives superior results for low to moderately high water vapor. The exception is for retrievals at the highest values of  $W$  (greater than about  $55\text{--}60 \text{ kg m}^{-2}$ ), where the retrievals begin to underestimate the actual water vapor. As a result a weighted average of the 19.35 ( $W_{19}$ ) and 22.235 GHz ( $W_{22}$ ) retrievals is used. When  $W_{22}$  is greater than

$53.4 \text{ kg m}^{-2}$ , the following weighting procedure is applied:

$$W = W_{22} + 1.75 - 0.263W_{19} + 4.31 \times 10^{-3}W_{19}^2.$$

This fit was determined by forcing the retrievals of  $W_{22}$  to agree, as well as possible, with the retrievals of  $W_{19}$ .

When compared to radiosonde measurements, the modified method provides substantial improvements over the previous method. In these retrievals the cloud temperature was set as the average of the monthly mean SST and a climatic mid-level cloud top temperature as determined from ISCCP data.  $H_\ell$  was set to 1.5 km. Using the radiosonde

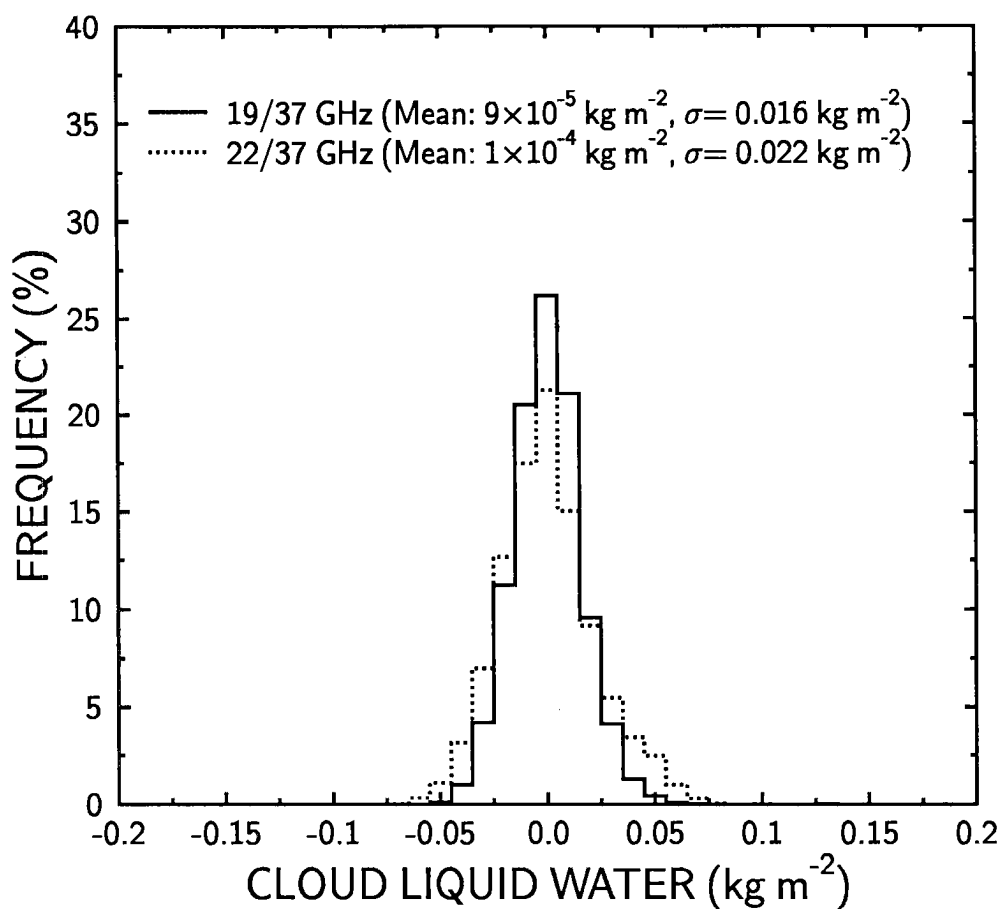


Figure B.7: Histogram of integrated cloud liquid water ( $\text{kg m}^{-2}$ ) retrieved from the cloud-free data set for the 19/37 GHz method (solid) and the 22/37 GHz method (dotted). The mean and standard deviation are also given.

database described in Chapter 2, the rms differences are reduced to  $1.4 \text{ kg m}^{-2}$  for the ICE data and  $4.6 \text{ kg m}^{-2}$  for the TCM Experiment data (see Figure B.8).

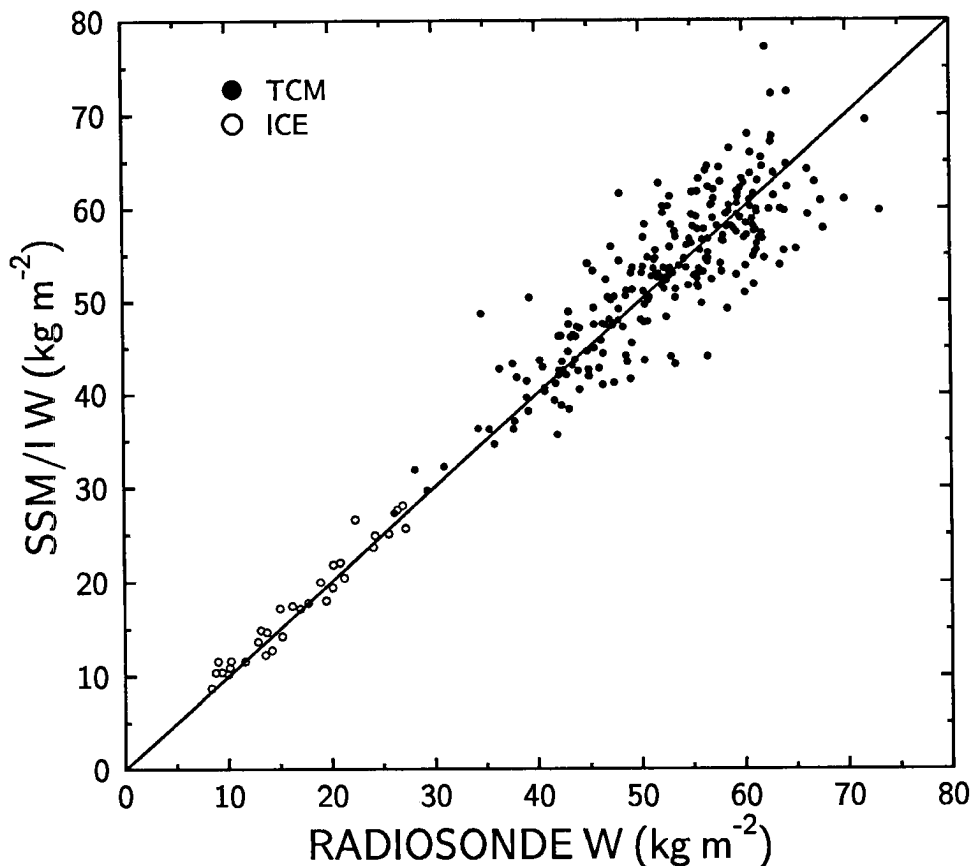


Figure B.8: Scatter diagram of retrievals of  $W$  for the improved algorithm versus near-coincident measurements of  $W$  from radiosondes for the International Cirrus Experiment (ICE) and the Tropical Cyclone Motion (TCM) Experiment. Also shown is the line of perfect agreement.

One final note concerns the specification of the effective cloud temperature. Properly speaking, it is the effective radiating temperature of the cloud that is of ultimate interest. There are several ways to define this quantity. One such way (e.g., Wu, 1979) is:

$$T_{eff,\nu} = \frac{\int_{z_b}^{z_t} T(z) \kappa_{\ell,\nu}(z) e^{-\tau_{\ell,\nu}(z_b,z)} dz}{\int_{z_b}^{z_t} \kappa_{\ell,\nu}(z) e^{-\tau_{\ell,\nu}(z_b,z)} dz} \quad (\text{B.8})$$

where  $T(z)$  is the temperature profile and  $z_t$  and  $z_b$  are the cloud top and cloud base heights, respectively. Unfortunately, (B.8) requires knowledge of the liquid water and temperature profiles, and the cloud base height. However, in many cases it is acceptable

to substitute a mean cloud temperature  $\bar{T}_c$  (i.e., the average of the cloud base and cloud top temperatures) for  $T_{eff,\nu}$ . In the context of global studies, a rough estimate of  $\bar{T}_c$  can be determined from a combination of IR and microwave satellite measurements (e.g., Pandey et al., 1983; Liu and Curry, 1993) provided that relatively thick ice clouds do not exist well above the water cloud. For regional studies a more accurate estimate of  $\bar{T}_c$  may be obtained with the aid of ground-based measurements.